UNIVERSITAT POLITÈCNICA DE CATALUNYA

Ph.D. in Environmental Engineering

Doctoral Thesis

Assessment of Dynamic Aerosol-Radiation Interaction in Atmospheric Models

---

Author:
Vincenzo Obiso

Advisors:
Dr. Oriol Jorba
Dr. Marco Pandolfi

Tutor:
Dr. Santiago Gassó

December 19, 2017

UNIVERSITAT POLITÈCNICA DE CATALUNYA
BARCELONATECH

Barcelona Supercomputing Center
Centro Nacional de Supercomputación

EXCELENCIA SEVERO OCHOA

A Margherita

Abstract

In this thesis an assessment of the parameterization of the Aerosol-Radiation Interaction (ARI) in online integrated meteorology-chemistry models has been conducted. The atmospheric aerosols can affect meteorology and climate mainly through the interaction with the radiation and the clouds. In particular, the ARI radiative effects are caused by the scattering and absorption of shortwave and longwave radiation by the particles, which thus directly affect the Earth energy balance and the heating rates in atmosphere. The estimates of these ARI radiative effects by Chemical Weather Forecast (CWF) models are still affected by significant uncertainty, mainly caused by a poor constraining of aerosol optical and microphysical properties. In order to identify the more important sources of uncertainty in parameterizing the aerosol properties in atmospheric models, we firstly carried out two sensitivity studies of aerosol optical properties and ARI radiative effects to reference microphysical properties for the particles assumed in a state-of-the-art online integrated meteorology-chemistry model, the NMMB-MONARCH.

In the first study, perturbed assumptions on size distribution, refractive index, mass density (±20%) and shape (spheroids) have been considered for mineral dust, organic carbon and sulfate, in order to generate variability in values and spectral dependence of mass scattering cross sections (simulated with a T-matrix code in the visible range) induced by the uncertainty affecting the particle microphysical properties. In general, size distribution and refractive index have been found to have the most important impacts on the scattering properties in most cases. Some constraints on these two properties (suitable for the north-western Mediterranean) have also been found by means of a comparison between simulated and observed mass scattering cross sections. The observations have been provided by the Institute of Environmental Assessment and Water Research (IDAEA-CSIC), after collecting 4-years aerosol measurements (at Montseny station - Spain) and applying Multilinear Regression (MLR) to scattering and mass concentration data. In general lower values of effective radius have been found more suitable for all the analyzed species and also a higher real refractive index for sulfate, with respect to the reference assumptions.

In the second study, size distribution and refractive index of mineral dust and organic carbon have been perturbed similarly to the first study and also two mixing states (internal and external) for a black carbon-sulfate mixture have been considered. The impacts of these perturbations on optical properties (optical depth, single scattering albedo and asymmetry factor, simulated with a T-matrix code) and ARI radiative effects (simulated in the shortwave region with the RRTMG: radiative transfer model implemented in the NMMB-MONARCH and widely used in global and regional weather and climate models) have been analyzed. Different impacts on the optical properties have been found for mineral dust and organic carbon, mainly due to the different mean size of the two species, while an enhanced absorption has been observed for the internal mixing between black carbon and sulfate. The perturbation-induced absolute variations of the ARI radiative effects have been found notable, especially in extreme aerosol events. However, the relative variations of the ARI radiative effects

with respect to base radiative fluxes (in absence of aerosols) have been found always lower than the perturbation range applied to size distribution and refractive index parameters.

As technical effort in this thesis, the full online coupling between aerosol module and radiation scheme in the NMMB-MONARCH has been implemented and also evaluated by comparing with observations the intensive optical properties (single scattering albedo and asymmetry factor) required by the RRTMG (radiation scheme of the model) and calculated during runtime. Global aerosol simulations for a 5-years period (2012-2016) have been run with the NMMB-MONARCH with activating the online coupling for all the species, based on the reference particle microphysical parameterization used in the model (mainly derived from the OPAC dataset). Observations from the Aerosol Robotic Network (AERONET: Version 2.0 - manually screened Level 1.5 inversion products) have been used, after filtering 59 stations based on the number of available data per month (a subset of 12 stations has further been selected for a more detailed analysis of the annual cycles of the two intensive optical properties). Based on the results of the two sensitivity studies, also a perturbed case has been defined by substituting the reference refractive indexes (taken from the OPAC database) with new refractive indexes for almost all the species (taken from recent literature). The impacts of these perturbations on the model skills in simulating intensive optical properties have been analyzed. In general the model has been found to subestimate the observed single scattering albedo and to overestimate the observed asymmetry factor in most stations. These observed main biases have been partially corrected by introducing the new refractive indexes: mainly a lower imaginary part for mineral dust, lower imaginary parts for both primary organic matter (POM) from urban/industry sources and secondary organic aerosol (SOA) from biogenic sources, and a higher real part for sulfate (in agreement with our first study). However, possible errors in the simulation of specific species (too low fine to coarse ratio for mineral dust, close to dust sources and at low altitudes, too high mass concentrations for black carbon and lack of small and scattering particles) have been identified as possible important contributors to the observed mean biases.

Hence, the three works carried out in this thesis produced very useful results for improving the model estimates of ARI radiative effects. In the sensitivity studies we found that size distribution and refractive index have the most significant impacts on the simulated optical properties and ARI radiative effects (with respect to mass density, shape and mixing state). Moreover we provided constraints on these properties (for the north-western Mediterranean) and also a quantification of the propagation of microphysical uncertainties throughout the optical and radiative simulations usually required by the online coupling in CWF models. In the third work, in addition to possible errors of aerosol mass simulations (identified for the NMMB-MONARCH) we found that suitable refractive indexes for the species can significantly improve the simulations of intensive optical properties and consequently the model estimates of ARI radiative effects.

Resumen

En esta tesis se ha realizado un análisis de la parametrización de la interacción Aerosol-Radiación (IAR) en modelos meteorológico-químicos integrados on-line. Los aerosoles atmosféricos pueden afectar a la meteorología y al clima principalmente mediante la interacción con la radiación y las nubes. En particular, los efectos radiativos IAR son causados por la dispersión y la absorción de la radiación de onda corta y larga por las partículas, que afectan directamente al balance energético de la Tierra y los flujos de calor en la atmósfera. Las estimaciones de los efectos radiativos IAR por los modelos de Predicción del Tiempo Químico (PTQ) se ven afectadas por una incertidumbre muy significativa, causada mayoritariamente por una pobre caracterización de las propiedades ópticas y microfísicas de los aerosoles. Con el objetivo de identificar las fuentes de incertidumbre más importantes en la parametrización de las propiedades de los aerosoles en los modelos atmosféricos, inicialmente realizamos dos estudios de sensibilidad de las propiedades ópticas y de los efectos radiativos IAR a las propiedades microfísicas de referencia de las partículas asumidas en un modelo meteorológico-químico integrado on-line, el NMMB-MONARCH.

En el primer estudio se han considerado perturbaciones de los valores por defecto de distribución de tamaños, índice de refracción, densidad de masa (±20%) y forma (esferoides) para el polvo mineral, el carbono orgánico y el sulfato, con el objectivo de generar variabilidad en valores y dependencia espectral de las eficiencias de dispersión (simuladas con código T-matrix en el rango visible) inducida por la incertidumbre que afecta las propiedades microfísicas de las partículas. En general, encontramos que la distribución de tamaños y el índice de refracción tienen el efecto más importante en las propiedades de dispersión de la radiación en la mayoría de los casos. Además, se han encontrado algunos ajustes para estas dos propiedades (adecuados para el noroeste del Mediterráneo) mediante la comparación entre valores simulados y observados de eficiencia de dispersión. Las observaciones, proporcionadas por el Instituto de Diagnóstico Ambiental y Estudios del Agua (IDAEA-CSIC), han sido derivadas utilizando medidas de aerosoles tomadas durante 4 años (en la estación Montseny, España) y aplicándoles una regresión multilineal a los datos de concentraciones de masa y de dispersión. En general hemos encontrado que valores menores de radio efectivo son más adecuados para todas las especies analizadas y también un índice de refracción real más elevado para el sulfato, con respecto a las suposiciones de referencia.

En el segundo estudio, la distribución de tamaños y el índice de refracción del polvo mineral y del carbono orgánico se han perturbado de forma similar al primer estudio y también se han considerado dos estados de mezcla (interna y externa) para una mezcla de carbono negro y sulfato. Se han analizado los impactos de estas perturbaciones en las propiedades ópticas (espesor óptico, albedo de dispersión simple y factor de asimetría, simuladas con un código T-matrix) y efectos radiativos IAR (simulados en la región de onda corta con el RRTMG: modelo de transferencia radiativa implementado en el NMMB-MONARCH y ampliamente usado en modelos climáticos y meteorológicos regionales y globales). Se han encontrado diferentes impactos en las propiedades ópticas para el polvo mineral

y el carbono orgánico, principalmente debido a las diferencias en tamaño medio de las dos especies, mientras se ha encontrado una absorción mayor para la mezcla interna entre carbono negro y sulfato. Se han encontrado notables variaciones absolutas de los efectos radiativos IAR inducidas por las perturbaciones, especialmente en eventos de muy alta concentración de aerosoles. Sin embargo, se ha encontrado que las variaciones relativas de los efectos radiativos IAR con respecto a los flujos radiativos de base (sin aerosoles) son siempre menores que el rango de perturbación aplicado a los parámetros de la distribución de tamaños de partículas y del índice de refracción.

Como esfuerzo técnico en esta tesis, se ha implementado el acoplamiento on-line entre el módulo de aerosoles y el esquema radiativo en el NMMB-MONARCH y también se han evaluado las propiedades ópticas intensivas (albedo de dispersión simple y factor de asimetría), requeridas por el RRTMG (esquema radiativo del modelo) y calculadas durante la ejecución, comparando con observaciones. Las simulaciones globales de aerosoles para un período de 5 años (2012-2016) se han ejecutado con el NMMB-MONARCH activando el acoplamiento on-line para todas las especies, basado en la parametrización microfísica de referencia para las partículas empleada en el modelo (principalmente derivada de la base de datos OPAC). Se han utilizado observaciones de la Aerosol Robotic Network (AERONET: Version 2.0 - datos de nivel 1.5 limpiados manualmente) de 59 estaciones seleccionadas utilizando como criterio la cantidad de datos disponibles por mes (además, se ha seleccionado un subconjunto de 12 estaciones para un análisis pormenorizado de los ciclos anuales de ambas propiedades ópticas intensivas). Basándonos en los resultados de los dos estudios de sensibilidad, también se ha definido un caso en el que se han sustituido los índices de refracción de referencia (obtenidos de la base de datos OPAC) con nuevos índices de refracción para casi todas las especies (derivados de la literatura científica reciente). Se ha analizado el impacto de estas variaciones en la capacidad del modelo de simular adecuadamente las propiedades ópticas intensivas. En general, el modelo subestima el albedo de dispersión simple observado y sobrestima el factor de asimetría en la mayoría de las estaciones. Estos errores sistemáticos identificados se han corregido parcialmente introduciendo los nuevos índices de refracción: principalmente una menor parte imaginaria para el polvo mineral, la materia orgánica primaria (POM), procedente de fuentes urbanas/industriales, y los aerosoles orgánicos secundarios (SOA), de fuentes biogénicas, además de una mayor parte real para el sulfato (al igual que en nuestro primer estudio). Sin embargo, posibles errores en la simulación de especies específicas (una fracción demasiado alta de partículas gruesas de polvo mineral, cerca de fuentes de polvo a bajas altitudes, concentraciones demasiado altas de carbono negro y falta de partículas finas de dispersión) se han identificado como posibles causantes de los errores sistemáticos identificados.

En conclusión, los tres trabajos realizados en esta tesis han producido resultados muy útiles para mejorar la estimación del modelo de los efectos radiativos IAR. En los estudios de sensibilidad hemos encontrado que la distribución de tamaños y el índice de refracción tienen los impactos más significativos en las propiedades ópticas simuladas y los efectos radiativos IAR (con respecto a la densidad de masa, la forma y el estado de mezcla). Además, encontramos ajustes en estas propiedades (para el noroeste del Mediterráneo) y también una cuantificación de la propagación de incertidumbres microfísicas en las simulaciones ópticas y radiativas requeridas normalmente por el acoplamiento on-line en modelos PTQ. En el tercer trabajo, además de los posibles errores en las simulaciones de masa de aerosoles (identificados para el NMMB-MONARCH) hemos encontrado que índices de refracción adecuados para las especies pueden mejorar significativamente las simulaciones de las propiedades ópticas intensivas y consecuentemente la estimación de los efectos radiativos IAR en los modelos atmosféricos.

Acknowledgements

I would like to especially thank my supervisors, Oriol and Marco. In these four years they always guided and supported me not only from a scientific point of view but also at human level, above all in some periods of discouragement (very typical for PhD students). I learnt very much from them, achieving thus the first important step of my scientific and professional formation. I know that this is a big luck and so thanks very much again. Special thanks also to Carlos, for the very useful scientific suggestions on my research work and also for assuring organization and economic stability to our group, essential elements to produce good scientific research.

Obviously I want to thank all my friends/colleagues, especially Francesco (fundamental support for my progresses with Python), Jaime and Enza (for their ability to listen to others and to give useful suggestions), Antonis (for the always instructive discussions) and Maria (for her kind and always useful help with the UPC issues). Thanks also to the PhD students: Rubén, Lluís, Bianca, Dani and Bala who shared with me their working space and meal times, contributing to create a comfortable work environment. Finally I would like to thank all the Earth Science people and especially the director, Paco, for creating a dynamic and very efficient department which contributed to increase the quality of our work. The final and more special thanks go to my girlfriend, Margherita, who really suffered my last month stress in the everyday life.

Funding sources

This work has been funded by the Spanish Ministry of Economy and Competitiveness [grant: CGL2013-46736-R] and by the ACTRIS Research Infrastructure Project of the European Union's Horizon 2020 research and innovation programme [grant agreement: No. 654169]. Further support has been provided by the Severo Ochoa Program, awarded by the Spanish Government [grant: SEV-2011-00067]. This work was also supported by the MINECO (Spanish Ministry of Economy and Competitiveness), the MAGRAMA (Spanish Ministry of Agriculture, Food and Environment) and FEDER funds under the PRISMA project [grant: CGL2012-39623-C02/00]. Further fundings have been provided by the European Union's Horizon 2020 research and innovation programme [grant agreement: No. 654109]. Vincenzo Obiso is funded by the Spanish Ministry of Economy and Competitiveness ['FPI-SO' grant: SVP-2013-067953].

Contents

Chapter 1

Introduction

1.1 Atmospheric aerosols and direct radiative effect

Atmospheric aerosols are solid/liquid particles suspended in air. Aerosols, cloud drops and raindrops are all considered particles but while almost all mass of cloud drops and raindrops (hydrometeors) is liquid water, aerosols contain large fractions of other material as well [Jacobson, 2005]. Aerosols exist with different sizes (from $\sim 10^{-3}$ to 10^{2} μm) and chemical compositions, depending on their formation mechanism and the physico-chemical processes (aging) occurred in their lifecycle [Jacobson, 2005]. Primary aerosols are directly emitted into the atmosphere by anthropogenic or natural sources while secondary aerosols form in atmosphere through gas-to-particle conversion from natural and anthropogenic gaseous precursors [Boucher et al., 2013]. Natural sources of primary aerosols and precursors can be wind erosion, oceans, volcanoes, terrestrial and marine ecosystems while anthropogenic sources are mainly fossilfuel and biofuel combustions, vegetation fires, urban and industrial processes. Major aerosol components in atmosphere are mineral dust, sea salt, primary organic matter, black carbon, sulfates, nitrates and secondary organic aerosols [Boucher et al., 2013].

Atmospheric aerosols can affect meteorology and climate mainly through the interaction with the electromagnetic radiation and with clouds. Following the Fifth Assessment Report (AR5) of the Intergovernmental Panel on Climate Change (IPCC), the aerosol radiative effects can be summarized as follows [Boucher et al., 2013]:

- the direct radiative effect refers to the changes in radiative fluxes due to Aerosol-Radiation Interaction (ARI radiative effects). Aerosols can indeed scatter and absorb shortwave and longwave radiation and also re-emit longwave radiation, thus directly affecting the radiation balances and the heating rates in atmosphere;
- the semidirect radiative effect is due to the atmosphere rapid adjustments caused by the ARI. Changes in radiative fluxes due to ARI generate indeed rapid atmospheric responses, including for example variation in atmospheric stability and cloud cover, which in turn further affect the radiative fluxes;
- the indirect radiative effect is due to the Aerosol-Cloud Interaction (ACI). Aerosols can act as cloud condensation nuclei (CCN) or ice nuclei (IN) affecting in this way the cloud properties (albedo and lifetime) and consequently the radiative fluxes.

All these aerosol radiative effects may be important for the atmospheric processes on a wide range of spatial and temporal scales [Baklanov et al., 2014]. In the atmosphere modeling community, however, while the important role of aerosols in climate studies has long been recognized, the aerosol impact in Numerical Weather Predictions (NWP) models is less well known [Mulcahy et al., 2014]. Traditionally, dynamic aerosol feedbacks were not considered in NWP models, due above all to the lack of computational power needed for calculations at high spatial and temporal resolutions [Baklanov et al., 2014]. In the last decade, thanks to a huge computational capacity increase, the integration of NWP models and Chemical Transport Models (CTM) has become possible and so Chemical Weather Forecast (CWF) models have been developed. The online integration between chemistry and meteorology models gives the possibility to couple the meteorological fields with the aerosol processes and so to evaluate two-way dynamic feedbacks between them [Baklanov, 2010]. A growing number of studies applying online integrated CWF models have become available in the last years, suggesting a clear positive impact of considering dynamic aerosol feedbacks on the weather forecasts [Baklanov et al., 2014]. The implementation of realistic dynamic feedbacks between aerosols and meteorology in high-resolution NWP models is being, therefore, increasingly recognized as an important tool to improve the accuracy of the short- and mid-term weather forecasts [Mulcahy et al., 2014].

Although the most important online integrated models consider (at least) dynamic ARI radiative effects, the level of parameterization details differs strongly between different models [Baklanov et al., 2014]. Implementing the dynamic ARI in CWF models mainly requires knowledge of the aerosol optical properties such as extinction coefficient, single scattering albedo and asymmetry factor. Hence, simulation of suitable aerosol dynamic concentrations (emission, transport, removal, etc.), assumptions for the particle microphysical properties (size distribution, refractive index, mixing state, shape, etc.), accuracy of the radiative transfer models (line-by-line, k-correlated, etc.) and water uptake parameterization (which affects the scattering properties of the particles) are all important sources of uncertainty and consequently of large differences between model estimates of ARI radiative effects [Baklanov et al., 2014]. A number of measurement-based approaches estimate the clear-sky shortwave ARI radiative effects (annual average) to be about $-5,5 \pm 0,2\ Wm^{-2}$ at the top of atmosphere (TOA) and $-8,8 \pm 0,7\ Wm^{-2}$ at surface, over the oceans, while $-4,9 \pm 0,7\ Wm^{-2}$ at the TOA and $-11,8 \pm 1,9\ Wm^{-2}$ at surface, over land [Yu et al., 2006]. However, CWF simulations derive a wide range of ARI radiative effect estimates that on average are smaller than the measurement-based estimates by about $30 - 40\%$ [Yu et al., 2006]. In the context of the climate change, Myhre et al. [2013b] provide a best estimate of the anthropogenic ARI radiative forcing of $-0,35 \pm 0,50\ Wm^{-2}$, highlighting that strong differences between model estimates persist and that the ARI radiative forcing is the main contributor to the Industrial Era forcing uncertainty. Errors in the estimation of aerosol optical properties are considered the main sources of the large uncertainty affecting the ARI radiative effect model estimates [Randles et al., 2013]. These errors are in turn substantially caused by an incomplete knowledge concerning the microphysical properties of the particles [Yu et al., 2006]. Hence further investigation on the parameterization of aerosol optical and microphysical properties in atmospheric models is clearly still needed.

1.2 Main objective

The main objective of this thesis has been the deep assessment of uncertainty sources and parameterization methods of the dynamic ARI in online integrated CWF models. This objective has been achieved by means of three specific objectives: i) sensitivity study of the aerosol scattering properties in the visible range to perturbed microphysical assumptions for the particles (presented in Chapter 3); ii) sensitivity study of shortwave ARI radiative effects to particle microphysical perturbations (presented in Chapter 4); iii) implementation and evaluation (analysis of aerosol intensive optical properties calculated during runtime) of the full online coupling between aerosol module and radiation scheme in a state-of-the-art CWF model, the Multiscale Online Nonhydrostatic AtmospheRe CHemistry model (NMMB-MONARCH) (presented in Chapters 2 and 5).

1.3 Specific objectives

A required research effort of this thesis has been the evaluation of the microphysical properties assumed for the aerosol species in the NMMB-MONARCH, the CWF model under development at the Earth Science department of the Barcelona Supercomputing Center (BSC). As already mentioned, indeed, the ARI parameterization in models requires the characterization of the aerosol optical properties which in turn are calculated starting from the particle microphysical properties [Boucher et al., 2013; Hand and Malm, 2007]. Hence, as specific objectives of this thesis, we carried out two sensitivity studies aiming to understand the relationship between aerosol microphysical and optical properties and to study the impact of uncertainties affecting the aerosol parameterization on the simulated shortwave radiative fluxes (and so on ARI radiative effects). In both studies, the default aerosol parameterization of the NMMB-MONARCH has been approximately taken as reference and perturbations on the particle microphysical parameters have been applied. In the first study, these microphysical perturbations have been used to generate variability in the calculation of aerosol mass scattering cross sections to be compared with observations. Our objective in this case has been assessing the sensitivity of the aerosol scattering properties to possible errors in the reference microphysical assumptions for the particles and to derive also some constraints for the microphysical parameters by means of the comparison with the observations. In the second study, the particle microphysical perturbations have been used instead to generate variability in the calculation of all the aerosol optical properties usually required by the radiative transfer models (namely optical depth, single scattering albedo and asymmetry factor) and consequently in the simulation of ARI radiative effects. Our objective in this case has been to quantify the propagation of the errors in the reference particle microphysical parameterization throughout the optical and radiative simulations necessary for the online coupling between aerosols and radiation in weather and climate models.

As technical effort in this thesis, the full online coupling between aerosol module and radiation scheme has been implemented in the NMMB-MONARCH model. The NMMB-MONARCH is a fully online integrated meteorology-chemistry model for short- and mid-term chemical weather forecasts, able to work both on regional and global scales. In particular, the online coupling already implemented for mineral dust [Pérez et al., 2011] has been extended to all the remaining aerosol species included in the aerosol module: sea salt, organic matter, black carbon and sulfate. The implementation of the full online coupling supplied the model with several new skills. The fundamental one is definitely the possibility to consider the dynamic feedbacks of all the aerosols on the meteorological variables (only through ARI at the moment) during runtime. A second very important skill is the possibility to easily generate offline suitable optical tables for each single species, starting from particle microphysical assumptions which can be modified and improved when desired. A typical evaluation of the full online coupling would require the simulation of ARI radiative effects and the analysis of their impact on the meteorological variables [Baklanov et al., 2014]. However, this seems to be a "second-level" model evaluation because it focuses on the impact of the ARI radiative effects on the simulation of meteorological variables. In other words, this kind of evaluation implicitly relies on the goodness of the aerosol optical properties, because it simply can not provide direct information on them. For this reason, we decided in this thesis work to carry out a more fundamental evaluation of the implemented full online coupling: a direct comparison with observations of the intensive optical properties (single scattering albedo and asymmetry factor) calculated during runtime in the radiation scheme of the NMMB-MONARCH (the optical depth has been already widely evaluated in the past). With this kind of evaluation we intended to address the following three key points: i) identifying eventual systematic biases (with respect to observations) in the intensive optical properties used by the model, which would lead to wrong ARI radiative effect estimates; ii) evaluating the microphysical properties assumed for the particles and also the impacts of a new set of refractive indexes (taken from recent literature) on the model skills in simulating intensive optical properties; iii) getting indirect information on the goodness of the simulated aerosol mixtures and so on possible lack or excess of specific species in the model simulations.

1.4 List of publications

Based on this thesis work the following publications have been produced:

Peer-reviewed papers

- Obiso, V., Pandolfi, M., Ealo, M. and Jorba, O. (2017). Impact of aerosol microphysical properties on mass scattering cross sections. *Journal of Aerosol Science*, 112, 68-82, http://dx.doi.org/10.1016/j.jaerosci.2017.03.001.
- Obiso, V. and Jorba, O. (2018). Aerosol-radiation interaction in atmospheric models: Idealized sensitivity study of simulated short-wave direct radiative effects to particle microphysical properties. *Journal of Aerosol Science*, 115, 46-61, http://dx.doi.org/10.1016/j.jaerosci.2017.10.004 (published online in October 2017).

Papers in preparation

- Obiso, V., Jorba, O., Pandolfi, M. and Pérez García-Pando, C. (unpublished). Aerosol intensive optical properties in the NMMB-MONARCH. *Atmospheric Chemistry and Physics*, in preparation.
- Gkikas, A., Obiso, V., Pérez García-Pando, C., Jorba, O., Hatzianastassiou, N., Vendrell, L., Basart, S., Gassó, S., and Baldasano, J. M. (2017). Direct radiative effects of intense Mediterranean desert dust outbreaks. *Atmospheric Chemistry and Physics Discussions*, https://doi.org/10.5194/acp-2017-932, in review.

Papers in proceedings

- Obiso, V., Pandolfi, M., Ealo, M. and Jorba, O. (2017). Impact of aerosol physical properties on mass scattering cross sections. *Air Pollution Modeling and its Application XXV: Proceedings of the* 35th *International Technical Meeting (ITM), Chania, Crete, Greece, 3 - 7 Oct. 2016.*

Conferences & Workshops

- Obiso V., Jorba O., Basart S., Baldasano J. M. and Nabat P. (2014). Modelling direct radiative effect of mineral dust with the NMMB/BSC-CTM for dust outbreak events over the Mediterranean in Summer 2012. EGU General Assembly 2014, Vienna, Austria, 27 Apr. - 2 May 2014.
- Obiso, V., Pandolfi, M., Ealo, M. and Jorba, O. (2016). Impact of aerosol physical properties on mass scattering cross sections. 35^{th} International Technical Meeting (ITM) on Air Pollution Modeling and its Application, Chania, Crete, Greece, 3 - 7 Oct. 2016.
- Gkikas, A., Obiso, V., Vendrell, L., Basart, S., Jorba O., Pérez García-Pando, C., Hatzianastassiou, N., Gassó, S. and Baldasano, J. M. (2016). Direct radiative effects induced by intense desert dust outbreaks over the broader Mediterranean basin. EGU General Assembly 2016, Vienna, Austria, 17 - 22 Apr. 2016.
- Jorba, O., Di Tomaso, E., Obiso, V., Spada, M., Guevara, M., Basart, S., Schutgens, N. A. J., Janjic, Z. and Pérez García-Pando, C. (2017). Atmospheric Chemistry with the online multiscale NMMB-MONARCH v1.0 model: global-regional evaluations and data assimilation capability. 26^{th} GLOREAM Meeting, Berlin, Germany, 27 - 29 Nov. 2017.

1.5 Organization of the manuscript

This manuscript is organized as follows: in Chapter 2, a general description of the NMMB-MONARCH with a focus on the implementation of the full online coupling between aerosol module and radiation scheme is given. In Chapters 3 and 4, the two sensitivity studies of aerosol scattering properties and ARI radiative effects, respectively, to perturbed particle microphysical properties are presented. In Chapter 5, the evaluation of the full online coupling through the analysis of the intensive optical properties of the model is reported. Finally, our general conclusions and future works are discussed in Chapter 6.

Chapter 2

Online coupling in the NMMB-MONARCH

The NMMB-MONARCH (Multiscale Online Nonhydrostatic AtmospheRe CHemistry) [Pérez et al., 2011; Jorba et al., 2012; Spada et al., 2013; Spada, 2015; Badia et al., 2017; Di Tomaso et al., 2017] is a fully online integrated meteorology-chemistry model for short- and mid-term Chemical Weather Forecasts (CWF). The meteorological core is the Nonhydrostatic Multiscale Model on the B-grid (NMMB) [Janjic and Gall, 2012], which allows simulations on different scales ranging from global to regional. The aerosol module of the NMMB-MONARCH includes 5 natural and anthropogenic species: mineral dust, sea salt, organic matter, black carbon and sulfate (currently, two additional components are being implemented in the model, nitrate and ammonium, but they have not been used in our work since we focused on the global scale, where a simplified aerosol scheme is used). The aerosol module is online coupled with the radiation scheme of the NMMB and with the gas-phase chemistry module of the model. Hence, two-ways dynamic feedbacks between meteorology, aerosols and gases are allowed. In this chapter, a description of the most important modules and processes working in the NMMB-MONARCH is given. A more detailed description of the full online coupling between the aerosol module and the radiation scheme, achieved in this thesis, is given in Section 2.5.

2.1 NMMB meteorological core

The meteorological model NMMB has been developed at the National Centers for Environmental Prediction (NCEP), based on the NCEP's regional Nonhydrostatic Mesoscale Model dynamic core in the Weather Research and Forecasting system (WRF NMM) [Janjic, 2003; Janjic et al., 2010]. The NMMB has been redesigned for the semi-staggered Arakawa B grid and uses regular and rotated latitude-longitude horizontal coordinate systems in global and regional domains, respectively. As vertical coordinate, the hybrid sigma-pressure system [Simmons and Burridge, 1981] with the Lorenz staggering is used [Janjic and Gall, 2012]. The nonhydrostatic dynamics (implemented through an add-on module) is obtained by relaxing the hydrostatic approximation in order to take into account, when needed, the effects of the vertical acceleration of the air masses. The dynamic equations are divided in two parts: i) base hydrostatic terms and ii) nonhydrostatic correction terms proportional to an only one parameter (defined as the ratio of the vertical acceleration to the gravity). Hence, the nonhydrostatic dynamics reduces to the hydrostatic one when this parameter approaches to zero [Janjic and Gall, 2012]. The conservation of several basic and derived dynamical and quadratic quantities is assured by the isotropic quadratic conservative finite-volume horizontal differencing employed in the model. In particular, the conservation of energy and enstrophy improves the accuracy of the nonlinear dynamics at all scales. Details about the numerical schemes used in the model can be found in Janjic [1977, 1979, 1984, 2003]; Janjic et al. [2001, 2011]. In general, the NMMB is designed for a broad range of spatial and temporal scales so that it can be used for both weather forecasts and climate previsions at regional and global scales [Janjic and Gall, 2012]. The regional NMMB has been used at NCEP as the regional North American Mesoscale (NAM) model since October 2011.

2.2 Aerosol processes

All the aerosol species are assumed to be externally mixed in the model and the life-cycle processes are parameterized using a sectional approach for mineral dust and sea salt and a bulk modal approach for organic matter, black carbon and sulfate. The same continuity equation for the dry mixing ratio (q) is separately solved for every size bin/mode (indexed by j) of each species:

$$\partial_t q_j + (\vec{v} \cdot \vec{\nabla})^{hor} q_j = F_j^{trb} + F_j^{prd} + \sum_n F_{j,n}^{snk}, \tag{2.1}$$

in which the superscript hor stands for "horizontal operator" and F^{trb}, F^{prd} and F^{snk} represent turbulence diffusion, production (emissions or secondary sources) and sink/mixing (sedimentation, dry and wet depositions, convective mixing) terms, respectively. The horizontal advection and turbulence diffusion terms are analogous to that for positive defined monotonic tracers in the NMMB (like moisture) [Janjic and Gall, 2012] while the other production/sink terms are briefly described below and reported in detail in Pérez et al. [2011] (from now onwards we omit for simplicity the bin/mode subscript j).

2.2.1 Water uptake

The water uptake of hydrophilic particles can affect several aerosol processes. In the model it is parameterized, following Chin et al. [2002], by correcting the dry particle properties through a hygroscopic growth factor (Φ), defined as the ratio of the dry (r_{dry}) to wet (r_{wet}) particle radius. All those processes affected by water uptake are parameterized for the hydrophilic species by extending the formulation used for mineral dust (dry species) [Pérez et al., 2011] to the wet case, that is by using the corrected wet properties instead of the dry properties. For example, the size distribution extremes, geometric radius and effective radius (generally indicated as r), the mass density (ρ) and the complex refractive index ($n = n_r + in_i$) of hydrophilic particles are affected by the hygroscopic growth and are parameterized as follows:

$$\begin{aligned} r_{wet} &= \Phi r_{dry}, \\ \rho_{wet} &= \rho_{dry} f_v + \rho_{wtr}(1 - f_v), \\ n_{r,wet} &= n_{r,dry} f_v + n_{r,wtr}(1 - f_v), \\ n_{i,wet} &= n_{i,dry} f_v + n_{i,wtr}(1 - f_v), \end{aligned} \tag{2.2}$$

where $f_v = \Phi^{-3}$ is the dry particle volume fraction and the subscript wtr stands for "water". The Φ values for each hydrophilic species and the corresponding relative humidity (RH) levels, both reported in Table 2.1 (Section 2.3), are taken from Chin et al. [2002].

2.2.2 Sedimentation and dry deposition

The sedimentation is the most efficient removal process for large particles and its parameterization is based on the definition of the gravitational settling velocity (v_g) (depending on the water uptake through wet radius and mass density):

$$v_g = \frac{4r_{wet}^2 g(\rho_{wet} - \rho_{air})C_c}{18\nu}, \tag{2.3}$$

in which g is the gravity acceleration, ν is the air viscosity and C_c is the Cunningham correction factor (which accounts for the reduced resistance of air viscosity when the particle size approaches the mean free path of the air molecules). Once calculated v_g for each layer, the sedimentation process for the dry mixing ratio is implicitly solved layer by layer, from column top to bottom, as follows:

$$q_l^{n+1} = q_l^n + q_{l-1}^{n+1}\frac{v_g \Delta t}{\Delta z_{l-1}} - q_l^{n+1}\frac{v_g \Delta t}{\Delta z_l}, \tag{2.4}$$

where n is the timestep index, l is the layer index, Δt and Δz are timestep and layer thickness, respectively.

At the bottom layer the dry deposition take places and its parameterization in the model is based on Zhang et al. [2001] (which includes simplified empirical parameterizations of the deposition processes detailed in Slinn [1982]). The deposition velocity (v_d) is expressed as the sum of the gravitational settling velocity and a layer resistance term:

$$v_d = v_g + \frac{1}{R_a + R_s}, \tag{2.5}$$

where R_a and R_s are aerodynamic and surface resistances, respectively. The aerodynamic resistance takes into account the bottom layer turbulence and it is calculated using the NMMB surface layer scheme (which in turn is based on the Monin-Obukhov similarity theory [Monin and Obukhov, 1954]) and the parameterization of viscous sublayers for land [Zilitinkevich, 1965] and water [Janjic, 1994]. On the other hand, the surface resistance includes the collection efficiencies for Brownian diffusion in the viscous sublayer, impaction and interception. The hygroscopic growth factor is introduced in the definition of R_s for those variables which depend on water uptake.

2.2.3 Wet deposition

The wet deposition due to precipitation is the most efficient removal process for small particles and in the model it is computed separately for grid-scale and convective (sub-grid) clouds, through a coupling with the standard cloud and precipitation schemes implemented in the NMMB: the grid-scale cloud microphysical scheme of Ferrier et al. [2002] and the convective adjustment scheme of Betts-Miller-Janjic (BMJ) [Betts, 1986; Janjic, 1994]. The model also includes different parameterizations for in-cloud (rainout after aerosol nucleation) and below-cloud (aerosol collection by precipitation) scavenging. The liquid-phase aerosol wet deposition flux (F) is computed layer by layer, from column top to bottom, as follows:

$$F_l = F_{l-1}(1 - \alpha f_e) + \Delta F_l, \tag{2.6}$$

in which f_e is the flux fractional loss due to evaporation, α is a tuning parameter representing the probability of evaporation of a rain droplet and ΔF is the flux gain due to the wet scavenging, whose explicit expression depends on the specific process considered.

For **grid-scale in-cloud scavenging**, it is parameterized as follows:

$$\Delta F|_{inc}^{grd} = \epsilon M \left(f_{liq} \frac{R_{liq}}{q_{liq}} + f_{ice} \frac{R_{ice}}{q_{ice}} \right), \tag{2.7}$$

where ϵ is a solubility parameter which expresses the fraction of aerosol loading in the gridcell, M, embedded in cloud liquid water and ice (which therefore can eventually precipitate), f_{liq} and f_{ice} are the fractions of liquid water and ice with respect to the total cloud water, R_{liq} and R_{ice} are their conversion rates (amount of cloud water in the two phases converted into rain in a timestep), respectively, and q_{liq} and q_{ice} the mixing ratios of the two cloud water components. It is important to note that in the model the scavenging is defined as the removal of aerosols from the gridcell and so the aerosol particles embedded in liquid water or ice droplets do not contribute to the in-cloud wet scavenging until they precipitate. Moreover, the in-cloud scavenging due to snow precipitation is not considered.

Since in the BMJ scheme the precipitation produced in a convective cloud is proportional to the total change of moisture in the cloud during the timestep (ΔH_{tot}), for **convective in-cloud scavenging** the flux gain term is calculated as follows:

$$\Delta F|_{inc}^{cnv} = -\epsilon M_{tot} \frac{\Delta H_{tot}}{H_{tot}}, \tag{2.8}$$

where H_{tot} and M_{tot} are the total moisture and aerosol mass loading in the convective cloud at the beginning of the timestep and the negative sign is due to the fact that ΔH_{tot} (always negative) produces a positive flux gain term.

Regarding the **below-cloud scavenging**, the parameterization is the same for both grid-scale and convective clouds and it is based on Slinn [1984]:

$$\Delta F|_{blw} = M \frac{c P_{liq} E_{liq}(D_{liq}, d)}{D_{liq}}, \tag{2.9}$$

where c is a numerical tuning factor, P_{liq} is the liquid precipitation rate (amount of liquid water precipitating in a timestep), E_{liq} is the capture efficiency of liquid water and D_{liq} and d are the diameters of rain droplets and aerosols, respectively. The below-cloud scavenging due to snow precipitation is parameterized in a very similar way.

2.2.4 Convective mixing

The convective mixing parameterization closely follows the principles of the BMJ scheme. After the convective in-cloud scavenging, the eventually remaining aerosol mass in the column is vertically mixed analogously to moisture:

$$\Delta q = (q_{ref} - q) \frac{\Delta t}{\tau / F(E)}, \tag{2.10}$$

in which Δq is the variation profile of the aerosol mixing ratio in a timestep Δt, q the mixing ratio profile at the beginning of the timestep and q_{ref} is a reference profile (following the shape of the reference moisture profile but normalized to the remaining aerosol amount), τ is the characteristic time-scale of the convective adjustment and $F(E)$ a cloud efficiency factor [Janjic, 1994].

2.3 Aerosol species

The microphysical parameterization of the 5 natural and anthropogenic aerosol species implemented in the model is mainly derived from the GOCART model [Chin et al., 2002] (which in turn is based on the OPAC database [Hess et al., 1998]), except for some parameters of mineral dust and sea salt. All the microphysical parameters used for the aerosols are reported in Table 2.1, while the main characteristics of the species parameterization are briefly reported in the following sections.

Table 2.1: **Microphysical parameters for the 5 aerosol species implemented in the NMMB-MONARCH: geometric radius (r_g), standard deviation (σ_g), effective radius (r_{eff}), real (n_r) and imaginary (n_i) refractive indexes, mass density (ρ) and hygroscopic growth factor (Φ). In the second column (Bins/Modes), *phob* stands for "hydrophobic mode" and *phil* for "hydrophilic mode". The bin/mode size ranges ($r_{min} - r_{max}$) used for the size integration are reported within parentheses close to the corresponding r_{eff} values. The 7 values of Φ apply only to the hydrophilic bins/modes of each species and are relative to *RH* levels of (0%; 50%; 70%; 80%; 90%; 95%; 99%). Only dry values for the parameters are reported, the wet values depend on *RH* and can be calculated using Equations 2.2. The refractive indexes reported are relative to the 0,550 μm wavelength.**

Parameters	**Bins**	**Mineral Dust**	**Sea Salt**
r_g $[\mu m]$	$bin1 - bin8$	$2,986 \cdot 10^{-1}$	$1,500 \cdot 10^{-1}$
σ_g	$bin1 - bin8$	$2,000$	$2,800$
r_{eff} $[\mu m]$	$bin1$	$1,493 \cdot 10^{-1}$ $(0,10 - 0,18)$	$1,441 \cdot 10^{-1}$ $(0,10 - 0,18)$
	$bin2$	$2,473 \cdot 10^{-1}$ $(0,18 - 0,30)$	$2,429 \cdot 10^{-1}$ $(0,18 - 0,30)$
	$bin3$	$4,536 \cdot 10^{-1}$ $(0,30 - 0,60)$	$4,499 \cdot 10^{-1}$ $(0,30 - 0,60)$
	$bin4$	$7,832 \cdot 10^{-1}$ $(0,60 - 1,00)$	$7,906 \cdot 10^{-1}$ $(0,60 - 1,00)$
	$bin5$	$1,318$ $(1,00 - 1,80)$	$1,358$ $(1,00 - 1,80)$
	$bin6$	$2,239$ $(1,80 - 3,00)$	$2,320$ $(1,80 - 3,00)$
	$bin7$	$3,802$ $(3,00 - 6,00)$	$4,135$ $(3,00 - 6,00)$
	$bin8$	$7,115$ $(6,00 - 10,0)$	$8,640$ $(6,00 - 15,0)$
n_r	$bin1 - bin8$	$1,530$	$1,500$
n_i	$bin1 - bin8$	$5,500 \cdot 10^{-3}$	$1,000 \cdot 10^{-8}$
ρ $[kg/m^3]$	$bin1 - bin4$	$2,500 \cdot 10^3$	$2,160 \cdot 10^3$
	$bin5 - bin8$	$2,650 \cdot 10^3$	$2,160 \cdot 10^3$
Φ	$bin1 - bin8$	$-$	$(1,0;\ 1,6;\ 1,8;\ 2,0;\ 2,4;\ 2,9;\ 4,8)$
Parameters	**Modes**	**Organic Matter**	**Black Carbon**
r_g $[\mu m]$	$phob - phil$	$2,120 \cdot 10^{-2}$	$1,180 \cdot 10^{-2}$
σ_g	$phob - phil$	$2,200$	$2,000$
r_{eff} $[\mu m]$	$phob - phil$	$1,003 \cdot 10^{-1}$ $(0,005 - 20,0)$	$3,937 \cdot 10^{-2}$ $(0,005 - 20,0)$
n_r	$phob - phil$	$1,530$	$1,750$
n_i	$phob - phil$	$6,000 \cdot 10^{-3}$	$4,400 \cdot 10^{-1}$
ρ $[kg/m^3]$	$phob - phil$	$1,800 \cdot 10^3$	$1,000 \cdot 10^3$
Φ	$phob$	$-$	$-$
	$phil$	$(1,0;\ 1,2;\ 1,4;\ 1,5;\ 1,6;\ 1,8;\ 2,2)$	$(1,0;\ 1,0;\ 1,0;\ 1,2;\ 1,4;\ 1,5;\ 1,9)$
Parameters	**Modes**	**Sulfate**	
r_g $[\mu m]$	$phil$	$6,950 \cdot 10^{-2}$	
σ_g	$phil$	$2,030$	
r_{eff} $[\mu m]$	$phil$	$2,434 \cdot 10^{-1}$ $(0,005 - 20,0)$	
n_r	$phil$	$1,430$	
n_i	$phil$	$1,000 \cdot 10^{-8}$	
ρ $[kg/m^3]$	$phil$	$1,700 \cdot 10^3$	
Φ	$phil$	$(1,0;\ 1,4;\ 1,5;\ 1,6;\ 1,8;\ 1,9;\ 2,2)$	

2.3.1 Mineral dust

The mineral dust module [Pérez et al., 2011] includes 8 hydrophobic and independent transport bins. A time-invariant sub-bin lognormal distribution (based on Zender et al. [2003]) is adopted to allow a more accurate treatment of the bin geometrical and optical properties. The mass density, taken from Nickovic et al. [2001], is different for sub-micron and super-micron bins in order to take into account the different mineralogy. The online emission process accounts for surface wind speed, turbulence, land use type, vegetation cover, erodibility, surface roughness, soil texture and moisture. The emission vertical flux is derived from the horizontal one using the empirical relationship of Marticorena and Bergametti [1995] and size-distributed according to an analytic tri-modal lognormal function [D'Almeida, 1987].

The mass fraction assigned to each transport bin is then given by the overlap between the source modes and the size interval of the bin. The mineral dust module has been exhaustively evaluated in Pérez et al. [2011] and Haustein et al. [2012] (for global and regional domains, respectively). For the simulations with the NMMB-MONARCH run in this thesis we used the dust global configuration of Pérez et al. [2011].

2.3.2 Sea salt

In the sea salt module [Spada et al., 2013] 8 hydrophilic size bins are separately transported and a time-invariant sub-bin lognormal distribution (based on Lewis and Schwartz [2004]) is used. The mass density is derived from Chin et al. [2002]. Five emission scheme [Monahan et al., 1986; Smith and Harrison, 1998; Gong, 2003; Mårtensson et al., 2003; Jaeglé et al., 2011], accounting for bubble-bursting and spume production, are available and online coupled with surface wind speed and sea surface temperature. Detailed evaluations of the sea salt module can be found in Spada et al. [2013] and Spada et al. [2015] (for global and regional domains, respectively). At global scale, the emission scheme of Jaeglé et al. [2011] (dependent on the sea surface temperature) has been found to produce the best model performance but also a significant overestimation of the tropical coarse optical depth during Summer, minimized when using the basic production scheme of Monahan et al. [1986]. For the simulations with the NMMB-MONARCH run in this thesis we used the emission scheme of Jaeglé et al. [2011].

2.3.3 Organic matter

The organic matter module includes 2 bulk modes (1 hydrophobic and 1 hydrophilic) for primary organic matter (POM from urban, industry and biomass burning sources) and 4 bulk modes (all hydrophilic) for secondary organic aerosol (SOA only from biogenic sources). The size distribution (the same lognormal for all the modes) and the mass density are both taken from Chin et al. [2002]. A phobic-to-philic conversion process is used to parameterize the aging of the POM particles (depending on a e-folding time of $1,2$ days [Chin et al., 2002]). The SOA production is implemented in two steps [Tsigaridis and Kanakidou, 2007]: i) oxidation of monoterpenes and isoprene and ii) gas-to-particle partitioning (producing the 4 SOA modes). The carbonaceous part (organic carbon) of the simulated organic matter is derived by dividing the organic matter concentration by the factor $1,8$ which is an intermediate hypothesis between urban and non-urban options suggested by the observations [Turpin and Lim, 2001; Aiken et al., 2008].

2.3.4 Black carbon

In the black carbon module, 2 bulk modes (1 hydrophobic and 1 hydrophilic) are implemented, with lognormal size distribution and mass density taken from Chin et al. [2002]. The same phobic-to-philic conversion mechanism used for POM is implemented for black carbon, with the same e-folding time.

2.3.5 Sulfate

The sulfate module considers only 1 hydrophilic mode, with lognormal size distribution and mass density taken from Chin et al. [2002]. A simplified sulfur chemical mechanism is implemented for the online production of sulfate [Spada, 2015], although a coupling with the full chemical mechanism of the model is possible. Three production channels are considered: i) oxidation of SO_2 (gas-phase),

ii) oxidation of dimethylsulfide (DMS: gas-phase) and iii) aqueous chemistry of SO_2. The needed chemical reactions (gas-phase reactions, gas-aqueous equilibria, acid-base equilibria, aqueous-phase reactions and a photolysis reaction) are constructed with the Kinetic Pre-Processor KPP [Sandu and Sander, 2006]. The reaction rates implemented are mainly those indicated in Sander et al. [2011] with the exception of DMS for which the rates are taken from Emmons et al. [2010]. At the end of the timestep, the sulfuric acid H_2SO_4 instantaneously condenses into sulfate aerosols and the aqueous contribution of the sulfate ion SO_4^{2-} is added.

2.4 Gas module

The gas-phase tropospheric chemistry module [Jorba et al., 2012] is inlined within the NMMB code. Chemical species are advected and mixed using the same numerical schemes implemented in the NMMB. The Carbon-Bond 2005 (CB05) chemical mechanism [Yarwood et al., 2005] and the Fast-J online photolysis scheme [Wild et al., 2000] are implemented. The dry deposition scheme follows Wesely [1989] while the cloud chemistry schemes of Byun and Ching [1999] and Foley et al. [2010] are used to resolve the cloud processes affecting the concentrations of air pollutants. The processes included are convective mixing, grid-scale and convective scavenging (only in-cloud) and wet deposition for both precipitating and non-precipitating clouds. The module transports 9 additional chemical species (precursors) needed for the SOA (monoterpenes, isoprene and 4 first oxidation products) and sulfate (SO_2, DMS, H_2O_2) secondary production. For further chemical species (OH, HO_2 and O_3) needed for the secondary aerosol production, both the options of using mean climatological values or NMMB-MONARCH tracers are available. For the simulations with the NMMB-MONARCH run in this thesis we set the global configuration using mean climatological values from Badia et al. [2017].

2.5 Radiation

By default, the NMMB-MONARCH simulates the Aerosol-Radiation Interaction (ARI) using constant seasonal distributions of aerosol mass concentrations (climatologies) and so can not consider dynamic feedbacks of the simulated aerosols on the meteorological variables. In this thesis work, the online coupling between the aerosol module and the radiation scheme of the model, already implemented only for mineral dust [Pérez et al., 2011], has been extended to all the aerosol species. Thanks to this full online coupling, the direct effect of the large spatio-temporal variability of all the simulated aerosols on the radiative transfer (and consequently on the meteorological variables) can now be taken into account during runtime. Moreover, a tool for the offline calculation of suitable optical properties for all the parameterized species (optical tables) has been added to the model. Hence, a complete description of the implemented full online coupling must include three main components: the radiation scheme of the NMMB (Section 2.5.1), the offline optical tool (Section 2.5.2) and the coupling programming (Section 2.5.3).

2.5.1 Radiation scheme

In the NMMB, the Rapid Radiative Transfer Model for Global Circulation Model applications (RRTMG) [Iacono et al., 2008] is implemented: a 1-D rapid and accurate radiative transfer model suitable for global and mesoscale/regional models (a list of global and regional models using the RRTMG as radiation scheme is reported in Iacono [2011]). The RRTMG is based on the Rapid Radiative Transfer Model (RRTM) of Mlawer et al. [1997]. The RRTM utilizes the k-correlated method [Fu and

Liou, 1992], an approximation technique to perform accelerated calculation of radiative fluxes with an extreme reduction of number of operations. Given a homogeneous layer and a spectral band (conveniently defined to take into account the most important spectrally active gaseous species), the radiative transfer operations are carried out using a small set of absorption coefficients (taken from the LBLRTM model [Clough and Iacono, 1995; Clough et al., 1992]) representative of all the band. This is possible thanks to a mapping of the absorption coefficients from the wavenumber space onto a new cumulative probability space, defined by the variable g (fraction of absorption coefficients smaller than a certain value). In this space the absorption coefficients have a regular increasing trend and so a mean value can be specified for each segment (g-point) of this smoothly varying function [Mlawer et al., 1997].

With respect to the RRTM, the RRTMG includes some new features in order to work as a callable routine of weather and climate models, such as a reduced number of g-points, a Montecarlo method (McICA [Barker et al., 2003]) to represent sub-grid cloud variability, new aerosol input flags and a new faster two-stream algorithm for multiple scattering radiative transfer [Oreopoulos and Barker, 1999]. The RRTMG has been designed to perform rapid calculations in order to save computation time. Obviously, these characteristics (and all the underlying approximations) cause the calculation precision to be slightly lower than that of more complex line-by-line or 3-D radiative transfer models available in literature. However, the RRTMG retains a good accuracy of $\sim 6\ W/m^2$ and $\sim 1,5\ W/m^2$ in the shortwave and longwave regions, respectively, compared to the LBLRTM (direct plus diffuse fluxes) [Iacono et al., 2008]. The RRTMG considers 14 spectral bands in the shortwave region and 16 bands in the longwave region, reported in Table 2.2. The model allows considering the effects of aerosol layers on the radiative transfer simulations by requiring as inputs layer optical depth, single scattering albedo and asymmetry factor of the aerosol mixture for each of the spectral bands. Hence, the radiation scheme of the model not only includes the radiative transfer model but also some interfacing subroutines in which the radiative simulations are initialized, according to ARI configuration and RRTMG requirements, and the aerosol layer optical properties are calculated using the needed model current variables.

Table 2.2: **Wavelength intervals ($\Delta\lambda$) of the RRTMG spectral bands in the shortwave and longwave regions.**

Band Number b	**Shortwave** $\Delta\lambda$ $[\mu m]$	**Longwave** $\Delta\lambda$ $[\mu m]$
1	$0,200 - 0,263$	$3,333 - 3,846$
2	$0,263 - 0,345$	$3,846 - 4,202$
3	$0,345 - 0,442$	$4,202 - 4,444$
4	$0,442 - 0,625$	$4,444 - 4,808$
5	$0,625 - 0,778$	$4,808 - 5,556$
6	$0,778 - 1,242$	$5,556 - 6,757$
7	$1,242 - 1,299$	$6,757 - 7,194$
8	$1,299 - 1,626$	$7,194 - 8,475$
9	$1,626 - 1,942$	$8,475 - 9,259$
10	$1,942 - 2,151$	$9,259 - 10,204$
11	$2,151 - 2,500$	$10,204 - 12,195$
12	$2,500 - 3,077$	$12,195 - 14,286$
13	$3,077 - 3,846$	$14,286 - 15,873$
14	$3,846 - 12,195$	$15,873 - 20,000$
15	–	$20,000 - 40,000$
16	–	$40,000 - 1000,000$

2.5.2 Optical tool

As mentioned in Section 2.5.1, the RRTMG requires optical depth, single scattering albedo and asymmetry factor of the aerosol layers to consider the particle effects on the radiative transfer simulations. Calculating these optical properties in turn requires detailed intensive optical properties for the particles (as explained below). Hence, in order to have more flexibility in calculating the optical properties for the aerosol species of the NMMB-MONARCH, we developed a tool able to generate offline optical tables (containing the intensive optical properties) based on specific microphysical assumptions suitable for each species. The key feature of the tool is that it can be easily re-configured with an improved microphysical parameterization for the particles. This means that the default optical tables used in the model for the online coupling can be replaced with new ones when desired and quite quickly (total computation time $\sim 2h$).

More in detail, the layer optical depth (τ) measures the fraction of radiative energy (at a certain wavelength λ) extinct through scattering and absorption by the particles present in a given homogeneous layer. It can be calculated as follows [Tegen and Lacis, 1996]:

$$\tau_\lambda = \frac{3Q_\lambda^{ext}}{4\rho r_{eff}} M \Delta Z, \tag{2.11}$$

where, in addition to the already introduced symbols, Q^{ext} is the mean extinction efficiency of the particle ensemble, r_{eff} the effective radius and M the layer mass concentration. Hence, τ is an extensive optical property because directly proportional to the aerosol mass concentration and to the thickness of the layer. The intensive part of the optical depth is the mass extinction cross section (k^{ext}):

$$k_\lambda^{ext} = \frac{3Q_\lambda^{ext}}{4\rho r_{eff}}, \tag{2.12}$$

which only depends on the microphysical properties of the particles. In addition to the mass density, indeed, the mean extinction efficiency is calculated as follows [Mishchenko et al., 2002]:

$$Q_\lambda^{ext} = \frac{\int Q_{s,\lambda}^{ext}(r, n_\lambda) \pi r^2 f(r) dr}{\int \pi r^2 f(r) dr}, \tag{2.13}$$

in which Q_s^{ext} is the extinction efficiency of a single particle (function of radius and complex refractive index) and $f(r)$ is the normalized particle number size distribution. The effective radius (representative radius of the ensemble [Hansen and Travis, 1974]) is defined as the projected-area-weighted mean radius [Mishchenko et al., 2002] and can be calculated as follows [Lesins et al., 2002]:

$$r_{eff} = r_g \exp\left(\frac{5}{2} \ln^2 \sigma_g\right), \tag{2.14}$$

where r_g and σ_g are the geometric radius and the standard deviation of the distribution, respectively.

The single scattering albedo (ω) and asymmetry factor (g) (ensemble mean properties) are intensive optical properties, because they only depend on the particle microphysical properties, and are calculated as follows [Mishchenko et al., 2002]:

$$\begin{aligned} \omega_\lambda &= \frac{\int \omega_{s,\lambda}(r, n_\lambda) Q_{s,\lambda}^{ext}(r, n_\lambda) \pi r^2 f(r) dr}{\int Q_{s,\lambda}^{ext}(r, n_\lambda) \pi r^2 f(r) dr}, \\ g_\lambda &= \frac{\int g_{s,\lambda}(r, n_\lambda) Q_{s,\lambda}^{sca}(r, n_\lambda) \pi r^2 f(r) dr}{\int Q_{s,\lambda}^{sca}(r, n_\lambda) \pi r^2 f(r) dr}, \end{aligned} \tag{2.15}$$

where ω_s, g_s and Q_s^{sca} are single scattering albedo, asymmetry factor and scattering efficiency of a single particle. The single scattering albedo is defined as the ratio of the scattering to the extinction efficiency:

$$\omega_{s,\lambda}(r, n_\lambda) = \frac{Q_{s,\lambda}^{sca}(r, n_\lambda)}{Q_{s,\lambda}^{ext}(r, n_\lambda)}, \tag{2.16}$$

and represents a fractional measure of the scattered energy with respect to the extinct energy (always $\omega_s \leq 1$). On the other hand, the asymmetry factor is defined as the first moment of the scattering phase function (P):

$$g_{s,\lambda}(r, n_\lambda) = \frac{1}{4\pi} \int_{4\pi} P_\lambda(\Theta) cos\Theta d\Omega, \tag{2.17}$$

where Θ is the scattering angle. It gives a measure of the scattered energy in the forward direction with respect to the total scattered energy ($0 < g_s \leq 1$ for scattering mainly in the forward direction and $g_s = 0$ for isotropic scattering) [Mishchenko et al., 2002].

The intensive optical properties can be simulated by optical codes starting from basic microphysical properties of the particles, such as size distribution (geometric radius, standard deviation and size range), complex refractive index (real and imaginary parts), mass density and shape. Obviously also the RH levels affect the optical calculations for the hydrophilic species since, as mentioned in Section 2.2.1, size distribution, refractive index and mass density are all affected by the uptaken water. In the implemented optical tool two optical codes, both exhaustively described in Mishchenko et al. [2002], have been included: a T-matrix code and a Mie code. A brief description of the two tools is given in the following paragraphs:

- The **T-matrix** method is a powerful exact technique for computing light scattering by polydisperse, randomly oriented, non-spherical (rotationally symmetric), homogeneous particles [Mishchenko and Travis, 1998]. The incident and the scattered electromagnetic fields are expanded in series of vector spherical wave functions, with the relation between the expansion coefficients established through the T-matrix [Mishchenko et al., 2004]. The T-Matrix is determined only by the particle microphysical properties (size parameter, aspect ratio, refractive index) and for a given incident field it allows calculating the scattered field, the scattering matrix and the optical cross sections [Mishchenko and Travis, 1998]. For "standard" particle microphysical parameters (not too extreme sizes or aspect ratios), the T-matrix code is able to produce very accurate results (five and more exact decimal places). Moreover, it has an automatic built-in convergence test which provides a very good estimate of the absolute accuracy of the computations [Mishchenko and Travis, 1998].

- The **Lorenz-Mie** theory allows calculating far-field light scattering by polydisperse, spherical, homogeneous particles. It can be exactly derived as a special case of the T-matrix theory for spherical particles. All the T-matrix equations, indeed, reduce to the corresponding equations of the Lorenz-Mie theory when spherically symmetric particles are considered [Mishchenko et al., 2002].

The tables generated by the optical tool contain intensive optical properties (k^{ext}, ω and g) for 61 wavelengths (OPAC spectrum: from $0,250$ to $40,000$ μm), 7 levels of RH (only for hydrophilic species: reported in Table 2.1) and 8 size bins (only for size-distributed species: see Section 2.3). Hydrophobic and hydrophilic modes of organic matter and black carbon share the same optical table, with the properties relative to $RH = 0\%$ intended for the hydrophobic modes. Only spherical particles are considered at the moment in the model and so the optical tool currently uses the Mie code (the T-matrix code could be alternatively used). The default microphysical parameters set in the tool for all the species are reported in Table 2.1. The spectral dry refractive index values for the 61 wavelengths have been entirely taken from the OPAC database, considering the following association (fully taken from the GOCART model) between aerosol species and OPAC components:

- mineral dust ↔ MIAM (mineral accumulation mode);
- sea salt ↔ SSAM (sea salt accumulation mode);
- organic matter ↔ WASO (water-soluble);
- black carbon ↔ SOOT (soot);
- sulfate ↔ SUSO (sulfate droplets).

The refractive index of water, required to calculate the wet refractive indexes of the aerosols, has been taken from Segelstein [1981].

2.5.3 Full coupling implementation

In addition to the intensive optical properties (optical tables: see Section 2.5.2), the calculation of the aerosol layer optical properties needed by the RRTMG (see Section 2.5.1) requires the layer mass concentrations simulated during runtime by the aerosol module (aerosol tracers: see Sections 2.2 and 2.3). The mass concentrations, indeed, are directly required for the calculation of the layer optical depth (Equation 2.11), which in turn is involved in the processing on the intensive optical properties required for providing the right inputs to the RRTMG.

More in detail, since the intensive optical properties from the optical tables are available for 61 wavelengths, they have to be firstly mapped onto the RRTMG bands. This means averaging within each band the table properties, with the spectral solar flux (S) used as weight function at each wavelength, as follows:

$$\begin{aligned} k_b^{ext} &= \frac{\sum_\lambda k_\lambda^{ext} S_\lambda}{\sum_\lambda S_\lambda}, \\ \omega_b &= \frac{\sum_\lambda \omega_\lambda S_\lambda}{\sum_\lambda S_\lambda}, \\ g_b &= \frac{\sum_\lambda g_\lambda S_\lambda}{\sum_\lambda S_\lambda}, \end{aligned} \tag{2.18}$$

in which the sums are defined over all the wavelengths falling within each RRTMG spectral band (indexed by b). Moreover, depending on the current layer RH level simulated by the model, the intensive optical properties from the tables, available for 7 RH levels, have to be interpolated (only for hydrophilic species). Finally, since the tracers are available for each bin/mode of the species, the layer optical depth of the mixture has to be calculated by summing all the bin/mode contributions (indexed by j), while single scattering albedo and asymmetry factor by means of τ-weighted means as follows:

$$\begin{aligned} \tau_b &= \sum_j \tau_{b,j} = \sum_j k^{ext}_{b,j} M_j \Delta z, \\ \omega_b &= \frac{\sum_j \omega_{b,j}\tau_{b,j}}{\sum_j \tau_{b,j}}, \\ g_b &= \frac{\sum_j g_{b,j}\omega_{b,j}\tau_{b,j}}{\sum_j \omega_{b,j}\tau_{b,j}}. \end{aligned} \tag{2.19}$$

From a programming point of view, the implementation of the full online coupling between the aerosol module and the radiation scheme required the achievement of two tasks: i) to make available the simulated aerosol tracers and ii) to integrate the optical tables in the radiation scheme and at each timestep. For the first task, the full link between the aerosol module and the radiation scheme has been achieved by extending to all the parameterized species the existing link for mineral dust, already implemented by Pérez et al. [2011]. The inputs/outputs of several subroutines have been modified to bring the simulated tracers from the general subroutine in which all the updated model variables are stored at each timestep to the specific subroutine in which the current aerosol layer optical properties are calculated. For the second task, the integration of the optical tables in the radiation scheme has been achieved following the similar code existing for the aerosol climatologies. New code instructions, added in the interfacing subroutines of the radiation scheme, allow reading the optical tables and processing the intensive optical properties (as explained above) to make them usable for the calculation of the layer optical properties of the aerosol mixture.

In addition to these main tasks, further effort has been made to improve the flexibility in the ARI configuration, to optimize the existing code and to modify the general outputs of the model. Regarding the model outputs, additional code has been added to extract the aerosol layer optical properties calculated in the radiation scheme at the desired wavelength (by default $0,550\ \mu m$) and to provide them as model outputs for evaluations and comparisons. More precisely, these output optical properties are relative to the RRTMG spectral band containing the $0,550\ \mu m$ wavelength: the differences from the single-wavelength properties have been found to be negligible, as explained in Section 5.3.2. Moreover, these output optical properties are not layer properties but column-integrated properties, derived from the layer optical properties through the same equations describing the bin/mode contributions to the aerosol mixture (Equations 2.19 with a layer index instead of the bin/mode index). Finally, these output optical properties have been extracted for the total mixture but also separately for each single species.

Chapter 3

Sensitivity of aerosol scattering to microphysical properties

3.1 Introduction

Atmospheric aerosols can scatter and absorb electromagnetic radiation, causing a redistribution of the radiative energy in the atmosphere [Boucher et al., 2013]. Even if the model parameterizations of this Aerosol-Radiation Interaction (ARI) have extremely improved over the last two decades [Myhre et al., 2013a], the ARI radiative forcing still contributes to dominate the uncertainty associated with the anthropogenic impact on the climate change [Myhre et al., 2013b]. Also the role of the natural aerosols in affecting the Earth's radiative balance through ARI is poorly constrained [Rap et al., 2013]. The ARI parameterization mainly consists in the characterization of the aerosol optical properties. Errors in the estimation of the aerosol optical properties, indeed, are main sources of the still large uncertainty affecting both the measurement-based [Yu et al., 2006; Zhang et al., 2016] and model [Randles et al., 2013] estimates of the ARI radiative effects and forcing. The optical properties in turn depend, in addition to radiation wavelength and aerosol mass concentration, on the microphysical properties of the particles, such as size distribution, refractive index, mixing state, shape, hygroscopicity and mass density [Boucher et al., 2013; Hand and Malm, 2007]. The uncertainty affecting the optical properties, indeed, is caused above all by an incomplete knowledge concerning the microphysical properties of the particles [Yu et al., 2006]. Hence, different assumptions on the microphysical properties can affect the calculation of the optical properties and so the assessments of the ARI radiative effects. For this reason, we considered a sensitivity study of the aerosol scattering to microphysical properties a recommendable first step to better parameterize the dynamic ARI in our online integrated meteorology-chemistry model NMMB-MONARCH (described in detail in Chapter 2).

In this chapter we present the numerical experiment carried out in order to assess the impact of perturbed aerosol microphysical properties on values and spectral dependence of simulated mass scattering cross sections (α^{sca} $[m^2/g]$: scattering coefficients per unit mass concentration). Local perturbations on the particle microphysical properties aimed to reproduce the uncertainty by which these are affected. Moreover, we provide constraints on these microphysical assumptions (suitable for the north-western Mediterranean basin), found by achieving the best agreement (compatibility of best fit parameters) between simulated and observed α^{sca}. The optical simulations have been performed with a T-Matrix code, for mineral dust, organic carbon and sulfate, at 3 wavelengths in the visible range ($0,450\ \mu m$; $0,525\ \mu m$; $0,635\ \mu m$). Reference values for size distribution, refractive index and mass density parameters (based on the default aerosol parameterization of the NMMB-MONARCH) have been perturbed of ±20% and spheroids with two different axial ratios have been considered as shape perturbations. The observations have been provided by the Institute of Environmental Assessment and Water Research (IDAEA-CSIC). From measurements of aerosol mass concentrations and optical properties, collected at the Montseny regional background station (Spain) during a 4-years campaign, α^{sca} have been derived through Multilinear Regression (MLR) applied to aerosol sources (mineral dust, aged organics and ammonium sulfate) at 3 visible wavelengths (the same we selected for the code calculations). These data, even if representative of the north-western Mediterranean basin, result compatible with the quite extended range of estimates available in literature [Hand and Malm, 2007].

The work presented in this chapter has been published in Obiso et al. [2017] (Journal of Aerosol Science). The chapter is organized as follows: in Section 3.2 the optical code used for the experiment is briefly described; in Section 3.3, a description of the observations used is given; in Sections 3.4 and 3.5, experiment setup and analysis methods, respectively, are presented; in Sections 3.6 and 3.7, the results are presented and discussed, respectively; in Section 3.8 our conclusions are finally reported.

3.2 Numerical tools

For the optical simulations, the T-matrix code by Mishchenko et al. [2002] has been used (already presented in Section 2.5.2). It allows computing light scattering by polydisperse, randomly oriented, non-spherical (rotationally symmetric), homogeneous particles [Mishchenko and Travis, 1998]. Two versions of the same code have been used, double- and extended-precision versions, in order to solve calculation convergence issues caused by considering high size parameters x (defined as $x = 2\pi r/\lambda$: ratio between the particle radius r and the radiation wavelength λ) for strongly nonspherical particles. This code appeared to be the most adequate for this experiment because of its flexibility and precision in calculating bulk optical properties to be compared with the observations.

3.3 Observations

We used a set of observed aerosol α^{sca} provided by the IDAEA-CSIC. Pandolfi et al. [2011] collected measurements of aerosol PM_{10} mass concentrations (gravimetric masses from $24h$ filters) and optical properties (scattering coefficients with Nephelometer AURORA 3000, Ecotech), in the period 2010-2014, at the Montseny regional background station (middle altitude emplacement within the Montseny Natural Park, Spain: $41°46'45,63"N$ - $02°21'28,92"E$; $720m$ a.s.l.). The frequency of the gravimetric samples was 3/4 samples per week ($24h$). The Nephelometer worked continuously with a raw resolution of 5 minutes, it was calibrated 3/4 times per year (using CO_2 as span gas) and zero adjusts were performed every $24h$. The Montseny station is a GAW[1] and ACTRIS[2] station, therefore instrument calibration and measurements were performed following the network standards and procedures (the data are continuously provided to these networks). The annual mean Relative Humidity (RH) at the sampling site is $\sim 75\% \pm 20\%$ (personal communication from Marco Pandolfi). In order to reduce the effects of hygroscopicity on the scattering properties of the particles, a RH threshold of 40% was set in the sampling cell by using a processor-controlled automatic heater inside the Nephelometer. This experimental procedure, which follows the ACTRIS standards, has been applied elsewhere (i.e.

---

[1] www.wmo.int/pages/prog/arep/gaw/gaw_home_en.html

[2] www.actris.eu

Pereira et al. [2011]; Anderson and Ogren [1998]). Hence, during the study period, the mean RH in the Nephelometer sampling cell was $\sim 28\% \pm 12\%$ [Pandolfi et al., 2011].

From these data, Ealo et al. [2017] derived α^{sca} at 3 visible wavelengths ($0,450$ μm; $0,525$ μm; $0,635$ μm) through MLR analysis (Nephelometer data were averaged over the gravimetric sampling time before performing the MLR). The MLR method has been previously used in order to calculate α^{sca} of chemical species, by considering the species concentrations (externally mixed) as dependent variables, the measured scattering coefficients as independent variables and the α^{sca} as regression coefficients [White and Macias, 1987; Hand and Malm, 2007]. But in Ealo et al. [2017], the MLR has been performed using sources of aerosols [Pandolfi et al., 2016] detected in the PM_{10} mass chemical speciated data [Querol et al., 2009] through the application of the Positive Matrix Factorization (PMF) model [Paatero, 1997] (a system able to recognize correlations in the variability of the mass concentrations of two or more different aerosol species and so to associate the correlated species with the same aerosol source). Hence, this MLR considered the source contributions to PM_{10} from the PMF model as dependent variables, instead of the chemical species concentrations, and so a single α^{sca} has been obtained for each source detected at the Montseny station. It is important to note that this different approach is based on a different assumption on the mixing state of the atmospheric aerosols [White and Macias, 1987]. In other words, the sources are supposed to be aerosol mixtures, dominated by a low number of species (from which they take the name) but including minor internally mixed species. Thus, the resulting regression coefficients in the MLR applied to sources represent α^{sca} of internally mixed aerosols (at least in a certain degree). Note that considering sources instead of externally mixed species in the MLR also reduces some collinearity issues and makes the regression coefficients less sensitive to data uncertainties [Hand and Malm, 2006].

At the Montseny station 7 sources were detected using the PMF model but in our work we used only 3 of them: mineral dust (traced by typical crustal elements such as Al, Ca, Ti, Rb, Sr), aged organics (traced mainly by organic carbon, with maxima in summer indicating a prevalent biogenic origin but with also a significant contribution from biomass burning) and ammonium sulfate (secondary inorganic source traced mainly by SO_4^{2-} and NH_4^+) [Pandolfi et al., 2016]. The biomass burning contribution to the aged organics source at Montseny has been found to be $\sim 30\%$ [Ealo et al., 2016] and it includes a certain amount of absorbing brown carbon and black carbon as minor species. Independent sources traced by other important species, such as black carbon or sea salt, have not been considered for this work for the following reasons. Black carbon contributes to $< 2\%$ to the PM_{10} mass at Montseny [Pandolfi et al., 2011] and so in this particular geographical area it is not a dominant species. In fact, it has not been detected as an isolated source by the PMF model but it is taken into account as a minor species in the aged organics source. Moreover, black carbon is a strongly absorbing species and so its contribution to the scattering can be considered negligible (in this work we analyzed only aerosol scattering properties). For sea salt, the PMF model detected the aged marine source (traced by Na and Cl and enriched in nitrates). However, as shown in Pandolfi et al. [2016], the contribution of this source to PM_{10} mass concentration is quite low at Montseny ($\sim 10\%$), compared to the contributions of the mineral dust ($\sim 17\%$), aged organics ($\sim 23\%$) and ammonium sulfate ($\sim 24\%$) sources. At Barcelona, for example, the absolute contribution to PM_{10} of the aged marine source was found more than 3 times higher compared to its contribution at Montseny [Pandolfi et al., 2016]. As a consequence, the MLR provided α^{sca} for the aged marine source with a relative error of $\sim 30\%$, value abundantly above the threshold of 15% (at $0,525$ μm) which we fixed in order to be able to derive significantly strict constraints on the microphysical properties of the modeled aerosol species. The observed α^{sca} for the 3 sources used in this work are reported in Table

3.1.

Table 3.1: **Observed α^{sca} of mineral dust, aged organics and ammonium sulfate sources. The reported wavelengths are $\lambda_1 = 0,450$ μm, $\lambda_2 = 0,525$ μm and $\lambda_3 = 0,635$ μm.**

Observations		Mineral Dust	Aged Organics	Ammonium Sulfate
α^{sca} $[m^2/g]$	λ_1	$1,046 \pm 0,130$	$1,990 \pm 0,258$	$5,860 \pm 0,256$
	λ_2	$1,262 \pm 0,106$	$1,414 \pm 0,212$	$4,508 \pm 0,210$
	λ_3	$1,429 \pm 0,096$	$0,916 \pm 0,190$	$3,092 \pm 0,188$

As mentioned above, with the MLR applied to sources, a possible internal mixing between dominant and minor species is taken into account. This more realistic representation of the atmospheric aerosols allowed us to tune the reference microphysical properties for the modeled species (derived from very general literature prescriptions) taking into account, in an indirect and simple way, also the effects of the internally mixed minor species on the ARI of the dominant species. Note that explicitly parameterizing this source internal mixing for the code calculations would be an unfeasible way due to the high variability in both the number and the mixing percentage of the minor species in the sources. Moreover, for our experiment we needed α^{sca} at more than one wavelength, since in addition to single-wavelength values we analyzed also the spectral dependence of α^{sca}. In literature many experimental estimates of aerosol α^{sca} are available: a survey of approximately 60 ground-based estimates produced since 1990 for different aerosol species, in different geographical locations, under a variety of monitoring conditions and with 4 different techniques used, has been published in Hand and Malm [2007]. However, it has to be noted that all these estimates are given at one wavelength (mainly $\sim 0,550$ μm) and furthermore they refer to aerosol species, not sources. Hence, given the lack of experimental α^{sca} estimates at more than one wavelength and given that the novelty of presenting α^{sca} of aerosol sources was able to enrich our analysis, this dataset appeared to be the most adequate for our experiment.

The data we used can be considered representative of the regional background of the north-western Mediterranean basin. It is true that in order to properly represent a "regional level", data from more than one station should be used. A high number of stations, indeed, measure for example gaseous compounds or PM mass concentrations at regional level in the north-western Mediterranean. However, in this region only the Montseny station provides long term PM_{10} mass chemical speciated data, needed to derive the observed α^{sca} of aerosol sources used in this work. Despite this, it is plenty of publications demonstrating that the Montseny station is representative of the typical regional background conditions in the north-western Mediterranean basin (i.e. Pandolfi et al. [2014]; Pérez et al. [2008]; Pey et al. [2009]). Finally, note that the α^{sca} experimental estimates we used, even if local data, fall within the quite extended range of experimental estimates available in literature (Table 3 of Hand and Malm [2007]: MLR method).

3.4 Experiment setup

In order to characterize the reference aerosol species (always dry and homogeneous in this work), four particle microphysical properties have been taken into account: size distribution (geometric radius r_g $[\mu m]$ and standard deviation σ_g [unitless]), refractive index (real n_r and imaginary n_i parts [unitless]), mass density (ρ $[kg/m^3]$) and shape (axial ratio χ [unitless]). We defined the reference microphysical properties following the default aerosol parameterization used in the NMMB-MONARCH (summarized in Table 2.1), which is mainly based on the OPAC database [Hess et al., 1998] except for some parameters of mineral dust and sea salt. Some deviations from this default parameterization have been required in this work. Regarding mineral dust, different mass densities for sub-micron and super-micron bins are considered in the NMMB-MONARCH, so for the bulk mineral dust of this work we derived a weighted mean of the original values. Regarding organic carbon, in order to take into account the biomass burning contribution (including absorbing brown carbon) to the aged organics source, the imaginary refractive index has been corrected using averages from modern estimates by Kirchstetter et al. [2004] and Shamjad et al. [2016], suitable for biomass burning organic aerosols. Finally, the OPAC refractive indexes for all the species have been linearly interpolated to derive the values at the three wavelengths of the experiment. The reference microphysical parameters used in this work for all the considered species are reported in Table 3.2.

In the aerosol modeling community, many important models use prescriptions (fully or partially) taken from the OPAC database in their particle parameterization [Baklanov et al., 2014]: for example GOCART [Chin et al., 2000, 2002, 2009] (which uses also the same association between modeled species and OPAC components considered in the NMMB-MONARCH), WRF-CMAQ [Pleim et al., 2008; Mathur et al., 2010; Wong et al., 2012], MEMO/MARS-aero [Moussiopoulos et al., 2012; Halmer et al., 2010], RegCM4-Chem [Zakey et al., 2006; Solmon et al., 2006; Shalaby et al., 2012] and RAMS/ICLAMS [Kallos et al., 2009; Solomos et al., 2011]. Nevertheless, we do not consider the reference properties used as optimal values for the aerosol microphysics. We decided to start our analysis from these reference properties, indeed, in order to test and potentially improve them. In other words, our main goal was not to start from "correct" reference values but, starting from widely used values, to find "correct" constraints for them. For this purpose, we applied perturbations spanning large ranges of values for the reference microphysical properties. These were supposed, indeed, to represent the large uncertainty affecting these properties and above all to cover suitable values for them. On the other hand, note that for the sensitivity study the "goodness" of the reference values is not a critical requirement.

After defining the reference microphysical properties, we performed calculations of integrated α^{sca} of mineral dust, organic carbon and sulfate, as follows [Tegen and Lacis, 1996]:

$$\alpha_{\lambda}^{sca} = \frac{3Q_{\lambda}^{sca}}{4\rho r_{eff}}, \tag{3.1}$$

where in addition to the already defined symbols Q^{sca} is the mean scattering efficiency (average performed over the projected surface size distribution) and r_{eff} the effective radius (defined as $r_{eff} = \bar{r^3}/\bar{r^2}$, with the averages performed over the normalized number size distribution [Hansen and Travis, 1974]). The calculations have been performed at 3 wavelengths in the visible range ($0,450\ \mu m$; $0,525\ \mu m$; $0,635\ \mu m$): the wavelengths at which the observations were available. In order to generate variability in the particle microphysical assumptions, we gave then as inputs to the T-Matrix code the reference microphysical properties independently perturbed: this means that when a property was perturbed the other ones were not. In particular, for each aerosol species, we considered perturbations of ±20% on size distribution (separately for r_g and σ_g), refractive index (separately for n_r and n_i) and mass density ρ; as perturbations for the spherical shape we considered two types of spheroid: moderate and extreme, averaging for each χ the oblate and the prolate options. In Table 3.2 also perturbed microphysical properties and corresponding case acronyms for all the species considered are reported.

Table 3.2: **Reference (marked with a *) and perturbed microphysical properties for all the considered species used for code simulations. The perturbation cases for size distribution, refractive index and mass density are named with the letters m (i.e. $minus$: -20%), r (i.e. $reference$) and p (i.e. $plus$: $+20\%$), applied separately to each parameter of the microphysical properties (for size distribution and refractive index the first letter refers to r_g and n_r, while the second letter to σ_g and n_i, respectively; for mass density the only one letter refers to ρ); the shape perturbation cases are indicated as ext (i.e. $extreme$ spheroid) and mod (i.e. $moderate$ spheroid), both cases including the oblate and the prolate options (the χ of the two options are reciprocals of each other). The cases rr (for size distribution and refractive index), r (for mass density) and sph (i.e. $sphere$, for shape) are omitted because they all coincide with the reference case, which we name ref for all the microphysical properties. The size distribution is log-normal and the size range from $0,001$ to $5,0$ μm (aerodynamic radius, in agreement with the PM_{10} definition) for all the species. The refractive index values within parentheses are relative to $0,450$ μm, $0,525$ μm and $0,635$ μm, respectively. The axial ratio is defined as $\chi = a/b$, where a is the axis perpendicular to the symmetry axis of the spheroid and b the parallel one: the value $\chi = 1$ indicates a sphere, while values $\chi > 1$ and $\chi < 1$ indicate oblate and prolate spheroids, respectively.**

Cases			**Mineral Dust**	**Organic Carbon**	**Sulfate**
Size Distribution	ref	r_g^* $[\mu m]$	$2,986 \cdot 10^{-1}$	$2,120 \cdot 10^{-2}$	$6,950 \cdot 10^{-2}$
		σ_g^*	$2,000$	$2,200$	$2,030$
		r_{eff}^* $[\mu m]$	$9,205 \cdot 10^{-1}$	$1,003 \cdot 10^{-1}$	$2,433 \cdot 10^{-1}$
	mm	$r_g = 0,8 \cdot r_g^*$ $[\mu m]$	$2,389 \cdot 10^{-1}$	$1,696 \cdot 10^{-2}$	$5,560 \cdot 10^{-2}$
		$\sigma_g = 0,8 \cdot \sigma_g^*$	$1,600$	$1,760$	$1,624$
		r_{eff} $[\mu m]$	$4,150 \cdot 10^{-1}$	$3,771 \cdot 10^{-2}$	$1,001 \cdot 10^{-1}$
	mr	$r_g = 0,8 \cdot r_g^*$ $[\mu m]$	$2,389 \cdot 10^{-1}$	$1,696 \cdot 10^{-2}$	$5,560 \cdot 10^{-2}$
		$\sigma_g = 1,0 \cdot \sigma_g^*$	$2,000$	$2,200$	$2,030$
		r_{eff} $[\mu m]$	$7,617 \cdot 10^{-1}$	$8,024 \cdot 10^{-2}$	$1,947 \cdot 10^{-1}$
	mp	$r_g = 0,8 \cdot r_g^*$ $[\mu m]$	$2,389 \cdot 10^{-1}$	$1,696 \cdot 10^{-2}$	$5,560 \cdot 10^{-2}$
		$\sigma_g = 1,2 \cdot \sigma_g^*$	$2,400$	$2,640$	$2,436$
		r_{eff} $[\mu m]$	$1,150$	$1,782 \cdot 10^{-1}$	$3,965 \cdot 10^{-1}$
	rm	$r_g = 1,0 \cdot r_g^*$ $[\mu m]$	$2,986 \cdot 10^{-1}$	$2,120 \cdot 10^{-2}$	$6,950 \cdot 10^{-2}$
		$\sigma_g = 0,8 \cdot \sigma_g^*$	$1,600$	$1,760$	$1,624$
		r_{eff} $[\mu m]$	$5,187 \cdot 10^{-1}$	$4,713 \cdot 10^{-2}$	$1,251 \cdot 10^{-1}$
	rp	$r_g = 1,0 \cdot r_g^*$ $[\mu m]$	$2,986 \cdot 10^{-1}$	$2,120 \cdot 10^{-2}$	$6,950 \cdot 10^{-2}$
		$\sigma_g = 1,2 \cdot \sigma_g^*$	$2,400$	$2,640$	$2,436$
		r_{eff} $[\mu m]$	$1,293$	$2,219 \cdot 10^{-1}$	$4,890 \cdot 10^{-1}$
	pm	$r_g = 1,2 \cdot r_g^*$ $[\mu m]$	$3,583 \cdot 10^{-1}$	$2,544 \cdot 10^{-2}$	$8,340 \cdot 10^{-2}$
		$\sigma_g = 0,8 \cdot \sigma_g^*$	$1,600$	$1,760$	$1,624$
		r_{eff} $[\mu m]$	$6,221 \cdot 10^{-1}$	$5,656 \cdot 10^{-2}$	$1,501 \cdot 10^{-1}$
	pr	$r_g = 1,2 \cdot r_g^*$ $[\mu m]$	$3,583 \cdot 10^{-1}$	$2,544 \cdot 10^{-2}$	$8,340 \cdot 10^{-2}$
		$\sigma_g = 1,0 \cdot \sigma_g^*$	$2,000$	$2,200$	$2,030$
		r_{eff} $[\mu m]$	$1,061$	$1,204 \cdot 10^{-1}$	$2,919 \cdot 10^{-1}$
	pp	$r_g = 1,2 \cdot r_g^*$ $[\mu m]$	$3,583 \cdot 10^{-1}$	$2,544 \cdot 10^{-2}$	$8,340 \cdot 10^{-2}$
		$\sigma_g = 1,2 \cdot \sigma_g^*$	$2,400$	$2,640$	$2,436$
		r_{eff} $[\mu m]$	$1,406$	$2,650 \cdot 10^{-1}$	$5,773 \cdot 10^{-1}$
Refractive Index	ref	n_r^*	$(1,530; 1,530; 1,530)$	$(1,530; 1,530; 1,530)$	$(1,432; 1,431; 1,429)$
		n_i^*	$(8,500; 6,650; 4,500) \cdot 10^{-3}$	$(1,730; 1,250; 0,696) \cdot 10^{-2}$	$(1,000; 1,000; 1,610) \cdot 10^{-8}$
	mm	$n_r = 0,8 \cdot n_r^*$	$(1,224; 1,224; 1,224)$	$(1,224; 1,224; 1,224)$	$(1,146; 1,145; 1,143)$
		$n_i = 0,8 \cdot n_i^*$	$(6,800; 5,320; 3,600) \cdot 10^{-3}$	$(1,384; 1,000; 0,557) \cdot 10^{-2}$	$(0,800; 0,800; 1,288) \cdot 10^{-8}$
	mr	$n_r = 0,8 \cdot n_r^*$	$(1,224; 1,224; 1,224)$	$(1,224; 1,224; 1,224)$	$(1,146; 1,145; 1,143)$
		$n_i = 1,0 \cdot n_i^*$	$(8,500; 6,650; 4,500) \cdot 10^{-3}$	$(1,730; 1,250; 0,696) \cdot 10^{-2}$	$(1,000; 1,000; 1,610) \cdot 10^{-8}$
	mp	$n_r = 0,8 \cdot n_r^*$	$(1,224; 1,224; 1,224)$	$(1,224; 1,224; 1,224)$	$(1,146; 1,145; 1,143)$
		$n_i = 1,2 \cdot n_i^*$	$(10,20; 7,980; 5,400) \cdot 10^{-3}$	$(2,076; 1,500; 0,835) \cdot 10^{-2}$	$(1,200; 1,200; 1,932) \cdot 10^{-8}$
	rm	$n_r = 1,0 \cdot n_r^*$	$(1,530; 1,530; 1,530)$	$(1,530; 1,530; 1,530)$	$(1,432; 1,431; 1,429)$
		$n_i = 0,8 \cdot n_i^*$	$(6,800; 5,320; 3,600) \cdot 10^{-3}$	$(1,384; 1,000; 0,557) \cdot 10^{-2}$	$(0,800; 0,800; 1,288) \cdot 10^{-8}$
	rp	$n_r = 1,0 \cdot n_r^*$	$(1,530; 1,530; 1,530)$	$(1,530; 1,530; 1,530)$	$(1,432; 1,431; 1,429)$
		$n_i = 1,2 \cdot n_i^*$	$(10,20; 7,980; 5,400) \cdot 10^{-3}$	$(2,076; 1,500; 0,835) \cdot 10^{-2}$	$(1,200; 1,200; 1,932) \cdot 10^{-8}$
	pm	$n_r = 1,2 \cdot n_r^*$	$(1,836; 1,836; 1,836)$	$(1,836; 1,836; 1,836)$	$(1,718; 1,717; 1,715)$
		$n_i = 0,8 \cdot n_i^*$	$(6,800; 5,320; 3,600) \cdot 10^{-3}$	$(1,384; 1,000; 0,557) \cdot 10^{-2}$	$(0,800; 0,800; 1,288) \cdot 10^{-8}$
	pr	$n_r = 1,2 \cdot n_r^*$	$(1,836; 1,836; 1,836)$	$(1,836; 1,836; 1,836)$	$(1,718; 1,717; 1,715)$
		$n_i = 1,0 \cdot n_i^*$	$(8,500; 6,650; 4,500) \cdot 10^{-3}$	$(1,730; 1,250; 0,696) \cdot 10^{-2}$	$(1,000; 1,000; 1,610) \cdot 10^{-8}$
	pp	$n_r = 1,2 \cdot n_r^*$	$(1,836; 1,836; 1,836)$	$(1,836; 1,836; 1,836)$	$(1,718; 1,717; 1,715)$
		$n_i = 1,2 \cdot n_i^*$	$(10,20; 7,980; 5,400) \cdot 10^{-3}$	$(2,076; 1,500; 0,835) \cdot 10^{-2}$	$(1,200; 1,200; 1,932) \cdot 10^{-8}$
Mass Density	ref	ρ^* $[kg/m^3]$	$2,506 \cdot 10^3$	$1,800 \cdot 10^3$	$1,700 \cdot 10^3$
	m	$\rho = 0,8 \cdot \rho^*$ $[kg/m^3]$	$2,005 \cdot 10^3$	$1,440 \cdot 10^3$	$1,360 \cdot 10^3$
	p	$\rho = 1,2 \cdot \rho^*$ $[kg/m^3]$	$3,007 \cdot 10^3$	$2,160 \cdot 10^3$	$2,040 \cdot 10^3$
Shape	ref	χ^*	$1,000$	$1,000$	$1,000$
	ext	χ-*oblate*	$2,200$	$2,200$	$2,200$
		χ-*prolate*	$4,500 \cdot 10^{-1}$	$4,500 \cdot 10^{-1}$	$4,500 \cdot 10^{-1}$
	mod	χ-*oblate*	$1,600$	$1,600$	$1,600$
		χ-*prolate*	$6,300 \cdot 10^{-1}$	$6,300 \cdot 10^{-1}$	$6,300 \cdot 10^{-1}$

3.5 Analysis methods

We compared simulated and observed α^{sca} associating mineral dust with the mineral dust source, organic carbon with the aged organics source and sulfate with the ammonium sulfate source. At first, we evaluated the sensitivity of α^{sca} values and spectral dependence to the different perturbed microphysical properties. Regarding the α^{sca} values, for each species and microphysical property we estimated the extent of the variability range (maximum minus minimum value generated by the perturbations: $\Delta\alpha^{sca,sim}$) of the simulated value at $0,525\ \mu m$ (intermediate wavelength of the experiment) with respect to the uncertainty (two times the standard error: $\Delta\alpha^{sca,obs}$) affecting the observed value at the same wavelength:

$$V_{ratio} = \frac{\Delta\alpha^{sca,sim}_{0,525}}{\Delta\alpha^{sca,obs}_{0,525}}. \tag{3.2}$$

The perturbation impact has been considered significant only when $V_{ratio} > 1$ (that is when the simulated range exceeds the error band of the observed value). Regarding the α^{sca} spectral dependence, instead, we estimated the extent of the variability range (maximum minus minimum value generated by the perturbations: Δs^{sim}) of the spectral dependence slope (s: from logarithmic linear fits, as explained below) of the simulated values with respect to the uncertainty (two times the fit standard error: Δs^{obs}) affecting the slope of the observed values:

$$S_{ratio} = \frac{\Delta s^{sim}}{\Delta s^{obs}}. \tag{3.3}$$

Again the perturbation impact has been considered significant only when $S_{ratio} > 1$.

The spectral dependence slopes have been derived by performing linear fits of the logarithmic spectral dependence of both simulated and observed α^{sca}, taking into account the measurement errors as weights for the observation fits. The linearity of $log(\alpha^{sca})$ versus $log(\lambda)$ is a first approximation of the more suitable second order polynomial dependence, describing a spectral variation of the Ångström exponent [Kaskaoutis et al., 2007]. Moreover its range of validity depends on the spectral position of the maximum of the α^{sca} (affected by the size distribution and the refractive index of the particles), since in conjunction with the maximum the α^{sca} spectral dependence trend must change even in the logarithmic scale and so the linearity hypothesis appears to be inapplicable. The α^{sca} spectral maximum originates from the resonances between diffracted and transmitted radiation arising in single-particle scattering events. The integration over whatever size distribution of a particle ensemble, indeed, smooths out the secondary resonances but preserves the principal maximum, which only spreads out [Hansen and Travis, 1974; Mishchenko et al., 2002]. The spectral position of the α^{sca} maximum moves together with the particle r_{eff} (for poly-disperse particles r_{eff} can be considered the representative size of the ensemble, regarding the scattering processes [Hansen and Travis, 1974]). For low values of σ_g ($\lesssim 1,6$) the maximum occurs for $\Delta\Phi_{eff} = 2x_{eff}(n_r - 1) \sim 4,1$ (being $\Delta\Phi_{eff}$ the phase shift of an electromagnetic wave passing through an effective particle of size parameter x_{eff} and real refractive index n_r [Hansen and Travis, 1974]) and for $n_r \sim 1,33$ it approximately corresponds to $x_{eff} \sim 2\pi$, that is $\lambda \sim r_{eff}$. With increasing σ_g ($\gtrsim 1,6$) the maximum slightly moves towards higher values of x_{eff} (fixed n_r), that is $\lambda \lesssim r_{eff}$, but always r_{eff} is an approximative indicator of its spectral position. On the other hand, with increasing n_r the maximum moves towards lower x_{eff} (fixed σ_g), that is $\lambda \gtrsim r_{eff}$. Hence, the effects of increasing σ_g and n_r more or less balance each other, so for example for $n_r \sim 1,5$ and $\sigma_g \sim 2$ again the maximum approximately occurs for $\lambda \sim r_{eff}$. The position of the maximum is very important in this work to analyze the α^{sca} spectral characteristics. However, in all the cases considered in this work the condition of linearity of the logarithmic spectral dependence of the α^{sca} has been considered satisfied, although with a variable degree of accuracy, except for two size distribution cases (mm and rm) and three refractive index cases (mm, mr and mp) of mineral dust (following the case nomenclature explained in Table 3.2). For these cases the α^{sca} maximum falls within the spectral range of the experiment and therefore they have been excluded from the linear fit analysis (although shown in the graphs). For the logarithmic linear fits we used the following formula:

$$log(\alpha_{\lambda}^{sca}) = s \cdot log\left(\frac{\lambda}{0,525}\right) + q, \tag{3.4}$$

where s is the mentioned slope, opposite of the α^{sca} Ångström exponent, and $q = log(\alpha_{0,525}^{sca})$ (fit estimate).

In order to complete the comparison analysis and to constrain the perturbed microphysical properties, we then performed a compatibility test on the best fit parameters s and q:

$$x_{test} = \frac{|x_{sim} - x_{obs}|}{\sqrt{\sigma_{x,sim}^2 + \sigma_{x,obs}^2}}, \tag{3.5}$$

where x is the current parameter (s or q) and σ_x its standard deviation (the least squares method fit errors have been assumed to be one standard deviation errors of normally distributed variables). The test has been performed, for each aerosol species, on the best fit parameters of all the perturbed simulations with respect to those of the corresponding observations. We defined the value of $x_{test} = 1,65$ as compatibility threshold for the single parameters (corresponding to a confidence interval of $\sim 90\%$) and we then considered two fits fully compatible when the total test score $t_{test} = s_{test} + q_{test} < 1,65$, partially compatible when $1,65 < t_{test} < 3,00$ and not compatible when $t_{test} > 3,00$.

3.6 Results

In Table 3.3 the compatibility test values for all the species and perturbation cases are reported. The following discussion about the constraints on the particle microphysical properties is based on this table.

3.6.1 Mineral dust

The **size distribution** perturbations (see Figure 3.1-A for the related spectral α^{sca}) do not have any significant effect on the α^{sca} spectral dependence ($S_{ratio} = 0,24$) while strongly affect the values of α^{sca} ($V_{ratio} = 3,8$), in the spectral range of the experiment (this clarification will be omitted but keeps true in the rest of the current analysis). The α^{sca} spectral maximum of mineral dust lies at longer wavelengths than those of the visible range (positive logarithmic linear spectral dependence slope in the visible range). With increasing effective radius, the α^{sca} maximum decreases, because of the inverse dependence of α^{sca} on r_{eff}, and moves towards longer wavelengths. This causes the α^{sca} values to decrease at all the considered wavelengths (due to both the maximum drop and shift) but leaves nearly unaffected the α^{sca} spectral dependence. Looking at Table 3.3 (size distribution rows): the reference case ref results s-compatible but q-incompatible; all the perturbed simulations reach the s-compatibility similarly to the reference case (best s_{test} from pm: 0,72) but now a simulation is q-compatible (best q_{test} from pm: 0,02) with the observations; the best total score is from pm ($t_{test} = 0,74$: full fit compatibility). The strong impact of the size distribution perturbations on the α^{sca} values makes the pm case fully fit compatible with the observations and this allows us to strictly

Table 3.3: **Results of the compatibility test on the best fit parameters, relative to reference and perturbation (of all the microphysical properties) cases, for all the considered species. In the second column the perturbation cases are reported: the acronyms are explained in Table 3.2. The size distribution cases *mm* and *rm* and the refractive index cases *mm*, *mr* and *mp* of mineral dust have been not included in the fit analysis for the reasons explained in Section 3.5.**

Cases		**Mineral Dust**		**Organic Carbon**		**Sulfate**	
		s_{test}	q_{test}	s_{test}	q_{test}	s_{test}	q_{test}
ref		1,00	8,85	1,15	7,34	4,05	10,77
Size Distribution	*mm*	–	–	1,39	10,65	2,86	27,59
	mr	1,19	4,50	0,81	5,73	2,94	10,96
	mp	1,03	13,93	2,22	7,49	6,25	21,70
	rm	–	–	1,04	5,55	1,48	18,01
	rp	0,93	16,71	2,47	7,03	6,94	25,98
	pm	0,72	0,02	0,73	1,82	0,30	12,02
	pr	0,91	12,23	1,43	8,26	4,95	11,96
	pp	0,88	18,75	2,67	6,39	7,46	30,08
Refractive Index	*mm*	–	–	0,54	7,16	0,20	59,77
	mr	–	–	0,59	7,30	0,20	59,77
	mp	–	–	0,63	7,44	0,20	59,77
	rm	1,12	8,46	1,11	7,47	4,05	10,77
	rp	0,90	9,22	1,19	7,22	4,05	10,77
	pm	1,09	9,19	1,52	13,14	6,04	0,84
	pr	0,98	9,60	1,56	13,02	6,04	0,84
	pp	0,89	9,98	1,59	12,91	6,04	0,84
Mass Density	*m*	0,99	5,26	1,15	9,75	4,05	3,24
	p	1,01	11,74	1,15	5,38	4,05	16,92
Shape	*ext*	1,15	8,50	1,03	4,98	3,49	16,48
	mod	1,03	8,76	1,11	6,51	3,85	12,74

constrain, in the north-western Mediterranean basin, the mineral dust size distribution parameters to the values $r_g = 3,583 \cdot 10^{-1}\ \mu m$ and $\sigma_g = 1,600$ ($r_{eff} = 6,221 \cdot 10^{-1}\ \mu m$).

The **refractive index** perturbations (see Figure 3.1-B for the related spectral α^{sca}) show a significant influence neither on the α^{sca} spectral dependence ($S_{ratio} = 0,11$) nor on the values of α^{sca} ($V_{ratio} = 0,30$). Fixed a size distribution, an increasing real part of the refractive index causes the α^{sca} spectral maximum to grow and to move towards longer wavelengths (while an increasing imaginary part just attenuates the whole scattering values). Due to the dust α^{sca} maximum position, these effects balance each other and so leave both α^{sca} values and spectral dependence nearly unaffected by the perturbations. Looking at Table 3.3 (refractive index rows): similarly to the reference case, all the perturbed simulations reach the s-compatibility (best s_{test} from *pp*: $0,89$) and no simulations the q-compatibility (best q_{test} from *rm*: $8,46$) with the observations; the best total score is from *rm* ($t_{test} = 9,58$: fit incompatibility). Since the impact of the refractive index perturbations on both α^{sca} values and spectral dependence is negligible, no fit compatibility is reached and so it is not possible to get any constraints on this microphysical property for mineral dust.

The **mass density** perturbations (see Figure 3.1-C for the related spectral α^{sca}) leave unaffected the α^{sca} spectral dependence ($S_{ratio} = 0,0087$) while have a not negligible impact on the α^{sca} values ($V_{ratio} = 1,3$). Since the mass density does not affect the calculation of the mean scattering efficiency, increasing its value does not cause any shift of the α^{sca} spectral maximum but only a drop. Hence, the α^{sca} values decrease (α^{sca} inversely depends on the mass density) but the α^{sca} spectral dependence remains unaffected. Looking at Table 3.3 (mass density rows): similarly to the reference case, all the perturbed simulations result s-compatible (best s_{test} from m: $0,99$) and no simulations q-compatible (best q_{test} from m: $5,26$) with the observations; the m case has the best total score ($t_{test} = 6,25$: fit incompatibility). The impact of the mass density perturbations on the α^{sca} values, even if sig-

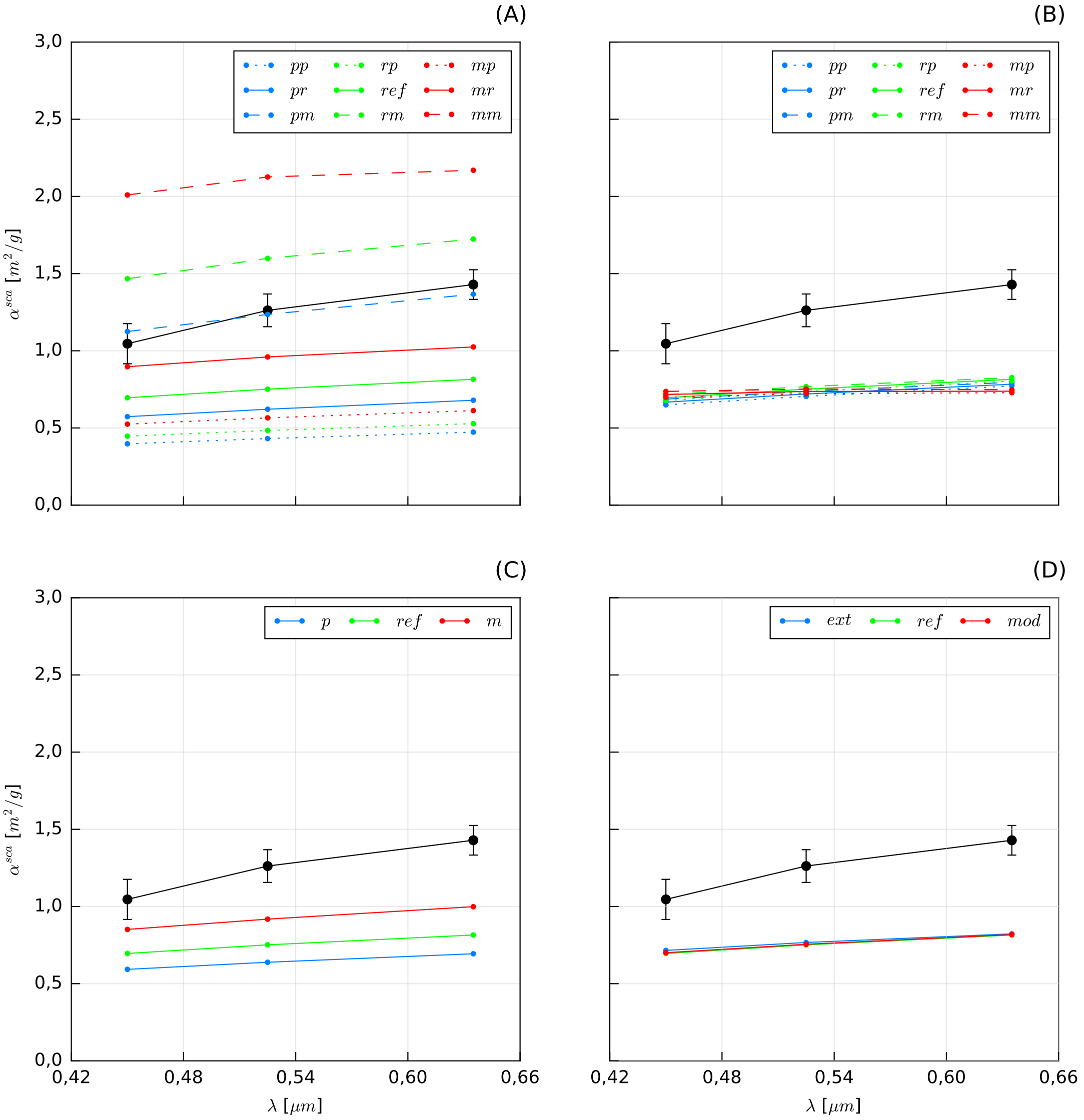

Figure 3.1: **Spectral α^{sca} at the 3 wavelengths of the experiment of mineral dust under: (A) size distribution, (B) refractive index, (C) mass density and (D) shape perturbations. The black points are the observed values with their error bands (see Table 3.1) while the different colored lines are the code calculation results (see Table 3.2 for case acronyms).**

nificant, does not produce any fit compatibility and so it does not allow us to strictly constrain this microphysical property for mineral dust.

The **shape** perturbations (see Figure 3.1-D for the related spectral α^{sca}) have a significant impact neither on the α^{sca} spectral dependence ($S_{ratio} = 0,073$) nor on the α^{sca} values ($V_{ratio} = 0,072$). Looking at Table 3.3 (shape rows): similarly to the reference case, all the perturbed simulations result s-compatible (best s_{test} from ref: $1,00$) and no simulations q-compatible (best q_{test} from ext: $8,50$) with the observations; the best total score is from the ext case ($t_{test} = 9,65$: fit incompatibility). Since the impact of the shape perturbations on both α^{sca} values and spectral dependence is negligible, no fit compatibility is achieved and so no constraints on this microphysical property for mineral dust can be derived.

3.6.2 Organic carbon

The **size distribution** perturbations (see Figure 3.2-A for the related spectral α^{sca}) affect significantly both the α^{sca} spectral dependence ($S_{ratio} = 2,0$) and the values of α^{sca} ($V_{ratio} = 6,0$). The α^{sca} spectral maximum of organic carbon lies at shorter wavelengths than those of the visible range (negative logarithmic linear spectral dependence slope in the visible range). An increasing effective radius causes the α^{sca} maximum to get closer to the experiment spectral range (the opposite of the dust case) and to decrease, due to the inverse dependence of α^{sca} on r_{eff}. For this reason, the α^{sca} values at first increase, because closer and closer to the maximum, but then start to decrease because the maximum drop becomes dominant. The α^{sca} spectral dependence trend keeps decreasing, although moderately variable. Looking at Table 3.3 (size distribution rows): the reference case ref results s-compatible but not q-compatible; all the perturbed simulations show different s-compatibilities (best s_{test} from pm: $0,73$) but similarly to the reference case are not q-compatible (best q_{test} from pm: $1,82$) with the observations; the best total score is from pm ($t_{test} = 2,55$: partial fit compatibility). The significant impact of the size distribution perturbations on both α^{sca} values and spectral dependence makes the pm case partially fit compatible with the observations, with a perfect coherence between the best fit parameters: pm has the best s_{test} and the best q_{test}, being though the q_{test} value above the single parameter compatibility threshold. This partial fit compatibility allows us to constrain, in the north-western Mediterranean basin, the organic carbon size distribution parameters to the values $r_g = 2,544 \cdot 10^{-2}\ \mu m$ and $\sigma_g = 1,760$ ($r_{eff} = 5,656 \cdot 10^{-2}\ \mu m$). However, the not full fit compatibility suggests that some adjustments derived from other microphysical properties could improve the agreement between code calculations and observations (see Section 3.7).

The **refractive index** perturbations (see Figure 3.2-B for the related spectral α^{sca}) show a negligible impact on the α^{sca} spectral dependence ($S_{ratio} = 0,53$) but a strong impact on the α^{sca} values (being the influence of the real part dominant) ($V_{ratio} = 9,7$). Due to the organic carbon α^{sca} maximum position, the effects of the increasing real refractive index (growth and shift of the α^{sca} maximum towards longer wavelengths) now do not balance each other and cause the α^{sca} values to increase, leaving though the α^{sca} spectral dependence nearly unaffected. Looking at Table 3.3 (refractive index rows): similarly to the reference case, all the perturbed simulations are s-compatible (best s_{test} from mm: $0,54$) and no simulations q-compatible (best q_{test} from mm: $7,16$) with the observations; the best total score is from mm ($t_{test} = 7,70$: fit incompatibility). The significant impact of the refractive index perturbations on the α^{sca} values is not able to generate any fit compatibility and so it does not allow us to derive any constraints on this microphysical property for organic carbon.

The **mass density** perturbations (see Figure 3.2-C for the related spectral α^{sca}) leave the α^{sca} spectral dependence unaffected ($S_{ratio} = 0,000036$) while have a relevant impact on the α^{sca} values

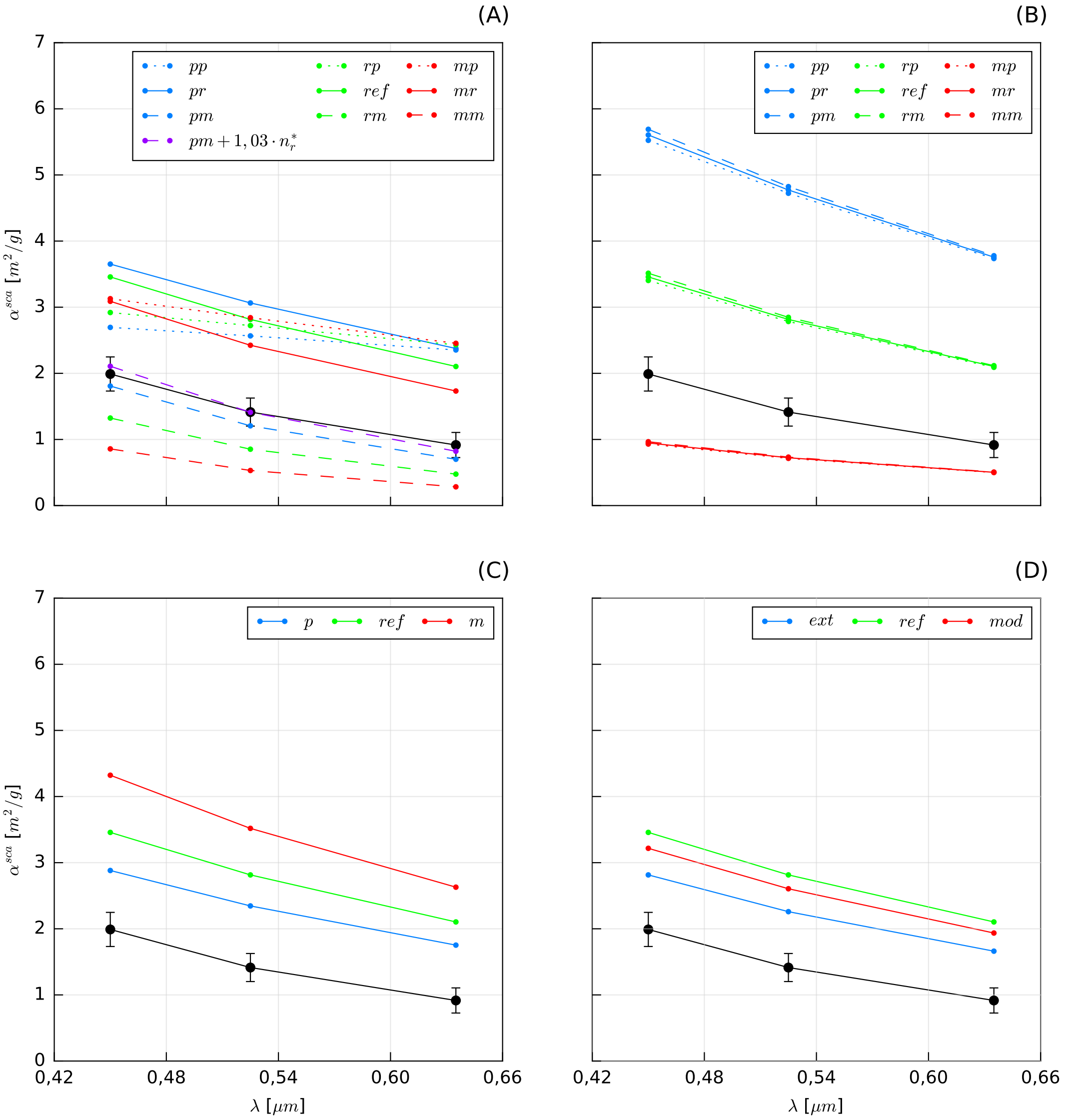

Figure 3.2: **Same as Figure 3.1 but for organic carbon.**

($V_{ratio} = 2,8$). The effects of changing the mass density is the same as for mineral dust, so the α^{sca} values decrease with increasing the mass density value but the α^{sca} spectral dependence remains unaffected. Looking at Table 3.3 (mass density rows): similarly to the reference case, all the perturbed simulations show s-compatibility (best s_{test} from ref, m and p: $1,15$) and q-incompatibility (best q_{test} from p: $5,38$) with the observations; the best total score is from the p case ($t_{test} = 6,53$: fit incompatibility). The impact of the mass density perturbations on the α^{sca} values is relevant but not able to produce any fit compatibility and so not useful to strictly constrain this microphysical property for organic carbon.

The **shape** perturbations (see Figure 3.2-D for the related spectral α^{sca}) do not affect the α^{sca} spectral dependence ($S_{ratio} = 0,063$) but, differently from the dust case, have a relevant impact on the α^{sca} values ($V_{ratio} = 1,3$). Looking at Table 3.3 (shape rows): similarly to the reference case, all the perturbed simulations reach the s-compatibility (best s_{test} from ext: $1,03$) and no simulations the q-compatibility (best q_{test} from ext: $4,98$) with the observations; the best total score is from the ext case ($t_{test} = 6,01$: fit incompatibility). The relevant impact of the shape perturbations on the α^{sca} values does not allow us to strictly constrain this microphysical property for organic carbon, because no fit compatibility is achieved.

3.6.3 Sulfate

The **size distribution** perturbations (see Figure 3.3-A for the related spectral α^{sca}) affect significantly both the α^{sca} spectral dependence ($S_{ratio} = 5,2$) and the values of α^{sca} ($V_{ratio} = 3,3$). The α^{sca} spectral maximum of sulfate lies at shorter wavelengths than those of the visible range (negative logarithmic linear spectral dependence slope in the visible range). An increasing effective radius has for sulfate the same effect as for organic carbon on the spectral maximum of the α^{sca}, so again the α^{sca} values at first increase and then start to decrease because the drop of the α^{sca} maximum becomes dominant with respect to its getting closer to the experiment spectral range. The α^{sca} spectral dependence trend keeps decreasing although significantly variable. Looking at Table 3.3 (size distribution rows): the reference case ref reaches neither the s-compatibility nor the q-compatibility; all the perturbed simulations show different s-compatibilities (best s_{test} from pm: $0,30$) but similarly to the reference case are not q-compatible (best q_{test} from ref: $10,77$) with the observations; the best total score is from pm ($t_{test} = 12,32$: fit incompatibility). The strong impact of the size distribution perturbations on both α^{sca} values and spectral dependence is not able to generate any fit compatibility and so to provide any strict constraints on this microphysical property for sulfate. Moreover, the best s_{test} (from pm: compatibility value) and the best q_{test} (from ref: incompatibility value) come from different cases. Hence, there seems to be an incoherence between the two best fit parameters (both significantly affected by the perturbations). This suggests that more microphysical properties for sulfate have to be tuned for the code to reproduce the experimental data (see Section 3.7).

The **refractive index** perturbations (see Figure 3.3-B for the related spectral α^{sca}) show a strong impact on both the α^{sca} spectral dependence ($S_{ratio} = 3,0$) and the α^{sca} values (being the influence of the imaginary part totally negligible, due to the very low values for sulfate) ($V_{ratio} = 9,1$). Due to the sulfate α^{sca} maximum position, again the unbalanced combined effects of the increasing real refractive index (growth and shift of the α^{sca} maximum towards longer wavelengths) cause the α^{sca} values to increase, but now affecting also the α^{sca} spectral dependence. Looking at Table 3.3 (refractive index rows): all the perturbed simulations show different s-compatibilities (best s_{test} from mm, mr and mp: $0,20$) and strongly different q-compatibilities (best q_{test} from pm, pr and pp: $0,84$) with the observations; the best total scores are from pm, pr and pp ($t_{test} = 6,88$: fit incompatibility). The im-

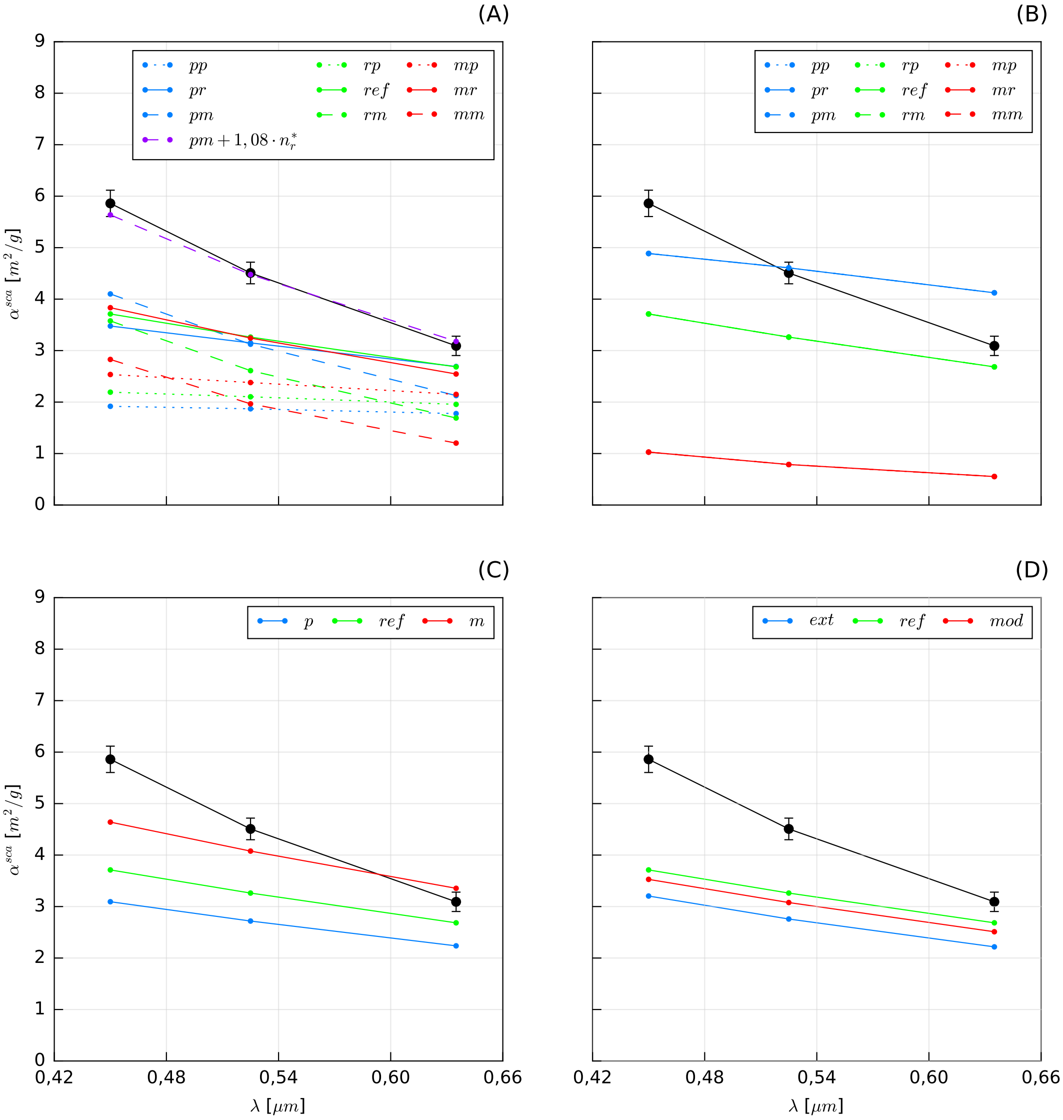

Figure 3.3: **Same as Figure 3.1 but for sulfate.**

pact of the refractive index perturbations on both α^{sca} values and spectral dependence is relevant but again not able to generate any fit compatibility and so useless to strictly constrain this microphysical property for sulfate. Moreover, again the best s_{test} (from mm, mr and mp: compatibility value) and the best q_{test} (from pm, pr and pp: compatibility value) come from different cases, showing a second incoherence between the two best fit parameters (both significantly affected by the perturbations). This confirms that more microphysical properties for sulfate have to be simultaneously changed in order to achieve a better agreement between code results and experimental data (see Section 3.7).

The **mass density** perturbations (see Figure 3.3-C for the related spectral α^{sca}) leave the α^{sca} spectral dependence unaffected ($S_{ratio} = 0,0020$) and affect only the α^{sca} values ($V_{ratio} = 3,2$). The effects of changing the mass density is the same as for the other aerosols, so the α^{sca} values decrease with increasing mass density, but the α^{sca} spectral dependence is not affected. Looking at Table 3.3 (mass density rows): similarly to the reference case, no perturbed simulations result s-compatible (best s_{test} from ref, m and p: $4,05$) nor q-compatible (best q_{test} from m: $3,24$) with the observations; the best total score is from the m case ($t_{test} = 7,29$: fit incompatibility). The not negligible impact of the mass density perturbations on the α^{sca} values is not able to generate any fit compatibility and so it makes impossible to strictly constrain this microphysical property for sulfate.

The **shape** perturbations (see Figure 3.3-D for the related spectral α^{sca}) do not affect significantly the α^{sca} spectral dependence ($S_{ratio} = 0,30$) but have a relevant impact on the α^{sca} values ($V_{ratio} = 1,2$). Looking at Table 3.3 (shape rows): similarly to the reference case, all the perturbed simulations show both s-incompatibility (best s_{test} from ext: $3,49$) and q-incompatibility (best q_{test} from ref: $10,77$) with the observations; the best total score is from the ref case ($t_{test} = 14,82$: fit incompatibility). Even if the impact of the shape perturbations on the α^{sca} values is not negligible, it is not useful to strictly constrain this microphysical property for sulfate, since it does not generate any fit compatibility.

3.7 Discussion

We found that the mineral dust α^{sca} values are only affected by the size distribution and, with a lower impact, by the mass density perturbations. On the other hand, no microphysical properties seem to have any impact on the α^{sca} spectral dependence. So, it seems that, due mainly to the size of the particles bigger than the visible wavelengths, the dust α^{sca} are quite stable with respect to the microphysical perturbations (in the spectral range of the experiment). The size distribution case pm reaches full fit compatibility with the observations ($t_{test} = 0,74$) and this allows us to strictly constrain the mineral dust size distribution. Other minor adjustments on the α^{sca} values could come only from the mass density perturbations, but they are useless in this case since the size distribution case pm has the best q_{test} (and also the best s_{test} even if the variability of the s_{test} values due to the size distribution perturbations has been found quantitatively insignificant). So, there seems to be a perfect coherence between the two best fit parameters. Hence, for mineral dust we confirm that, in the north-western Mediterranean basin, the prescriptions derived from our analysis are (being the refractive index values relative to $0,450\ \mu m$; $0,525\ \mu m$; $0,635\ \mu m$, respectively):

$$\begin{aligned} \text{Size distribution: } & r_g = 3,583 \cdot 10^{-1} \mu m \\ & \sigma_g = 1,600 \\ & r_{eff} = 6,221 \cdot 10^{-1} \mu m; \\ \text{Refractive index: } & n_r = (1,530; 1,530; 1,530) \quad \text{(reference)} \\ & n_i = (8,500; 6,650; 4,500) \cdot 10^{-3} \quad \text{(reference);} \\ \text{Mass density: } & \rho = 2,506 \cdot 10^3 kg/m^3 \quad \text{(reference);} \\ \text{Shape: } & \chi = 1,000 \quad \text{(reference).} \end{aligned}$$

Hence, it seems that smaller dust particles (higher geometric radius but lower standard deviation) than the reference ones reach the north-western Mediterranean basin. Regarding the other perturbed microphysical properties, the reference prescriptions seem to describe well the mineral dust source in this geographical area.

The organic carbon α^{sca} values are affected mainly by refractive index (real part), size distribution and, with a lower impact, by mass density and shape perturbations. The α^{sca} spectral dependence, instead, is significantly affected only by the size distribution perturbations. So, the organic carbon α^{sca} appear to be less stable than the mineral dust ones with respect to the microphysical perturbations, due mainly to the size of the particles smaller than the visible wavelengths. The size distribution case *pm* reaches partial fit compatibility with the observations ($t_{test} = 2,55$) and this allows us to constrain the organic carbon size distribution. However, despite the perfect coherence between the best fit parameters, the α^{sca} values of the size distribution case *pm* result a little "too low" with respect to the observations. Hence, in order to achieve the full fit compatibility, since the refractive index (real part) has the strongest impact on the α^{sca} values, we tried to apply an adequate real refractive index increase to the size distribution case *pm*. We found an optimal increase to be of 3% with respect to the reference values. In this composite case (the violet line in Figure 3.2-A), both the s-compatibility and the q-compatibility of the size distribution case *pm* improve ($s_{test} = 0,70$ and $q_{test} = 0,13$) and the full fit compatibility is achieved ($t_{test} = 0,83$). This result allows us to strictly constrain simultaneously size distribution and real refractive index for organic carbon. Hence, for organic carbon, in the north-western Mediterranean basin, the prescriptions derived from our analysis are (being the refractive index values relative to $0,450\ \mu m$; $0,525\ \mu m$; $0,635\ \mu m$, respectively):

$$\begin{aligned} \text{Size distribution: } & r_g = 2,544 \cdot 10^{-2} \mu m \\ & \sigma_g = 1,760 \\ & r_{eff} = 5,656 \cdot 10^{-2} \mu m; \\ \text{Refractive index: } & n_r = (1,576; 1,576; 1,576) \\ & n_i = (1,730; 1,250; 0,696) \cdot 10^{-2} \quad \text{(reference);} \\ \text{Mass density: } & \rho = 1,800 \cdot 10^3 kg/m^3 \quad \text{(reference);} \\ \text{Shape: } & \chi = 1,000 \quad \text{(reference).} \end{aligned}$$

Hence, smaller organic carbon particles (higher geometric radius but lower standard deviation) and with a slightly higher real refractive index (in the visible range) than the reference particles seem to be representative of the north-western Mediterranean basin. Regarding mass density and shape instead, the reference prescriptions seem to describe well the aged organics source in this geographical area.

The sulfate α^{sca} values are mainly affected by the refractive index (real part) and, with a lower impact, by size distribution, mass density and shape perturbations. On the other hand, the α^{sca}

spectral dependence is only affected by size distribution and refractive index perturbations. So, it seems that the sulfate α^{sca} are the most unstable with respect to the microphysical perturbations, due to the particle size approximately comparable with the visible wavelengths. For sulfate, no perturbation cases reach any fit compatibility with the observations. The size distribution case pm has the best s_{test} while ref has the best q_{test}. On the other hand, the refractive index case mr has the best s_{test} but pr has the best q_{test} (considering only the real part of the refractive index since the imaginary part has not any influence). Hence, in order to solve these incoherences and to achieve full fit compatibility, since the refractive index (real part) has the strongest impact on the α^{sca} values, we tried to consider the size distribution case pm with an increased real refractive index. We found an optimal increase to be of 8% with respect to the reference values. In this composite case (the violet line in Figure 3.3-A), the s-compatibility of the pm size distribution case (best value) gets a little worse but remains very good ($s_{test} = 0,76$), while the q-compatibility improves significantly ($q_{test} = 0,30$). So, applying this small real refractive index perturbation to the size distribution case pm produces full fit compatibility ($t_{test} = 1,06$), allowing us to constrain simultaneously size distribution and refractive index also for sulfate. Hence, for sulfate, in the north-western Mediterranean basin, the prescriptions derived from our analysis are (being the refractive index values relative to $0,450\ \mu m$; $0,525\ \mu m$; $0,635\ \mu m$, respectively):

$$\begin{aligned}
\text{Size distribution: } & r_g = 8,340 \cdot 10^{-2} \mu m \\
& \sigma_g = 1,624 \\
& r_{eff} = 1,501 \cdot 10^{-1} \mu m; \\
\text{Refractive index: } & n_r = (1,547; 1,545; 1,543) \\
& n_i = (1,000; 1,000; 1,610) \cdot 10^{-8} \quad \text{(reference)}; \\
\text{Mass density: } & \rho = 1,700 \cdot 10^3 kg/m^3 \quad \text{(reference)}; \\
\text{Shape: } & \chi = 1,000 \quad \text{(reference)}.
\end{aligned}$$

Hence, smaller sulfate particles (higher geometric radius but lower standard deviation) and with a higher real refractive index (in the visible range) than the reference particles seem to be representative of the north-western Mediterranean basin. Regarding mass density and shape, again the reference prescriptions appear to be adequate to describe the ammonium sulfate source in this geographical area.

3.8 Conclusions

Through a comparison between code simulations and observations, we assessed the sensitivity of simulated α^{sca} (values and spectral dependence) of mineral dust, organic carbon and sulfate to perturbed microphysical properties (size distribution, refractive index, mass density and shape) and also constrained these properties in the north-western Mediterranean basin. We observed that the impact of the microphysical assumptions on the scattering properties mainly depends on the size of the particles. The species with mean size smaller than (organic carbon) or almost comparable with (sulfate) the visible wavelengths (spectral range of this experiment) appear, indeed, to be more unstable with respect to the perturbations. Size distribution and refractive index, however, have been found to have dominant impacts on the simulated α^{sca} with respect to mass density and shape in most cases. We performed code simulations using reference microphysical properties for the particles (used in the NMMB-MONARCH) derived from very general literature prescriptions but widely used in the aerosol modeling community. We then applied perturbations on these reference properties in order to reproduce the great uncertainty affecting them. As observations, we used α^{sca} of aerosol sources detected at the Montseny regional background station. The aerosol sources are supposed to be a more realistic representation of the aerosols in atmosphere and allowed us to take into account the effects of minor internally mixed species on the ARI of the dominant species (which are the modeled species).

Chapter 4

Impact of aerosol properties on direct radiative effects

4.1 Introduction

The assessments of the radiative effects and forcing due to Aerosol-Radiation Interaction (ARI), from both natural and anthropogenic aerosols, are still affected by significant uncertainty [Myhre et al., 2013b; Rap et al., 2013]. The ARI features are mainly defined by the characterization of the aerosol optical properties, which indeed strongly contribute to the uncertainty affecting measurement-based and model estimates of ARI radiative effects [Yu et al., 2006; Randles et al., 2013]. The aerosol optical properties for model simulations are calculated with optical codes starting from particle microphysical properties, such as size distribution, refractive index, mixing state, mass density, shape and hygroscopicity [Boucher et al., 2013; Hand and Malm, 2007]. Hence, different particle microphysical assumptions can affect the calculation of the optical properties and therefore the model assessments of the ARI radiative effects [Yu et al., 2006]. In the last two decades, many sensitivity studies of simulated radiative fluxes to aerosol microphysical and optical properties have been published. However, in most works the analysis has been carried out on single aerosol species, either mineral dust [Liao and Seinfeld, 1998; Tegen and Lacis, 1996], carbonaceous aerosols [Bauer et al., 2010], sulfate [Nemesure et al., 1995] or black carbon-sulfate mixture [Lesins et al., 2002]. Moreover, different microphysical parameters with very different experiment setups (perturbations considered, simulation configurations, analysis methods, etc.) have been investigated. Hence, even if all these works agree that the microphysical assumptions for the particles can have relevant impacts on the ARI radiative effect model estimates, it appears to be difficult to find results relative to different properties or species that are directly comparable.

In this chapter we present a systematic and detailed study on the propagation of particle microphysical perturbations, applied to several microphysical parameters of natural and anthropogenic aerosol species, on the optical and radiative simulations usually required by the ARI implementation in weather and climate models. Our analysis, therefore, has been carried out at two levels: i) impact of the particle microphysical perturbations on layer radiative properties and ii) consequent impact on shortwave direct radiative effects, at the top of atmosphere (TOA) and at surface (SFC). We used numerical codes and aerosol parameterization implemented in our online integrated meteorology-chemistry model NMMB-MONARCH (described in detail in Chapter 2) but also widely used in other atmospheric models. Hence our results are suitable for the weather and climate modeling community. Several important global aerosol species usually considered in aerosol models have been separately investigated: mineral dust and organic carbon, in order to study particles with different sizes (producing results suitable in a certain degree for other species with similar sizes), and black carbon and sulfate, in order to analyze also the particle mixing state. All the particles have been considered spherical, dry and homogeneous. Local perturbations have been applied to the size distribution and refractive index parameters for mineral dust and organic carbon. The perturbation range ($\pm 20\%$) has been set to represent, in a first approximation, uncertainties affecting the aerosol microphysical parameters. Our main objective, however, was not to accurately represent realistic experimental uncertainties but to consider a homogeneous (and reasonable) perturbation range for all the species and microphysical properties. On the other hand, for the black carbon-sulfate mixture two different mixing states (internal and external) have been considered. Starting from these perturbed microphysical assumptions, layer optical depth (τ), single scattering albedo (ω) and asymmetry factor (g) have been calculated for all the species and their perturbation-induced relative spreads evaluated in all the shortwave region. We then performed one-column radiative transfer simulations with and without activating idealized aerosol layers (shortwave and clear-sky conditions) in order to separately calculate direct radiative effects (at the TOA and at SFC) under perturbations of different properties and aerosol species. Again, we did not aim to simulate realistic direct radiative effects (for which mass transport has to be simulated with integrated meteorology-chemistry models) but to focus the analysis on the radiative sensitivity to the perturbations of the particle microphysical properties. Increasing values of mass concentration for each species have been set in the homogeneous layers in order to simulate 3 aerosol events of increasing intensity. In order to provide results suitable for general atmospheric scenarios (for example different meteorological and geographical assumptions), the perturbation-induced variability ranges of the direct radiative effects have been evaluated against the base net fluxes in absence of aerosols.

The work presented in this chapter has been published in Obiso and Jorba [2018] (Journal of Aerosol Science). This chapter is organized as follows: in Section 4.2, the numerical tools used are introduced; in Sections 4.3, 4.4 and 4.5, the setup details for aerosol properties and radiative simulations are reported; in Sections 4.6 and 4.7, the results of the experiment are presented (separately for each aerosol species) and discussed, respectively; in Section 4.8, detailed conclusions from our results are presented.

4.2 Numerical tools

For the optical simulations, the T-matrix code by Mishchenko et al. [2002] has been used (already presented in Section 2.5.2). It allows computing light scattering by polydisperse, randomly oriented, non-spherical (rotationally symmetric), homogeneous particles [Mishchenko and Travis, 1998]. This code appeared to be the most adequate for this experiment because of its flexibility and high precision.

For the radiative simulations, we used the RRTMG_SW [Iacono et al., 2008] (already presented in Section 2.5.1) in the stand-alone version. The model divides the shortwave region (from $0,200$ to $12,195$ μm) in 14 spectral bands (reported in Table 2.2), and allows considering the presence of aerosol layers in atmosphere by requiring as inputs layer optical depth, single scattering albedo and asymmetry factor of the aerosol mixture for each of these spectral bands. The RRTMG_SW is implemented as radiative scheme in the NMMB-MONARCH and is also used in many important models (a list of global and regional models using the RRTMG is reported in Iacono [2011]) and therefore it has been considered an appropriate tool for our sensitivity study.

4.3 Microphysical properties

We considered four important global aerosol species in this work: mineral dust, organic carbon, black carbon and sulfate. The following microphysical properties have been considered to characterize the reference aerosol species: size distribution (geometric radius r_g [μm] and standard deviation σ_g [unitless]), refractive index (real n_r and imaginary n_i parts [unitless]) and mass density (ρ [kg/m^3]). All the aerosol species have always been considered spherical, homogeneous and in dry conditions (relative humidity effects on the particle optical properties have not been analyzed). We defined the reference microphysical properties following the aerosol parameterization used in the NMMB-MONARCH (summarized in Table 2.1). Some deviations from this default parameterization have been required in this work. First, the NMMB-MONARCH model considers different values of dust mass density for sub-micron and super-micron bins and so for the bulk mineral dust considered in this work we derived a weighted mean of the original values. Second, since organic carbon includes particles with very different absorbing capabilities, we modified the default imaginary refractive index in the visible range in order to make it more compatible with the mean of the experimental estimates reported in Liu et al. [2015].

In order to generate variability in the aerosol microphysical parameterization for the sensitivity study, we perturbed all the reference parameters of the relevant microphysical properties (always in this work marked with '*'). For mineral dust and organic carbon we multiplied the reference parameters of size distribution (r_g^* and σ_g^* separately) and refractive index (n_r^* and n_i^* separately) for perturbation factors: m (i.e. $minus$), r (i.e. $reference$) and p (i.e. $plus$). The values ($m = 0,8$; $r = 1,0$; $p = 1,2$) have been selected for all the parameters. It is important to note that the two microphysical properties have been perturbed separately, so when the size distribution was perturbed the reference refractive index values were used and vice versa. Also, for each microphysical property the two parameters have been perturbed independently but allowing the composite perturbations (in order to expand the perturbation space [Zhao et al., 2013]). So 9 perturbation cases for each property have been derived. Mass density and shape have not been directly perturbed in this work because in Obiso et al. [2017] they have been found in most of the cases to be less important than size distribution and refractive index in affecting the aerosol scattering properties. Also the impact of shape on the intensive properties (ω and g) has been found negligible compared to that of size distribution and refractive index (results not shown). On the other hand, black carbon and sulfate have been considered as a mixture in two different mixing states: external (em) and internal (im). For the em case, the single species reference microphysical properties have been used to separately calculate the spectral optical properties of black carbon and sulfate. These properties have been then coupled a posteriori to derive the layer radiative properties of the externally mixed species, as explained in Section 4.4. For the im case, we supposed at first that all the sulfate mass condenses on the black carbon particles with a constant ratio (R) of the black carbon volume (V) to the total volume (in the following equations bc and su indicate black carbon and sulfate, respectively):

$$R = \frac{V_{bc}}{V_{bc+su}}. \tag{4.1}$$

We then imposed the conservation of the sulfate mass concentration:

$$\int (V_{bc+su} - V_{bc})\rho_{su} N_{bc} f_{bc}(r) dr = M_{su}, \tag{4.2}$$

where, in addition to the already introduced symbols, f is the normalized particle number size distribution (log-normal in our case), N is the particle number concentration and M the mass concentration.

Finally, from Equations 4.1 and 4.2, we derived the following formula for R:

$$R = \frac{\rho_{su} M_{bc}}{\rho_{su} M_{bc} + \rho_{bc} M_{su}}. \tag{4.3}$$

The value $R = 0,357$ has been calculated after setting the mass concentrations for black carbon and sulfate (see Section 4.4). Once derived the volume ratio, the microphysical properties of the internally mixed species have been calculated as follows:

$$\begin{aligned} r_g &= r^*_{g,bc} R^{-1/3}, \\ \sigma_g &= \sigma^*_{g,bc}, \\ n_r &= n^*_{r,bc} R + n^*_{r,su}(1 - R), \\ n_i &= n^*_{i,bc} R + n^*_{i,su}(1 - R), \\ \rho &= \rho^*_{bc} R + \rho^*_{su}(1 - R). \end{aligned} \tag{4.4}$$

Hence, the internally mixed particles have been modeled as homogeneous particles with mean refractive index and mass density (so well-mixed particles). The size distribution has been derived by shifting that of black carbon according to the fixed volume ratio, in order to take into account the size increase due to the internal mixing with sulfate. Moreover, with this procedure the total mass concentration of the two species results conserved while the number concentration of the internally mixed species equals that of black carbon.

In Table 4.1 reference and perturbed size distribution and refractive index values (also due to the different mixing states) for all the species considered are reported. The perturbation cases for mineral dust and organic carbon are named starting from the perturbation factors m, r and p defined above: the first factor refers to r_g and n_r while the second one to σ_g and n_i, for size distribution and refractive index respectively. The rr cases (i.e. the reference cases) for the two properties are the same case, which we named ref in order to avoid confusion. Regarding the black carbon-sulfate mixture, the external mixing case em has been considered as the reference case in the sensitivity analysis while the internal mixing case im as the perturbation case. A log-normal size distribution, over the size range from $0,001$ to $5,0$ μm (aerodynamic radius: coherently with the definition of PM_{10}), has been considered for all the species. For each couple of size distribution parameters, the corresponding effective radius (r_{eff}) is also reported (for poly-disperse particles r_{eff} can be considered as the representative size of the ensemble [Hansen and Travis, 1974]), which is defined as the projected-area-weighted mean radius [Mishchenko et al., 2002] and can be easily calculated as follows [Lesins et al., 2002]:

$$r_{eff} = r_g \exp\left(\frac{5}{2} \ln^2 \sigma_g\right). \tag{4.5}$$

As already mentioned, the mass density has not been directly perturbed in this work but it affects the aerodynamic radius involved in the definition of the size range [DeCarlo et al., 2004].

4.4 Layer radiative properties

Spectral extinction efficiency (Q^{ext}), single scattering albedo and asymmetry factor of mineral dust and organic carbon (for all the perturbation cases), black carbon, sulfate and the internally mixed species have been calculated with the T-matrix code, providing as inputs all the microphysical parameters defined in Section 4.3. The calculations have been performed at all the wavelengths of the OPAC database [Hess et al., 1998] (which provides the reference refractive indexes for all the species) covering

Table 4.1: **Reference and perturbed microphysical parameters for all the considered species: geometric radius (r_g) and standard deviation (σ_g), real (n_r) and imaginary (n_i) refractive indexes. For simplicity, only the refractive indexes at $0,550\ \mu m$ have been reported. The reference mass density (ρ) used for the considered species are (in kg/m^3): $2,506 \cdot 10^3$ (mineral dust), $1,800 \cdot 10^3$ (organic carbon), $1,000 \cdot 10^3$ (black carbon) and $1,700 \cdot 10^3$ (sulfate). For the internally mixed species a value of $1,450 \cdot 10^3$ has been derived from the last of Equations 4.4. The perturbation case acronyms have been defined in Section 4.3.**

	Size Distribution			**Refractive Index**		
Cases	**Parameters**	**Mineral Dust**	**Organic Carbon**	**Parameters**	**Mineral Dust**	**Organic Carbon**
ref	r_g^* [μm]	$2,986 \cdot 10^{-1}$	$2,120 \cdot 10^{-2}$	n_r^*	$1,530$	$1,530$
	σ_g^*	$2,000$	$2,200$	n_i^*	$5,500 \cdot 10^{-3}$	$6,000 \cdot 10^{-3}$
	r_{eff}^* [μm]	$9,205 \cdot 10^{-1}$	$1,003 \cdot 10^{-1}$			
mm	r_g [μm]	$2,389 \cdot 10^{-1}$	$1,696 \cdot 10^{-2}$	n_r	$1,224$	$1,224$
	σ_g	$1,600$	$1,760$	n_i	$4,400 \cdot 10^{-3}$	$4,800 \cdot 10^{-3}$
	r_{eff} [μm]	$4,150 \cdot 10^{-1}$	$3,771 \cdot 10^{-2}$			
mr	r_g [μm]	$2,389 \cdot 10^{-1}$	$1,696 \cdot 10^{-2}$	n_r	$1,224$	$1,224$
	σ_g	$2,000$	$2,200$	n_i	$5,500 \cdot 10^{-3}$	$6,000 \cdot 10^{-3}$
	r_{eff} [μm]	$7,617 \cdot 10^{-1}$	$8,024 \cdot 10^{-2}$			
mp	r_g [μm]	$2,389 \cdot 10^{-1}$	$1,696 \cdot 10^{-2}$	n_r	$1,224$	$1,224$
	σ_g	$2,400$	$2,640$	n_i	$6,600 \cdot 10^{-3}$	$7,200 \cdot 10^{-3}$
	r_{eff} [μm]	$1,150$	$1,782 \cdot 10^{-1}$			
rm	r_g [μm]	$2,986 \cdot 10^{-1}$	$2,120 \cdot 10^{-2}$	n_r	$1,530$	$1,530$
	σ_g	$1,600$	$1,760$	n_i	$4,400 \cdot 10^{-3}$	$4,800 \cdot 10^{-3}$
	r_{eff} [μm]	$5,187 \cdot 10^{-1}$	$4,713 \cdot 10^{-2}$			
rp	r_g [μm]	$2,986 \cdot 10^{-1}$	$2,120 \cdot 10^{-2}$	n_r	$1,530$	$1,530$
	σ_g	$2,400$	$2,640$	n_i	$6,600 \cdot 10^{-3}$	$7,200 \cdot 10^{-3}$
	r_{eff} [μm]	$1,293$	$2,219 \cdot 10^{-1}$			
pm	r_g [μm]	$3,583 \cdot 10^{-1}$	$2,544 \cdot 10^{-2}$	n_r	$1,836$	$1,836$
	σ_g	$1,600$	$1,760$	n_i	$4,400 \cdot 10^{-3}$	$4,800 \cdot 10^{-3}$
	r_{eff} [μm]	$6,221 \cdot 10^{-1}$	$5,656 \cdot 10^{-2}$			
pr	r_g [μm]	$3,583 \cdot 10^{-1}$	$2,544 \cdot 10^{-2}$	n_r	$1,836$	$1,836$
	σ_g	$2,000$	$2,200$	n_i	$5,500 \cdot 10^{-3}$	$6,000 \cdot 10^{-3}$
	r_{eff} [μm]	$1,061$	$1,204 \cdot 10^{-1}$			
pp	r_g [μm]	$3,583 \cdot 10^{-1}$	$2,544 \cdot 10^{-2}$	n_r	$1,836$	$1,836$
	σ_g	$2,400$	$2,640$	n_i	$6,600 \cdot 10^{-3}$	$7,200 \cdot 10^{-3}$
	r_{eff} [μm]	$1,406$	$2,650 \cdot 10^{-1}$			
Cases	**Parameters**	**Black Carbon**	**Sulfate**	**Parameters**	**Black Carbon**	**Sulfate**
em	r_g^* [μm]	$1,180 \cdot 10^{-2}$	$6,950 \cdot 10^{-2}$	n_r^*	$1,750$	$1,430$
	σ_g^*	$2,000$	$2,030$	n_i^*	$4,400 \cdot 10^{-1}$	$1,000 \cdot 10^{-8}$
	r_{eff}^* [μm]	$3,922 \cdot 10^{-2}$	$2,433 \cdot 10^{-1}$			
im	r_g [μm]	$1,664 \cdot 10^{-2}$		n_r	$1,544$	
	σ_g	$2,000$		n_i	$1,570 \cdot 10^{-1}$	
	r_{eff} [μm]	$5,530 \cdot 10^{-2}$				

the spectral bands of the RRTMG_SW. Following Liao and Seinfeld [1998], we then derived the band optical properties by averaging the spectral optical properties within the RRTMG_SW spectral bands, using the solar flux (S) as weight function at each wavelength (λ), as follows:

$$\begin{aligned} Q_b^{ext} &= \frac{\sum_\lambda Q_\lambda^{ext} S_\lambda}{\sum_\lambda S_\lambda}, \\ \omega_b &= \frac{\sum_\lambda \omega_\lambda S_\lambda}{\sum_\lambda S_\lambda}, \\ g_b &= \frac{\sum_\lambda g_\lambda S_\lambda}{\sum_\lambda S_\lambda}, \end{aligned} \tag{4.6}$$

in which the sums are defined over all the wavelengths falling within each RRTMG_SW spectral band (indexed by b).

Once the band optical properties have been calculated, we derived the corresponding layer radiative properties to be given as inputs to the RRTMG_SW, namely layer optical depth, single scattering albedo and asymmetry factor, for all the species. For single and internally mixed species, layer single scattering albedo and asymmetry factor (intensive properties) coincide with the corresponding band optical properties while the layer optical depth has been calculated with the following formula [Tegen and Lacis, 1996]:

$$\tau_b = \frac{3Q_b^{ext}}{4\rho r_{eff}} M \Delta Z, \tag{4.7}$$

in which, in addition to the already presented symbols, ΔZ is the atmospheric layer thickness. The layer radiative properties of the externally mixed species have been then calculated by coupling that of black carbon and sulfate, as follows:

$$\begin{aligned} \tau_b &= \tau_{b,bc} + \tau_{b,su}, \\ \omega_b \tau_b &= \omega_{b,bc}\tau_{b,bc} + \omega_{b,su}\tau_{b,su}, \\ g_b \omega_b \tau_b &= g_{b,bc}\omega_{b,bc}\tau_{b,bc} + g_{b,su}\omega_{b,su}\tau_{b,su}. \end{aligned} \tag{4.8}$$

Equation 4.7 for the layer optical depth requires assumptions on layer thickness and mass concentration. Following Liao and Seinfeld [1998], we supposed the aerosols located in 2 idealized homogeneous layers, with different heights and thicknesses, one for mineral dust and one for the anthropogenic species. This configuration with idealized layers has been tested against a more complex and realistic configuration with aerosol profiles covering several layers: in the context of our analysis the two configurations have been found to give substantially the same results and so the more simple configuration with idealized layers has been preferred. Within the layers, we then set appropriate mass concentrations for each species, aiming to simulate 3 aerosol events of increasing intensity: *weak*, *strong* and *extreme*. In literature there is no well defined methodology to identify the strength of aerosol events but many researchers have used the aerosol optical depth (good measure of the aerosol load in the entire atmospheric column) for this purpose [Gkikas et al., 2009]. Following this approach, mass concentrations able to produce suitable layer optical depths defining the 3 aerosol events have been set. Only optical depths (τ_4) relative to the 4^{th} spectral band ($0,442 - 0,625\ \mu m$) have been used to define the events because this band includes the central wavelength of the visible range ($0,550\ \mu m$), usually considered for model estimate comparisons of aerosol optical depth [Kinne et al., 2006]. However, the spectral variability of the optical depth, not used for the event definition, has been considered in the optical analysis. The *extreme* event values have been selected in order to simulate very intense outbreaks registered over the Mediterranean basin for mineral dust ($\tau_4 = 3,0$) [Pérez et al., 2006; Cachorro et al., 2008], and heavily polluted urban areas (as for example Chinese mega cities) for the anthropogenic aerosols ($\tau_4 = 1,0$) [Chan and Yao, 2008; Xia et al., 2006]. The *strong* event values, simply defined as half of the *extreme* values, have been selected to simulate important dust outbreaks in the Mediterranean and moderately polluted urban areas, respectively. Finally, the *weak* event values aimed to approximately simulate events of ordinary intensity, as for example could be produced by the climatological aerosol background far from sources ($\tau_4 = 0,1$ for all the species). In Table 4.2 layer thicknesses, mass concentrations and corresponding layer optical depths defining the 3 events for all the considered species are reported. It is important to note that for mineral dust and organic carbon this event definition refers to the reference species. In the perturbed simulations the mass concentrations are conserved while the layer optical depths change according to the variability of microphysical and optical properties. Moreover, in the case of the black carbon-sulfate mixture, the 3 events have been defined separately for black carbon and sulfate: the conserved mass concentration of the mixture, for both external and internal mixing cases, is simply given by the sum of the two single species mass concentrations while the layer optical depth changes depending on the mixing state.

Table 4.2: **Layer thicknesses (Δz), mass concentrations (M) and corresponding layer optical depths (τ_4) relative to the 4^{th} spectral band ($0,442 - 0,625\ \mu m$), set to define the 3 aerosol events for all the considered species.**

Parameters	Aerosol Events	Mineral Dust	Organic Carbon	Black Carbon	Sulfate
$\Delta z\ [m]$	–	$3700 - 4500$	$0 - 1100$	$0 - 1100$	$0 - 1100$
$M\ [kg/m^3]$	*weak*	$1,472 \cdot 10^{-7}$	$0,304 \cdot 10^{-7}$	$0,092 \cdot 10^{-7}$	$0,282 \cdot 10^{-7}$
	strong	$1,472 \cdot 15 \cdot 10^{-7}$	$0,304 \cdot 5 \cdot 10^{-7}$	$0,092 \cdot 5 \cdot 10^{-7}$	$0,282 \cdot 5 \cdot 10^{-7}$
	extreme	$1,472 \cdot 30 \cdot 10^{-7}$	$0,304 \cdot 10 \cdot 10^{-7}$	$0,092 \cdot 10 \cdot 10^{-7}$	$0,282 \cdot 10 \cdot 10^{-7}$
τ_4	*weak*	$0,1$	$0,1$	$0,1$	$0,1$
	strong	$1,5$	$0,5$	$0,5$	$0,5$
	extreme	$3,0$	$1,0$	$1,0$	$1,0$

For all the species, we evaluated the particle microphysical perturbation impact on the layer radiative properties (generically indicated with x) by means of relative spreads (Δ), that is the ratios of the perturbation-induced spreads of the mean layer radiative properties (maximum $< x >^+$ minus minimum $< x >^-$) to the mean reference properties (marked with '*'):

$$\Delta_x = \frac{< x >^+ - < x >^-}{< x^* >}. \tag{4.9}$$

All the means have been calculated over the RRTMG_SW spectral bands using the band solar flux as weight function. Note that the bands $3 \leq b \leq 6$ (approximately visible-near infrared bands, see Table 2.2) contain more than 75% of the total flux. The definition used for the relative spreads has been found to be the most appropriate to describe the effective impact of the perturbed layer radiative properties on the direct radiative effect simulations (among other tested definitions). Note that the relative spreads in general do not depend on the aerosol event intensity, since the optical depth is directly proportional to the mass concentration (the same for reference and perturbed layer radiative properties) and single scattering albedo and asymmetry factor are intensive properties. For the black carbon-sulfate mixture, the relative spreads between internal (perturbation case) and external (reference case) mixing cases have been calculated.

4.5 Direct radiative effects

The RRTMG_SW has been configured to simulate radiative fluxes during summer, at mid-latitudes and over land. For this purpose, we set a "Standard Mid-Latitude Summer Atmosphere" structure (with 51 vertical layers) as input file for the code and the summer solstice day (21 of June) as simulation date (this affects the scaling of the solar flux depending on the Sun-Earth distance). The radiative fluxes, and consequently the direct radiative effects, are highly sensitive to the geophysical context selected for the simulations (mainly to the solar zenith angle: SZA). For this reason, in order to provide results suitable for general atmospheric scenarios, in this work we analyzed only relative variations of the direct radiative effects, meaning variations always evaluated against base net radiative fluxes (simulated in absence of aerosols, see below). However, the SZA has been found to have a relevant impact also on the relative variations of the direct radiative effects. Hence, we performed simulations for 4 different SZA (20°, 40°, 60° and 80°) providing therefore results ranging between extreme cases (not always coinciding with extreme SZA values). For each SZA we set a different surface albedo, following Briegleb et al. [1986]. At first, we selected 4 surface types suitable for mid-latitude lands, each one composed of a primary (I) and a secondary (II) component with different relative contributions (percentages within parentheses):

1. I: cultivated ground (80%) - II: tall grassland (20%);
2. I: grassland (80%) - II: shrubland (20%);
3. I: shrubland (80%) - II: grassland (20%);
4. I: woodland (80%) - II: grassland (20%).

We then calculated the averages of the broadband albedos relative to the 4 surface types reported in Table 2 of Briegleb et al. [1986] (spectrally integrated albedos weighted by the TOA solar flux: assumed to be valid for $SZA = 60°$). Note that considering broadband albedos instead of spectrally variable albedos has been found to have a negligible impact ($\lesssim 5\%$) on our results. Finally, we derived our albedos (A) for different SZA using the following formula of Briegleb et al. [1986] (the already defined μ_s is the cosine of the SZA):

$$A(\mu_s) = A_{60} \frac{(1+d)}{(1+2d\mu_s)}, \tag{4.10}$$

where A_{60} is the reference surface albedo at $SZA = 60°$ and d is an empirical correction factor ($d = 0,4$ for all the surface types selected [Briegleb et al., 1986]). The surface albedos used in this work (derived through the described procedure) are reported in Table 4.3. Moreover, the surface has been assumed Lambertian (isotropic reflected radiation) and the clear-sky option has been selected (no cloud layers) for all the simulations. The aerosol layers have been activated separately for mineral dust, organic carbon and the black carbon-sulfate mixture with all the properties and assumptions described in Sections 4.3 and 4.4.

Table 4.3: **Broadband surface albedos (A) for all the solar zenith angles (SZA) set for the radiative flux simulations (from Briegleb et al. [1986]).**

SZA	A [%]
20°	15, 1
40°	16, 4
60°	18, 9
80°	23, 3

From the RRTMG_SW outputs, we used the integrated (summed up over all the spectral bands) net radiative fluxes at the TOA ($F_{toa} = F_{toa}^{\downarrow} - F_{toa}^{\uparrow}$) and at SFC ($F_{sfc} = F_{sfc}^{\downarrow} - F_{sfc}^{\uparrow}$) to calculate the shortwave direct radiative effects (E) as the instantaneous net flux variations arising from activating and deactivating the aerosol layers (a and 0 mean with and without aerosols, respectively):

$$\begin{aligned} E_{toa} &= F^{a}_{toa} - F^{0}_{toa} = F^{\uparrow 0}_{toa} - F^{\uparrow a}_{toa}, \\ E_{sfc} &= F^{a}_{sfc} - F^{0}_{sfc}. \end{aligned} \tag{4.11}$$

Negative direct radiative effects indicate higher upward fluxes at the TOA and lower downward fluxes at SFC with aerosols (hence cooling in both cases) and vice versa. Always in this work "lower" and "higher" direct radiative effects refer to their intensity, independently of their sign. Hence, negative and positive effects increase when they become more negative and more positive, respectively, and vice versa. For each aerosol species, we then calculated the relative variability ranges of the direct radiative effects (Γ), at the TOA and at SFC, as the ratios of their perturbation-induced variability ranges (maximum E^{+} minus minimum E^{-}: taken always positive) to the net fluxes in absence of aerosols:

$$\begin{aligned} \Gamma_{toa} &= \frac{|E^{+}_{toa} - E^{-}_{toa}|}{F^{0}_{toa}}, \\ \Gamma_{sfc} &= \frac{|E^{+}_{sfc} - E^{-}_{sfc}|}{F^{0}_{sfc}}. \end{aligned} \tag{4.12}$$

This definition has been adopted in order to evaluate the perturbation-induced variability ranges taking into account the geophysical context in which the direct radiative effects are simulated (measured by the base net fluxes simulated in absence of aerosols) and so to provide results suitable for general atmospheric scenarios. For the black carbon-sulfate mixture, the relative variability ranges produced by considering internal mixing (perturbation case) or external mixing (reference case) have been calculated.

4.6 Results

We carried out the result analysis at two levels: i) impact of particle microphysical perturbations on layer radiative properties (Δ) and ii) consequent impact on direct radiative effects (Γ). In this section the results are presented separately for mineral dust, organic carbon and the black carbon-sulfate mixture. Note that only the figures of direct radiative effects for $SZA = 60°$ are shown (the results for all the SZA are presented in the tables).

4.6.1 Mineral dust

The **size distribution** perturbations have a remarkable impact on τ ($\Delta_{\tau} = 152,3\%$) and negligible impacts on g and ω ($\Delta_{g} = 9,8\%$; $\Delta_{\omega} = 7,5\%$). As shown in Figure 4.1-A, an increasing particle size (r_{eff}) causes the spectral maximum of τ (scattering maximum [Hansen and Travis, 1974]: for reference mineral dust occurring for $0,778 < \lambda < 1,242$ μm) to shift towards longer wavelengths and to decrease in intensity (due to its inverse dependence on r_{eff}: see Equation 4.7). The opposite occurs for decreasing r_{eff} (this obvious statement is omitted in the rest of the current analysis). Consequently, in more than half of the considered shortwave region (approximately for $\lambda < 2,151$ μm) τ decreases with increasing r_{eff} while the opposite occurs in the other bands. In all the dominant spectral bands ($3 \leq b \leq 6 \rightarrow 0,345 < \lambda < 1,242$ μm: bands containing more than 75% of the solar flux) τ is very highly perturbed: the highest absolute spreads are $\sim$(0, 20; 3, 03; 6, 07) (between pp and mm, for

$0,442 < \lambda < 0,625$ μm) in *weak*, *strong* and *extreme* events, respectively. Due to the shift of the scattering spectral maximum, ω (Figure 4.1-B) decreases in the first bands and increases in the last bands with increasing r_{eff} (more evidently for $\lambda < 0,625$ and for $\lambda > 2,500$ μm, respectively, where the absorption of the reference dust is important with respect to the scattering). However, in almost all the dominant bands ω is slightly affected by the perturbations: the highest absolute spread is $\sim 0,16$ (between *pp* and *mm*, for $0,345 < \lambda < 0,442$ μm). Finally, g (Figure 4.1-C) increases with increasing r_{eff} in almost all the bands (more evidently for $\lambda < 0,625$ and $\lambda > 1,299$ μm) because larger particles scatter more in the forward direction. However, in almost all the dominant bands g is nearly unaffected by the perturbations: the highest absolute spread is $\sim 0,12$ (between *mm* and *pp*, for $0,345 < \lambda < 0,442$ μm).

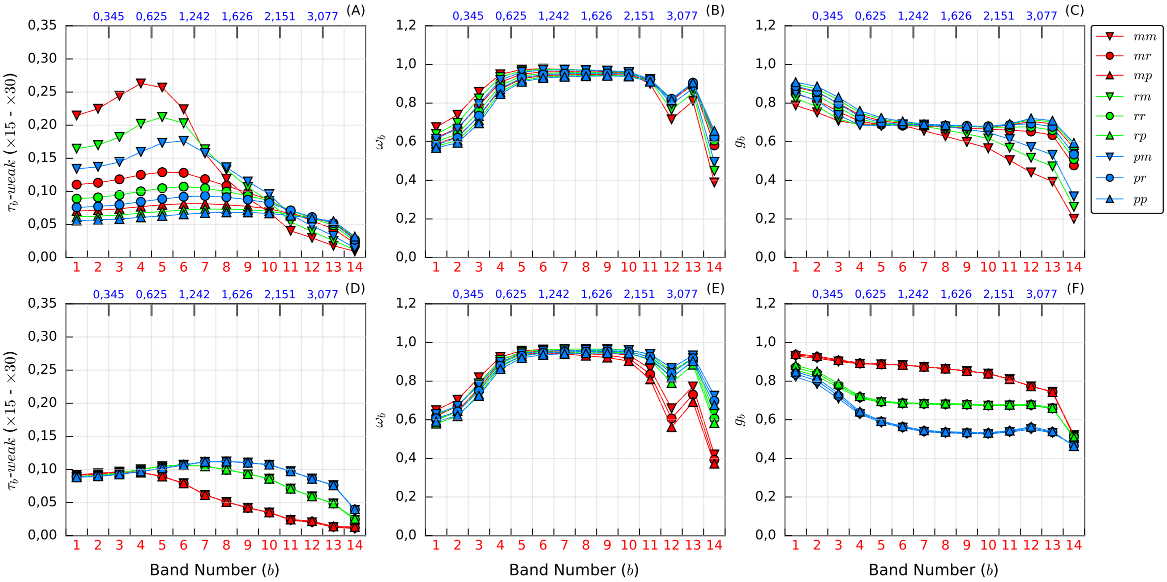

Figure 4.1: **Layer optical depth (τ), single scattering albedo (ω) and asymmetry factor (g), in function of the spectral bands (b), produced by perturbations of size distribution (A, B, C) and refractive index (D, E, F) for mineral dust. The optical depth is plotted only in the *weak* event, since it is enough scaling the y-axis values (by the factors within parentheses in the y-axis label) to obtain the values in *strong* and *extreme* events, respectively. The wavelengths reported at the top of the subplots (in μm) represent division wavelengths between different spectral bands and are a subset of that for all the spectral bands reported in Table 2.2. The perturbation case acronyms in the legend are explained in Section 4.3.**

The direct radiative effects simulated under size distribution perturbations stay negative and increase in intensity with decreasing r_{eff} coherently with the behavior of τ (with more sensitivity to σ_g than to r_g), both at the TOA (Figure 4.2-A) and at SFC (Figure 4.2-B) and in all the 3 events (in agreement with Liao and Seinfeld [1998]). These features remain for all the SZA but for $SZA = 20°$ the *rp* and *pp* cases produce very small positive direct radiative effects (< 1 W/m^2) at the TOA in the *weak* event. The perturbation-induced variability of the direct radiative effects can be remarkable, both at the TOA and at SFC: the highest absolute ranges are $\sim$(17; 142; 189 W/m^2) at the TOA (between *pp* and *mm*) and $\sim$(20; 222; 280 W/m^2) at SFC (between *pp* and *mm*), in *weak*, *strong* and *extreme* events, respectively (considering all the SZA). The corresponding relative variability ranges (Table 4.4) are in general larger at SFC ($\Gamma < 33,9\%$) than at the TOA ($\Gamma < 19,0\%$). Note that from their definition it is quite obvious that the relative variability ranges increase with the aerosol event intensity and so this information is omitted in the rest of this analysis.

Table 4.4: **Relative variability ranges of direct radiative effects (Γ) at the TOA and at SFC, in the** 3 **events, for size distribution and refractive index perturbations for mineral dust. The values within parentheses indicate the Γ variability due to the different SZA used for the radiative simulations (minimum and maximum of Γ not necessarily corresponding to extreme SZA). The values of the base net fluxes in absence of aerosols for the** 4 **different SZA are (in W/m^2): $\sim$ (1068; 824), (856; 645), (539; 385) and (172; 101), at (TOA; SFC) and for $SZA = 20°$, $40°$, $60°$, $80°$, respectively.**

Mineral Dust Perturbations:		**Size Distribution**		**Refractive Index**	
Parameters	**Aerosol Events**	**TOA**	**SFC**	**TOA**	**SFC**
Γ [%]	*weak*	$(1,0;\ 7,8)$	$(2,2;\ 10,7)$	$(0,8;\ 5,8)$	$(1,6;\ 7,8)$
	strong	$(13,3;\ 16,9)$	$(15,7;\ 27,7)$	$(10,2;\ 16,0)$	$(18,8;\ 25,5)$
	extreme	$(16,5;\ 19,0)$	$(16,2;\ 33,9)$	$(15,5;\ 18,8)$	$(20,2;\ 33,0)$

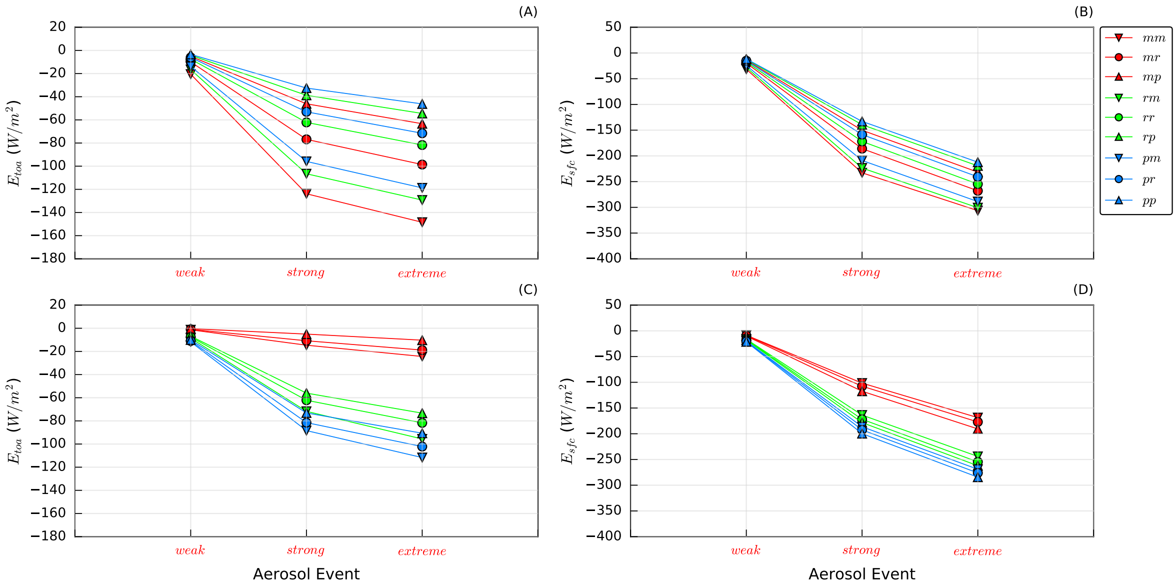

Figure 4.2: **Direct radiative effects (E) at the TOA and at SFC, in the** 3 **events (for $SZA = 60°$), produced by perturbations of size distribution (A, B) and refractive index (C, D) for mineral dust. The perturbation case acronyms in the legend are explained in Section 4.3.**

The **refractive index** perturbations have significant impacts on g and τ ($\Delta_g = 40,1\%$; $\Delta_\tau = 22,0\%$) and a negligible impact on ω ($\Delta_\omega = 3,8\%$). As shown in Figure 4.1-D, an increasing real refractive index causes the spectral maximum of τ to shift towards longer wavelengths and to increase in intensity, while perturbing the imaginary part does not have any significant impact on τ (more or less an enhanced absorption balances a reduced scattering and vice versa). Consequently, in the first bands (approximately for $\lambda < 0,625$ μm) τ remains almost unaffected by the perturbations while it increases with increasing n_r in the other bands. Only in two dominant spectral bands (b = 5, 6), therefore, τ is moderately perturbed: the highest absolute spreads are $\sim$(0,03; 0,42; 0,84) (between *mp* and *rm*, for $0,778 < \lambda < 1,242$ μm) in *weak*, *strong* and *extreme* events, respectively. The shift of the scattering spectral maximum causes ω (Figure 4.1-E) to decrease in the first bands and to increase in the last bands with increasing n_r (more evidently for $\lambda < 0,625$ and for $\lambda > 1,942$ μm, respectively), while a larger n_i reduces ω in all the bands, as expected. However, in all the dominant bands ω is nearly unaffected by the perturbations: the highest absolute spread is $\sim 0,10$ (between *pp* and *mm*, for $0,345 < \lambda < 0,442$ μm). Finally, g (Figure 4.1-F) decreases in all the bands with increasing n_r (more evidently for $0,345 < \lambda < 3,846$ μm) since a higher real part enhances reflection and refraction by the particles and consequently the backward scattering [Hansen and Travis, 1974], while perturbing n_i leaves unaffected g. In all the dominant bands g is considerably affected by the perturbations: the highest absolute spread is of $\sim 0,33$ (between *pm* and *mp*, for $0,778 < \lambda < 1,242$ μm).

The direct radiative effects simulated under refractive index perturbations stay negative and increase in intensity with increasing n_r and decreasing n_i at the TOA (Figure 4.2-C) and with increasing both n_r and n_i at SFC (Figure 4.2-D) (with more sensitivity to n_r than to n_i), in all the 3 events (in agreement with Liao and Seinfeld [1998] regarding n_i). These features remain for all the SZA but for $SZA < 60°$ the simulations with reduced n_r (*mm*, *mr* and *mp*) produce in some cases positive direct radiative effects at the TOA (always preserving though the same mutual quantitative relations). The perturbation-induced variability of the direct radiative effects again can be relevant, both at the TOA and at SFC: the highest absolute ranges are $\sim$(11; 109; 165 W/m^2) at the TOA (between *mp* and *pm*) and $\sim$(13; 173; 272 W/m^2) at SFC (between *mm* and *pp*), in *weak*, *strong* and *extreme* events, respectively (considering all the SZA). The corresponding relative variability ranges (Table 4.4) are in general more extended at SFC ($\Gamma < 33,0\%$) than at the TOA ($\Gamma < 18,8\%$).

4.6.2 Organic carbon

The **size distribution** perturbations have significant impacts on τ, g and ω ($\Delta_\tau = 84,1\%$; $\Delta_g = 78,9\%$; $\Delta_\omega = 35,8\%$). As shown in Figure 4.3-A, an increasing r_{eff} causes the spectral maximum of τ to shift towards longer wavelengths and to decrease in intensity (as for mineral dust but with the scattering maximum of the reference species occurring at shorter wavelengths than those considered in this work). Consequently, in the first bands (approximately for $\lambda < 0,625$ μm) τ at first increases with increasing r_{eff} but then starts to decrease (the maximum drop becomes dominant on its getting closer to the first bands), while it keeps increasing in the other bands. In all the dominant spectral bands τ is considerably perturbed: the highest absolute spreads are $\sim$(0,11; 0,55; 1,09) (between *mm* and *pr*, for $0,345 < \lambda < 0,442$ μm) in *weak*, *strong* and *extreme* events, respectively. Due to the shift of the scattering spectral maximum, ω (Figure 4.3-B) increases in almost all the bands with increasing r_{eff} (more evidently for $\lambda > 0,625$ μm, where the absorption is dominant with respect to the scattering by very small particles). However, only in two dominant bands (b = 5, 6) ω is strongly affected by the perturbations: the highest absolute spread is $\sim 0,42$ (between *mm* and *rp*, for $0,778 < \lambda < 1,242\ \mu m$). Finally, g (Figure 4.3-C) increases in all the bands with increasing r_{eff}, as expected. In all the dominant bands g is significantly affected by the perturbations: the highest absolute spread is $\sim 0,49$ (between mm and pp, for $0,778 < \lambda < 1,242\ \mu m$).

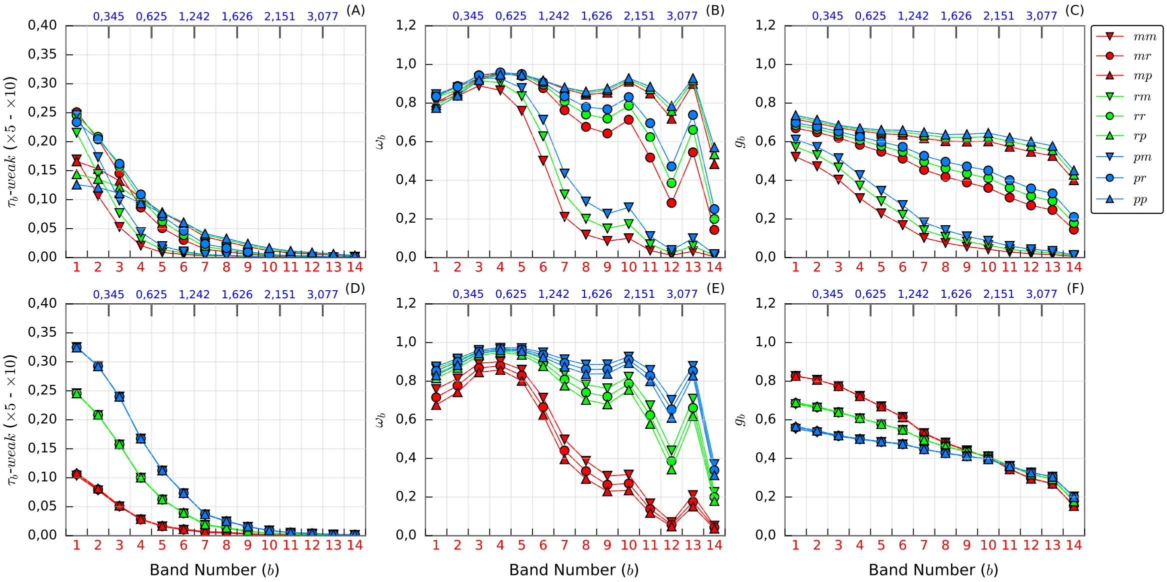

Figure 4.3: **Same as Figure 4.1 but for organic carbon.**

The direct radiative effects simulated under size distribution perturbations stay negative and at first increase in intensity with increasing r_{eff} starting then to decrease following the same behavior of τ, both at the TOA (Figure 4.4-A) and at SFC (Figure 4.4-B), in all the 3 events. These features remain for all the SZA but for $SZA = 80°$ the mp case generates the most intense negative direct radiative effect at SFC instead of pr. The perturbation-induced variability of the direct radiative effects is moderate, both at the TOA and at SFC: the highest absolute ranges are $\sim$(6; 24; 38 W/m^2) at the TOA (between mm and pr) and $\sim$(8; 35; 65 W/m^2) at SFC (between mm and pr), in *weak*, *strong* and *extreme* events, respectively (considering all the SZA). The corresponding relative variability ranges (Table 4.5) are in general more important at SFC ($\Gamma < 20,3\%$) than at the TOA ($\Gamma < 10,8\%$).

Table 4.5: **Same as Table 4.4 but for organic carbon.**

Organic Carbon Perturbations:		**Size Distribution**		**Refractive Index**	
Parameters	**Aerosol Events**	**TOA**	**SFC**	**TOA**	**SFC**
Γ [%]	*weak*	(0, 3; 2, 9)	(0, 7; 5, 9)	(1, 3; 6, 0)	(2, 2; 11, 0)
	strong	(1, 6; 8, 5)	(3, 9; 16, 9)	(6, 0; 15, 4)	(10, 9; 26, 2)
	extreme	(3, 1; 10, 8)	(7, 9; 20, 3)	(10, 9; 19, 3)	(20, 4; 30, 1)

The **refractive index** perturbations have a remarkable impact on τ ($\Delta_\tau = 137,7\%$) and significant impacts on ω and g ($\Delta_\omega = 32,1\%$; $\Delta_g = 29,3\%$). As shown in Figure 4.3-D, an increasing real refractive index causes the spectral maximum of τ to shift towards longer wavelengths and to increase in intensity, while perturbing the imaginary refractive index does not show any significant impact on τ. Consequently, in almost all the bands (more evidently for $\lambda < 1,626\ \mu m$) τ increases with increasing n_r. In all the dominant spectral bands τ is very highly perturbed: the highest absolute spreads are $\sim$(0, 19; 0, 95; 1, 90) (between mm and pm, for $0,345 < \lambda < 0,442\ \mu m$) in *weak*, *strong*

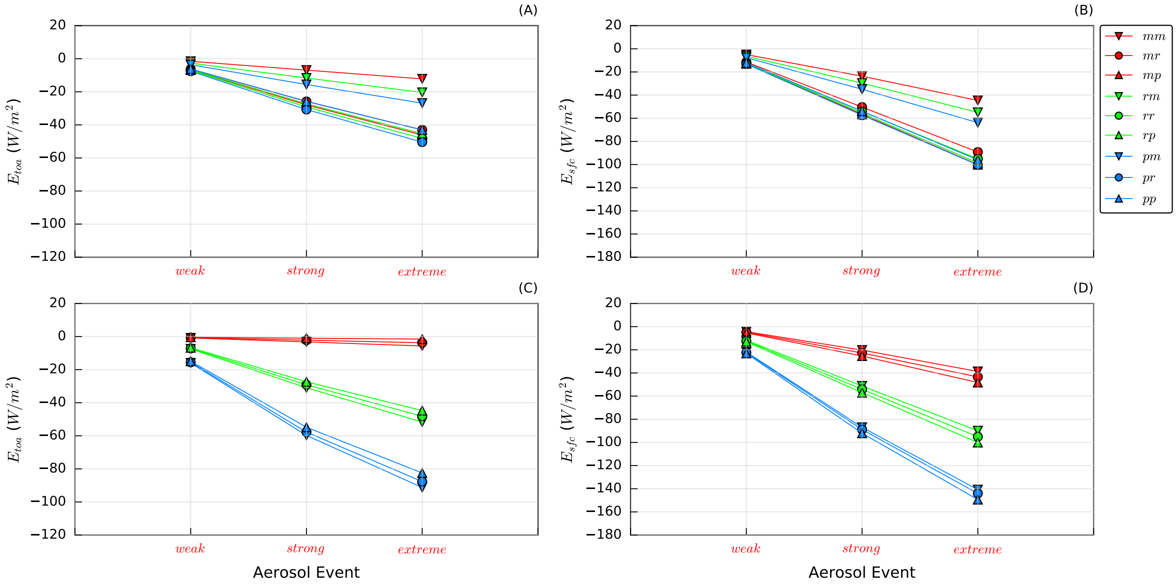

Figure 4.4: **Same as Figure 4.2 but for organic carbon.**

and *extreme* events, respectively. The shift of the scattering spectral maximum causes ω (Figure 4.3-E) to increase in all the bands with increasing n_r (more evidently for $\lambda > 0,625$ μm as for the increasing r_{eff}), while a larger n_i reduces ω in all the bands, as expected. Only in two dominant bands (b = 5, 6), however, ω is strongly affected by the perturbations: the highest absolute spread is $\sim 0,32$ (between mp and pm, for $0,778 < \lambda < 1,242$ μm). Finally, g (Figure 4.3-F) decreases in almost all the bands with increasing n_r (more evidently for $\lambda < 1,626$ μm and except for $\lambda > 2,151$ μm: in the limit $2\pi r_{eff}/\lambda \to 0$, g deviates more rapidly for larger values of n_r from its zero value for Rayleigh scattering [Hansen and Travis, 1974]), while perturbing n_i has a negligible impact on g. In all the dominant bands g is moderately affected by the perturbations: the highest absolute spread is of $\sim 0,26$ (between pm and mm, for $0,345 < \lambda < 0,442$ μm).

The direct radiative effects simulated under refractive index perturbations stay negative and increase in intensity with increasing n_r and decreasing n_i at the TOA (Figure 4.4-C) and with increasing both n_r and n_i at SFC (Figure 4.4-D) (with much more sensitivity to n_r than to n_i), in all the 3 events. These features remain for all the SZA but for $SZA < 60°$ the simulations with reduced n_r produce in some cases positive direct radiative effects at the TOA. The perturbation-induced variability of the direct radiative effects can be considerable, both at the TOA and at SFC: the highest absolute ranges are $\sim$(16; 65; 116 W/m^2) at the TOA (between mp and pm) and $\sim$(19; 90; 168 W/m^2) at SFC (between mm and pp), in *weak*, *strong* and *extreme* events, respectively (considering all the SZA). The corresponding relative variability ranges (Table 4.5) are in general more important at SFC ($\Gamma < 30,1\%$) than at the TOA ($\Gamma < 19,3\%$).

4.6.3 Black carbon-sulfate mixture

The **mixing state** perturbation has relevant impacts on ω and g ($\Delta_\omega = 49,2\%$; $\Delta_g = 37,7\%$) and a less important impact on τ ($\Delta_\tau = 18,4\%$). Changing the mixing state means perturbing both size distribution and refractive index and so it is very difficult to isolate the effects of these perturbations on the layer radiative properties. However, the internally mixed species seems to behave like a smaller and more absorbing species than the externally mixed species (regarding the scattering it is very difficult to infer information). As shown in Figure 4.5-A, indeed, in the internal mixing case the spectral maximum of τ seems to shift towards shorter wavelengths and tends to grow. Consequently, τ in the internal mixing case is higher in the first two bands ($\lambda < 0,345\ \mu m$) and slightly lower in the other bands (more evidently for $0,345 < \lambda < 1,942\ \mu m$) (in agreement with Lesins et al. [2002]). In all the dominant spectral bands, therefore, τ is weakly perturbed: the highest absolute spreads between internal and external mixing cases are $\sim(0,04;\ 0,20;\ 0,39)$ (for $0,625 < \lambda < 0,778\ \mu m$) in *weak*, *strong* and *extreme* events, respectively. The internally mixed species also has a lower ω (Figure 4.5-B) in all the bands (more evidently for $0,263 < \lambda < 2,500\ \mu m$) (in agreement with Lesins et al. [2002]). In all the dominant bands ω is strongly affected by the perturbations: the highest absolute spread between internal and external mixing cases is $\sim 0,34$ (for $0,778 < \lambda < 1,242\ \mu m$). Finally, also g (Figure 4.5-C) in the internal mixing case is lower in almost all the bands (approximately for $\lambda > 0,345\ \mu m$). In all the dominant bands also g is highly affected by the perturbations: the highest absolute spread between internal and external mixing cases is $\sim 0,28$ (for $0,778 < \lambda < 1,242\ \mu m$). Following the explanations given for mineral dust and organic carbon, the described variations of the layer radiative properties could be interpreted as results of the combined effects of decreasing the size and increasing the absorption of the particles.

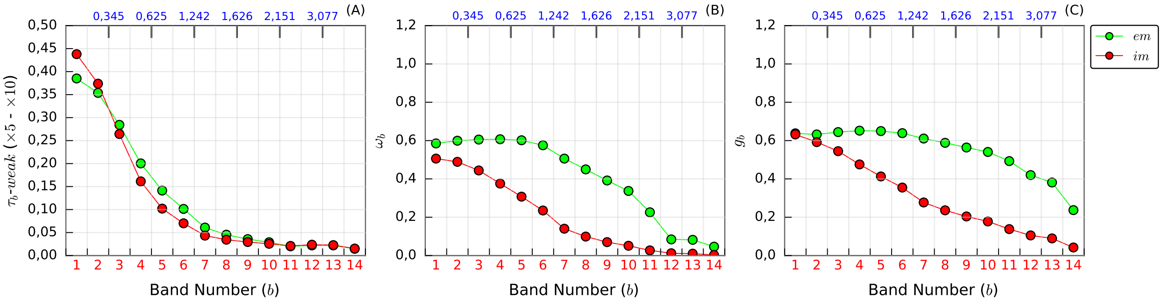

Figure 4.5: **Same as Figure 4.1 but for the black carbon-sulfate mixture. Note that in this case only the mixing state is perturbed.**

The direct radiative effects simulated under different mixing states are always positive at the TOA (Figure 4.6-A) (due to the strong absorption of black carbon) and negative at SFC (Figure 4.6-B). The *im* case generates more intense direct radiative effects, that is more positive at the TOA and more negative at SFC. These features remain for all the SZA. The perturbation-induced variability of the direct radiative effects is quite low, both at the TOA and at SFC: the highest absolute ranges are $\sim$(7; 19; 22 W/m^2) at the TOA and $\sim$(12; 34; 31 W/m^2) at SFC, in *weak*, *strong* and *extreme* events, respectively (considering all the SZA). The corresponding relative variability ranges (Table 4.6) are slightly more important at SFC ($\Gamma < 6,2\%$) than at the TOA ($\Gamma < 5,7\%$).

Table 4.6: **Same as Table 4.4 but for the black carbon-sulfate mixture.**

Black Carbon-Sulfate Mixture Perturbation:		**Mixing State**	
Parameters	**Aerosol Events**	**TOA**	**SFC**
Γ [%]	*weak*	$(0,6;\ 2,9)$	$(1,4;\ 3,0)$
	strong	$(1,7;\ 5,5)$	$(4,1;\ 6,2)$
	extreme	$(1,9;\ 5,7)$	$(3,8;\ 4,9)$

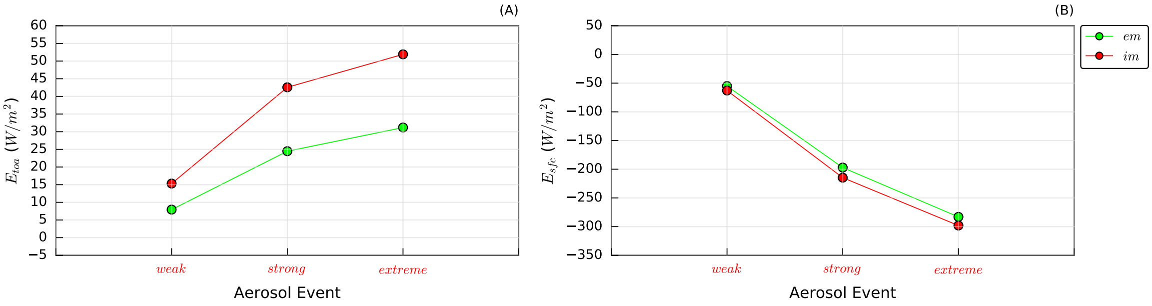

Figure 4.6: **Same as Figure 4.2 but for the black carbon-sulfate mixture. Note that in this case only the mixing state is perturbed.**

4.7 Discussion

Regarding the impact of the particle microphysical perturbations on the layer radiative properties, a very different behavior between mineral dust and organic carbon has been observed. For mineral dust, τ is more sensitive to the size distribution while g to the refractive index (ω is weakly affected by both the properties). For organic carbon, instead, τ is more sensitive to the refractive index while g to the size distribution (ω is more or less equally affected by the two properties). These differences seem to be caused mainly by the very different mean sizes of the two species. The maximum of the aerosol scattering efficiency, indeed, approximately occurs for $\lambda \sim r_{eff}$ and changes its spectral position depending on the particle microphysical properties (both size distribution and refractive index) [Hansen and Travis, 1974]. Clearly the effects of the particle microphysical perturbations on the layer radiative properties strongly depend on the original spectral position of the scattering maximum (as can be inferred from Figures 4.1 and 4.3). Even if the layer radiative properties of organic carbon seem to be more sensitive (higher relative spreads) than that of mineral dust to the particle microphysical properties (at least in the shortwave region considered in this work), note that the relative spreads of the two aerosol species are not directly comparable, because even if generated by the same particle microphysical perturbations they refer to different reference layer radiative properties. Regarding the black carbon-sulfate mixture, ω and g seem to be more sensitive than τ to the mixing state. The internal mixing between black carbon and sulfate reduces the number of particles in the layer (the sulfate particles disappear but the total mass is conserved) but makes the black carbon particles larger (higher geometric cross section) and with a slightly reduced imaginary refractive index (from $4,400 \cdot 10^{-1}$ it becomes $1,570 \cdot 10^{-1}$, at $0,550$ μm). This causes the total extinction to remain approximately the same, the total absorption to increase and the forward scattering to decrease.

Also the perturbation-induced variations of the direct radiative effects show different features for mineral dust and organic carbon, coherently with the perturbation impacts on the layer radiative properties. For mineral dust, despite the highly different impact on τ, size distribution and refractive index perturbations produce more or less comparable relative variability ranges, both at the TOA and at SFC and in all the 3 events. This could be explained considering that the refractive index perturbations have a significant impact on g in dominant spectral bands (in which also ω_g is very high). In general, an increasing g causes the direct radiative effects to become less negative (or more positive) both at the TOA and at SFC. This causes the relative variability ranges produced by the refractive index perturbations to be enhanced since the simulations with increasing τ have decreasing g (and vice versa) in the dominant bands. For organic carbon, instead, the refractive index perturbations produce higher relative variability ranges than the size distribution perturbations, both at the TOA and at SFC and in the 3 aerosol events. This is firstly caused by the higher impact on τ of the refractive index perturbations. However, also the impacts on g seem to have again a role, given that the g spreads are produced in dominant spectral bands (with also high ω values) for both size distribution and refractive index perturbations. As for mineral dust, indeed, the impact on g of the refractive index perturbations enhances the relative variability ranges (decreasing g for simulations with increasing τ). The opposite occurs for the size distribution perturbations because now the simulations with increasing τ have also increasing g and this limits the extents of the relative variability ranges. The ω spreads are more pronounced in not dominant spectral bands for both size distribution and refractive index perturbations and also have approximately the same features for the two properties. However, in general an increasing ω causes the direct radiative effects to become more negative (or less positive) at the TOA and less negative at SFC. Hence, in both cases the perturbation impact on ω causes the relative variability ranges to be slightly enhanced at the TOA and reduced at SFC (simulations with increasing τ have also increasing ω). Regarding the black carbon-sulfate mixture, despite the lower τ in the dominant spectral bands, the internally mixed species generates more intense direct radiative effects both at the TOA (more positive) and at SFC (more negative). The strong impact of the mixing state on ω, indeed, causes the internally mixed particles to be much more absorbing and so to overbalance the small τ reduction (the diffuse fluxes are strongly depleted). The relative variability ranges, however, remain small both at the TOA and at SFC and in all the 3 events. This is due to both the low impact of the mixing state on τ and to the balancing effect of the ω perturbation-induced variation. Note that at SFC the relative variability ranges in the *extreme* events are lower than in the *strong* event. This is probably due to the strong depletion of the diffuse fluxes caused by the very low ω of the mixture (due to the presence of black carbon), which in the *extreme* event limits the perturbation-induced variations of the direct radiative effects (above all at SFC).

4.8 Conclusions

In this work, we carried out a systematic and detailed study on the propagation of particle microphysical perturbations on the optical and radiative simulations usually required by the ARI implementation in weather and climate models. Our analysis has been carried out at two levels: i) impact of particle microphysical perturbations on layer radiative properties and ii) consequent impact on shortwave direct radiative effects, at the TOA and at SFC. We set a simple idealized experiment, carried out with numerical tools widely used in the atmosphere modeling community, in order to isolate and analyze the radiative sensitivity to the particle microphysical parameterization in weather and climate models.

We found consistent results with Liao and Seinfeld [1998] regarding the sign of the direct radiative effect variations induced by local perturbations of size distribution and imaginary refractive index of mineral dust, both at the TOA and at SFC. Moreover, we found results in agreement with Lesins et al. [2002] regarding the variations of optical depth and single scattering albedo due to a different mixing state between black carbon and sulfate (in particular the enhanced absorption in the internal mixing case) but an opposite result regarding the asymmetry factor: Lesins et al. [2002] found a higher value at $0,550\ \mu m$ in the internal mixing case while in this work we found a lower value in almost all the spectral bands for the internally mixed species. This different result can be explained by the opposite assumptions made to parameterize the homogeneous internal mixing between the two species. Lesins et al. [2002] considered, indeed, a coagulation of a smaller mode (black carbon) into a larger mode (sulfate), which caused the internally mixed species to be larger than both the single species (and so to have a higher g at $0,550$ μm than the externally mixed species). In this work, instead, we considered a condensation of the sulfate particles (larger species) on the black carbon particles (smaller species), which caused the internally mixed species to act as a smaller species than the externally mixed one (and so to have a lower g in almost all the bands).

In general, we found that the size distribution perturbations can produce more important relative variability ranges of direct radiative effects (considering the highest values produced by the variable SZA) for mineral dust than for organic carbon, while the refractive index perturbations produce almost comparable relative variability ranges for the two aerosol species, both at the TOA and at SFC and in all the 3 aerosol events. Changing the mixing state of the black carbon-sulfate mixture produces in general minor relative variability ranges. Looking at all the particle microphysical perturbations for all the considered species, we found the following relative variability ranges: $\Gamma < 7,8\%$ and $\Gamma < 11,0\%$ in the *weak* event, $\Gamma < 16,9\%$ and $\Gamma < 27,7\%$ in the *strong* event, $\Gamma < 19,3\%$ and $\Gamma < 33,9\%$ in the *extreme* event, at the TOA and at SFC, respectively. The highest relative variability range at the TOA ($\Gamma = 19,3\%$) is produced by the refractive index perturbations of organic carbon while at SFC ($\Gamma = 33,9\%$) by the size distribution perturbations of mineral dust, in the *extreme* event. However, the relative variability ranges never exceed the perturbation range applied to the size distribution and refractive index parameters ($\pm 20\% \rightarrow 40\%$), not even in the *extreme* event. This result can be considered as a quantitative measure of the propagation of the particle microphysical perturbations on the optical and radiative simulations usually performed in weather and climate models: **local perturbations within a certain range on the particle microphysical properties produce variability ranges of direct radiative effects always within the perturbation range applied, if evaluated against the base net radiative fluxes in absence of aerosols.** In other words, uncertainties on the most important aerosol microphysical parameters propagate on the simulated direct radiative effects mainly with a loss of strength. To conclude, the perturbation-induced absolute variations of the direct radiative effects have been found to be large, above all in *strong* and *extreme* events, and so potentially capable of significantly affecting the meteorological variables in weather and climate simulations. Hence, this work confirms and highlights the importance of improving the microphysical parameterization of the aerosols in atmospheric models, in order to achieve better model assessments of the ARI radiative effects and so better meteorological forecasts and climate predictions.

Chapter 5

Aerosol intensive optical properties in the NMMB-MONARCH

5.1 Introduction

We present in this chapter the evaluation of the aerosol intensive optical properties required by the full online coupling between aerosol module and radiation scheme in the NMMB-MONARCH (presented in Section 2.5): single scattering albedo (ω) and asymmetry factor (g). The optical depth (τ) of the different species has been extensively evaluated in the past by Pérez et al. [2011] and Haustein et al. [2012] (mineral dust), Spada et al. [2013] and Spada et al. [2015] (sea salt) and Spada [2015] (organic matter, black carbon and sulfate). Moreover, a further τ deep evaluation for all the species (after important updates implemented in the NMMB-MONARCH) has been recently carried out for the period 2012-2016. Some results of this evaluations, relative to 2012, are presented as supplementary material in Appendix B. Nevertheless, the intensive optical properties ω and g of the model have never been directly evaluated. In literature very few studies report on model evaluations of intensive optical properties (and mostly relative to ω), even if these are recognized to be crucial parameters controlling the radiative impact of the aerosols [Lacagnina et al., 2015; Andrews et al., 2006]. While the scattering species enhance the general cooling of the Earth system, indeed, the low ω values of the absorbing particles can cause the sign of the aerosol direct radiative effects to change [Lacagnina et al., 2015]. Within the framework of the Aerosol Comparisons between Observations and Models (AeroCom), while simulated aerosol optical depth and direct radiative forcing have been widely evaluated [Kinne et al., 2006; Schulz et al., 2006; Myhre et al., 2013a], the intensive optical properties have been only partially considered. Myhre et al. [2013a] evaluated ω of anthropogenic species simulated by 16 state-of-the-art models in the AeroCom Phase II exercise. They found the range of simulated ω to be large, with most values lying between $0,9$ and $1,0$ and the lowest ω simulated near the Equator (mainly due to large black carbon and organic emissions from biomass burnings). Uncertainties in the simulated ω above all of black carbon and organic aerosols have been found to significantly contribute to the model differences in simulating the anthropogenic direct radiative forcing. Lacagnina et al. [2015] evaluated ω over the global oceans based on measurements by the Polarization and Anisotropy of Reflectances for Atmospheric Sciences coupled with Observations from a Lidar (PARASOL) satellite. They compared the measured ω with simulations by 7 AeroCom (Phase II) models and found the models to simulate more uniform (both spatially and seasonally) and in general higher ω than the observed values by the satellite. The observed ω indeed exhibit a high variability not captured by the models above all far from the aerosol sources (maybe due to errors in the transport or also in the microphysical parameterization of the aerosols). Also, high diversity in magnitude and spatial pattern has been found to exist among the models. Takemura et al. [2002] simulated column-integrated ω of the principal tropospheric aerosols by means of an aerosol transport model coupled with the CCSR/NIES global circulation model. They evaluated the simulated ω against observations from the Aerosol Robotic Network (AERONET), finding general substantial agreement except for a subestimation of the observed ω in desert regions. Curci et al. [2015] used aerosol mass profiles (at AERONET locations in Europe and North America) simulated by different models within the Air Quality Model Evaluation International Initiative (AQMEII-2) to calculate aerosol optical properties under a range of common microphysical assumptions. They compared the optical properties with AERONET inversion data, finding a general subestimation of the observed ω (with weak correlation) and a general overestimation of the observed g (with slightly better correlation) at the $0,440\ \mu m$ wavelength. Hence, from the few available studies on model evaluations of intensive optical properties it seems clear that the performance of the state-of-the-art models is quite variable and in general poor. This general context suggests that still large uncertainties in the aerosol microphysical and optical parameterization exist in the atmospheric models and so that further investigation is needed to better assess and constrain the uncertainty sources.

In this work aerosol concentrations for a period of 5 years (2012-2016) and over a global domain have been simulated with the NMMB-MONARCH with activating the full online coupling based on the default particle microphysical assumptions used in the model. The simulated intensive optical properties at $0,550\ \mu m$ have been compared with AERONET Version 2.0 inversion data (manually screened Level 1.5 data) from 59 selected stations. A global evaluation of the model performance in simulating ω and g has been firstly carried out for the full set of 59 stations. A more detailed comparison (including annual cycles and values of ω and g) has been then performed for a subset of 12 stations, selected based on well defined criteria. A new set of refractive indexes has been also selected for all the species from recent literature in order to run a perturbed case and evaluate the impact of the new refractive indexes on the model skills in simulating intensive optical properties. To the best knowledge of the authors, this kind of perturbed analysis represents a novelty in the context of the few studies regarding model simulations of intensive optical properties available in literature. Note that the evaluation of the simulated aerosol concentrations is out of the scope of this work. Our main objective was indeed evaluating the microphysical assumptions for the modeled species (in particular regarding the reference refractive indexes, taken from the OPAC dataset [Hess et al., 1998]) through the analysis of the intensive optical properties. Obviously we are aware that errors in the simulation of the aerosol concentrations (emission, transport, depositions, etc.) affect the particle mixtures and consequently their intensive optical properties. However, the combined analysis of aerosol concentrations and microphysical properties is a problem with too many variables to be addressed at once. However, simulated and observed timeseries of optical depth per species (indirect measure of the mass concentrations), relative to 2012, are reported for the subset stations as supplementary material in Appendix B.

The results of this work will be published in the paper Obiso et al. [ults], currently under preparation. This chapter is organized as follows: in Sections 5.2 and 5.3 observations and configuration details for the model simulations are presented, respectively; in Section 5.4 the work results are presented and discussed (separately for the global evaluation for the full set stations and the detailed reference and perturbed analysis for the subset stations) and in Section 5.5 our conclusions are presented.

5.2 Observations

Observations taken from AERONET [Holben et al., 1998] have been used for our evaluation of the full online coupling. In detail, we used Version 2.0 inversion products [Holben et al., 2006] (from now onwards we omit this clarification) and, as first attempt, we selected only Level 2 data. For our purpose of the 5-years study, we aimed to select AERONET stations providing a number of daily data (daily averages) per month greater than a fixed threshold, over the 5 years and for all the months. However, there is a lack of Level 2 inversion data. Li et al. [2014] suggested that the majority of AERONET stations are cut away when the filter $\tau_{440} > 0,4$ is applied (among other Level 2 quality-assurance criteria listed in Table 3 of Holben et al. [2006]). They pointed out, indeed, that the observations with low optical depth represent the bulk of the data for many stations. Hence, following Li et al. [2014], we finally performed a manual screening of the Level 1.5 data by applying all the quality-assurance criteria of Holben et al. [2006] except filtering for $\tau_{440} > 0,40$. In this way we obtained "almost Level 2" data without missing the majority of stations. With this procedure, after fixing the threshold of 20 daily data per month and the 2012-2016 period, we selected 59 stations (indicated with black dots in Figure 5.1). This full set of 59 stations has been used for a global evaluation of the model performance in simulating the aerosol intensive optical properties.

A subset of 12 stations (depicted by blue circles in Figure 5.1) has been then selected for a more detailed graphical and statistical analysis (including also a perturbed analysis) taking into account (a posteriori) the loss of accuracy of the AERONET inversion data corresponding to low optical depths [Dubovik et al., 2000]. The 12 subset stations have been selected, indeed, by applying the 3 following criteria:

1. Observed optical depth: we selected stations in which the monthly medians of the observed τ from AERONET have been found to be above the threshold of $0,1$ for more than 6 months. The threshold of $0,1$ has been set in order to achieve a good compromise between number of stations and data accuracy. The period of 6 months assures then an acceptable accuracy of the observations for more than half year.

2. Aerosol type: we tried to have the same number of subset stations dominated by natural and anthropogenic aerosols. In most of the stations mineral dust has been found to dominate on the natural species and organic matter on the anthropogenic species. Note that organic matter includes Secondary Organic Aerosols (SOA) from biogenic precursors and consequently the classification of organic matter as an anthropogenic species is more correct in stations close to urban or industrialized areas (as most of our stations dominated by anthropogenic aerosols are).

3. Geographical position: we aimed to cover all the continents with the subset stations. Unfortunately in South America and central Africa (where extensive wildfires usually occur) no stations satisfying the applied criteria have been found. Neither Australia is represented in our subset due to the lack of suitable stations.

Note that some more stations dominated by mineral dust and organic matter satisfied the first criterion. However, in order to make more heterogeneous the detailed analysis on the subset stations we discarded some stations very close and similar to other included ones. In order to have more stations with significant presence of sea salt and sulfate, we then "manually" added 3 more stations not fully satisfying the first criterion (but showing a detectable signal of observed optical depth in more than one month). In this way, we selected 6 stations dominated by natural species and 6 by anthropogenic species (with different dominant single species), satisfying therefore the second criterion. Also, 2 of the additional stations are both in North America and this allowed us to better satisfy also the third criterion (only one station was indeed originally found in America after applying the first criterion).

The map of all the selected stations (full set and subset) is reported in Figure 5.1. Among the subset stations, 4 stations are located in North Africa and Middle East, close to dust sources (Sahara and Arabian Deserts, respectively): Cairo_EMA_2 (Egypt) and Masdar_Institute (United Arab Emirates) are also close to the urban areas of Cairo and Abu Dhabi, respectively, Tamanrasset_INM (Algeria) is in the middle of the Sahara Desert at a considerable altitude (1377 m) and KAUST_Campus (Saudi Arabia) on the Red Sea coast. In Africa we have also Pretoria_CSIR-DPSS (South Africa), an urban station located in the city of Pretoria (at high altitude: 1449 m). In Europe, Malaga (southern Spain) is an urban/coastal station very close to the northern coast of Africa while Venise (northern Italy) is located in the Adriatic Sea close to a strongly industrialized area. Other stations in Asia are Lahore (Pakistan) and Beijing (China), both urban stations located in very large metropolitan areas (Lahore and Beijing, respectively). Finally, 2 stations in USA are Fresno_2 (California), located in Fresno city and close also to large natural parks, and GSFC (Maryland), located in a small town (Greenbelt) between the cities of Washington and Baltimore. The third american station is La_Parguera (Puerto Rico), pure coastal stations on the Caribbean Sea coast.

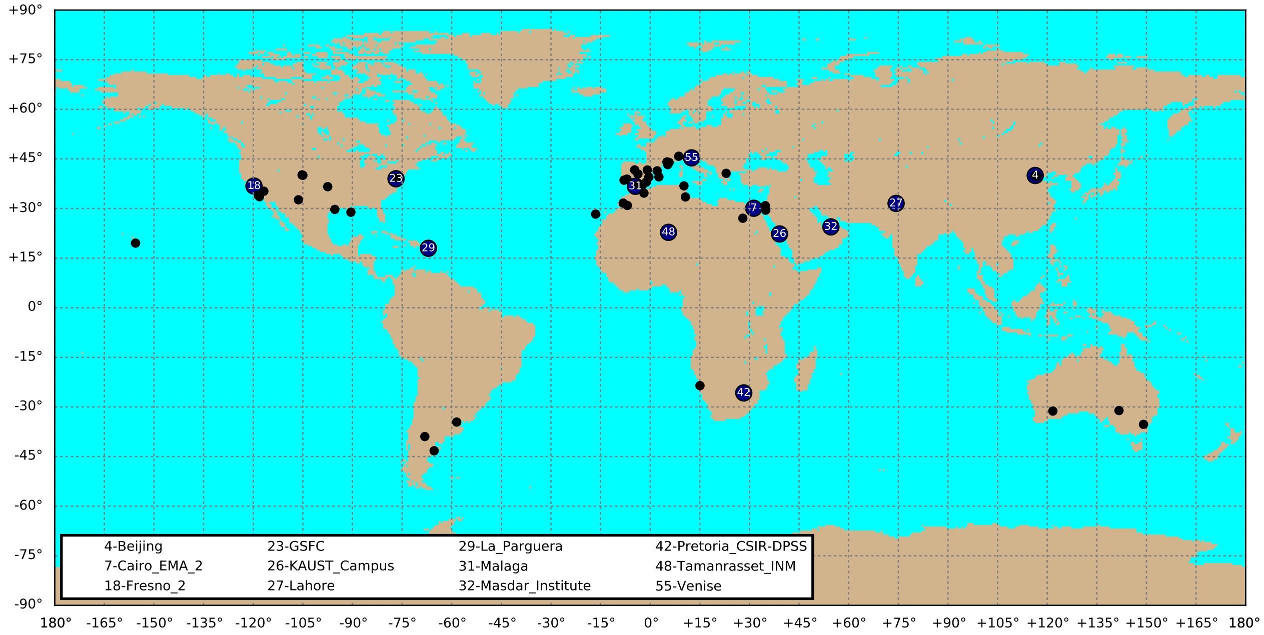

Figure 5.1: **Map of all the selected AERONET stations. The subset stations are marked with the blue circles while the remaining stations of the full set with black dots. Only the subset stations are reported in the legend with the numbers indicating the corresponding positions in the full list of stations reported in Table 5.2 (Section 5.4.1).**

For each station we extracted daily averaged τ, ω and g of the observed aerosol mixture at 3 available wavelengths: $0,440$; $0,675$ and $0,870$ μm. We then derived the corresponding values at $0,550$ μm (not included among the AERONET measurement wavelengths) by performing a second-order polynomial fit. In the visible range, indeed, measured ω and g of aerosol mixtures generally show an almost linear wavelength dependence with possible second-order terms depending on the microphysical characteristics of the mixture [Eck et al., 2001; Dubovik et al., 2002]. A second-order fit therefore appeared to be more adequate with respect to linear interpolations for example used in Takemura et al. [2002] and Nikitidou and Kazantzidis [2013]. The mid-visible wavelength has been selected for our analysis because it is the wavelength usually used for model comparisons [Kinne et al., 2006]. Moreover, literature values for the aerosol refractive indexes (required for our perturbed analysis) have been found mostly at wavelengths very close to $0,550\ \mu m$ (see Section 5.3.2).

5.3 Model simulations

The NMMB-MONARCH has been configured to run global meteorology-aerosol simulations over the period 2012-2016 (5-years period) with initializing the meteorological fields every $24h$ by means of NCEP FNL[1] analyses. A spin-up period of 1 year has been previously run to generate a realistic aerosol background for the simulations. The horizontal resolution for the global domain has been set to $lon \times lat = 1,4° \times 1,0°$ and 48 vertical layers have been considered. The radiative call timestep has been set to $3600\ s$ while the model outputs have been saved every $3h$ (simulation time). The emission databases (offline) and models (online) used for primary aerosols and gaseous precursors in our simulations are detailed in Section 5.3.1. The simulations have been run in *Marenostrum 4*[2], a supercomputer hosted by the Barcelona Supercomputing Center (BSC). Each year of simulation required $\sim 30h$ with 136 parallelized processors.

The full online coupling has been activated for the simulations and so aerosol optical depth, single scattering albedo and asymmetry factor have been calculated in the radiation scheme of the model (at $0,550\ \mu m$) using dynamic mass concentrations from the aerosol module and optical tables for each species (as explained in Section 2.5.3). The model outputs have been post-processed offline to be compared with the AERONET observations. At first, the model outputs have been temporally collocated to the observations, in order to make the comparison at the same dates. The daily means of the model outputs have been then calculated, considering only 4 diurnal outputs ($9h$, $12h$, $15h$, $18h$ UTC) because AERONET provides only diurnal measurements. Finally, the model outputs at the exact station coordinates have been derived from the grid point values by performing bilinear interpolations. The analysis of the intensive optical properties extracted from the radiation scheme of the model represents the reference case (REF) in this work, since these properties are calculated starting from the default microphysical parameterization used in the aerosol module of the NMMB-MONARCH (summarized in Table 2.1). However, also a perturbed case (PTB) has been included in this work, defined by assuming new literature values for the refractive indexes of the species. The setup details for the PTB case are given in Section 5.3.2.

5.3.1 Emissions

For our simulations the following emissions of primary aerosols and gaseous precursors have been considered. Anthropogenic emissions (aircraft, ships, industries, ground transport, heating/cooling of buildings and waste treatment) of organic carbon, black carbon and SO_2 have been taken from the HTAP_v2.2[3] inventory [Janssens-Maenhout et al., 2015]. The HTAP_v2.2 dataset consists of $0,1° \times 0,1°$ monthly grid maps for the year 2010. Biomass burning emissions (forest, grassland and agricultural waste fires) of organic carbon, black carbon, SO_2 and dimethylsulfide (DMS) have been

---

[1] https://doi.org/10.5065/D6M043C6

[2] https://www.bsc.es/marenostrum/marenostrum

[3] http://edgar.jrc.ec.europa.eu/htap_v2/

taken from the GFASv1.2[4] dataset [Kaiser et al., 2012]. This inventory reports daily emissions at a $0,1° \times 0,1°$ spatial resolution from 2012 to 2016. Emissions from global open burning of domestic waste (organic carbon, black carbon and SO_2) from Wiedinmyer et al. [2014], for 2010 and at a $0,1° \times 0,1°$ spatial resolution, have been also considered due to their substantial contribution especially for organic carbon and in developing and poor countries. This emission source is not included neither in HTAP_v2.2 nor in GFASv1.2. DMS production fluxes from oceans have been introduced by using the emissions provided by MOZART-4[5] (which refer to DMS simulations for the year 2000). Finally, the MEGAN v2.04 model [Guenther et al., 2006] has been coupled with the NMMB-MONARCH to produce online emission fluxes of monoterpenes and isoprene, biogenic precursors of SOA. For all the inventories mentioned, the emission fluxes have been conservatively interpolated onto the model grid and allocated to different model layers depending on the emission source (homogeneously introduced in each model vertical layer from the top of the plume to the ground).

5.3.2 Perturbed case

In order to improve the model simulation of the intensive optical properties, we generated new optical tables by means of the offline optical tool implemented in the model (presented in Section 2.5.2). The perturbed microphysical parameterization for the particles has been defined by considering only refractive index changes for the following reasons. Regarding the size distribution, mineral dust and sea salt particles are size distributed over 8 bins in the model. Hence perturbations of size distribution (for these species just a sub-bin distribution) would produce in these cases negligible variations in the intensive optical properties. The “effective” size distribution of dust and sea salt, indeed, is given by the mass distribution over the bins. For the bulk species instead (organic matter, black carbon and sulfate), size distribution perturbations would generate inconsistency with all those model processes involving the particle size. Regarding mass density and shape, we found in Obiso et al. [2017] (work presented in Chapter 3) that these properties have in most cases a minor impact on the aerosol scattering properties with respect to size distribution and refractive index. Moreover, the impact of shape on particle intensive optical properties has been investigated during the preparation of Obiso and Jorba [2018] (work presented in Chapter 4) and again substantially negligible impacts have been found (results not shown in the final version of the paper).

In order not to repeat the model simulations, the optical properties for the PTB case have been entirely calculated with an offline procedure. This means that: i) the perturbed optical tables have been generated only at $0,550\ \mu m$ (the only wavelength selected for the comparison with AERONET data); ii) only the dynamic aerosol concentrations have been taken from the model simulations; iii) the final perturbed optical properties have been calculated using the same equations used in the model (Equations 2.19, considering also the interpolation due to the layer relative humidity and the column-integration of the optical properties). A reliability test on this offline procedure has been performed in order to prevent numerical issues from causing unwanted deviations in the calculation results. The reference optical properties have been re-calculated with the offline procedure and compared with the model outputs. The results have been found identical until the third digit (errors $\lesssim 0,2\%$). Note that the optical properties from the model are relative to the RRTMG spectral band which includes the $0,550\ \mu m$ wavelength (as explained in Section 2.5.3) while that calculated with the offline procedure are exact single-wavelength properties. Hence, the good test result assures that the two procedures lead to substantially identical results and that therefore the optical properties from the model can be

---

[4] http://gmes-atmosphere.eu/oper_info/global_nrt_data_access/gfas_ftp/

[5] http://cdp.ucar.edu

considered as relative to $0,550\ \mu m$.

We defined the new refractive indexes by taking from recent literature updated values for all the species (the reference values are taken from OPAC and so probably are outdated for some species). Mostly values retrieved in experimental works have been preferred. Only for black carbon we selected values recommended by a review [Bond and Bergstrom, 2006]. Selecting suitable refractive indexes for each species is not easy. A large variability indeed exists in literature also for the same species, which comes from experimental diversities mainly regarding experiment setups, measuring instruments, observed species (different mixtures, sources, physico-chemical conditions, etc.), numerical tools and particle microphysics (refractive indexes are always inferred by assuming a particle microphysical parameterization and comparing numerical calculations with scattering and absorption measurements [Bond and Bergstrom, 2006]). Moreover, selecting the association between simulated and observed species is a potential source of additional errors, since obviously the model has its limitations in simulating the real atmospheric aerosols. The most complex species to be parameterized is organic matter, because this definition usually includes several organic components: primary organic matter (POM) and SOA from anthropogenic, biogenic and biomass burning sources, which have very different absorption characteristics [Kanakidou et al., 2005]. Currently our model considers the same refractive index for all the simulated organic components. Hence, in order to partially take into account the organic diversity we decided to implement for the PTB case a more detailed microphysical parameterization by assuming different refractive indexes for POM and SOA. The new refractive indexes selected for all the species are reported in Table 5.1 and briefly presented in the following list (note that all the values are relative to wavelengths very close to $0,550\ \mu m$):

- **Mineral dust**: Denjean et al. [2016] collected in situ aircraft measurements of Saharan mineral dust transported over the western Mediterranean basin in June-July 2013 during the Aerosol Direct Radiative Impact on the regional climate in the MEDiterranean region (ADRIMED) airborne campaign within the ChArMEx[6] research program. They derived vertical distributions of real and imaginary parts of the refractive index at $0,530\ \mu m$ as functions of the scattering Ångström exponent (Å_{sca}: from $0,450$ to $0,770\ \mu m$). For our mineral dust we considered an average of the refractive index values corresponding to $\text{Å}_{sca} < 0,3$ (all measured at altitudes above $3000\ m$), supposed to be more representative of a pure mineral dust. With respect to the reference values of the model, the new real part is substantially the same (from $1,530$ to $1,531$), while the imaginary part is significantly lower: from $5,500 \cdot 10^{-3}$ to $2,500 \cdot 10^{-3}$ ($-54,5\%$). The new imaginary part therefore implies a higher ω for mineral dust and also a lower g (mainly for coarse bins: see Section 5.4.2 for more details about the refractive index effects on the intensive optical properties).

- **Sea salt**: Irshad et al. [2009] presents real and imaginary refractive index of sea salt inferred from extinction spectra of laboratory generated salt aerosols (from $1\ \mu m$ to $20\ \mu m$). For wavelengths $\lesssim 2,5\ \mu m$ they found the real part to tend towards a constant value, which they fixed using the value at $0,500\ \mu m$ (the shortest wavelength at which they took measurements). On the other hand, they found the imaginary part to tend towards zero for wavelengths $\lesssim 1,4\ \mu m$. Hence, for our work we used the value at $0,500\ \mu m$ retrieved in dry conditions for the real part and a negligible value to represent the null imaginary part. With respect to the reference values of the model, the new real part is slightly higher: from $1,500$ to $1,557$ ($+3,8\%$), while the imaginary

---

[6] http://charmex.lsce.ipsl.fr

part is unchanged ($1,000 \cdot 10^{-8}$). The new real part therefore enhances the τ-fraction of the fine bins in the mixture and also reduces g (for all the bins).

- **Organic matter**: Shepherd et al. [2017] recorded refractive indexes of organic materials extracted from atmospheric aerosol samples (over a wide wavelength range) using optical trapping techniques combined with Mie spectroscopy. They found the real refractive index of organics from urban locations (London) to follow a Cauchy equation from $0,460$ to $0,700$ μm and found also a non detectable absorption for this sample. Nakayama et al. [2012] investigated the wavelength dependence of real and imaginary refractive index (at $0,405$; $0,532$ and $0,781$ μm) of SOA originating from ozonolysis (2 experimental runs with different initial O_3 concentrations) and photooxidation of α-pinene. They found the real part slightly increasing with decreasing wavelength and negligible values for the imaginary part at all the 3 wavelengths. Moreover, Liu et al. [2013] obtained refractive index of SOA produced by ozonolysis of α-pinene, limonene and aromatic cathecol (in the range from $0,220$ to $1,200$ μm). They found again a Cauchy relation in the visible range for the real part and very low values for the imaginary part. As already mentioned, for the PTB case we considered different refractive indexes for POM and SOA components of organic matter. Hence, for our POM from anthropogenic sources (fossil-fuel combustion, traffic, industries, home cooking, etc.) we used the real value at $0,550$ μm of Shepherd et al. [2017] (urban sample) and a negligible value for the imaginary part. For the SOA from biogenic sources we used instead averages between the values of Nakayama et al. [2012] at $0,532$ μm (only SOA from ozonolysis of α-pinene) and Liu et al. [2013] at $0,550$ μm (only SOA from ozonolysis of α-pinene and limonene). With respect to the reference values used in the model for organic matter, the new real parts are slightly lower both for POM: from $1,530$ to $1,501$ ($-1,9\%$), and SOA: from $1,530$ to $1,486$ ($-2,9\%$). The new imaginary parts instead are substantially negligible ($< 2,500 \cdot 10^{-5}$) (the reference organic matter presents a moderate absorption at $0,550$ μm, with an imaginary refractive index of $6,000 \cdot 10^{-3}$). The new real parts therefore reduce the τ-fraction of organic matter in the mixture and also slightly enhance g. The new negligible imaginary parts, instead, enhance ω while do not have any significant effects on g for organic matter.

  Regarding brown carbon, Tang et al. [2016] carried out measurements of scattering properties of laboratory generated brown carbon (proxy formed from the aqueous reaction of ammonium sulfate and methylglyoxal) at 2 visible wavelengths ($0,532$ and $0,402$ μm). From these measurements they retrieved the real refractive index for brown carbon, found to be almost constant in function of the reaction time. Kirchstetter et al. [2004] studied the wavelength dependence of light absorption by aerosols from near-ultraviolet to near-infrared wavelengths. They found different spectral dependence for particles produced by biomass burnings (dominated by brown carbon) and motor vehicles (dominated by black carbon) and retrieved the imaginary refractive index of brown carbon (from $0,350$ to $0,700$ μm). For our brown carbon, we selected for the real part the average of all the retrieved values at $0,532$ μm by Tang et al. [2016] (relative to different reaction times) while for the imaginary part we took the value at $0,550$ μm of Kirchstetter et al. [2004]. With respect to the reference values used in the model for organic matter, the real part is almost unchanged (from $1,530$ to $1,535$) and the imaginary part is significantly higher: from $6,000 \cdot 10^{-3}$ to $3,000 \cdot 10^{-2}$ ($+400\%$). The new imaginary part therefore would imply lower ω for organic matter above all in areas affected by wildfires. However, in this work these new values for brown carbon have not been used to parameterize POM from biomass burning sources because the selected subset stations dominated by anthropogenic aerosols are all in urban/industrialized areas or close to biogenic sources (where “white” organic matter is supposed to be dominant with respect to brown carbon from biomass burnings).

- **Black carbon**: Bond and Bergstrom [2006] carried out a wide investigative review of the inferred refractive indexes for black carbon (mostly at $0,550\ \mu m$) available in literature. They hypothesized that only a strongly absorbing black carbon with a single refractive index exists and that the variability in the reported values is only due to (variable) void fractions in the materials. Thanks to this assumptions they succeeded in recommending a range of suitable values for the black carbon refractive index to be used in meteorological and climate models. We selected the intermediate values of the recommended range at $0,550\ \mu m$. With respect to the reference values of the model the new values are higher for both the real part: $1,750$ to $1,850$ ($+5,7\%$), and above all the imaginary part: from $4,400 \cdot 10^{-1}$ to $7,100 \cdot 10^{-1}$ ($+61,4\%$). The new real part therefore would imply a higher τ-fraction in the mixture and also a lower g for black carbon. The new imaginary part, instead, would further reduce ω (without any significant effects on g). However, as explained in Section 5.4.2, these new refractive index values have not been applied in this work because the absorbing effect of black carbon has been found to be already too strong in the REF case (maybe due to too high simulated mass concentrations).

- **Sulfate**: Freedman et al. [2009] investigated the optical properties of internally mixed particles composed of dicarboxilic acids and ammonium sulfate, and retrieved the refractive indexes of the single species at $0,532\ \mu m$. They found that the retrieved value for the internal mixture significantly deviates from the volume-weighted average of the two pure components. Also they stated that the compounds used in the experiment do not absorb at $0,532\ \mu m$. A similar result has also been found by Gosse et al. [1997], which obtained negligible values for the imaginary refractive index of ammonium sulfate at short wavelengths ($\lesssim 1\ \mu m$). For our sulfate we used the value retrieved at $0,532\ \mu m$ by Freedman et al. [2009] for the real part and a negligible value for the imaginary part. With respect to the reference values of the model, the new real part is higher: from $1,430$ to $1,546$ ($+8,1\%$) while the imaginary part results unchanged ($1,000 \cdot 10^{-8}$). Note that the new value for the real part is in excellent agreement with the constraint on the sulfate real refractive index found in Obiso et al. [2017] ($+8\%$ with respect to the same reference value used in this work). This new real part therefore implies higher τ-fraction in the mixture and also a lower g for sulfate.

5.4 Results

For each station and month, the daily means of both simulated and observed ω and g have been assembled over the 5 years and the distribution medians have been computed as the month representative values. The monthly medians have been preferred to the monthly means because better representative values for not normally distributed datasets [Li et al., 2014] (less sensitive to the outliers). The 10^{th} and 90^{th} percentiles have also been computed to represent the data monthly variability (effect of the daily mixture variations over the 5 years). The global evaluation of the model performance for the full set stations is presented in the following Section 5.4.1 while the detailed analysis for the subset stations in Section 5.4.2.

Table 5.1: **New refractive index values for all the species (real, n_r, and imaginary, n_i, parts) selected for the PTB case from recent literature. All the values are retrieved at the wavelengths reported within parentheses (the acronym VIS stands for "visible range").**

Parameters	**Mineral Dust**	**Sea Salt**
n_r	$1,531\ (0,530\ \mu m)$ [Denjean et al., 2016]	$1,557\ (0,500\ \mu m)$ [Irshad et al., 2009]
n_i	$2,500 \cdot 10^{-3}\ (0,530\ \mu m)$ [Denjean et al., 2016]	$1,000 \cdot 10^{-8}$ (VIS) [Irshad et al., 2009]
Parameters	**Primary Organic Matter**	**Secondary Organic Aerosol**
n_r	Urban: $1,501\ (0,550\ \mu m)$ [Shepherd et al., 2017] Brown Carbon: $1,535\ (0,532\ \mu m)$ [Tang et al., 2016]	Biogenic: $1,486\ (0,532;\ 0,550\ \mu m)$ [Nakayama et al., 2012] [Liu et al., 2013]
n_i	Urban: $1,000 \cdot 10^{-8}\ (0,550\ \mu m)$ [Shepherd et al., 2017] Brown Carbon: $3,000 \cdot 10^{-2}\ (0,550\ \mu m)$ [Kirchstetter et al., 2004]	Biogenic: $2,500 \cdot 10^{-5}\ (0,532;\ 0,550\ \mu m)$ [Nakayama et al., 2012] [Liu et al., 2013]
Parameters	**Black Carbon**	**Sulfate**
n_r	$1,850\ (0,550\ \mu m)$ [Bond and Bergstrom, 2006]	$1,546\ (0,532\ \mu m)$ [Freedman et al., 2009]
n_i	$7,100 \cdot 10^{-1}\ (0,550\ \mu m)$ [Bond and Bergstrom, 2006]	$1,000 \cdot 10^{-8}$ (VIS) [Freedman et al., 2009] [Gosse et al., 1997]

5.4.1 Global analysis for the full set of stations

In Table 5.2 the 59 selected stations with relative geographical information, statistics (correlation coefficient: r and mean bias: b) and annual τ-fractions (Y) are listed. The row colors indicate the stations clearly dominated by one of the 5 species, that is with $Y \geq 0,40$ for the dominant species. Note that since ω and g are intensive optical properties, their value does not depend on the absolute amount of aerosols but only on the type of mixture. Each species, indeed, contributes to the mixture (with its properties) proportionally to its τ-fraction. The correlation coefficient and the mean bias (simulated minus observed values) have been calculated based on the monthly medians and give a direct quantitative information on the agreement between simulated and observed annual cycles and values, respectively, of ω and g. The mean bias has been preferred to the relative mean bias because it is supposed to be a more clear and direct estimate of the mean "distance" between variables ranging only from 0 to 1. The mean bias significant digits, indeed, can be directly read as percent variations with respect to the total value range of the variables. For the analysis, 3 indicative levels of importance for correlation and mean bias have been set. The positive correlation levels have been considered: weak for $r < 0,3$; moderate for $0,3 \leq r < 0,7$ and strong for $r \geq 0,7$ (the negative coefficients have not been classified). On the other hand, the same categories for the mean bias levels have been defined for $|b| < 0,03$; $0,03 \leq |b| < 0,07$ and $|b| \geq 0,07$, respectively.

The stations clearly dominated by mineral dust are 16. Regarding ω, the median of the correlations is negative ($\overline{r_\omega} = -0,32$) and the median of the mean biases is moderate negative ($\overline{b_\omega} = -0,035$). The correlation is moderate in only 3 stations ($0,42 \leq r_\omega \leq 0,47$) and weak in other 3 stations ($0,14 \leq r_\omega \leq 0,17$) (negative in the remaining stations: clarification omitted in the rest of this analysis). Most of the stations then show negative mean biases ($-0,07 \leq b_\omega \leq -0,01$) while only 3 stations show positive mean biases ($0,04 \leq b_\omega \leq 0,13$) and 2 stations a null mean bias. Regarding

Table 5.2: **Full list (in alphabetical order) of the** 59 **AERONET stations selected with the method explained in Section 5.2. The data reported are: longitude (***lon***), latitude (***lat***) and height (***hgt***); correlation coefficient (***r***) and mean bias (***b***) relative to the monthly medians of single scattering albedo (ω) and asymmetry factor (***g***); annual τ-fractions (***Y***) for simulated mineral dust (DU), sea salt (SS), organic matter (OM), black carbon (BC) and sulfate (SU). The row colors indicate the dominant species in each station, defined as the species with $Y \geq 0,40$, based on the following color legend: ● mineral dust; ● sea salt; ● organic matter; ● black carbon; ● sulfate.**

#	**Name**	lon [°]	lat [°]	hgt [m]	r_ω	b_ω	r_g	b_g	Y_{DU}	Y_{SS}	Y_{OM}	Y_{BC}	Y_{SU}
1	Badajoz	−7, 0	38, 9	186, 0	−0, 68	0, 01	0, 61	0, 06	0, 30	0, 17	0, 22	0, 07	0, 24
2	Barcelona	2, 1	41, 4	125, 0	−0, 23	−0, 05	−0, 07	0, 07	0, 23	0, 17	0, 23	0, 09	0, 28
3	Beijing-CAMS	116, 3	39, 9	106, 0	0, 62	−0, 10	0, 78	0, 02	0, 14	0, 01	0, 41	0, 18	0, 26
4	Beijing	116, 4	40, 0	92, 0	0, 81	−0, 10	0, 85	0, 02	0, 15	0, 01	0, 42	0, 18	0, 25
5	BSRN_BAO_Boulder	−105, 0	40, 0	1604, 0	−0, 88	0, 00	0, 73	0, 04	0, 08	0, 07	0, 45	0, 15	0, 24
6	Burjassot	−0, 4	39, 5	30, 0	−0, 75	0, 01	0, 07	0, 06	0, 33	0, 15	0, 20	0, 07	0, 24
7	Cairo_EMA_2	31, 3	30, 1	70, 0	−0, 73	−0, 03	0, 61	0, 05	0, 56	0, 03	0, 22	0, 05	0, 15
8	Canberra	149, 1	−35, 3	600, 0	0, 36	0, 02	0, 48	0, 09	0, 00	0, 34	0, 36	0, 08	0, 22
9	Carpentras	5, 1	44, 1	100, 0	0, 24	−0, 01	−0, 12	0, 05	0, 19	0, 11	0, 30	0, 10	0, 30
10	Cart_Site	−97, 5	36, 6	318, 0	0, 36	−0, 05	−0, 22	0, 03	0, 09	0, 12	0, 39	0, 12	0, 29
11	CEILAP-BA	−58, 5	−34, 6	10, 0	0, 39	0, 00	0, 44	0, 04	0, 00	0, 23	0, 50	0, 11	0, 16
12	CEILAP-Neuquen	−68, 1	−39, 0	271, 0	0, 18	0, 08	−0, 59	0, 01	0, 01	0, 33	0, 35	0, 09	0, 22
13	Eilat	34, 9	29, 5	15, 0	0, 46	−0, 02	0, 33	0, 07	0, 63	0, 03	0, 11	0, 03	0, 21
14	El_Farafra	28, 0	27, 1	92, 0	−0, 70	−0, 06	−0, 33	0, 06	0, 84	0, 02	0, 06	0, 02	0, 06
15	El_Segundo	−118, 4	33, 9	25, 0	0, 54	−0, 12	0, 07	−0, 03	0, 08	0, 09	0, 45	0, 23	0, 16
16	Evora	−7, 9	38, 6	293, 0	−0, 61	−0, 01	0, 34	0, 05	0, 30	0, 15	0, 23	0, 08	0, 25
17	Fowlers_Gap	141, 7	−31, 1	181, 0	0, 40	0, 03	0, 32	0, 02	0, 01	0, 41	0, 32	0, 08	0, 18
18	Fresno_2	−119, 8	36, 8	100, 0	0, 70	−0, 07	0, 87	0, 01	0, 09	0, 07	0, 52	0, 16	0, 16
19	Frioul	5, 3	43, 3	40, 0	−0, 71	−0, 01	0, 23	0, 04	0, 18	0, 12	0, 30	0, 10	0, 30
20	Gobabeb	15, 0	−23, 6	405, 0	0, 47	−0, 04	0, 81	0, 01	0, 17	0, 08	0, 48	0, 15	0, 12
21	Goldstone	−116, 8	35, 2	1100, 0	0, 24	0, 03	0, 79	−0, 02	0, 11	0, 09	0, 43	0, 16	0, 20
22	Granada	−3, 6	37, 2	680, 0	−0, 79	0, 13	−0, 38	0, 09	0, 42	0, 11	0, 19	0, 06	0, 21
23	GSFC	−76, 8	39, 0	87, 0	0, 72	−0, 02	−0, 26	0, 06	0, 03	0, 06	0, 30	0, 11	0, 50
24	Ispra	8, 6	45, 8	235, 0	−0, 56	−0, 06	0, 08	0, 06	0, 15	0, 09	0, 34	0, 12	0, 31
25	Izana	−16, 5	28, 3	2391, 0	0, 47	−0, 07	0, 16	0, 11	0, 60	0, 22	0, 08	0, 02	0, 08
26	KAUST_Campus	39, 1	22, 3	11, 2	0, 17	−0, 07	−0, 52	0, 05	0, 58	0, 01	0, 08	0, 02	0, 30
27	Lahore	74, 3	31, 5	270, 0	0, 83	−0, 05	0, 87	−0, 01	0, 15	0, 01	0, 51	0, 14	0, 18
28	Lake_Lefroy	121, 7	−31, 3	300, 0	0, 27	0, 11	−0, 25	0, 03	0, 01	0, 39	0, 36	0, 09	0, 16
29	La_Parguera	−67, 0	18, 0	12, 4	0, 32	−0, 01	−0, 20	0, 04	0, 30	0, 53	0, 11	0, 02	0, 04
30	Madrid	−3, 7	40, 5	680, 0	−0, 01	0, 02	0, 25	0, 07	0, 34	0, 12	0, 22	0, 08	0, 25
31	Malaga	−4, 5	36, 7	40, 0	0, 42	0, 00	0, 32	0, 06	0, 47	0, 11	0, 17	0, 05	0, 20
32	Masdar_Institute	54, 6	24, 4	4, 0	−0, 66	−0, 05	0, 13	0, 05	0, 77	0, 02	0, 06	0, 02	0, 13
33	Mauna_Loa	−155, 6	19, 5	3397, 0	−0, 82	0, 10	0, 78	0, 13	0, 03	0, 77	0, 10	0, 03	0, 08
34	MD_Science_Center	−76, 6	39, 3	15, 0	0, 70	−0, 03	0, 58	0, 08	0, 03	0, 06	0, 29	0, 11	0, 51
35	Medenine-IRA	10, 6	33, 5	33, 5	0, 14	−0, 07	0, 46	0, 03	0, 79	0, 05	0, 07	0, 02	0, 07
36	Murcia	−1, 2	38, 0	69, 0	−0, 24	0, 03	−0, 25	0, 06	0, 37	0, 15	0, 19	0, 07	0, 23
37	NEON_CVALLA	−105, 2	40, 2	1539, 0	−0, 90	0, 01	0, 60	0, 03	0, 08	0, 06	0, 49	0, 16	0, 21
38	OHP_OBSERVATOIRE	5, 7	43, 9	680, 0	−0, 15	−0, 04	−0, 38	0, 06	0, 19	0, 11	0, 29	0, 10	0, 30
39	Ouarzazate	−6, 9	30, 9	1136, 0	−0, 91	0, 04	0, 66	0, 01	0, 78	0, 03	0, 09	0, 02	0, 07
40	Oujda	−1, 9	34, 7	620, 0	−0, 91	0, 05	0, 48	0, 04	0, 59	0, 07	0, 16	0, 04	0, 14
41	Palma_de_Mallorca	2, 6	39, 6	10, 0	0, 61	−0, 04	−0, 16	0, 07	0, 35	0, 16	0, 20	0, 06	0, 23
42	Pretoria_CSIR-DPSS	28, 3	−25, 8	1449, 0	0, 95	−0, 03	0, 89	0, 03	0, 00	0, 03	0, 57	0, 17	0, 22
43	Saada	−8, 2	31, 6	420, 0	−0, 35	−0, 04	0, 71	0, 03	0, 69	0, 05	0, 13	0, 03	0, 10
44	Santa_Monica_Colg	−118, 5	34, 0	55, 0	0, 53	−0, 15	0, 24	−0, 03	0, 06	0, 09	0, 45	0, 23	0, 15
45	SEDE_BOKER	34, 8	30, 9	480, 0	−0, 06	−0, 05	−0, 13	0, 05	0, 67	0, 03	0, 10	0, 03	0, 17
46	Tabernas_PSA-DLR	−2, 4	37, 1	500, 0	−0, 50	−0, 00	0, 04	0, 08	0, 42	0, 13	0, 18	0, 05	0, 21
47	Table_Mountain	−105, 2	40, 1	1689, 0	−0, 55	−0, 03	0, 62	0, 04	0, 07	0, 06	0, 51	0, 16	0, 20
48	Tamanrasset_INM	5, 5	22, 8	1377, 0	−0, 29	−0, 07	−0, 08	−0, 00	0, 88	0, 01	0, 05	0, 01	0, 04
49	Thessaloniki	23, 0	40, 6	60, 0	−0, 11	−0, 02	0, 20	0, 08	0, 23	0, 06	0, 26	0, 07	0, 37
50	Trelew	−65, 3	−43, 2	15, 0	−0, 66	0, 10	−0, 06	0, 05	0, 00	0, 61	0, 20	0, 05	0, 13
51	Tunis_Carthage	10, 2	36, 8	10, 0	0, 14	−0, 01	0, 72	0, 05	0, 46	0, 10	0, 18	0, 05	0, 21
52	Univ_of_Houston	−95, 3	29, 7	65, 0	0, 77	−0, 05	0, 78	0, 05	0, 11	0, 23	0, 29	0, 11	0, 26
53	USC_SEAPRISM	−118, 1	33, 6	31, 0	0, 71	−0, 11	−0, 05	−0, 02	0, 07	0, 11	0, 44	0, 21	0, 17
54	Valladolid	−4, 7	41, 7	705, 0	−0, 52	0, 03	0, 45	0, 06	0, 25	0, 17	0, 22	0, 07	0, 29
55	Venise	12, 5	45, 3	10, 0	−0, 36	−0, 04	0, 66	0, 06	0, 15	0, 09	0, 30	0, 11	0, 35
56	WaveCIS_Site_CSI_6	−90, 5	28, 9	32, 7	0, 21	−0, 01	0, 43	0, 06	0, 07	0, 36	0, 25	0, 07	0, 25
57	White_Sands_HELSTF	−106, 3	32, 6	1207, 2	0, 49	−0, 03	−0, 65	0, 02	0, 11	0, 13	0, 41	0, 12	0, 23
58	XiangHe	117, 0	39, 8	36, 0	0, 89	−0, 10	0, 88	0, 01	0, 14	0, 01	0, 41	0, 19	0, 25
59	Zaragoza	−0, 9	41, 6	250, 0	−0, 16	0, 07	0, 39	0, 06	0, 26	0, 16	0, 21	0, 07	0, 30

g, the median of the correlations is weak ($\overline{r_g} = 0,24$) and the median of the mean biases is moderate positive ($\overline{b_g} = 0,05$). The correlation is strong in 2 stations ($r_g = 0,71$ and $0,72$), moderate in 6 stations ($0,32 \leq r_g \leq 0,66$) and weak in 3 stations ($0,04 \leq r_g \leq 0,16$). Almost all the stations then show a positive mean bias ($0,01 \leq b_g \leq 0,11$) and only one station a null mean bias. Hence, in the stations clearly dominated by mineral dust the model tends to subestimate the observed ω and also to substantially miss their annual cycle. On the other hand, the model clearly tends to overestimate the observed g but it partially captures their annual cycle. These general behaviors (above all relatively to the mean biases) could be mainly related to two factors: a too much absorbing mineral dust or/and a too low fine to coarse ratio for the dust particles. Note that the stations with positive or null mean ω biases (Granada: #22, Malaga: #31, Ouarzazate: #39, Oujda: #40 and Tabernas_PSA-DLR: #46) are all relatively close each other (between Morocco and southern Spain), indicating a different behavior of the model in this geographical region maybe due to a higher simulated fine to coarse ratio.

In the 4 stations clearly dominated by sea salt the median of the ω correlations is negative ($\overline{r_\omega} = -0,17$) and the median of the mean biases is moderate positive ($\overline{b_\omega} = 0,065$). In only 2 stations the correlation is moderate ($r_\omega = 0,32$ and $0,40$). The mean bias instead is positive in 3 stations ($0,03 \leq b_\omega \leq 0,10$) and negative in only one station ($b_\omega = -0,01$). Regarding g, the median of the correlations is weak ($\overline{r_g} = 0,13$) and the median of the mean biases is moderate positive ($\overline{b_g} = 0,045$). The correlation is strong in only one station ($r_g = 0,78$) and moderate in another one ($r_g = 0,32$). All the stations show then positive mean biases ($0,02 \leq b_g \leq 0,13$). Since the stations clearly dominated by sea salt are only 4 it is hard to get clear tendencies of the model regarding the annual cycles. The model indeed partially captures the annual cycle of the observed ω in 2 stations but totally misses it in the remaining 2. The same happens for g. Regarding the mean biases, instead, it seems more clear that the model tends to overestimate both the observed ω and g. Since sea salt is a totally scattering species, these positive mean biases could be related to an excessive presence of coarse sea salt particles in the simulated mixture (probably due to the emission scheme used, as reported in Section 2.3.2). Mauna_Loa (#33), for example, is located on a small island at a very high altitude. The bilinear interpolation in this case fails in resolving the island and obviously leads to overestimations of the observed coarse salt concentrations in the station.

The stations clearly dominated by organic matter are also 16. The median of the ω correlations is moderate ($\overline{r_\omega} = 0,535$) and the median of the mean biases is moderate negative ($\overline{b_\omega} = -0,045$). The correlation is strong in 6 stations ($0,70 \leq r_\omega \leq 0,95$), moderate in other 6 stations ($0,39 \leq r_\omega \leq 0,62$) and weak in only one station ($r_\omega = 0,24$). The mean bias is then negative in most of the stations ($-0,15 \leq b_\omega \leq -0,03$), positive in only 2 stations ($b_\omega = 0,01$ and $0,03$) and null in other 2 stations. Regarding g, the median of the correlations is strong ($\overline{r_g} = 0,755$) and the median of the mean biases is weak positive ($\overline{b_g} = 0,015$). Most of the stations show a strong correlation ($0,73 \leq r_g \leq 0,89$), 3 stations a moderate correlation ($0,34 \leq r_g \leq 0,62$) and 2 station a weak correlation ($r_g = 0,07$ and $0,24$). The mean bias is then positive in most of the stations ($0,01 \leq b_g \leq 0,04$) and negative in 5 stations ($-0,03 \leq b_g \leq -0,01$) (no stations show null mean biases). Hence, the model in the stations clearly dominated by organic matter again tends to subestimate the observed ω (more than in the dust-dominated stations) but well captures their annual cycle. On the other hand, the model again tends to overestimate the observed g (less than in the dust-dominated stations) but captures very well their annual cycle. The negative mean ω biases in these stations could be mainly related to two factors: a too much absorbing organic carbon or/and a too high presence of black carbon. Most of the organic-dominated stations, indeed, are located in urban/industrialized areas or close to biogenic sources (in which "white" organics should be dominant with respect to absorbing brown carbon).

Moreover, in all these stations the fractions of black carbon are very large ($0,11 \leq Y_{BC} \leq 0,23$) with respect for example to the stations dominated by natural aerosols ($0,02 \leq Y_{BC} \leq 0,08$).

In the only 2 stations clearly dominated by sulfate, the median of the ω correlations is strong ($\overline{r_\omega} = 0,71$) while the median of the mean biases is weak negative ($\overline{b_\omega} = -0,025$). The stations show very similar strong correlations ($r_\omega = 0,72$ and $0,70$) and negative mean biases ($b_\omega = -0,02$ and $-0,03$). Regarding g, the median of the correlations is weak ($\overline{r_g} = 0,16$) and the median of the mean biases is strong positive ($\overline{b_g} = 0,07$). The 2 stations show very different correlations ($r_g = 0,58$ and $-0,26$) but again very similar positive mean biases ($b_g = 0,06$ and $0,08$). Hence, in the stations clearly dominated by sulfate (even if only 2) the model captures very well the annual cycle of the observed ω but slightly subestimates their values. On the other hand, the model captures quite well the observed g annual cycle in one station but totally misses it in the other one. An overestimation of the observed g is instead evident in both the stations. These mean biases, regarding both ω and g, could be related to a general subestimation of sulfate (totally scattering species) by the model in these stations and also to a too high g value for the reference sulfate of the model. Note that again the considerable presence of black carbon ($Y_{BC} = 0,11$ in both stations) could contribute to the negative mean ω biases.

5.4.2 Detailed analysis for the subset of stations

A coarse characterization of the 12 subset stations has been achieved based on the Y values of Table 5.2: the stations have been considered dominated by natural species (mineral dust and sea salt) when $Y_{DU} + Y_{SS} > Y_{OM} + Y_{BC} + Y_{SU}$ and by anthropogenic species (organic matter, black carbon and sulfate) in the opposite case. As already mentioned, organic matter is not a pure anthropogenic species since it includes also SOA from biogenic precursors. However, in this work it has been classified as anthropogenic species because most of our stations dominated by anthropogenic species are located in urban or industrialized areas. In Figure 5.2 the monthly τ-fractions (X) for the 12 subset stations are reported. The station numbers indicate their positions in the full list reported in Table 5.2. The monthly information given by the X bars allows a more detailed characterization of the subset stations, based on the annual evolution of the simulated mixture.

Among the stations dominated by natural aerosols (subplots A, B, C, D, E, F of Figure 5.2), the 4 stations close to dust sources (Cairo_EMA_2, KAUST_Campus, Masdar_Institute and Tamanrasset_INM) show very large fractions of mineral dust during all the year, as expected. Cairo_EMA_2 shows also a significant presence of anthropogenic species (from urban emissions in Cairo city), above all from July to December when the mineral dust fractions decrease. Sulfate is then significantly present in KAUST_Campus and less in Masdar_Institute (where maybe also more significant organic aerosols are expected from the urban emissions in Abu Dhabi). Finally, Tamanrasset_INM (totally surrounded by the Sahara Desert) is coherently dominated by mineral dust during all the year. Note that in all the 4 stations the mineral dust fractions increase in the spring months and also shows peaks during summer in KAUST_Campus and Masdar_Institute. In stations far from dust sources (La_Parguera and Malaga) the mineral dust fractions increase mainly in the summer months (transported dust). Malaga coherently presents also significant fractions of anthropogenic species (mainly from urban emissions) and a little sea salt (above all during winter). Finally La_Parguera (totally surrounded by the Caribbean Sea) is largely dominated by sea salt during almost all the year, as expected.

Among the stations dominated by anthropogenic species (subplots G, H, I, J, K, L of Figure 5.2), organic matter and black carbon seem to dominate with respect to sulfate in stations within strong

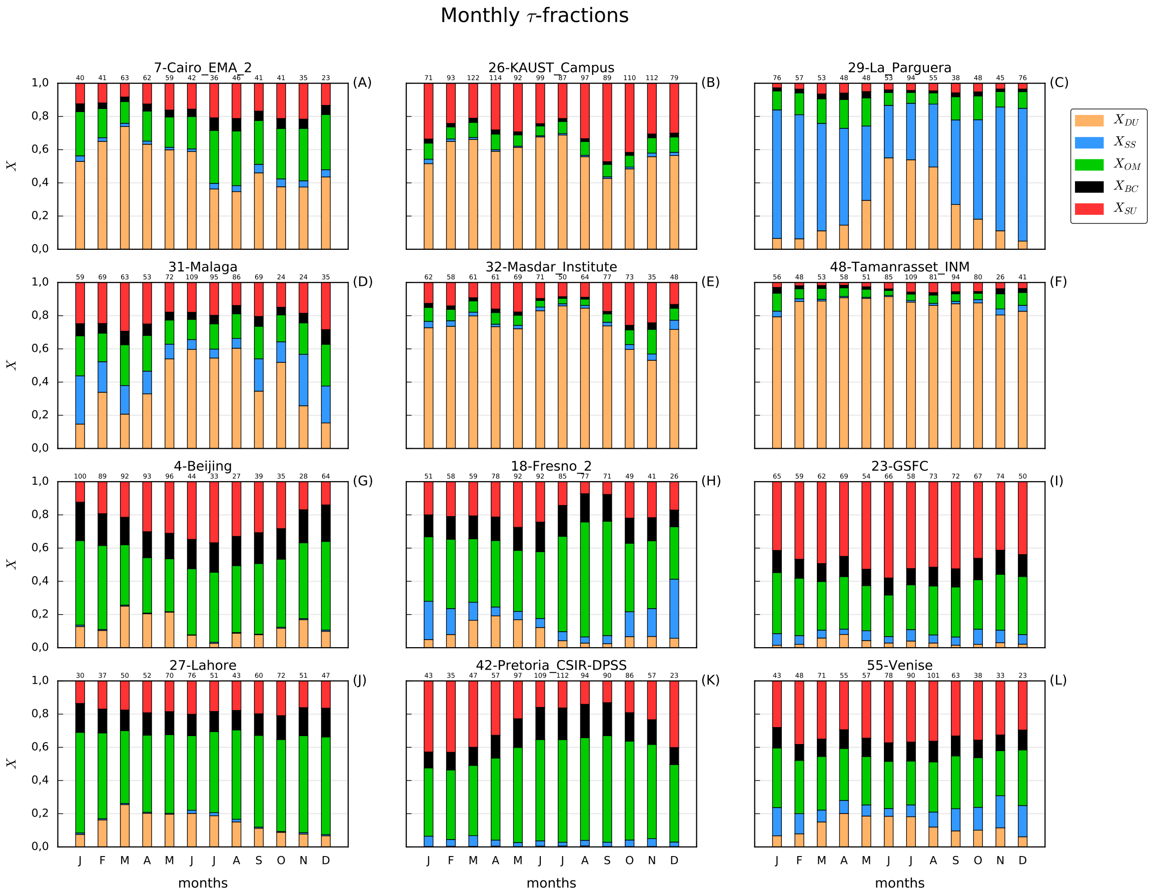

Figure 5.2: **Monthly τ-fractions (X) of mineral dust (DU), sea salt (SS), organic matter (OM), black carbon (BC) and sulfate (SU) in the 12 subset stations. The numbers at the top of each bar indicate the amount of daily means (data points) included in the monthly distributions (over the five years 2012-2016).**

urban emission areas (Beijing, Lahore and Pretoria_CSIR-DPSS) and urban areas close to biogenic sources (Fresno_2). Sulfate is instead more important in GSFC, indicating a simulated anthropogenic aerosol background not strongly influenced by organic sources. Finally the simulated mixture in Venise is almost equally affected by organic matter and sulfate (mainly from industry emissions) during all the year. Note a reduction of the black carbon fractions in GSFC and Venise with respect to the other stations, indicating higher model emissions of black carbon by urban sources. Also, while in GSFC, Lahore and Venise the annual cycle of the anthropogenic species is approximately constant (note only slight increases of the sulfate fraction during summer in GSFC), in Beijing sulfate shows pronounced increases during summer and in Pretoria_CSIR-DPSS organic matter (and black carbon) clearly increases in the summer and autumn months. Note also in Fresno_2 a clear peak of organic matter and black carbon in July, August and September, probably due to wildfire events simulated by the model in these months over the considered 5-years period (as confirmed by the peaks of the 90^{th} percentile of the simulated τ in Figure A.1). Finally note that mineral dust affects in a certain degree the simulated mixture in Beijing, Fresno_2, Lahore and Venise (mainly during spring) while sea salt appears only in Fresno_2 and Venise (mainly during winter).

In Figures 5.3 and 5.4 the monthly medians of simulated and observed ω and g, respectively, with the 10^{th} and 90^{th} percentiles are plotted for the 12 subset stations. The analysis for ω and g in the REF case is reported in the following Sections 5.4.2.1 and 5.4.2.2 (for stations dominated by natural and anthropogenic species, respectively) and implicitly refers to these figures. In Section 5.4.2.3 the results of the PTB case are then discussed.

5.4.2.1 Stations dominated by natural species

The stations dominated by natural aerosols: Cairo_EMA_2, KAUST_Campus, La_Parguera, Malaga, Masdar_Institute and Tamanrasset_INM, are reported in subplots A, B, C, D, E, F, respectively, of Figures 5.3 and 5.4.

Single scattering albedo. The observed ω annual cycle is partially captured by the model in La_Parguera and Malaga ($r = 0,32$ and $r = 0,42$, respectively). A weak correlation is then registered in KAUST_Campus ($r = 0,17$) and negative correlations in the other stations ($-0,73 \leq r \leq -0,29$). The model subestimates the observed ω in almost all the stations ($-0,07 \leq b \leq -0,01$) and shows a null mean bias only in Malaga. The stations close to dust sources show moderate and strong negative mean biases ($-0,07 \leq b \leq -0,03$). The lowest simulated ω in Cairo_EMA_2 (drop in March), KAUST_Campus (minima in March and July) and Masdar_Institute (small drop in March and depression from June to August) occur in perfect conjunction with increases of mineral dust in the simulated mixture (see Figure 5.2). In Tamanrasset_INM the strong negative mean bias is produced by the flat annual cycle of the simulated ω (due to the homogeneous simulated mixture). Note that these stations are easily reached by coarse dust particles which have a lower ω with respect to the fine particles at $0,550$ μm (the maximum of the scattering efficiency approximately occurs when the particle mean size is similar to the wavelength [Hansen and Travis, 1974]). This means that a too high fraction of coarse particles could also contribute to the negative mean biases in these stations (above all for Cairo_EMA_2, KAUST_Campus and Masdar_Institute which are located at low altitudes). In La_Parguera (dominated by sea salt in most of the months) the weak negative mean bias ($b = -0,01$) is mainly caused by the increasing mineral dust fraction in the summer months. In the rest of the months, indeed, the high simulated ω of sea salt produce a good agreement with the observations. In Malaga the enhanced mineral dust in the summer months causes the simulated ω to

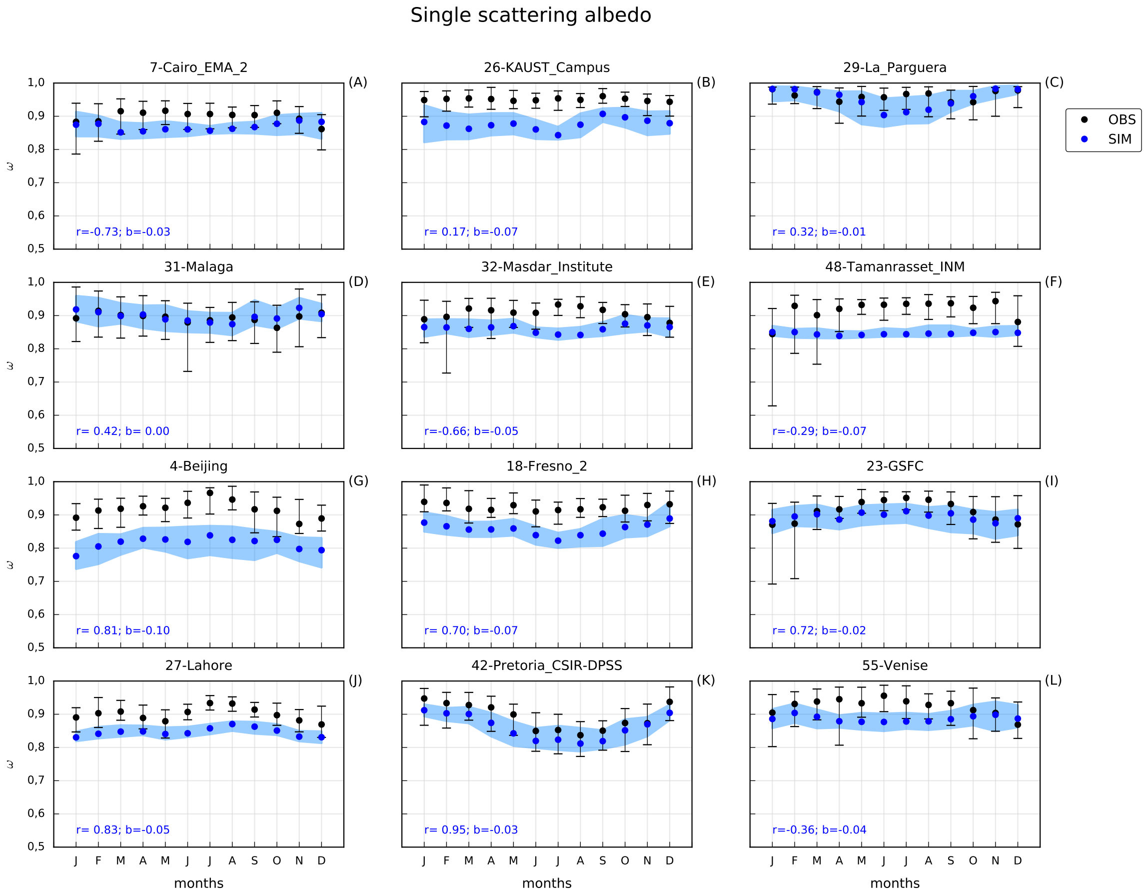

Figure 5.3: **Simulated (REF case) and observed single scattering albedo (ω) of the aerosol mixture in the 12 subset stations (in alphabetic order from left to right and from top to bottom). The circle points are the monthly medians while error bars (observations) and shadowed regions (simulations) represent the 10^{th} and 90^{th} percentiles. The correlation coefficient (r) and the mean bias (b) on the monthly medians are also reported. The station numbers indicate the corresponding positions in the full list reported in Table 5.2.**

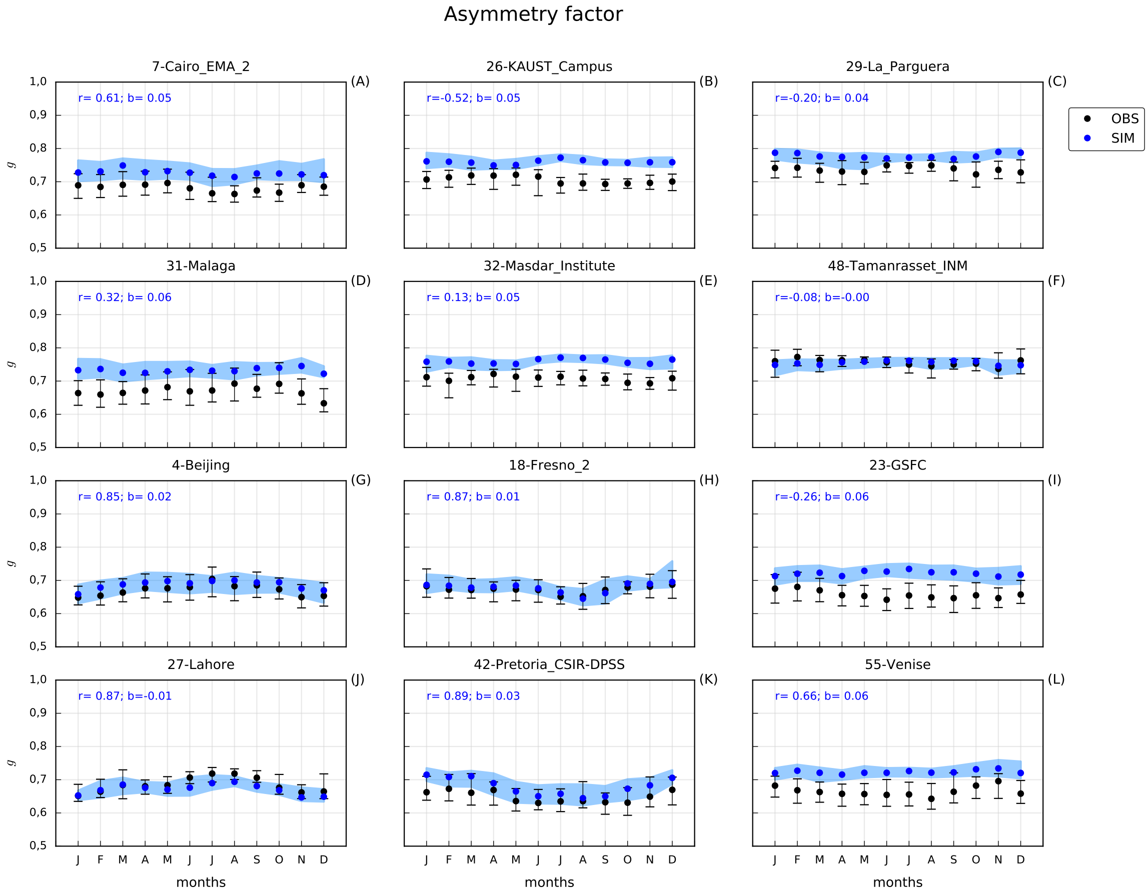

Figure 5.4: **Same as Figure 5.3 but for asymmetry factor (g).**

slightly decrease but no negative mean bias is generated. This different behavior however seems to be more related to lower observed ω than to higher simulated ω with respect to the other stations. Hence, maybe a missing of absorbing particles by the model in this station could compensate for the low ω values of our reference mineral dust.

The analysis of the single scattering albedo in the considered stations dominated by natural aerosols clearly suggests that our mineral dust should have a higher ω (in almost all the stations). It is well known [Hansen and Travis, 1974] that an increasing imaginary refractive index causes ω to decrease (and vice versa) because of a larger absorption efficiency (for all the aerosol species at $0,550\ \mu m$). Actually the imaginary refractive index assumed for mineral dust in our model is too high compared with the selected literature value [Denjean et al., 2016] (the new refractive indexes for the species are discussed in Section 5.3.2), which therefore seems to be more suitable in most of the considered stations. On the other hand, the scattering efficiency (and so the single species τ-fraction in the mixture) increases with the real refractive index for particles with size smaller than the considered wavelength [Hansen and Travis, 1974]. The refractive index of sea salt seems to be quite well constrained in literature but the new selected real part [Irshad et al., 2009] is slightly higher than our reference value. This new value, therefore, would slightly enhance the presence of fine sea salt particles in the mixture (the coarse bins have $r_{eff} > 0,550\ \mu m$). However, in La_Parguera (pure coastal station) it should not significantly affect the sea salt fractions and consequently the simulated ω.

Asymmetry factor. The observed g annual cycle is well captured by the model in Cairo_EMA_2 ($r = 0,61$) and partially captured in Malaga ($r = 0,32$). A weak correlation is then observed in Masdar_Institute ($r = 0,13$) while negative correlations in the other stations ($-0,52 \leq r \leq -0,08$). The model overestimates the observed g in almost all the stations ($0,04 \leq b \leq 0,06$) and shows a null mean bias only in Tamanrasset_INM. In 3 of the 4 stations close to dust sources an equal positive mean bias ($b = 0,05$) is registered. The highest simulated g values in Cairo_EMA_2 (peak in March), KAUST_Campus (mainly maximum in July) and Masdar_Institute (mainly maxima from June to August) again occur in perfect conjunction with the increases of mineral dust in the simulated mixture. Note that the coarse dust particles (more present in these stations) have also higher g with respect to the fine particles (larger particles generally scatter more in the forward direction [Hansen and Travis, 1974]) and so also a too high dust coarse fraction could contribute to these positive mean biases. Tamanrasset_INM is an exception, since despite it is located in the middle of the Saharan Desert it shows a null mean bias. This good agreement seems again to be more related to higher observed g (coarse observed dust) than to lower simulated g with respect to the other stations. Note that the subestimation of the observed ω in this station requires a higher ω for mineral dust which would cause the simulated g to decrease (see below). Hence maybe a missing of coarse dust particles by the model (above all from January to June) could compensate for a too high g of our mineral dust (this station is located at high altitude and so probably the model simulates too high fractions of fine dust particles). In La_Parguera and Malaga (far from dust sources) the higher presence of mineral dust during summer seems not to locally alter the almost flat simulated annual cycles of g. This detail could be related to a higher fine to coarse ratio in these stations with respect to the stations close to dust sources (coherently with the result found in Section 5.4.1 for Malaga). In Malaga, indeed, the background species during summer are smaller than the coarse dust particles (which therefore should produce g increases if present). Also in La_Parguera, the background species is mainly sea salt but the coarse particle of sea salt have lower g than the coarse particles of mineral dust (which again therefore should produce g increases if present). Anyway, the positive mean biases in both stations

($b = 0,04$ and $b = 0,06$ in La_Parguera and Malaga, respectively) could be strongly caused also by a missing of small species by the model: scattering species in La_Parguera (above all during spring, autumn and winter) and absorbing species in Malaga (coherently with the analysis of ω).

The analysis of the asymmetry factor in the considered stations dominated by natural aerosols suggests that our mineral dust should have a lower g (in most of the stations). An increasing imaginary refractive index causes g to increase (and vice versa) due to a higher absorption of the refracted rays inside the particles (mainly for coarse particles at $0,550\ \mu m$) [Hansen and Travis, 1974]. Hence the selected lower imaginary part for mineral dust is confirmed to be a more suitable option also regarding g. On the other hand, an increasing real refractive index causes g to decrease due to an enhanced refraction inside the particles which in turn enhances the backward scattering (for all the aerosol species at $0,550\ \mu m$) [Hansen and Travis, 1974]. Hence the slightly higher real part for sea salt (selected literature value) could help to partially reduce the observed positive mean bias in La_Parguera.

5.4.2.2 Stations dominated by anthropogenic species

The stations dominated by anthropogenic aerosols: Beijing, Fresno_2, GSFC, Lahore, Pretoria_CSIR-DPSS and Venise, are reported in subplots G, H, I, J, K, L, respectively, of Figures 5.3 and 5.4.

Single scattering albedo. The model captures very well the observed ω annual cycle in almost all the stations ($r \geq 0,70$ with a peak of $r = 0,95$ in Pretoria_CSIR-DPSS) and produces a negative correlation only in Venise ($r = -0,36$). The model then subestimates the observed ω in all the stations ($-0,10 \leq b \leq -0,02$). Despite the very good correlations (except for Venise in which though the bad correlation seems to be mainly caused by the mineral dust increases during spring and summer: see Figure 5.2), negative mean biases with variable intensity result in all the stations. Organic matter and black carbon seem to be the main responsible for the moderate and strong negative mean biases in stations located in urban areas: Beijing ($b = -0,10$), Fresno_2 ($b = -0,07$), Lahore ($b = -0,05$) and Pretoria_CSIR-DPSS ($b = -0,03$). However, a lower imaginary refractive index for black carbon seems to be unrealistic, since our reference value is already lower than the selected literature value [Bond and Bergstrom, 2006]. For the same reason, achieving a less important presence of black carbon in the mixture by decreasing its real refractive index also appears to be not advisable. Hence for black carbon maybe only a reduction of the simulated concentrations could be a feasible way to increase the simulated ω in these stations. Regarding organic matter, our reference imaginary refractive index (the same for POM and SOA at the moment) is too high with respect to the selected literature values for both anthropogenic POM [Shepherd et al., 2017] and SOA from biogenic sources [Nakayama et al., 2012; Liu et al., 2013]. It is true that considering a fraction of brown carbon in the organic matter from biomass burnings (source considered in the model: see Section 5.3.1) would require an enhancement of the absorption (more in the UV but also at $0,550\ \mu m$) [Kirchstetter et al., 2004]. However, as already mentioned, all these 4 stations are located in urban areas or close to biogenic sources and therefore a lower imaginary refractive index for organic matter seems to be more appropriate in these stations. Note that only in Fresno_2 some wildfire events are detected (in July, August and September) but the simulated ω accentuate their subestimation of the observations during these events. This could be related again to too high fractions of black carbon (maybe caused by too strong emissions also in conjunction with wildfires) which could therefore hide the need of a more absorbing organic matter. Also our reference real refractive index for organic matter is slightly higher than the selected literature values, for both POM and SOA. Hence, these new values could generate a reduction of the organic matter fractions (mean size smaller than $0,550\ \mu m$) that would facilitate the increase of the simulated ω due to higher fractions of sulfate in these stations. Sulfate, indeed, already has the maximum ω (totally scattering species) and so only with a more intense presence in the mixture can cause the simulated ω to increase (above all in Beijing, during the summer increase of sulfate). On the other hand, In GSFC and Venise organic matter and black carbon have lower fractions than in the other stations (even if black carbon, due to its extremely low ω, maybe significantly contributes to the negative mean biases also in these stations). In GSFC the weak negative mean bias ($b = -0,02$) could be corrected by higher fractions of sulfate (dominant species). Higher fractions of sulfate can been achieved by increasing its real refractive index (mean size smaller than $0,550\ \mu m$) which indeed results lower than the selected literature value [Freedman et al., 2009]. This result is in perfect agreement with Obiso et al. [2017]. Finally, in Venise the moderate negative mean bias ($b = -0,04$) seems to be more related to the significant presence of mineral dust in the spring and summer months (which causes also the bad correlation in this station). However, the main corrections suggested by the analysis in the other stations (less absorbing organic matter, higher presence of sulfate and lower black carbon fractions) could contribute to reduce the negative mean bias also in this station.

The analysis of single scattering albedo in the considered stations dominated by anthropogenic aerosols suggests that our reference organic matter should have a higher ω, sulfate should be more present in the monthly mixtures and black carbon less present. These corrections can be achieved by using a lower imaginary refractive index for organic matter and a higher real part for sulfate. Both these changes are in agreement with the selected literature values for the PTB case. For black carbon, instead, probably only a reduction of the simulated mass concentrations can positively contribute to decrease the negative mean biases in all the considered stations. The selected literature values for the refractive index, indeed, are higher than our reference values for both real and imaginary parts and so would cause the negative mean biases to increase in intensity in all the stations.

Asymmetry factor. The model captures very well the observed g annual cycle in Beijing ($r = 0,85$), Fresno_2 ($r = 0,87$), Lahore ($r = 0,87$) and Pretoria_CSIR-DPSS ($r = 0,89$). A moderate correlation is then registered in Venise ($r = 0,66$) and a negative one in GSFC ($r = -0,26$). The model overestimates the observed g in almost all the stations ($0,01 \leq b \leq 0,06$) and subestimates them only in Lahore ($b = -0,01$). The mean bias is positive but contained in intensity (even negative in Lahore) in stations located in urban areas: Beijing ($b = 0,02$), Fresno_2 ($b = 0,01$) and Pretoria_CSIR-DPSS ($b = 0,03$). This result appears to be coherent with the fact that organic matter (small species) is dominant with respect to sulfate in these stations. Reducing the imaginary refractive index of organic matter, indeed, would have a negligible impact on its g values (too small particles). Moreover, the small reductions of its real part would contribute to further increase the simulated g (even if probably very slightly). Hence, the correction of the low positive mean biases in these stations can come only from the increasing real refractive index for sulfate (not dominant species), which would cause the simulated g to significantly decrease. On the other hand, the higher real refractive index for sulfate could contribute more significantly to reduce the pronounced positive mean biases in GSFC (mainly during summer, in conjunction with increases of the sulfate fraction) and Venise ($b = 0,06$ in both stations). However in these stations the missing of small (and not absorbing) particles by the model seems to be a more significant contributor to the positive mean biases. Finally, the presence of black carbon in the mixture also causes g to decrease, as clearly visible in Fresno_2 in conjunction with the wildfire events (black carbon has also an extremely low g due to its very small size). Hence, the low positive mean biases (and even negative) resulting in Beijing, Fresno_2, Lahore and Pretoria_CSIR-DPSS could be partially due to the extreme fractions of black carbon, which therefore would hide a subestimation of small and scattering particles also in these stations.

The analysis of asymmetry factor in the considered stations dominated by anthropogenic aerosols clearly confirms that sulfate should have a higher real refractive index, in agreement with the selected literature value, and so a lower g. For organic matter, instead, the selected lower imaginary refractive indexes for POM and SOA would have negligible impacts on g while the slightly lower real parts would cause a minor g increase (probably less important than the g reduction of sulfate).

5.4.2.3 Perturbed analysis

As highlighted in the discussion for the REF case, almost all the refractive index corrections suggested by the analysis result in agreement with the new set of literature values selected for the PTB case (presented in Section 5.3.2). Only for black carbon the literature values seem to clearly contradict the corrections required and therefore they have not been applied in this work. Without a necessary evaluation of the correctness of the model emission and transport processes, indeed, applying the new refractive index for black carbon would only enlarge the masking of the microphysical evaluation of the other species (above all organic matter). Actually it is for example a known problem in the NMMB-MONARCH a too large lifetime assumed for black carbon in atmosphere (9 days) [Spada, 2015], which surely contributes to the extremely large simulated fractions of black carbon. The variations of the simulated ω and g caused by the new refractive indexes have been tested separately for natural and anthropogenic aerosols in order to isolate and better analyze them. Moreover, since these variations are approximately the same in similar stations, the analysis of the perturbations has been focused only on some representative stations. The plots with the perturbed analysis for the remaining subset stations are reported as supplementary material in Appendix A.

Perturbed ω and g of the natural species are plotted in Figures 5.5, 5.6 and 5.7 for Cairo_EMA_2, KAUST_Campus and La_Parguera, respectively. Note that in these stations (dominated by natural species) the new refractive indexes have been applied only for mineral dust (decrease of the imaginary part: $\sim -54,5\%$) and sea salt (increase of the real part: $\sim +3,8\%$). In the following analysis the variations Δr and Δb mean "perturbed minus reference" correlations and mean biases, respectively.

Regarding ω, in all the 3 stations the correlation improves ($\Delta r = +0,16$ in Cairo_EMA_2; $\Delta r = +0,06$ in KAUST_Campus; $\Delta r = +0,10$ in La_Parguera) and the negative mean bias reduces, as expected ($\Delta b = +0,03$ in Cairo_EMA_2; $\Delta b = +0,04$ in KAUST_Campus; $\Delta b = +0,01$ in La_Parguera). The largest increases of the simulated ω in the PTB case always occur in conjunction with the maxima of the mineral dust fractions. In stations close to dust sources (Cairo_EMA_2 and KAUST_Campus) notable improvements are evident with respect to the REF case regarding both correlation and mean bias. The less absorbing mineral dust, indeed, causes the simulated ω to significantly increase and also to better follow the observed annual cycle. In La_Parguera, as expected the increases of the sea salt fraction are negligible and therefore cause negligible variations in the simulated ω (as already mentioned, the increasing real refractive index enhances only the fractions of fine sea salt particles, presumably not dominant in a pure coastal station). However, again the less absorbing mineral dust causes an evident increase of the simulated ω in the summer months and consequently a better agreement with the observations.

Regarding g, in all the 3 stations the correlation gets worse ($\Delta r = -0,02$ in Cairo_EMA_2; $\Delta r = -0,16$ in KAUST_Campus; $\Delta r = -0,21$ in La_Parguera) but the positive mean bias reduces, as expected ($\Delta b = -0,01$ in all cases). Again the largest decreases of the simulated g in the PTB case occur in conjunction with higher fractions of mineral dust. In Cairo_EMA_2 and KAUST_Campus (close to dust sources) the less absorbing mineral dust causes the simulated g to decrease in all the

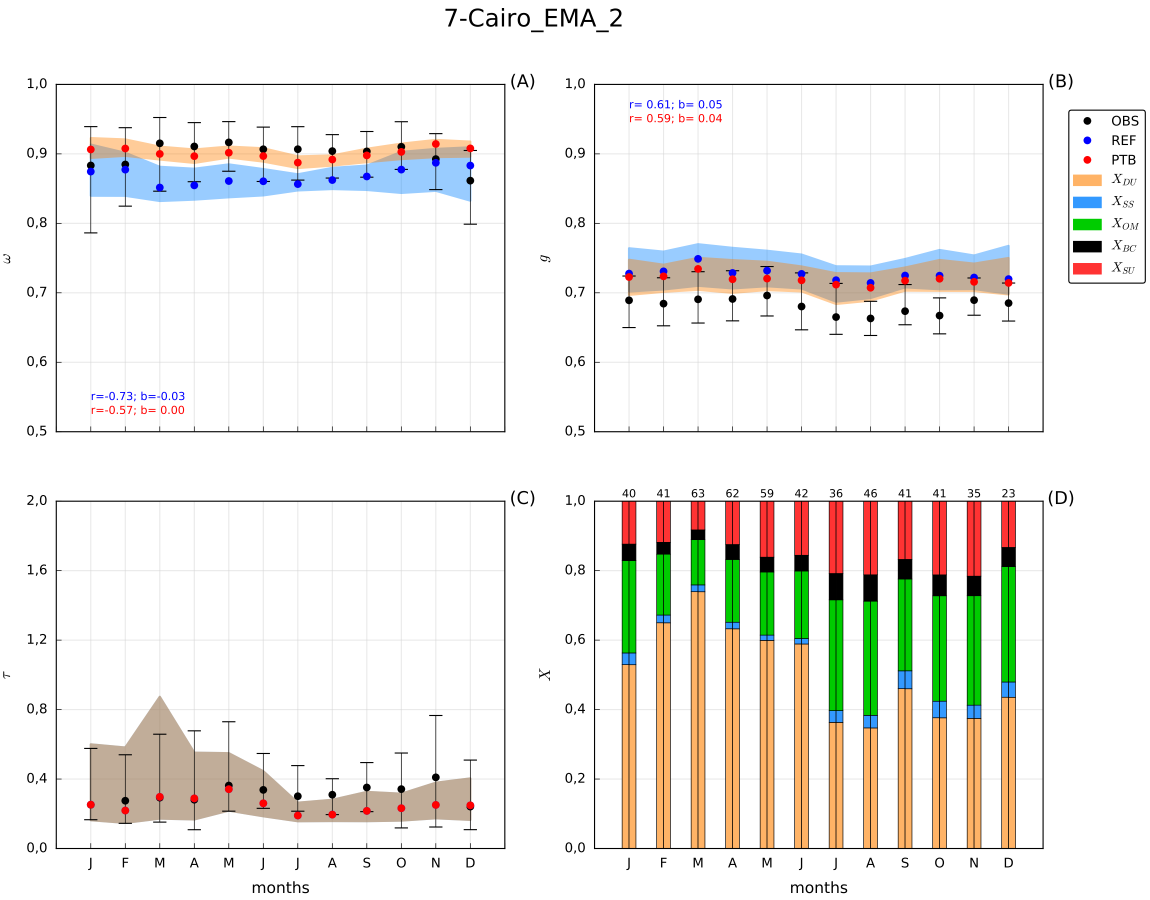

Figure 5.5: **Simulated (REF and PTB cases) and observed: (A) single scattering albedo (ω), (B) asymmetry factor (g), (C) optical depth (τ) and (D) monthly τ-fractions (X) of mineral dust (DU), sea salt (SS), organic matter (OM), black carbon (BC) and sulfate (SU), in Cairo_EMA_2. The PTB case in this station includes variations of the refractive index only for mineral dust and sea salt.**

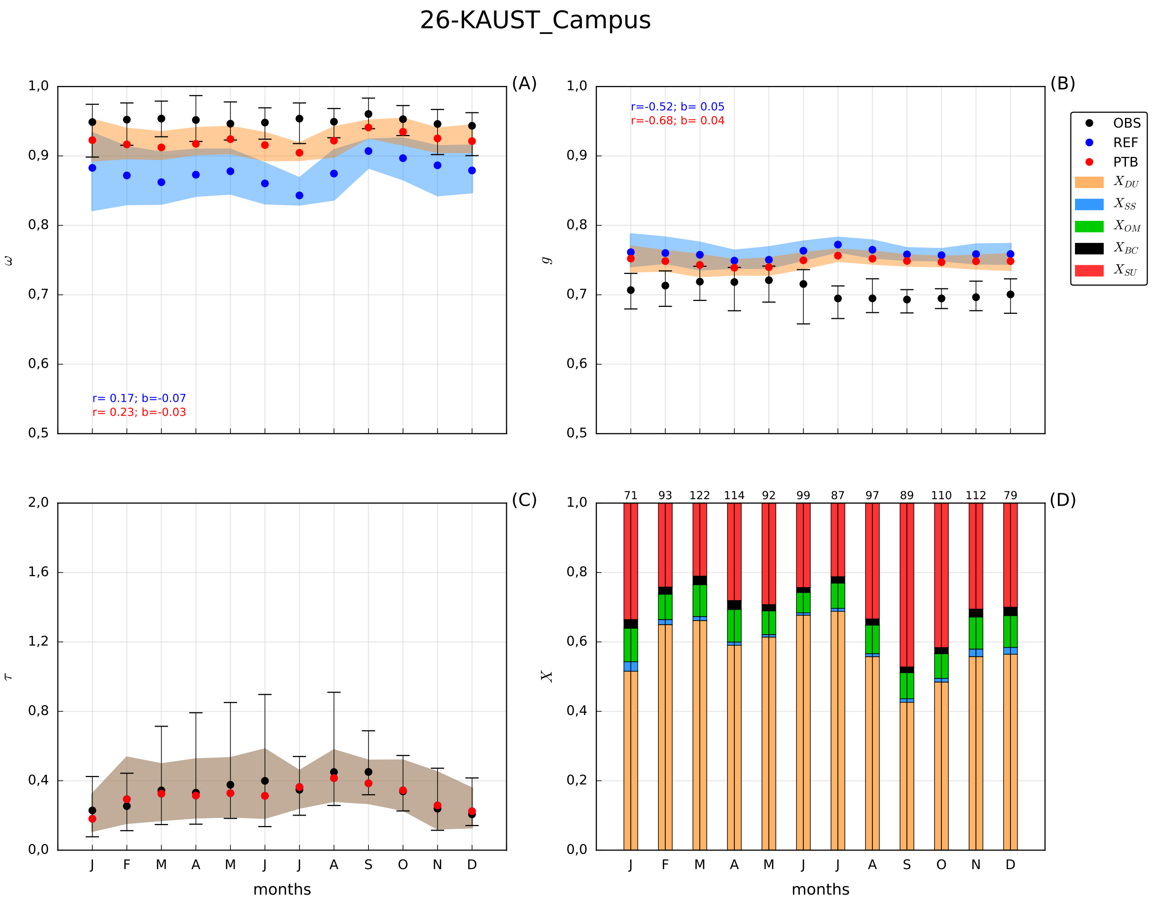

Figure 5.6: **As for Figure 5.5 but in KAUST_Campus.**

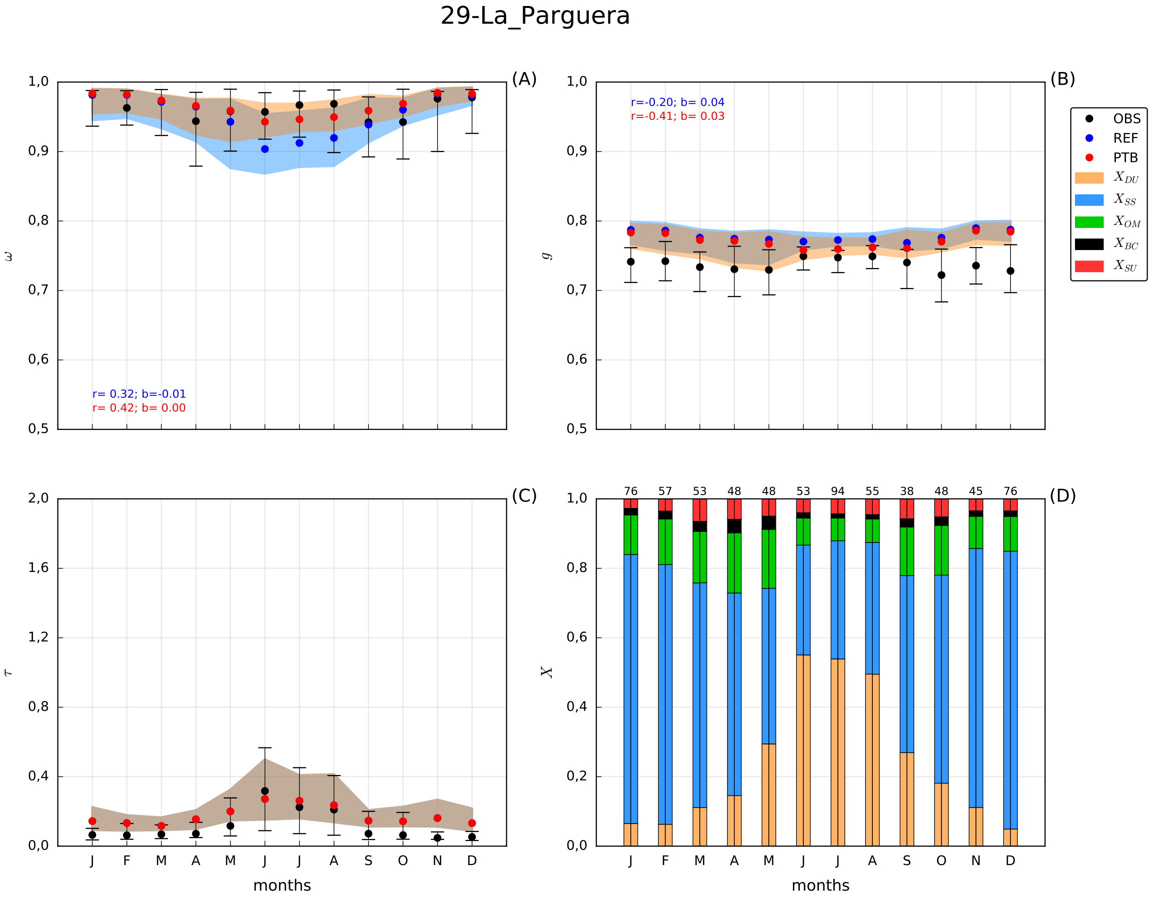

Figure 5.7: **Same as Figure 5.5 but in La_Parguera.**

months and the positive mean biases observed in the REF case to reduce, even if the variations are less important than for ω (the decreasing imaginary refractive index reduces g mainly for coarse dust particles). Evidently a stronger g reduction is needed in these stations, which could be for example produced by a higher fine to coarse ratio for mineral dust. Moreover, the g variations cause the correlations to get worse but mainly in KAUST_Campus, in which it is bad also in the REF case. In La_Parguera, while the higher real refractive index of sea salt causes the simulated g to decrease only very slightly (as expected), the evident decreases of the perturbed g during summer, due to mineral dust, cause the positive bias of the REF case to reduce but the anticorrelation to accentuate. The bias in the months dominated by sea salt evidently needs higher fractions of small and not absorbing particles to be reduced.

Perturbed ω and g for the anthropogenic species are reported in Figures 5.8, 5.9 and 5.10 for Beijing, Fresno_2 and GSFC, respectively. In these stations (dominated by anthropogenic species) the new refractive indexes have been applied only for organic matter (negligible imaginary parts for both POM and SOA and slight decrease of the real parts: $\sim -1,9\%$ for POM and $\sim -2,9\%$ for SOA) and sulfate (increase of the real part: $\sim +8,1\%$).

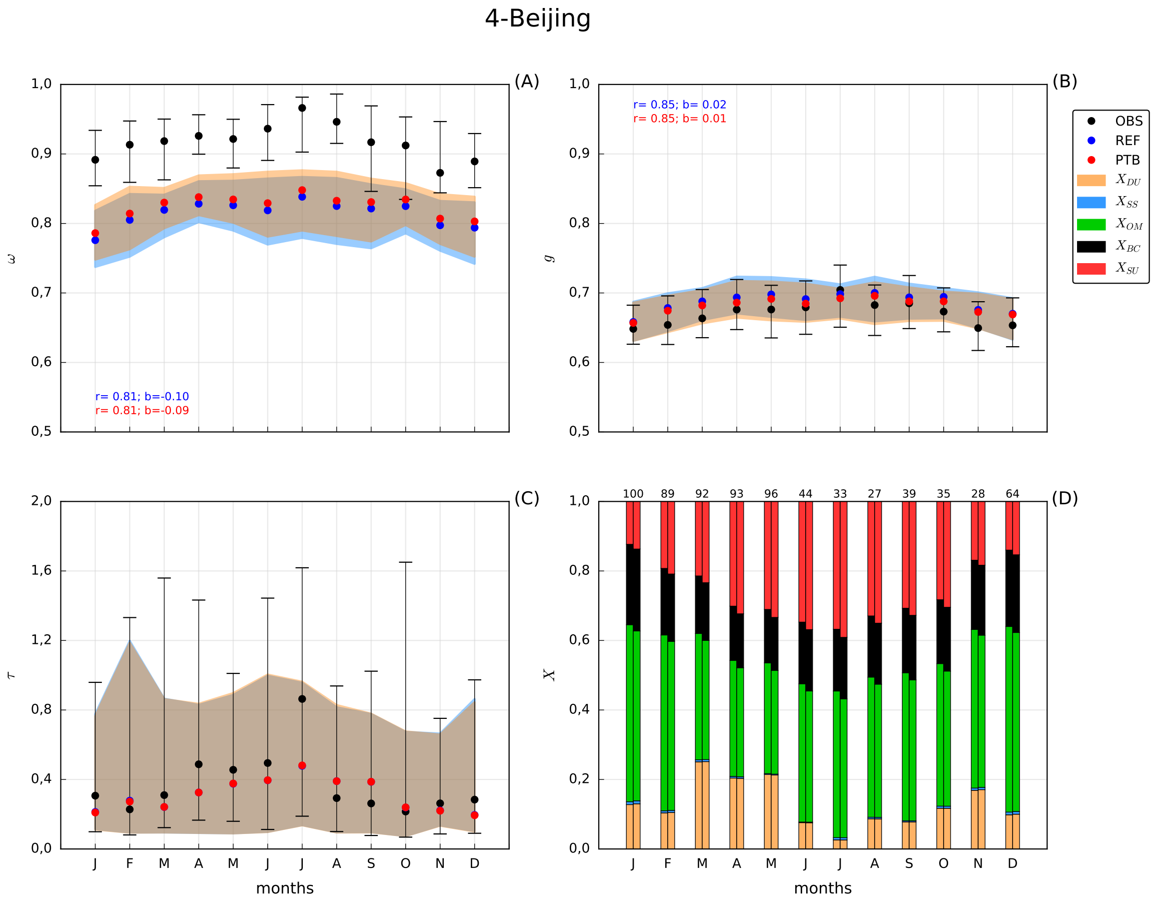

Figure 5.8: **Same as Figure 5.5 but in Beijing. Note that the PTB case in this station includes variations of the refractive index only for organic matter and sulfate.**

Regarding ω, in all the 3 stations the correlation show very small variations ($\Delta r = 0$ in Beijing; $\Delta r = +0,01$ in Fresno_2; $\Delta r = -0,01$ in GSFC) while the negative mean bias reduces, as expected ($\Delta b = +0,01$ in Beijing, $\Delta b = +0,02$ in Fresno_2; $\Delta b = +0,01$ in GSFC). The variations of the

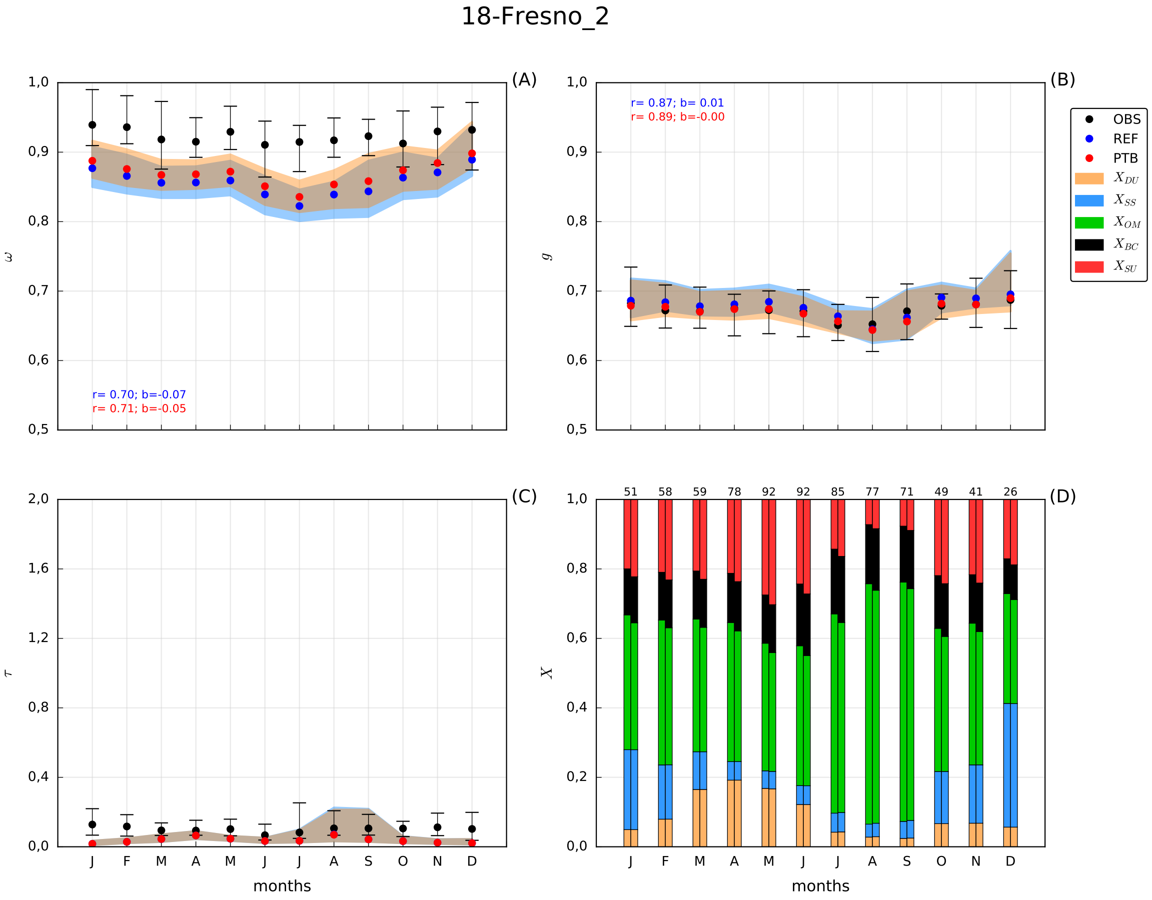

Figure 5.9: **Same as Figure 5.5 but in Fresno_2. Note that the PTB case in this station includes variations of the refractive index only for organic matter and sulfate.**

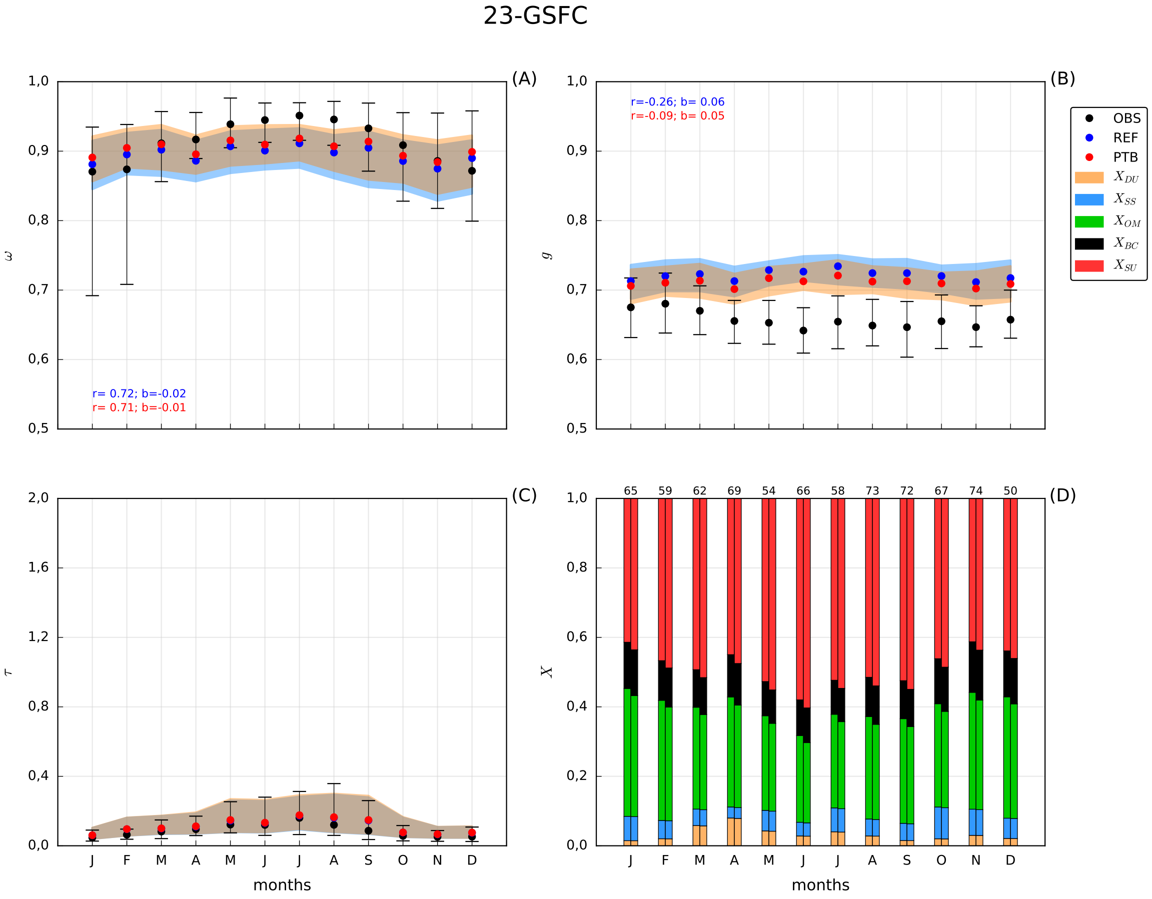

Figure 5.10: **Same as Figure 5.5 but in GSFC. Note that the PTB case in this station includes variations of the refractive index only for organic matter and sulfate.**

simulated ω in the PTB case are coherent with the corrections introduced in all the 3 stations: a less absorbing organic matter (and also slightly less present) and a more present sulfate cause the simulated ω to increase and consequently the negative mean biases of the REF case to reduce in all the stations. However these variations result absolutely insufficient to fill the gap between simulated and observed ω (mainly in Beijing and Fresno_2), probably due to the strong absorbing effect of black carbon in the model. This confirms that only a decrease of the mass concentrations of black carbon could cause a significant reduction of the negative mean biases in these stations. The correlations remain substantially unaffected in all the 3 stations.

Regarding g, the correlation improves in 2 of the 3 stations ($\Delta r = 0$ in Beijing; $\Delta r = +0,02$ in Fresno_2; $\Delta r = +0,17$ in GSFC) and the positive mean bias reduces, as expected, in all the 3 stations ($\Delta b = -0,01$ in all cases). The reduction of the positive mean biases of the REF case due to the higher real refractive index for sulfate (dominant on the enhancement due to the slightly lower real parts for organic matter) seems to be more important in GSFC, as expected (even if the mean bias numerical variations are the same in the 3 stations). However, while in Beijing and Fresno_2 the originally low positive mean bias (presumably caused also by the high black carbon fractions) result almost fully corrected (as expected), in GSFC the variations of the simulated g are evidently insufficient. This confirms that only a higher presence of small and scattering particles could significantly reduce the positive mean bias in this station. To conclude, the correlation remains substantially unaffected in Beijing and Fresno_2 while it significantly improves in GSFC (even if it keeps negative).

5.5 Conclusions

We carried out a direct evaluation of the intensive optical properties required by the full online coupling implemented in the NMMB-MONARCH. Simulated ω and g have been compared with AERONET Version 2.0 (manually screened Level 1.5) inversion data after assembling monthly means for each month over 5 years (2012-2016). In addition to the reference microphysical parameterization used in the model (REF case), also new refractive indexes taken from recent literature have been evaluated for almost all the species (PTB case) by studying the variations produced in the simulated properties by the new values. At first a global evaluation of the model performance for the full set of 59 selected AERONET stations has been carried out. In most stations the model tends to subestimate the observed ω and overestimates the observed g (in agreement with Curci et al. [2015]). A more detailed analysis (including also the perturbed analysis) has been then focused on a subset of 12 stations, selected based on observed τ levels, dominant aerosol species and geographical locations. Even if the correct simulation of the observed aerosol mixtures (only mentioned but not deeply investigated in this work) is a critical element for the evaluation of the intensive optical properties, our analysis produced some general recommendations (supported by the experimental values) about the refractive indexes to be used in the NMMB-MONARCH. With respect to the reference values used in the model, a lower imaginary refractive index ($2,500 \cdot 10^{-3}$) is more suitable for mineral dust. The mean biases found in stations close to dust sources (negative regarding ω, in agreement with Takemura et al. [2002], and positive regarding g), however, have been partially attributed to possible too high fractions of coarse dust particles in these stations (above all for stations located at low altitudes). Organic matter should have a negligible imaginary refractive index ($< 2,500 \cdot 10^{-5}$ for both POM and SOA components) at least close to urban/industrialized areas or biogenic sources. A separate parameterization for POM from urban/industry and biomass burning sources, however, would be an important improvement in the model since it could allow assigning suitable imaginary refractive indexes to these very different primary organic components. For black carbon, the model has been found to simulate too high mass concentrations, maybe due to a too high lifetime implemented in the black carbon module or to too strong emissions above all in urban areas. In Beijing for example the surface in situ black carbon has been found to explain $\sim 3\%$ of $PM_{2.5}$ from 2012 to 2015 [Lang et al., 2017], which leads to an approximate τ-fraction (calculated using average mass extinction cross sections and considering only aerosol species implemented in our model) of $\sim 10\%$, while our τ-fraction in Beijing is $\sim 20\%$ in all months. Decreasing real and imaginary parts of the black carbon refractive index to reduce its strong effect on the intensive optical properties appears to be unrealistic considering the recommended values from the selected literature. This strong presence of black carbon (detected in almost all the stations dominated by anthropogenic aerosols) made also impossible to evaluate the necessity of considering brown carbon as a fraction of POM in a station affected by wildfire events. Finally, a higher real refractive index $(1,546)$ has been found to be clearly more suitable for sulfate, in agreement with Obiso et al. [2017]. In addition to the mentioned problems regarding the aerosol mass simulation (dust fine to coarse ratio and black carbon), in general lack of specific species has been identified as a possible cause of systematic biases affecting the analyzed intensive optical properties. Above all increases of small and scattering species have been found to be possible efficient corrections to pronounced mean biases in more than one station (negative for ω and positive for g). Note that for example the presence of nitrate in stations dominated by anthropogenic aerosols could have a positive impact on the negative mean ω biases. Nitrate (under implementation in the NMMB-MONARCH) is indeed usually parameterized as a pure scattering species with a size similar to sulfate size (and even larger due to coagulation processes). For the positive mean g biases, however, smaller particles are needed as could be for example “white” organic aerosols.

Chapter 6

Conclusions and future works

In this thesis a deep assessment of the Aerosol-Radiation Interaction (ARI) in atmospheric models has been conducted. This included two sensitivity studies of aerosol optical properties and ARI radiative effects to the microphysical parameterization assumed for the particles and also the evaluation of the full online coupling of the aerosol module with the radiation scheme implemented in the NMMB-MONARCH model. A summary of the main results obtained in these specific works is presented in the following Section 6.1, while the consequent recommendations about possible future works are illustrated in Section 6.2.

6.1 Summary

- In Chapter 3 the sensitivity study of aerosol scattering properties to particle microphysical parameters has been presented. In particular, the impact of perturbed size distribution, refractive index, mass density (±20%) and shape (spheroids) of mineral dust, organic carbon and sulfate on values and spectral dependence (at 3 visible wavelengths) of simulated mass scattering cross sections has been analyzed. Moreover some constraints on the microphysical parameters (suitable for the north-western Mediterranean basin) have been derived by means of a comparison between simulated and observed mass scattering cross sections. Size distribution and refractive index have been found to have the most important impact on the mass scattering cross sections in most cases. Mass density and above all the shape of the particles, instead, have been found to have minor impacts. From the comparison with observations, the lognormal size distributions have been constrained to $r_g = 3,583 \cdot 10^{-1}$ μm and $\sigma_g = 1,600$ (geometric radius and standard deviation, respectively) for mineral dust, to $r_g = 2,544 \cdot 10^{-2}$ μm and $\sigma_g = 1,760$ for organic carbon and to $r_g = 8,340 \cdot 10^{-2}$ μm and $\sigma_g = 1,624$ for sulfate. Note that in all cases these size distribution parameters lead to lower mean size (simulated species too large with respect to the observed particles). Regarding the refractive index, instead, constraints only for the real part of organic carbon and sulfate have been derived: $n_r = 1,576$ and $n_r = 1,545$, respectively, at $0,525$ μm. Note that especially for sulfate the increase of the real refractive index has been found to be indispensable to achieve a good agreement between simulated and observed mass scattering cross sections.

- In Chapter 4 the sensitivity of shortwave ARI radiative effects to aerosol microphysical properties has been presented. Again ±20% perturbations have been applied to reference parameters of size distribution and refractive index of mineral dust and organic carbon, while two different mixing states (internal and external) have been considered for a black carbon-sulfate mixture. The perturbation impact on optical depth (τ), single scattering albedo (ω) and asymmetry factor (g) (in the shortwave region) has been firstly analyzed. Radiative simulations with idealized aerosol layers have been then performed (separately for each species and perturbation case) considering 3 aerosol events of increasing intensity. The microphysical perturbation impact on shortwave radiative fluxes and so ARI radiative effects have been finally evaluated. Different sensitivities of the optical properties of mineral dust and organic carbon to the perturbed microphysical properties have been observed, mainly due to the different mean size of the two species. The internal mixing between black carbon and sulfate has been found to produce more absorption with respect to the external mixing. Regarding the radiative simulations, the perturbation-induced absolute variations of the ARI radiative effects have been found to be very significant, above all in extreme aerosol events (up to 189 Wm^{-2} at the top of atmosphere and up to 280 Wm^{-2} at surface). However, the relative variability ranges have been found to never exceed the perturbation range applied to size distribution and refractive index parameters. Hence, local perturbations on particle microphysical parameters produce variability ranges of ARI radiative effects within the perturbation range applied, if evaluated against the base net radiative fluxes in absence of aerosols.

- In Chapter 5 the first evaluation of the full online coupling between aerosols and radiation implemented in the NMMB-MONARCH has been presented. In particular the intensive optical properties (ω and g at $0,550$ μm) calculated during runtime by the model have been evaluated. Aerosol simulations on a global domain for a 5-years (2012-2016) period have been performed with the model and the output intensive optical properties compared with AERONET screened Level 1.5 inversion data (from 59 stations). The global performance of the model for the full set of stations has been firstly evaluated. A more detailed analysis has been then carried out for a subset of 12 stations, selected following well defined criteria (observed optical depth, aerosol characterization and geographical locations). Finally, a new set of refractive indexes (taken from recent literature) has been evaluated for almost all the species with a focus on the variations induced by the new values in the comparison between simulated and observed intensive optical properties. From the global performance analysis, we found clear evidence that the model tends to subestimate the observed ω and to overestimate the observed g in most stations. This result has been confirmed in the detailed analysis and partially corrected by introducing the new refractive indexes. The new lower imaginary refractive index for mineral dust has been found to be more suitable: $n_i = 2,500 \cdot 10^{-3}$ ($-54,5\%$ with respect to our reference value). Also for organic matter we found the new lower imaginary parts to be more adequate both for POM (only from urban/industry sources): $n_i \sim 0$, and SOA (only from biogenic sources): $n_i = 2,500 \cdot 10^{-5}$ (our reference organic matter has the same imaginary refractive index of $6,000 \cdot 10^{-3}$, at $0,550$ μm, for both the organic components). Finally, for sulfate the higher new real part has been found to be advisable: $1,546$ ($+8,1\%$, in perfect agreement with the constraint found in Obiso et al. [2017], work presented in Chapter 3). In general a too low fine to coarse fraction for mineral dust (close to dust sources and at low altitudes) and a missing of small and scattering species (for example nitrate or "white" organic aerosols) have been found to probably contribute to most of the observed model biases. To conclude, black carbon fractions have been found to be too high in the model simulations (maybe due to too strong emissions in urban areas or to a too high lifetime in the model) and consequently to significantly contribute to the negative mean biases observed for ω in stations dominated by anthropogenic aerosols.

6.2 Future works

The scientific results found in the specific works composing this thesis suggest some recommendations and research lines to follow in order to improve the dynamic ARI implementation in the NMMB-MONARCH and so the model skills in simulating the ARI radiative effects. In Chapter 5 mineral dust has been found to be too much absorbing at $0,550\ \mu m$ with respect to recent observations. In this regard it would be useful to examine in depth the imaginary refractive indexes of all the dust mineralogy components, with a focus on their spectral variability. The independent transport of several dust mineral components in the NMMB-MONARCH, indeed, is currently under implementation and therefore the correct parameterization of their different absorption capabilities will be necessary in future. The constraints on the size distribution (lower mean size) for mineral dust (bulk) found in Chapter 3 can not be directly applied because mineral dust is size distributed in 8 bins in the model and so its effective size distribution is represented by the mass fractions in fine and coarse bins. However, this constraint can be seen as an useful indication in agreement with the hypothesis of too high dust coarse fractions proposed in Chapter 5 to explain some mean biases (in stations close to dust sources and at low altitudes). Hence, maybe also a revision of the dust mass distribution over the bins could be planned in the future.

A clear recommendation arising from our studies is also the development of a more detailed parameterization for organic matter. It is evident indeed that the independent transport of different POM components should be implemented in the model. At least POM from urban and industry sources and POM from biomass burning sources should be separately transported, since these components have very different absorption capabilities and usually dominate in different geographical areas. The new imaginary refractive indexes found in Chapter 5 should be then assigned to the two independent POM components and to SOA in order to considerably improve the model estimate of the radiative impact of organic matter. Moreover, the constraints on the organic carbon size distribution parameters (lower mean size) found in Chapter 3 could be directly applied even if this should be followed by a revision of all the model processes involving the aerosol size. Note that the effect of these size constraints on the results found in Chapter 5 should be explored, since they could lead to a reduction of the positive mean g biases observed in stations dominated by anthropogenic aerosols.

For sulfate only an update of the microphysical properties seems to be suggested by our analysis. The constraints found in Chapter 3 for real refractive index (confirmed in Chapter 5) and size distribution should be implemented in the model, with consequent revision of the size-dependent processes. Note that again the change of size for sulfate could have significant impacts on the results found in Chapter 5, which should be explored. Regarding black carbon, the most evident suggestions for future works is a revision of emission (especially injection height), transport and lifetime parameterization in the model. In Chapter 5, indeed, black carbon has been found to have too high mass concentrations, mainly in stations located in urban areas. Once revised the correctness of the mass concentration simulation, the refractive indexes should be updated with the literature values selected in Chapter 5. A possible internal mixing between black carbon and sulfate (explored in Chapter 4) has been found to lead to lower ω with respect to the external mixing case. This means that the negative mean ω biases found in stations dominated by anthropogenic aerosols (results found in Chapter 5) would get worse if considering the internal mixing between sulfate and black carbon. However, also this option should be better explored after revising the correctness of the black carbon mass concentration simulation.

Another important research line would be exploring the impact of nitrate on the intensive optical properties simulated in Chapter 5. The nitrate module is currently under implementation in the

NMMB-MONARCH with a parameterization similar to that of sulfate (so substantially a scattering species with mean size comparable with the sulfate size). Hence, its presence in the simulated mixture could lead to a reduction of the negative mean ω biases observed in stations dominated by anthropogenic aerosols. Note though that probably the positive mean biases regarding g observed in these stations, partially attributed to a lack of small particles, would not be substantially affected by the presence of nitrate. To conclude, recently the uptake of ammonia with some types of SOA have been found to lead to brown carbon formation [Updyke et al., 2012]. Hence the implementation of ammonium in the aerosol module of the NMMB-MONARCH (currently under development) could open another research line to explore, that is the formation of absorbing SOA to be implemented in the model.

More in general, in order to improve the ARI parameterization in atmospheric models, some assorted recommendations based on the analyses carried out in this thesis can be provided to the atmosphere modeling community. The key point we addressed in this thesis is how to better constrain the most important microphysical parameters for the aerosol species usually considered in models and actually this thesis provides some constraints on these microphysical parameters (mainly size distribution and refractive index). However, always in our analyses the microphysical perturbations have been separately applied to different microphysical properties and some perturbation compositions have been considered only in a certain degree. Hence, an evident improvement would be approaching this kind of sensitivity analysis with multi-parameter statistical analysis methods. Zhao et al. [2013], for example, conducted a sensitivity study of the radiative fluxes at the top of atmosphere (TOA), simulated with the Community Atmosphere Model version 5 (CAM5), to 16 model parameters (mainly cloud properties and aerosol emission tuning factors). They used a quasi-Montecarlo (QMC) sampling approach to effectively explore the high-dimensional parameter space (with uniform probability distributions for the parameters) and also used a variance-based sensitivity analysis to show the relative contributions of the single parameters to the total output variance. In our opinion this kind of analysis applied to all the particles microphysical parameters, with a focus on size distribution and refractive index, could represent a more efficient way to constrain them. This approach, indeed, would allow considering a very large range of values for each parameter and also taking into account a high number of interactions between different parameters (hugely increasing therefore the perturbation space). Obviously this kind of analysis requires much more computational power with respect to the single-property sensitivity analyses carried out in this thesis (and usually performed in the modeling community).

On the other hand, more detailed observations of aerosol optical and microphysical properties are strongly needed to improve the aerosol microphysical parameterization in models. For example an increased spatial coverage for measurements of aerosol intensive optical properties (mainly outside Europe and USA) would be very important to improve the model evaluations. Also, systematic refractive index measurements at many wavelengths, covering both shortwave and longwave regions, would help significantly to improve the ARI parameterization in models. This would avoid, indeed, the necessity of interpolating few measured refractive indexes (mainly available in the visible range) to obtain the values for all the spectral bands considered in the model radiative schemes. Even if most of the solar radiative energy is transported by the visible and near infrared wavelengths, indeed, the aerosol spectral activity at longer wavelengths can also have an impact on the model estimates of ARI radiative effects.

Bibliography

Aiken, A. C., Decarlo, P. F., Kroll, J. H., Worsnop, D. R., Huffman, J. A., Docherty, K. S., Ulbrich, I. M., Mohr, C., Kimmel, J. R., Sueper, D., Sun, Y., Zhang, Q., Trimborn, A., Northway, M., Ziemann, P. J., Canagaratna, M. R., Onasch, T. B., Alfarra, M. R., Prevot, A. S. H., Dommen, J., Duplissy, J., Metzger, A., Baltensperger, U., and Jimenez, J. L. (2008). O/C and OM/OC Ratios of Primary, Secondary, and Ambient Organic Aerosols with High-Resolution Time-of-Flight Aerosol Mass Spectrometry. *Environmental Science & Technology*, 42:4478–4485.

Anderson, T. L. and Ogren, J. A. (1998). Determining Aerosol Radiative Properties Using the TSI 3563 Integrating Nephelometer. *Aerosol Science and Technology*, 29:57–69.

Andrews, E., Sheridan, P. J., Fiebig, M., McComiskey, A., Ogren, J. A., Arnott, P., Covert, D., Elleman, R., Gasparini, R., Collins, D., Jonsson, H., Schmid, B., and Wang, J. (2006). Comparison of methods for deriving aerosol asymmetry parameter. *Journal of Geophysical Research*, 111, D05S04.

Badia, A., Jorba, O., Voulgarakis, A., Dabdub, D., Pérez García-Pando, C., Hilboll, A., Gonçalves, M., and Janjic, Z. (2017). Description and evaluation of the Multiscale Online Nonhydrostatic AtmospheRe CHemistry model (NMMB-MONARCH) version 1.0: gas-phase chemistry at global scale. *Geoscientific Model Development*, 10:609–638.

Baklanov, A. (2010). Chemical weather forecasting: a new concept of integrated modelling. *Advances in Science & Research*, 4:23–27.

Baklanov, A., Schlünzen, K., Suppan, P., Baldasano, J. M., Brunner, D., Aksoyoglu, S., Carmichael, G., Douros, J., Flemming, J., Forkel, R., Galmarini, S., Gauss, M., Grell, G., Hirtl, M., Joffre, S., Jorba, O., Kaas, E., Kaasik, M., Kallos, G., Kong, X., Korsholm, U., Kurganskiy, A., Kushta, J., Lohmann, U., Mahura, A., Manders-Groot, A., Maurizi, A., Moussiopoulos, N., Rao, S. T., Savage, N., Seigneur, C., Sokhi, R. S., Solazzo, E., Solomos, S., Sørensen, B., Tsegas, G., Vignati, E., Vogel, B., and Zhang, Y. (2014). Online coupled regional meteorology chemistry models in Europe: current status and prospects. *Atmospheric Chemistry and Physics*, 14:317–398.

Barker, H. W., Pincus, R., and Morcrette, J.-J. (2003). The Monte-Carlo Independent Column Approximation: Application within large-scale models. In *Proceedings of the GCSS/ARM Workshop on the Representation of Cloud Systems in Large-Scale Models, Kananaskis, Alberta, Canada, 20-24 May 2002.*

Bauer, S. E., Menon, S., Koch, D., Bond, T. C., and Tsigaridis, K. (2010). A global modeling study on carbonaceous aerosol microphysical characteristics and radiative effects. *Atmospheric Chemistry and Physics*, 10:7439–7456.

Betts, A. K. (1986). A new convective adjustment scheme. Part 1: Observational and theoretical basis. *Quarterly Journal of the Royal Meteorological Society*, 112:693–709.

Bond, T. C. and Bergstrom, R. W. (2006). Light Absorption by Carbonaceous Particles: An Investigative Review. *Aerosol Science and Technology*, 40:27–67.

Boucher, O., Randall, D., Artaxo, P., Bretherton, C., Feingold, G., Forster, P., Kerminen, V.-M., Kondo, Y., Liao, H., Lohmann, U., Rasch, P., Satheesh, S. K., Sherwood, S., Stevens, B., and Zhang, X. Y. (2013). Clouds and Aerosols. In Stocker, T. F., Qin, D., Plattner, G.-K., Tignor, M., Allen, S. K., Boschung, J., Nauels, A., Xia, Y., Bex, V., and Midgley, P. M., editors, *Climate Change 2013: The Physical Science Basis. Contribution of Working Group I to the Fifth Assessment Report of the Intergovernmental Panel on Climate Change.* Cambridge University Press, Cambridge, United Kingdom and New York, NY, USA.

Briegleb, B. P., Minnis, P., Ramanathan, V., and Harrison, E. (1986). Comparison of Regional Clear-Sky Albedos Inferred from Satellite Observations and Model Computations. *Journal of Climate and Applied Meteorology*, 25:214–226.

Byun, D. and Ching, J. (1999). Science Algorithms of the EPA Models-3 Community Multiscale Air Quality (CMAQ) Modeling System. *U.S. Environmental Protection Agency*, EPA/600/R-99/030.

Cachorro, V. E., Toledano, C., Prats, N., Sorribas, M., Mogo, S., Berjón, A., Torres, B., Rodrigo, R., de la Rosa, J., and De Frutos, A. M. (2008). The strongest desert dust intrusion mixed with smoke over the Iberian Peninsula registered with Sun photometry. *Journal of Geophysical Research*, 113, D14S04.

Chan, C. K. and Yao, X. (2008). Air pollution in mega cities in China. *Atmospheric Environment*, 42:1–42.

Chin, M., Diehl, T., Dubovik, O., Eck, T. F., Holben, B. N., Sinyuk, A., and Streets, D. G. (2009). Light absorption by pollution, dust, and biomass burning aerosols: a global model study and evaluation with AERONET measurements. *Annales Geophysicae*, 27:3439–3464.

Chin, M., Ginoux, P., Kinne, S., Torres, O., Holben, B. N., Duncan, B. N., Martin, R. V., Logan, J. A., Higurashi, A., and Nakajima, T. (2002). Tropospheric Aerosol Optical Thickness from the GOCART Model and Comparisons with Satellite and Sun Photometer Measurements. *Journal of the Atmospheric Sciences*, 59:461–483.

Chin, M., Rood, R. B., Lin, S.-J., Müller, J.-F., and Thompson, A. M. (2000). Atmospheric sulfur cycle simulated in the global model GOCART: Model description and global properties. *Journal of Geophysical Research*, 105(D20):24671–24687.

Clough, S. A. and Iacono, M. J. (1995). Line-by-line calculation of atmospheric fluxes and cooling rates: 2. Application to carbon dioxide, ozone, methane, nitrous oxide and the halocarbons. *Journal of Geophysical Research*, 100(D8):16519–16535.

Clough, S. A., Iacono, M. J., and Moncet, J.-L. (1992). Line-by-line calculation of atmospheric fluxes and cooling rates: Application to water vapor. *Journal of Geophysical Research*, 97(D14):15761–15785.

Curci, G., Hogrefe, C., Bianconi, R., Im, U., Balzarini, A., Baró, R., Brunner, D., Forkel, R., Giordano, L., Hirtl, M., Honzak, L., Jiménez-Guerrero, P., Knote, C., Langer, M., Makar, P. A., Pirovano, G., Pérez, J. L., San José, R., Syrakov, D., Tuccella, P., Werhahn, J., Wolke, R., Žabkar, R., Zhang, J., and Galmarini, S. (2015). Uncertainties of simulated aerosol optical properties induced by assumptions on aerosol physical and chemical properties: An AQMEII-2 perspective. *Atmospheric Environment*, 115:541–552.

D'Almeida, G. A. (1987). On the variability of desert aerosol radiative characteristics. *Journal of Geophysical Research*, 92:3017–3026.

DeCarlo, P. F., Slowik, J. G., Worsnop, D. R., Davidovits, P., and Jimenez, J. L. (2004). Particle Morphology and Density Characterization by Combined Mobility and Aerodynamic Diameter Measurements. Part 1: Theory. *Aerosol Science and Technology*, 38:1185–1205.

Denjean, C., Cassola, F., Mazzino, A., Triquet, S., Chevaillier, S., Grand, N., Bourrianne, T., Momboisse, G., Sellegri, K., Schwarzenbock, A., Freney, E., Mallet, M., and Formenti, P. (2016). Size distribution and optical properties of mineral dust aerosols transported in the western Mediterranean. *Atmospheric Chemistry and Physics*, 16:1081–1104.

Di Tomaso, E., Schutgens, N. A. J., Jorba, O., and Pérez García-Pando, C. (2017). Assimilation of MODIS Dark Target and Deep Blue observations in the dust aerosol component of NMMB-MONARCH version 1.0. *Geoscientific Model Development*, 10:1107–1129.

Dubovik, O., Holben, B. N., Eck, T. F., Smirnov, A., Kaufman, Y. J., King, M. D., Tanré, D., and Slutsker, I. (2002). Variability of Absorption and Optical Properties of Key Aerosol Types Observed in Worldwide Locations. *Journal of the Atmospheric Sciences*, 59:590–608.

Dubovik, O., Smirnov, A., Holben, B. N., King, M. D., Kaufman, Y. J., Eck, T. F., and Slutsker, I. (2000). Accuracy assessments of aerosol optical properties retrieved from Aerosol Robotic Network (AERONET) Sun and sky-radiance measurements. *Journal of Geophysical Research*, 105:9791–9806.

Ealo, M., Alastuey, A., Pérez, N., Ripoll, A., Querol, X., and Pandolfi, M. (2017). From air quality to climate: Impact of aerosol sources on optical properties at urban, regional and continental levels in the north-western Mediterranean. *Atmospheric Chemistry and Physics Discussions*, accepted for publication in Atmospheric Chemistry and Physics.

Ealo, M., Alastuey, A., Ripoll, A., Pérez, N., Minguillón, M. C., Querol, X., and Pandolfi, M. (2016). Detection of Saharan dust and biomass burning events using near-real-time intensive aerosol optical properties in the north-western Mediterranean. *Atmospheric Chemistry and Physics*, 16:12567–12586.

Eck, T. F., Holben, B. N., Dubovik, O., Smirnov, A., Slutsker, I., Lobert, J. M., and Ramanathan, V. (2001). Column-integrated aerosol optical properties over the Maldives during the northeast monsoon for 1998-2000. *Journal of Geophysical Research*, 106(D22):28,555–28,566.

Emmons, L. K., Walters, S., Hess, P. G., Lamarque, J.-F., Pfister, G. G., Fillmore, D., Granier, C., Guenther, A., Kinnison, D., Laepple, T., Orlando, J., Tie, X., Tyndall, G., Wiedinmyer, C., Baughcum, S. L., and Kloster, S. (2010). Description and evaluation of the Model for Ozone and Related chemical Tracers, version 4 (MOZART-4). *Geoscientific Model Development*, 3:43–67.

Ferrier, B. S., Jin, Y., Lin, Y., Black, T., Rogers, E., and DiMego, G. (2002). Implementation of a new grid-scale cloud and precipitation scheme in the NCEP Eta Model. In *Proceedings of the 15th Conference on Numerical Weather Prediction, San Antonio, Texas, 12-16 August 2002*, pages 280–283. American Meteorological Society, Boston, Massachusetts.

Foley, K. M., Roselle, S. J., Appel, K. W., Bhave, P. V., Pleim, J. E., Otte, T. L., Mathur, R., Sarwar, G., Young, J. O., Gilliam, R. C., Nolte, C. G., Kelly, J. T., Gilliland, A. B., and Bash, J. O. (2010). Incremental testing of the Community Multiscale Air Quality (CMAQ) modeling system version 4.7. *Geoscientific Model Development*, 3:205–226.

Freedman, M. A., Hasenkopf, C. A., Beaver, M. R., and Tolbert, M. A. (2009). Optical Properties of Internally Mixed Aerosol Particles Composed of Dicarboxylic Acids and Ammonium Sulfate. *The Journal of Physical Chemistry A*, 113:13584–13592.

Fu, Q. and Liou, K. N. (1992). On the Correlated k-Distribution Method for Radiative Transfer in Nonhomogeneous Atmospheres. *Journal of the Atmospheric Sciences*, 49(22):2139–2156.

Gkikas, A., Hatzianastassiou, N., and Mihalopoulos, N. (2009). Aerosol events in the broader Mediterranean basin based on 7-year (2000-2007) MODIS C005 data. *Annales Geophysicae*, 27:3509–3522.

Gong, S. L. (2003). A parameterization of sea-salt aerosol source function for sub and super-micron particles. *Global Biogeochemical Cycles*, 17(4):1097.

Gosse, S. F., Wang, M., Labrie, D., and Chylek, P. (1997). Imaginary part of the refractive index of sulfates and nitrates in the 0.7-2.6μm spectral region. *Applied Optics*, 36(16):3622–3634.

Guenther, A., Karl, T., Harley, P., Wiedinmyer, C., Palmer, P. I., and Geron, C. (2006). Estimates of global terrestrial isoprene emissions using MEGAN (Model of Emissions of Gases and Aerosols from Nature). *Atmospheric Chemistry and Physics*, 6:3181–3210.

Halmer, G., Douros, I., Tsegas, G., and Moussiopoulos, N. (2010). Using a coupled meteorological and chemical transport modelling scheme to evaluate the impact of the aerosol direct effect on pollutant concentration fields in Paris. In *Proceedings of the 31th NATO/SPS International Technical Meeting on Air Pollution Modelling and its Application (ITM2010), Turin, Italy, 27 Sep.-1 Oct. 2010.*

Hand, J. L. and Malm, W. C. (2006). *Review of the IMPROVE Equation for Estimating Ambient Light Extinction Coefficients.*

Hand, J. L. and Malm, W. C. (2007). Review of aerosol mass scattering efficiencies from groud-based measurements since 1990. *Journal of Geophysical Research*, 112, D16203.

Hansen, J. E. and Travis, L. D. (1974). Light scattering in planetary atmospheres. *Space Science Reviews*, 16:527–610.

Haustein, K., Pérez, C., Baldasano, J. M., Jorba, O., Basart, S., Miller, R. L., Janjic, Z., Black, T., Nickovic, S., Todd, M. C., Washington, R., Müller, D., Tesche, M., Weinzierl, B., Esselborn, M., and Schladitz, A. (2012). Atmospheric dust modeling from meso to global scales with the online NMMB/BSC-Dust model - Part 2: Experimental campaigns in Northern Africa. *Atmospheric Chemistry and Physics*, 12:2933–2958.

Hess, M., Köpke, P., and Schult, I. (1998). Optical Properties of Aerosols and Clouds: The Software Package OPAC. *Bulletin of the American Meteorological Society*, 79(5):831–844.

Holben, B. N., Eck, T. F., Slutsker, I., Smirnov, A., Sinyuk, A., Schafer, J., Giles, D., and Dubovik, O. (2006). Aeronet's Version 2.0 quality assurance criteria. *Proceedings SPIE*, 6408(64080Q).

Holben, B. N., Eck, T. F., Slutsker, I., Tanré, D., Buis, J. P., Setzer, A., Vermote, E., Reagan, J. A., Kaufman, Y. J., Nakajima, T., Lavenu, F., Jankowiak, I., and Smirnov, A. (1998). AERONET-A federated instrument network and data archive for aerosol characterization. *Remote Sensing of Environment*, 66:1–16.

Iacono, M. J. (2011). Application of Improved Radiation Modeling to General Circulation Models. *Atmospheric and Environmental Research*, Final Technical Report:1–39.

Iacono, M. J., Delamere, J. S., Mlawer, E. J., Shephard, M. W., Clough, S. A., and Collins, W. D. (2008). Radiative forcing by long-lived greenhouse gases: Calculations with the AER radiative transfer models. *Journal of Geophysical Research*, 113(D13103).

Irshad, R., Grainger, R. G., Peters, D. M., McPheat, R. A., Smith, K. M., and Thomas, G. (2009). Laboratory measurements of the optical properties of sea salt aerosol. *Atmospheric Chemistry and Physics*, 9:221–230.

Jacobson, M. Z. (2005). *Fundamentals of Atmospheric Modeling.* Cambridge University Press, New York, USA.

Jaeglé, L., Quinn, P. K., Bates, T. S., Alexander, B., and Lin, J.-T. (2011). Global distribution of sea salt aerosols: new constraints from in situ and remote sensing observations. *Atmospheric Chemistry and Physics*, 11:3137–3157.

Janjic, Z., Janjic, T., and Vasic, R. (2011). A class of conservative fourth order advection schemes and impact of enhanced formal accuracy on extended range forecasts. *Monthly Weather Review*, 139:1556–1568.

Janjic, Z. I. (1977). Pressure gradient force and advection scheme used for forecasting with steep and small scale topography. *Contributes to Atmospheric Physics*, 150:186–199.

Janjic, Z. I. (1979). Forward-backward scheme modified to prevent two-grid interval noise and its application in sigma coordinate models. *Contributes to Atmospheric Physics*, 52:69–84.

Janjic, Z. I. (1984). Non-linear advection schemes and energy cascade on semi-staggered grids. *Monthly Weather Review*, 112:1234–1245.

Janjic, Z. I. (1994). The step-mountain eta coordinate model: further developments of the convection, viscous sublayer, and turbulence closure schemes. *Monthly Weather Review*, 122:927–945.

Janjic, Z. I. (2003). A nonhydrostatic model based on a new approach. *Meteorology and Atmospheric Physics*, 82:271–285.

Janjic, Z. I. and Gall, R. (2012). Scientific Documentation of the NCEP Nonhydrostatic Multiscale Model on the B Grid (NMMB). Part 1 Dynamics. *NCAR Technical Note*, NCAR/TN-489+STR.

Janjic, Z. I., Gall, R., and Pyle, M. E. (2010). Scientific Documentation for the NMM Solver. *NCAR Technical Note*, NCAR/TN-477+STR.

Janjic, Z. I., Gerrity, J. P., and Nickovic, S. (2001). An alternative approach to nonhydrostatic modeling. *Monthly Weather Review*, 129:1164–1178.

Janssens-Maenhout, G., Crippa, M., Guizzardi, D., Dentener, F., Muntean, M., Pouliot, G., Keating, T., Zhang, Q., Kurokawa, J., Wankmüller, R., Denier van der Gon, H., Kuenen, J. J. P., Klimont, Z., Frost, G., Darras, S., Koffi, B., and Li, M. (2015). HTAP_v2.2: a mosaic of regional and global emission grid maps for 2008 and 2010 to study hemispheric transport of air pollution. *Atmospheric Chemistry and Physics*, 15:11411–11432.

Jorba, O., Dabdub, D., Blaszczak-Boxe, C., Pérez, C., Janjic, Z., Baldasano, J. M., Spada, M., Badia, A., and Gonçalves, M. (2012). Potential significance of photoexcited NO_2 on global air quality with the NMMB/BSC chemical transport model. *Journal of Geophysical Research*, 117(D13).

Kaiser, J. W., Heil, A., Andreae, M. O., Benedetti, A., Chubarova, N., Jones, L., Morcrette, J.-J., Razinger, M., Schultz, M. G., Suttie, M., and van der Werf, G. R. (2012). Biomass burning emissions estimated with a global fire assimilation system based on observed fire radiative power. *Biogeosciences*, 9:527–554.

Kallos, G., Solomos, S., and Kushta, J. (2009). Air quality - Meteorology Interaction Processes in the ICLAMS Modeling System. In *30th NATO/SPS International Technical Meeting on Air Pollution Modelling and its Application, San Francisco, 18-22 May 2009.*

Kanakidou, M., Seinfeld, J. H., Pandis, S. N., Barnes, I., Dentener, F. J., Facchini, M. C., Van Dingenen, R., Ervens, B., Nenes, A., Nielsen, C. J., Swietlicki, E., Putaud, J. P., Balkanski, Y., Fuzzi, S., Horth, J., Moortgat, G. K., Winterhalter, R., Myhre, C. E. L., Tsigaridis, K., Vignati, E., Stephanou, E. G., and Wilson, J. (2005). Organic aerosol and global climate modelling: a review. *Atmospheric Chemistry and Physics*, 5:1053–1123.

Kaskaoutis, D. G., Kambezidis, H. D., Hatzianastassiou, N., Kosmopoulos, P. G., and Badarinath, K. V. S. (2007). Aerosol climatology: dependence of the Ångström exponent on wavelength over four AERONET sites. *Atmospheric Chemistry and Physics Discussions*, 7:7347–7397. Revision for further review not submitted.

Kinne, S., Schulz, M., Textor, C., Guibert, S., Balkanski, Y., Bauer, S. E., Berntsen, T., Berglen, T. F., Boucher, O., Chin, M., Collins, W., Dentener, F., Diehl, T., Easter, R., Feichter, J., Fillmore, D., Ghan, S., Ginoux, P., Gong, S., Grini, A., Hendricks, J., Herzog, M., Horowitz, L., Isaksen, I., Iversen, T., Kirkevåg, A., Kloster, S., Koch, D., Kristjansson, J. E., Krol, M., Lauer, A., Lamarque, J. F., Lesins, G., Liu, X., Lohmann, U., Montanaro, V., Myhre, G., Penner, J. E., Pitari, G., Reddy, S., Seland, O., Stier, P., Takemura, T., and Tie, X. (2006). An AeroCom initial assessment - optical properties in aerosol component modules of global models. *Atmospheric Chemistry and Physics*, 6:1815–1834.

Kirchstetter, T. W., Novakov, T., and Hobbs, P. V. (2004). Evidence that the spectral dependence of light absorption by aerosols is affected by organic carbon. *Journal of Geophysical Research*, 109(D21208).

Lacagnina, C., Hasekamp, O. P., Bian, H., Curci, G., Myhre, G., van Noije, T., Schulz, M., Skeie, R. B., Takemura, T., and Zhang, K. (2015). Aerosol single-scattering albedo over the global oceans: Comparing PARASOL retrievals with AERONET, OMI, and AeroCom models estimates. *Journal of Geophysical Research: Atmospheres*, 120:9814–9836.

Lang, J., Zhang, Y., Zhou, Y., Cheng, S., Chen, D., Guo, X., Chen, S., Li, X., Xing, X., and Wang, H. (2017). Trends of $PM_{2.5}$ and Chemical Composition in Beijing, 2000-2015. *Aerosol and Air Quality Research*, 17:412–425.

Lesins, G., Chylek, P., and Lohmann, U. (2002). A study of internal and external mixing scenarios and its effect on aerosol optical properties and direct radiative forcing. *Journal of Geophysical Research*, 107(D10):AAC5 1–AAC5 12.

Lewis, E. R. and Schwartz, S. E. (2004). *Sea Salt Aerosol Production: Mechanism, Methods, Measurements, and Models.* Washington DC, USA.

Li, J., Carlson, B. E., Dubovik, O., and Lacis, A. A. (2014). Recent trends in aerosol optical properties derived from AERONET measurements. *Atmospheric Chemistry and Physics*, 14:12271–12289.

Liao, H. and Seinfeld, J. H. (1998). Radiative forcing by mineral dust aerosols: sensitivity to key variables. *Journal of Geophysical Research*, 103(D24):31637–31645.

Liu, P., Zhang, Y., and Martin, S. T. (2013). Complex Refractive Indices of Thin Films of Secondary Organic Materials by Spectroscopic Ellipsometry from 220 to 1200 nm. *Environmental Science & Technology*, 47:13594–13601.

Liu, P. F., Abdelmalki, N., Hung, H.-M., Wang, Y., Brune, W. H., and Martin, S. T. (2015). Ultraviolet and visible complex refractive indices of secondary organic material produced by photooxidation of the aromatic compounds toluene and m-xylene. *Atmospheric Chemistry and Physics*, 15:1435–1446.

Mårtensson, E. M., Nilsson, E. D., de Leeuw, G., Cohen, L. H., and Hansson, H.-C. (2003). Laboratory simulations and parameterization of the primary marine aerosol production. *Journal of Geophysical Research*, 108(D9):4297.

Marticorena, B. and Bergametti, G. (1995). Modeling the atmospheric dust cycle: 1. Design of a soil-derived dust emission scheme. *Journal of Geophysical Research*, 100(D8):16415–16430.

Mathur, R., Pleim, J., Wong, D., Otte, T., Gilliam, R., Roselle, S., Young, J., Binkowski, F., and Xiu, A. (2010). The WRF-CMAQ integrated on-line modeling system: development, testing, and initial applications. In *Air Pollution Modeling and Its Application XX*, pages 155–159. Springer.

Mishchenko, M. I. and Travis, L. D. (1998). Capabilities and limitations of a current FORTRAN implementation of the T-matrix method for randomly oriented, rotationally symmetric scatterers. *Journal of Quantitative Spectroscopy and Radiative Transfer*, 60:309–324.

Mishchenko, M. I., Travis, L. D., and Lacis, A. A. (2002). *Scattering, Absorption and Emission of Light by Small Particles*. Cambridge University Press, Cambridge, UK.

Mishchenko, M. I., Videen, G., Babenko, V. A., Khlebtsov, N. G., and Wriedt, T. (2004). T-matrix theory of electromagnetic scattering by particles and its applications: a comprehensive reference database. *Journal of Quantitative Spectroscopy and Radiative Transfer*, 88:357–406.

Mlawer, E. J., Taubman, S. J., Brown, P. D., Iacono, M. J., and Clough, S. A. (1997). Radiative transfer for inhomogeneous atmosphere: RRTM, a validated correlated-k model for the longwave. *Journal of Geophysical Research*, 102(D14):16663–16682.

Monahan, E. C., Spiel, D. E., and Davidson, K. L. (1986). A Model of Marine Aerosol Generation Via Whitecaps and Wave Disruption. In Monahan, E. C. and Mac Niocaill, G., editors, *Oceanic Withecaps*, pages 167–174. D. Reidel, Norwell, Massachusetts, USA.

Monin, A. S. and Obukhov, A. M. (1954). Basic laws of turbulent mixing in the surface layer of the atmosphere. *Contrib. Geophysical Institute of the Academy of Sciences of the USSR*, 24(151):163–187.

Moussiopoulos, N., Douros, I., Tsegas, G., Kleanthous, S., and Chourdakis, E. (2012). An air quality management system for policy support in Cyprus. *Advances in Meteorology*, 2012, 959280.

Mulcahy, J. P., Walters, D. N., Bellouin, N., and Milton, S. F. M. (2014). Impacts of increasing the aerosol complexity in the Met Office global numerical weather prediction model. *Atmospheric Chemistry and Physics*, 14:4749–4778.

Myhre, G., Samset, B. H., Schulz, M., Balkanski, Y., Bauer, S., Berntsen, T. K., Bian, H., Bellouin, N., Chin, M., Diehl, T., Easter, R. C., Feichter, J., Ghan, S. J., Hauglustaine, D., Iversen, T., Kinne, S., Kirkevag, A., Lamarque, J.-F., Lin, G., Liu, X., Lund, M. T., Luo, G., Ma, X., van Noije, T., Penner, J. E., Rasch, P. J., Ruiz, A., Seland, O., Skeie, R. B., Stier, P., Takemura, T., Tsigaridis, K., Wang, P., Wang, Z., Xu, L., Yu, H., Yu, F., Yoon, J.-H., Zhang, K., Zhang, H., and Zhou, C. (2013a). Radiative forcing of the direct aerosol effect from AeroCom Phase II simulations. *Atmospheric Chemistry and Physics*, 13:1853–1877.

Myhre, G., Shindell, D., Bréon, F.-M., Collins, W., Fuglestvedt, J., Huang, J., Koch, D., Lamarque, J.-F., Lee, D., Mendoza, B., Nakajima, T., Robock, A., Stephens, G., Takemura, T., and Zhang, H. (2013b). Anthropogenic and Natural Radiative Forcing. In Stocker, T. F., Qin, D., Plattner, G.-K., Tignor, M., Allen, S. K., Boschung, J., Nauels, A., Xia, Y., Bex, V., and Midgley, P. M., editors, *Climate Change 2013: The Physical Science Basis. Contribution of Working Group I to the Fifth Assessment Report of the Intergovernmental Panel on Climate Change*. Cambridge University Press, Cambridge, United Kingdom and New York, NY, USA.

Nakayama, T., Sato, K., Matsumi, Y., Imamura, T., Yamazaki, A., and Uchiyama, A. (2012). Wavelength Dependence of Refractive Index of Secondary Organic Aerosols Generated during the Ozonolysis and Photooxidation of α-Pinene. *Scientific Online Letters on the Atmosphere*, 8:119–123.

Nemesure, S., Wagener, R., and Schwartz, S. E. (1995). Direct shortwave forcing of climate by the anthropogenic sulfate aerosol: Sensitivity to particle size, composition and relative humidity. *Journal of Geophysical Research*, 100(D12):26105–26116.

Nickovic, S., Kallos, G., Papadopoulos, A., and Kakaliagou, O. (2001). A model for prediction of desert dust cycle in the atmosphere. *Journal of Geophysical Research*, 106(D16):18113–18129.

Nikitidou, E. and Kazantzidis, A. (2013). On the differences of ultraviolet and visible irradiance calculations in the Mediterranean basin due to model- and satellite-derived climatologies of aerosol optical properties. *International Journal of Climatology*, 33:2877–2888.

Obiso, V. and Jorba, O. (2018). Aerosol-radiation interaction in atmospheric models: idealized sensitivity study of simulated short-wave direct radiative effects to particle microphysical properties. *Journal of Aerosol Science*, 115:46–61. Published online in October 2017.

Obiso, V., Jorba, O., Pandolfi, M., and Pérez García-Pando, C. (unpublished results). Aerosol intensive optical properties in the NMMB-MONARCH. *Atmospheric Chemistry and Physics*, in preparation.

Obiso, V., Pandolfi, M., Ealo, M., and Jorba, O. (2017). Impact of aerosol microphysical properties on mass scattering cross sections. *Journal of Aerosol Science*, 112:68–82.

Oreopoulos, L. and Barker, H. W. (1999). Accounting for subgrid-scale cloud variability in a multi-layer 1D solar radiative transfer algorithm. *Quarterly Journal of the Royal Meteorological Society*, 125:301–330.

Paatero, P. (1997). Least squares formulation of robust non-negative factor analysis. *Chemometrics and Intelligent Laboratory Systems*, 37:23–35.

Pandolfi, M., Alastuey, A., Pérez, N., Reche, C., Castro, I., Shatalov, V., and Querol, X. (2016). Trends analysis of PM source contributions and chemical tracers in NE Spain during 2004-2014: A multi-exponential approach. *Atmospheric Chemistry and Physics*, 16:11787–11805.

Pandolfi, M., Cusack, M., Alastuey, A., and Querol, X. (2011). Variability of aerosol optical properties in the Western Mediterranean Basin. *Atmospheric Chemistry and Physics*, 11:8189–8203.

Pandolfi, M., Querol, X., Alastuey, A., Jimenez, J. L., Jorba, O., Day, D., Ortega, A., Cubison, M. J., Comerón, A., Sicard, M., Mohr, C., Prévôt, A. S. H., Minguillón, M. C., Pey, J., Baldasano, J. M., Burkhart, K. F., Seco, R., Peñuelas, J., van Drooge, B. L., Artiñano, B., Di Marco, C., Nemitz, E., Schallhart, S., Metzger, A., Hansel, A., Lorente, J., Ng, S., Jayne, J., and Szidat, S. (2014). Effects of sources and meteorology on particulate matter in the Western Mediterranean Basin: An overview of the DAURE campaign. *Journal of Geophysical Research: Atmospheres*, 119:4978–5010.

Pereira, S. N., Wagner, F., and Silva, A. M. (2011). Seven years of measurements of aerosol scattering properties, near the surface, in the southwestern Iberia Peninsula. *Atmospheric Chemistry and Physics*, 11:17–29.

Pérez, C., Haustein, K., Janjic, Z., Jorba, O., Huneeus, N., Baldasano, J. M., Black, T., Basart, S., Nickovic, S., Miller, R. L., Perlwitz, J. P., Schulz, M., and Thomson, M. (2011). Atmospheric dust modeling from meso to global scales with the online NMMB/BSC-Dust model - Part 1: Model description, annual simulations and evaluation. *Atmospheric Chemistry and Physics*, 11:13001–13027.

Pérez, C., Nickovic, S., Pejanovic, G., Baldasano, J. M., and Özsoy, E. (2006). Interactive dust-radiation modeling: A step to improve weather forecasts. *Journal of Geophysical Research*, 111, D16206.

Pérez, N., Pey, J., Castillo, S., Viana, M., Alastuey, A., and Querol, X. (2008). Interpretation of the variability of levels of regional background aerosols in the Western Mediterranean. *Science of the Total Environment*, 407:527–540.

Pey, J., Pérez, N., Castillo, S., Viana, M., Moreno, T., Pandolfi, M., Lopez-Sebastian, J. M., Alastuey, A., and Querol, X. (2009). Geochemistry of regional background aerosols in the Western Mediterranean. *Atmospheric Research*, 94:422–435.

Pleim, J., Young, J., Wong, D., Gilliam, R., Otte, T., and Mathur, R. (2008). Two-way coupled meteorology and air quality modeling. In Borrego, C. and Miranda, A. I., editors, *Air Pollution Modeling and Its Application XIX*, pages 496–504. Springer, the Netherlands. ISBN 978-1-4020-8452-2.

Querol, X., Alastuey, A., Pey, J., Cusack, M., Pérez, N., Mihalopoulos, N., Theodosi, C., Gerasopoulos, E., Kubilay, N., and Koçak, M. (2009). Variability in regional background aerosols within the Mediterranean. *Atmospheric Chemistry and Physics*, 9:4575–4591.

Randles, C. A., Kinne, S., Myhre, G., Schulz, M., Stier, P., Fischer, J., Doppler, L., Highwood, E., Ryder, C., Harris, B., Huttunen, J., Ma, Y., Pinker, R. T., Mayer, B., Neubauer, D., Hitzenberger, R., Oreopoulos, L., Lee, D., Pitari, G., Di Genova, G., Quaas, J., Rose, F. G., Kato, S., Rumbold, S. T., Vardavas, I., Hatzianastassiou, N., Matsoukas, C., Yu, H., Zhang, F., Zhang, H., and Lu, P. (2013). Intercomparison of shortwave radiative transfer schemes in global aerosol modeling: results from the AeroCom Radiative Transfer Experiment. *Atmospheric Chemistry and Physics*, 13:2347–2379.

Rap, A., Scott, C. E., Spracklen, D. V., Bellouin, N., Forster, P. M., Carslaw, K. S., Schmidt, A., and Mann, G. (2013). Natural aerosol direct and indirect radiative effects. *Geophysical Research Letters*, 40:3297–3301.

Sander, R., Baumgaertner, A., Gromov, S., Harder, H., Jöckel, P., Kerkweg, A., Kubistin, D., Regelin, E., Riede, H., Sandu, A., Taraborrelli, D., Tost, H., and Xie, Z.-Q. (2011). The atmospheric chemistry box model CAABA/MECCA-3.0. *Geoscientific Model Development*, 4:373–380.

Sandu, A. and Sander, R. (2006). Technical note: Simulating chemical systems in Fortran90 and Matlab with the Kinetic PreProcessor KPP-2.1. *Atmospheric Chemistry and Physics*, 6:187–195.

Schulz, M., Textor, C., Kinne, S., Balkanski, Y., Bauer, S., Berntsen, T., Berglen, T., Boucher, O., Dentener, F., Guibert, S., Isaksen, I. S. A., Iversen, T., Koch, D., Kirkevåg, A., Liu, X., Montanaro, V., Myhre, G., Penner, J. E., Pitari, G., Reddy, S., Seland, Ø., Stier, P., and Takemura, T. (2006). Radiative forcing by aerosols as derived from the AeroCom present-day and pre-industrial simulations. *Atmospheric Chemistry and Physics*, 6:5225–5246.

Segelstein, D. J. (1981). *The complex refractive index of water.* University of Missouri (Master's Thesis), Kansas City, Missouri.

Shalaby, A., Zakey, A. S., Tawfik, A. B., Solmon, F., Giorgi, F., Stordal, F., Sillman, S., Zaveri, R. A., and Steiner, A. L. (2012). Implementation and evaluation of online gas-phase chemistry within a regional climate model (RegCM-CHEM4). *Geoscientific Model Development*, 5:741–760.

Shamjad, P. M., Tripathi, S. N., Thamban, N. M., and Vreeland, H. (2016). Refractive Index and Absorption Attribution of Highly Absorbing Brown Carbon Aerosols from an Urban Indian City-Kanpur. *Scientific Reports*, 6, 37735.

Shepherd, R. H., King, M. D., Marks, A., Brough, N., and Ward, A. D. (2017). Determination of the refractive index of insoluble organic extracts from atmospheric aerosol over the visible wavelength range using optical tweezers. *Atmospheric Chemistry and Physics Discussions*, in review.

Simmons, A. J. and Burridge, D. M. (1981). An energy and angular momentum conserving vertical finite-difference scheme and hybrid vertical coordinates. *Monthly Weather Review*, 109:758–766.

Slinn, W. G. N. (1982). Predictions for particle deposition to vegetative canopies. *Atmospheric Environment*, 16:1785–1794.

Slinn, W. G. N. (1984). Precipitation scavenging. In Randerson, D., editor, *Atmospheric Science and Power Production*, pages 466–532. OSTI, Oak Ridge.

Smith, M. H. and Harrison, N. M. (1998). The sea spray generation function. *Journal of the Atmospheric Sciences*, 29:189–190.

Solmon, F., Giorgi, F., and Liousse, C. (2006). Aerosol modelling for regional climate studies: application to anthropogenic particles and evaluation over a European/African domain. *Tellus B*, 58:51–72.

Solomos, S., Kallos, G., Kushta, J., Astitha, M., Tremback, C., Nenes, A., and Levin, Z. (2011). An integrated modeling study on the effects of mineral dust and sea salt particles on clouds and precipitation. *Atmospheric Chemistry and Physics*, 11:873–892.

Spada, M. (2015). *Development and evaluation of an atmospheric aerosol module implemented within the NMMB/BSC-CTM.* Polytechnic University of Catalonia (Ph.D. Thesis), Barcelona, Spain.

Spada, M., Jorba, O., Pérez García-Pando, C., Janjic, Z., and Baldasano, J. M. (2013). Modeling and evaluation of the global sea-salt aerosol distribution: sensitivity to size-resolved and sea-surface temperature dependent emission schemes. *Atmospheric Chemistry and Physics*, 13:11735–11755.

Spada, M., Jorba, O., Pérez García-Pando, C., Janjic, Z., and Baldasano, J. M. (2015). On the evaluation of global sea-salt aerosol models at coastal/orographic sites. *Atmospheric Environment*, 101:41–48.

Takemura, T., Nakajima, T., Dubovik, O., Holben, B. N., and Kinne, S. (2002). Single-Scattering Albedo and Radiative Forcing of Various Aerosol Species with a Global Three-Dimensional Model. *Journal of Climate*, 15(4):333–352.

Tang, M., Alexander, J. M., Kwon, D., Estillore, A. D., Laskina, O., Young, M. A., Kleiber, P. D., and Grassian, V. H. (2016). Optical and Physicochemical Properties of Brown Carbon Aerosol: Light Scattering, FTIR Extinction Spectroscopy, and Hygroscopic Growth. *The Journal of Physical Chemistry A*, 120:4155–4166.

Tegen, I. and Lacis, A. A. (1996). Modeling of particle size distribution and its influence on the radiative properties of mineral dust aerosol. *Journal of Geophysical Research*, 101(D14):19237–19244.

Tsigaridis, K. and Kanakidou, M. (2007). Secondary organic aerosol importance in the future atmosphere. *Atmospheric Environment*, 41:4682–4692.

Turpin, B. J. and Lim, H. J. (2001). Species contributions to $PM_{2.5}$ mass concentrations: Revisiting common assumptions for estimating organic mass. *Aerosol Science and Technology*, 35:602–610.

Updyke, K. M., Nguyen, T., and Nizkorodov, S. A. (2012). Formation of brown carbon via reactions of ammonia with secondary organic aerosols from biogenic and anthropogenic precursors. *Atmospheric Environment*, 63:22–31.

Wesely, M. L. (1989). Parameterization of surface resistances to gaseous dry deposition in regional-scale numerical models. *Atmospheric Environment*, 23(6):1293–1304.

White, W. H. and Macias, E. S. (1987). On measurement error and the empirical relationship of atmospheric extinction to aerosol composition in the non-urban West. In Bhardwaja, P. S., editor, *Visibility Protection: Research and Policy Aspects*, pages 783–794. Air Pollution Control Association (now A&WMA), Pittsburgh.

Wiedinmyer, C., Yokelson, R. J., and Gullett, B. K. (2014). Global Emissions of Trace Gases, Particulate Matter, and Hazardous Air Pollutants from Open Burning of Domestic Waste. *Environmental Science & Technology*, 48:9523–9530.

Wild, O., Zhu, X., and Prather, M. J. (2000). Fast-J: Accurate Simulation of In- and Below-Cloud Photolysis in Tropospheric Chemical Models. *Journal of Atmospheric Chemistry*, 37(3):245–282.

Wong, D. C., Pleim, J., Mathur, R., Binkowski, F., Otte, T., Gilliam, R., Pouliot, G., Xiu, A., Young, J. O., and Kang, D. (2012). WRF-CMAQ two-way coupled system with aerosol feedback: software development and preliminary results. *Geoscientific Model Development*, 5:299–312.

Xia, X. A., Chen, H. B., Wang, P. C., Zhang, W. X., Goloub, P., Chatenet, B., Eck, T. F., and Holben, B. N. (2006). Variation of column-integrated aerosol properties in a Chinese urban region. *Journal of Geophysical Research*, 111, D05204.

Yarwood, G., Rao, S., Yocke, M., and Whitten, G. Z. (2005). UPDATES TO THE CARBON BOND CHEMICAL MECHANISM: CB05. *Final Report for U.S. EPA*, RT-04-00675.

Yu, H., Kaufman, Y. J., Chin, M., Feingold, G., Remer, L. A., Anderson, T. L., Balkanski, Y., Bellouin, N., Boucher, O., Christopher, S., DeCola, P., Kahn, R., Koch, D., Loeb, N., Reddy, M. S., Schulz, M., Takemura, T., and Zhou, M. (2006). A review of measurement-based assessments of the aerosol direct radiative effect and forcing. *Atmospheric Chemistry and Physics*, 6:613–666.

Zakey, A. S., Solmon, F., and Giorgi, F. (2006). Implementation and testing of a desert dust module in a regional climate model. *Atmospheric Chemistry and Physics*, 6:4687–4704.

Zender, C. S., Bian, H., and Newman, D. (2003). Mineral Dust Entrainment And Deposition (DEAD) model: Description and 1990s dust climatology. *Journal of Geophysical Research*, 108(D14).

Zhang, L., Gong, S., Padro, J., and Barrie, L. (2001). A size-segregated particle dry deposition scheme for an atmospheric aerosol module. *Atmospheric Environment*, 35:549–560.

Zhang, Z., Meyer, K., Yu, H., Platnich, S., Colarco, P., Liu, Z., and Oreopoulos, L. (2016). Shortwave direct radiative effects of above-cloud aerosols over global oceans derived from 8 years of CALIOP and MODIS observations. *Atmospheric Chemistry and Physics*, 16:2877–2900.

Zhao, C., Liu, X., Qian, Y., Yoon, J., Hou, Z., Lin, G., McFarlane, S., Wang, H., Yang, B., Ma, P.-L., Yan, H., and Bao, J. (2013). A sensitivity study of radiative fluxes at the top of atmosphere to cloud-microphysics and aerosol parameters in the community atmosphere model CAM5. *Atmospheric Chemistry and Physics*, 13:10969–10987.

Zilitinkevich, S. S. (1965). Bulk characteristics of turbulence in the atmospheric planetary boundary layer. *Trudy GGO*, 167:49–52.

Appendices

Appendix A

Supplementary material for Chapter 5

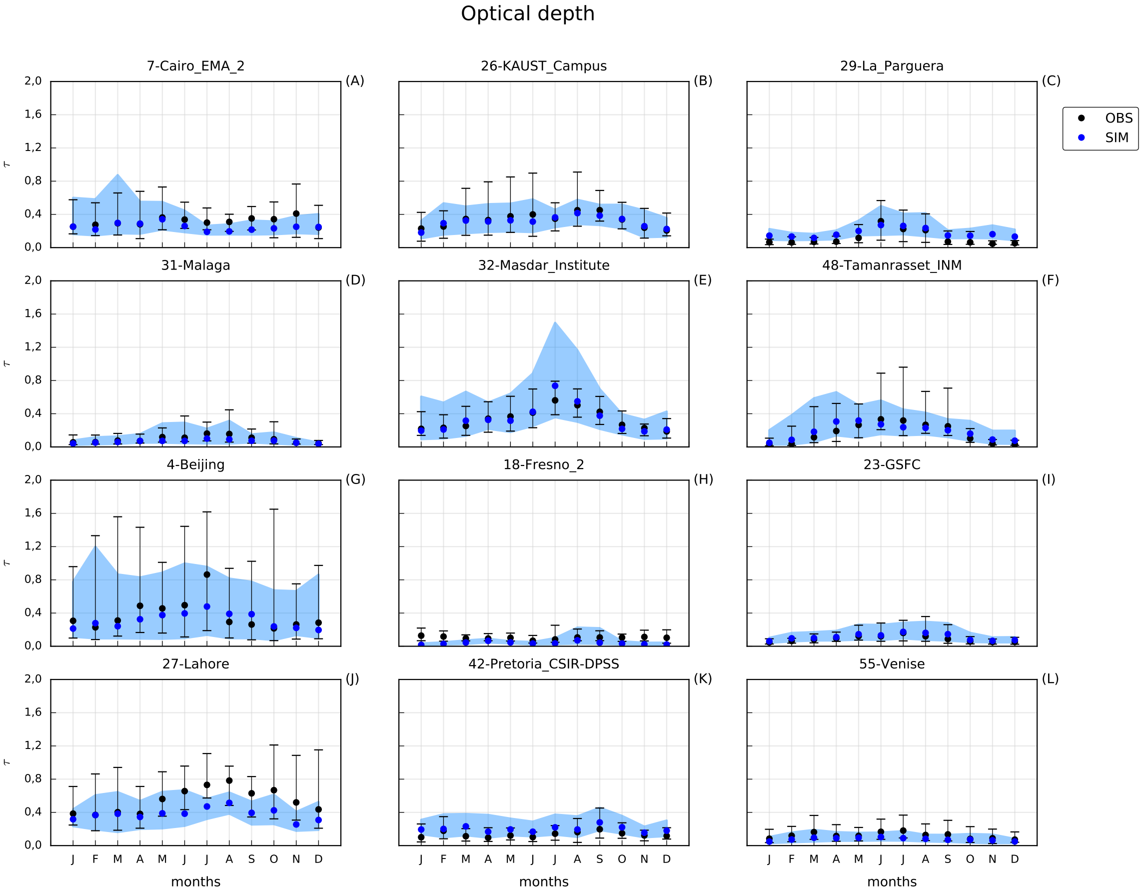

Figure A.1: **Annual trends of simulated (REF case) and observed optical depth (τ) of the aerosol mixture in the 12 subset stations (in alphabetic order from left to right and from top to bottom). The circle points are the monthly medians while error bars (observations) and shadowed regions (simulations) represent the 10^{th} and 90^{th} percentiles. The correlation coefficient (r) and the absolute mean bias (b) on the monthly medians are also reported. The station numbers indicate the corresponding positions in the full list reported in Table 5.2.**

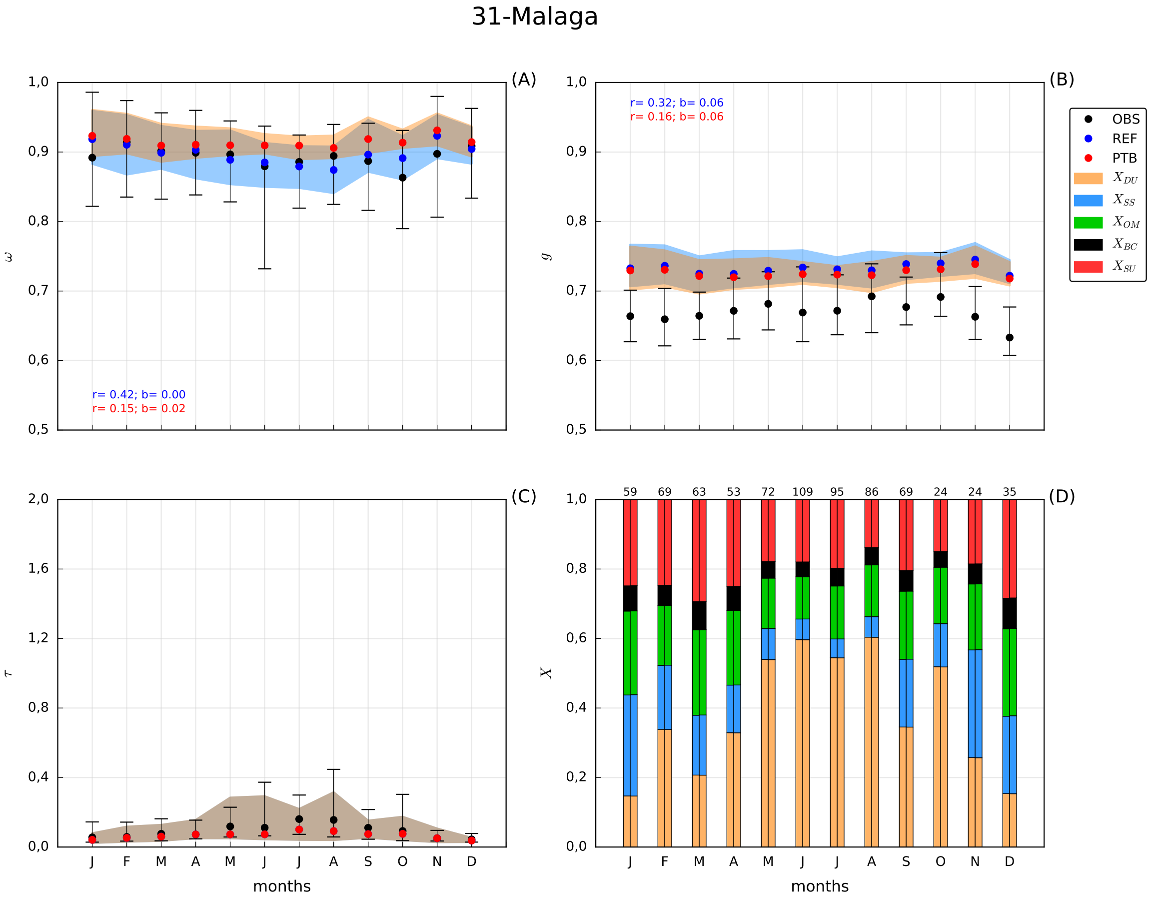

Figure A.2: **Same as Figure 5.5 but in Malaga.**

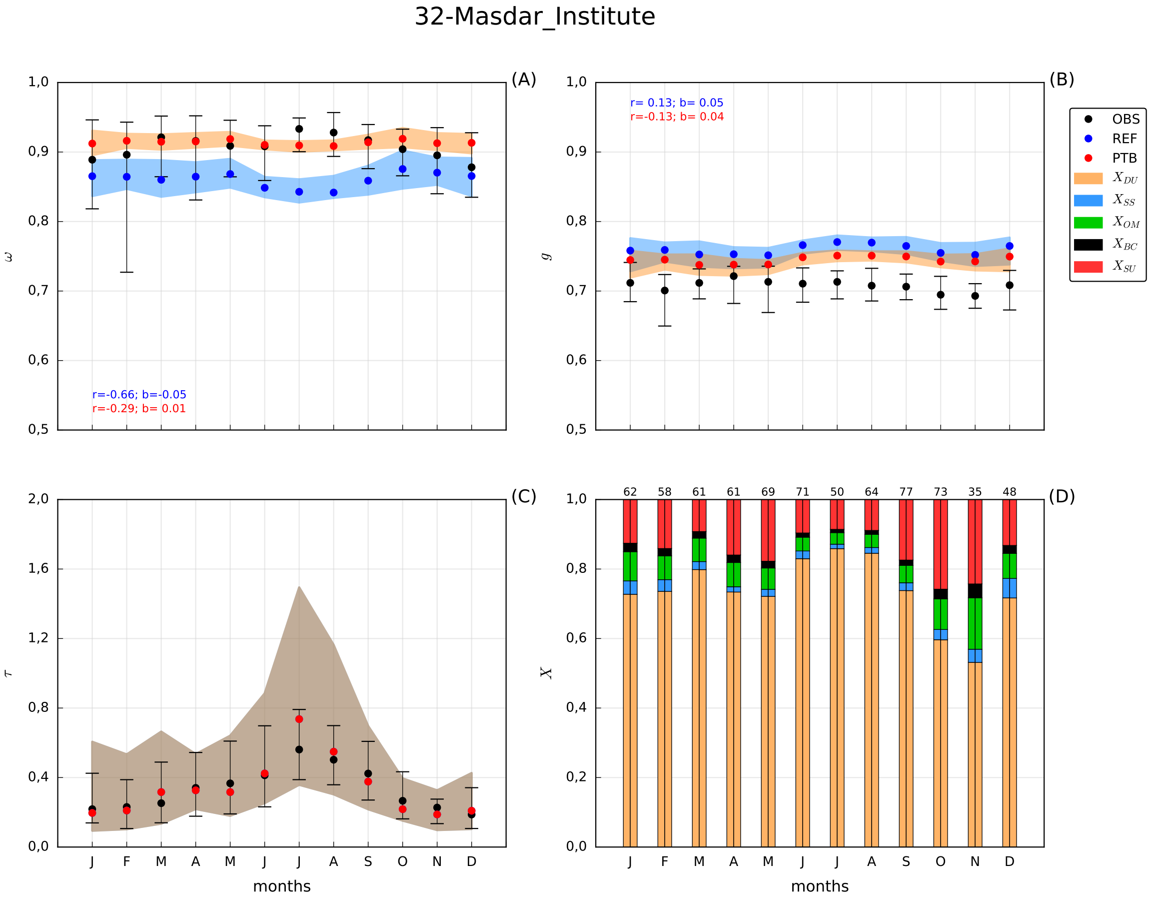

Figure A.3: **Same as Figure 5.5 but in Masdar_Institute.**

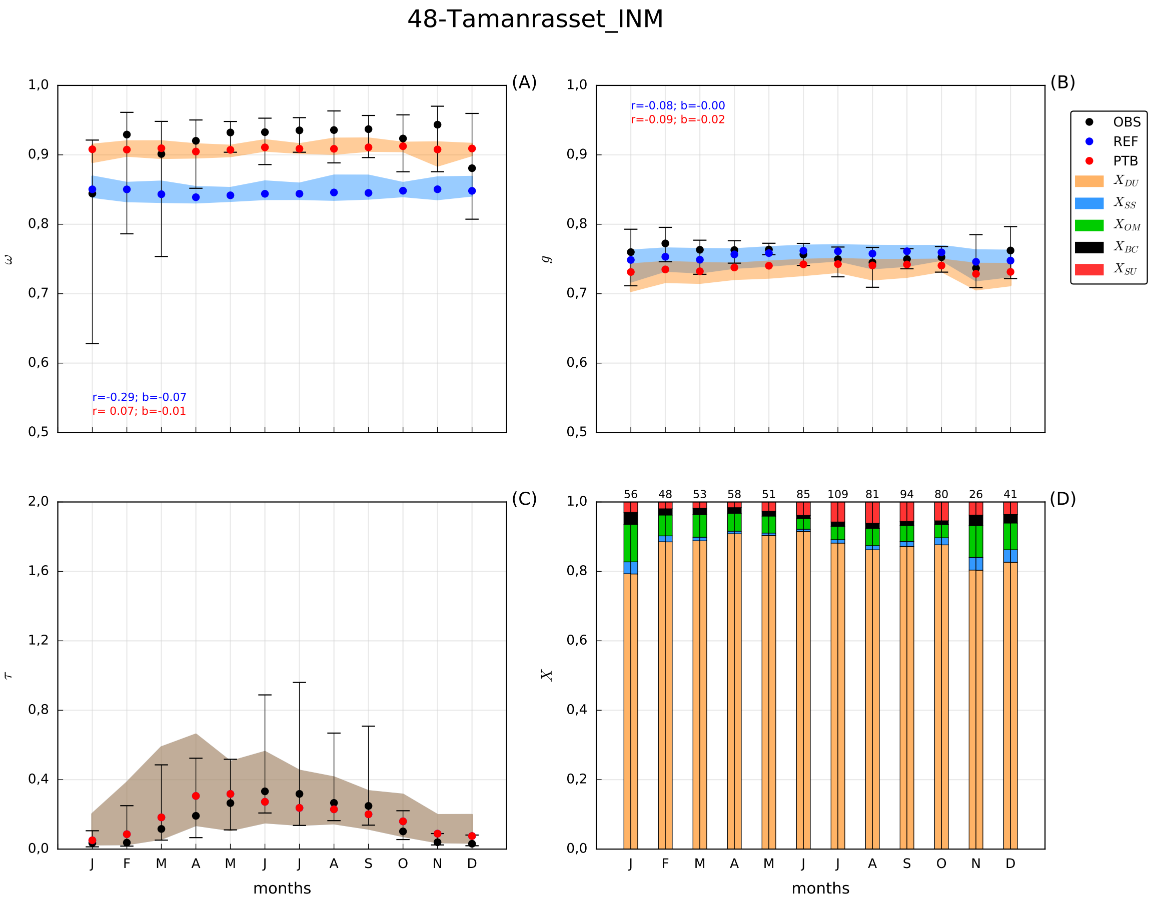

Figure A.4: **Same as Figure 5.5 but in Tamanrasset_INM.**

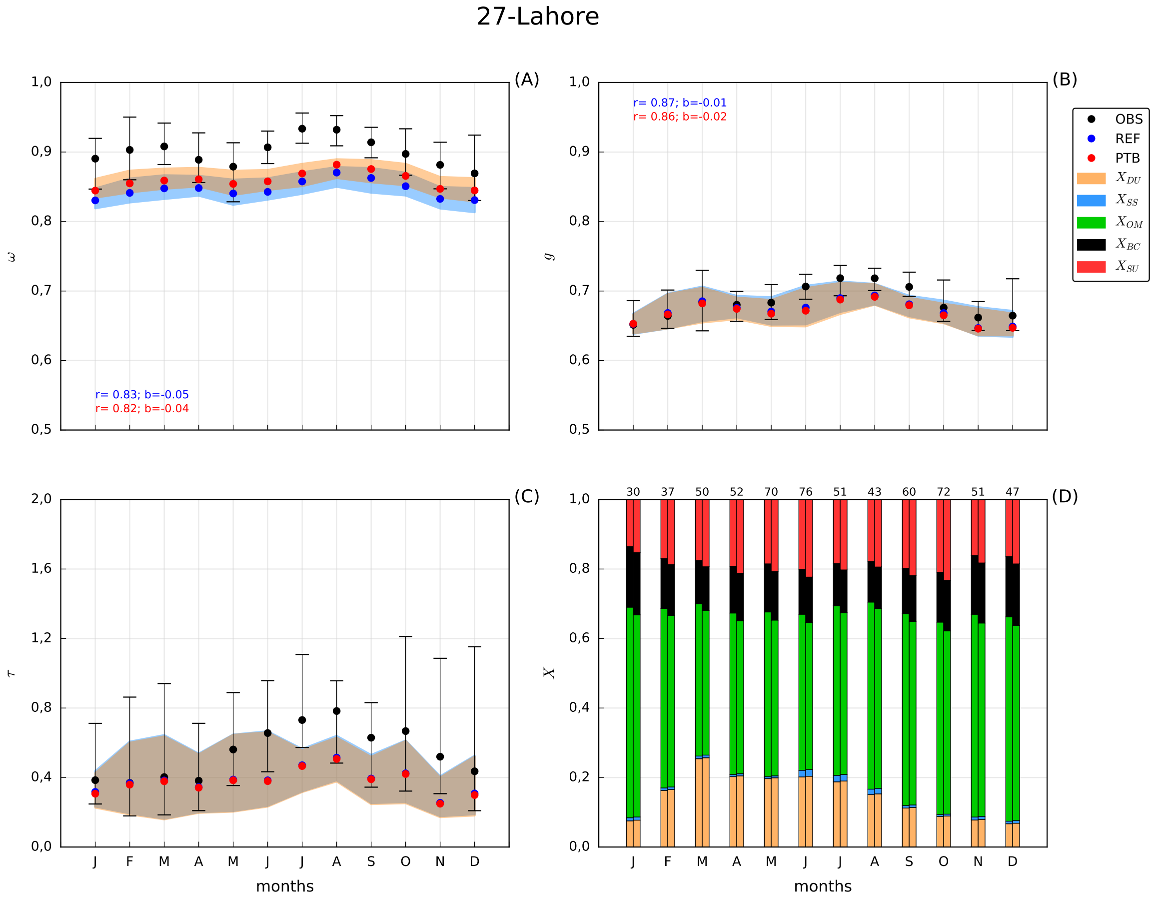

Figure A.5: **Same as Figure 5.5 but in Lahore. Note that the PTB case in this station includes variations of the refractive index only for organic matter and sulfate.**

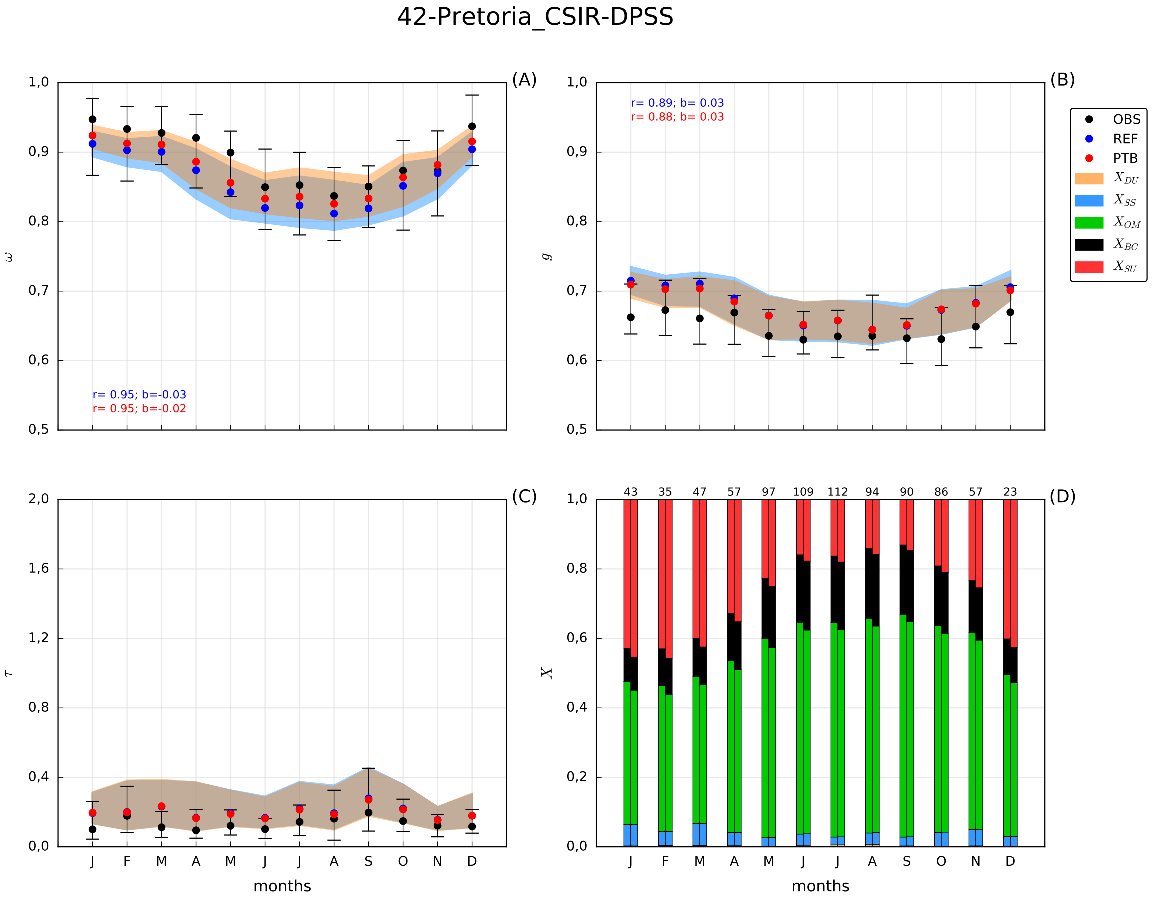

Figure A.6: **Same as Figure 5.5 but in Pretoria_CSIR-DPSS. Note that the PTB case in this station includes variations of the refractive index only for organic matter and sulfate.**

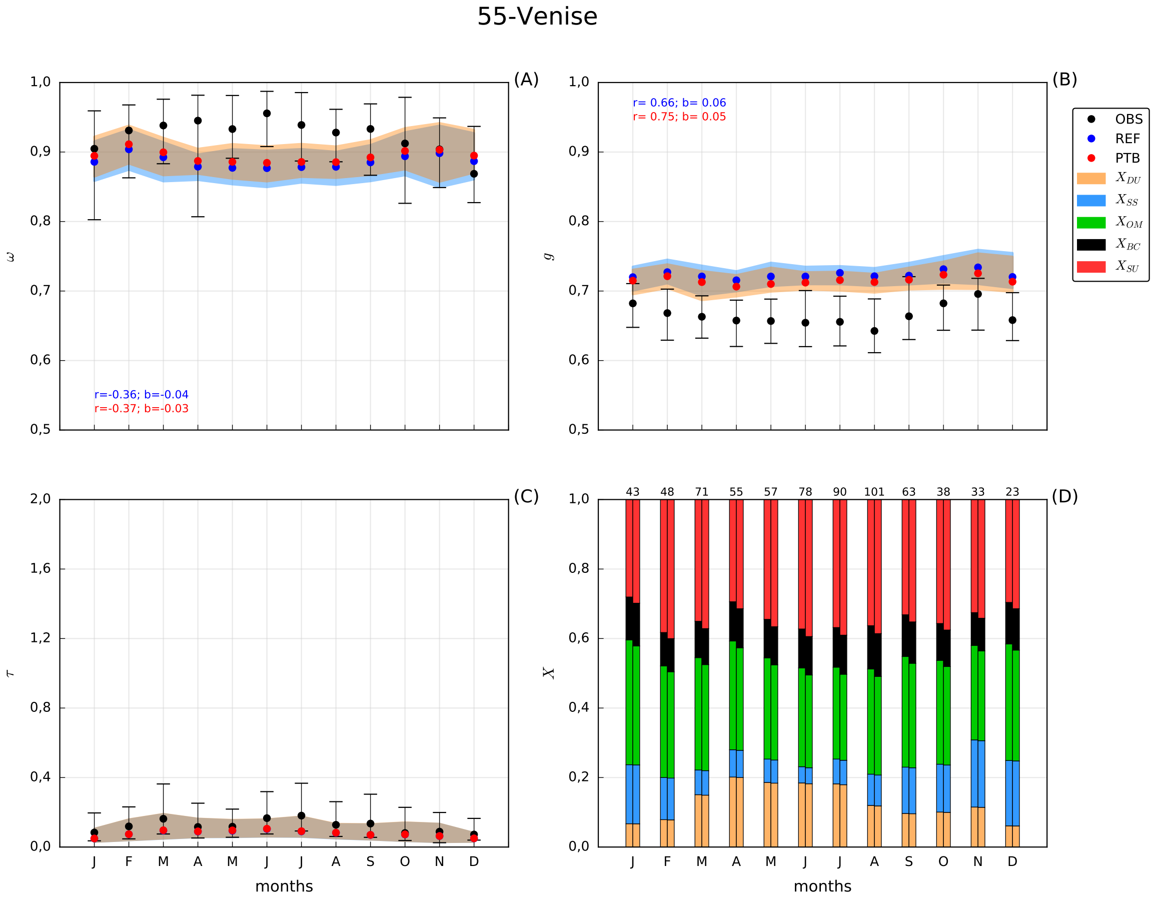

Figure A.7: **Same as Figure 5.5 but in Venise. Note that the PTB case in this station includes variations of the refractive index only for organic matter and sulfate.**

Appendix B

Global evaluation of NMMB-MONARCH aerosol optical depth

A global evaluation of the NMMB-MONARCH aerosol optical depth (AOD) against AERONET direct-sun Level 2 data has been recently carried out (at $0,550$ μm and for the period 2012-2016) at the Earth Science department of the Barcelona Supercomputing Center. In this annex we report some results relative to the year 2012: scatter plots (linear and logarithmic) per region, global statistical maps (the acronyms RMSE and FGE stand for Root Mean Square Error and Fractional Gross Error, respectively) and AOD timeseries per species in the AERONET stations considered as subset stations in this work.

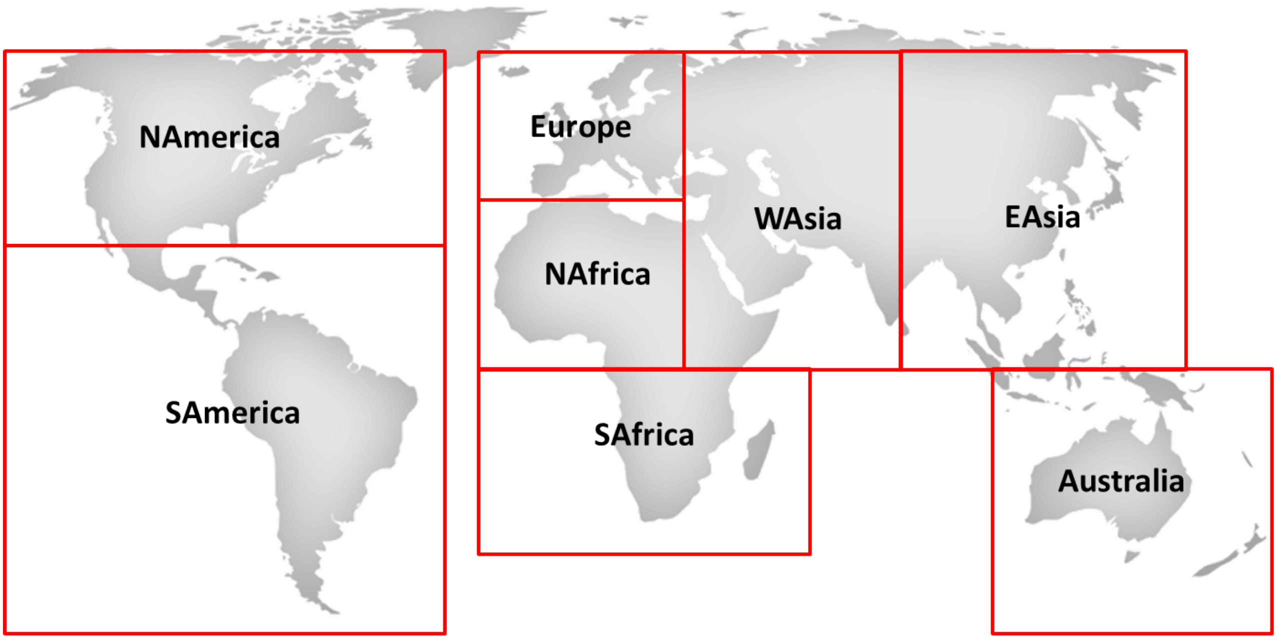

Figure B.1: **Map of regions defined for the global evaluation.**

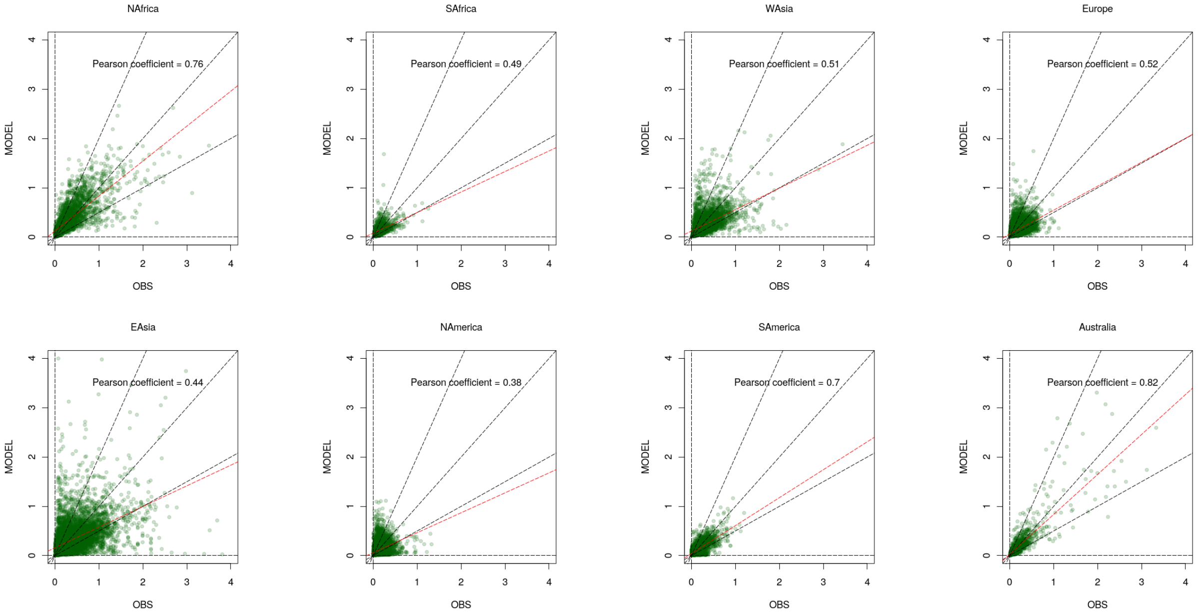

NAfrica

SAfrica

WAsia

Europe

EAsia

NAmerica

SAmerica

Australia

Figure B.2: **Scatter plots per region for 2012.**

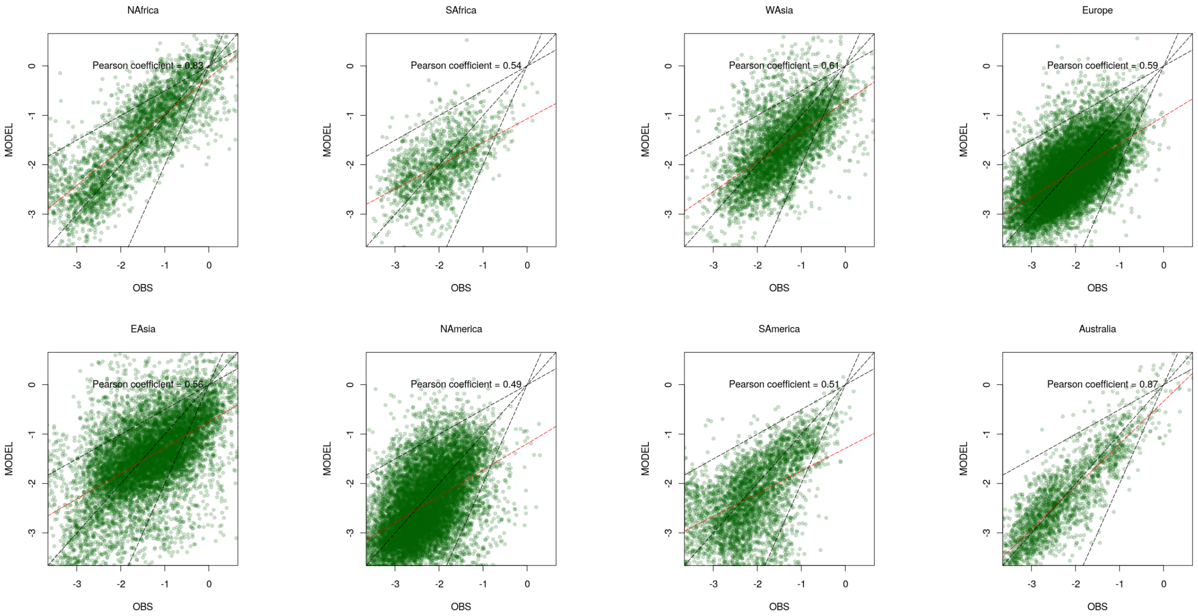

Figure B.3: **Scatter plots (log-scale) per region for 2012.**

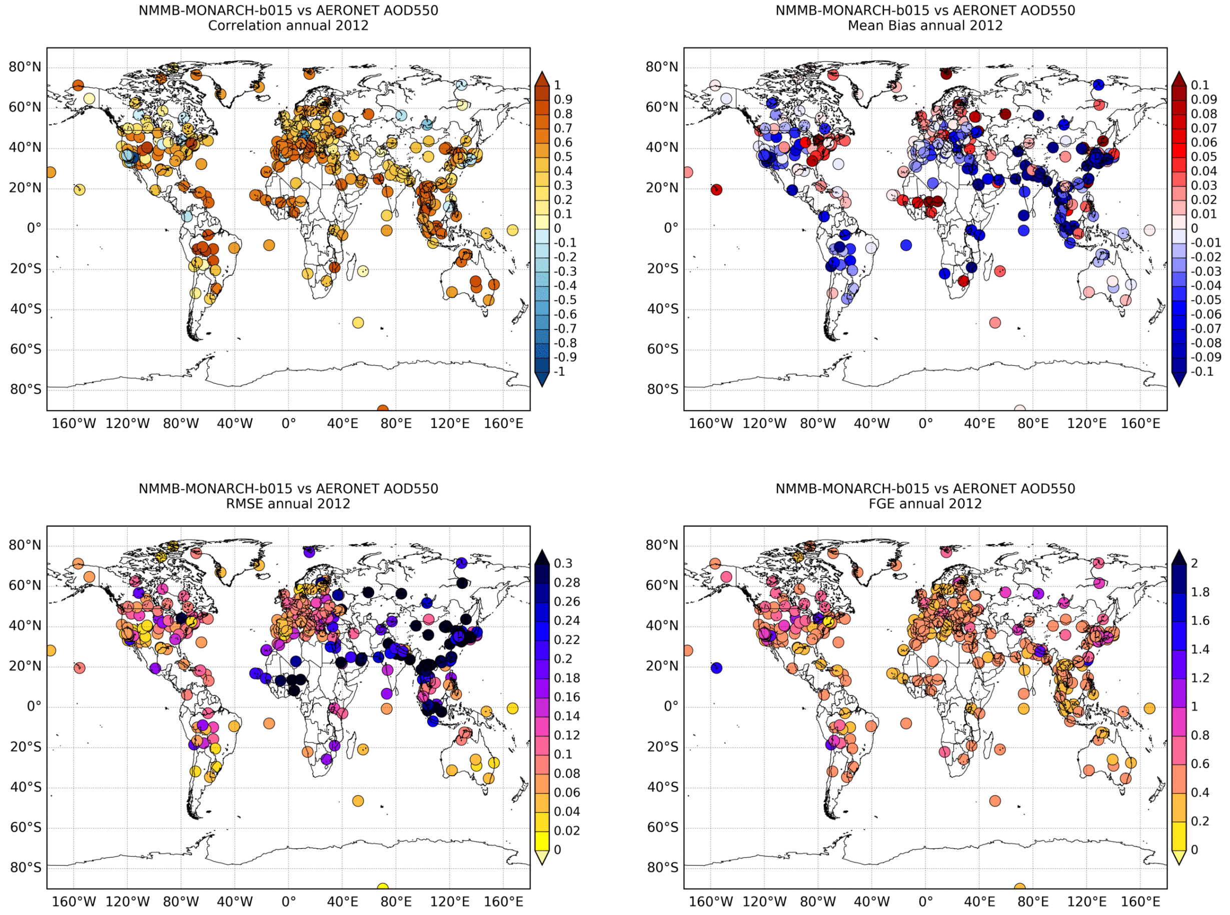

Figure B.4: **Global statistical maps for 2012.**

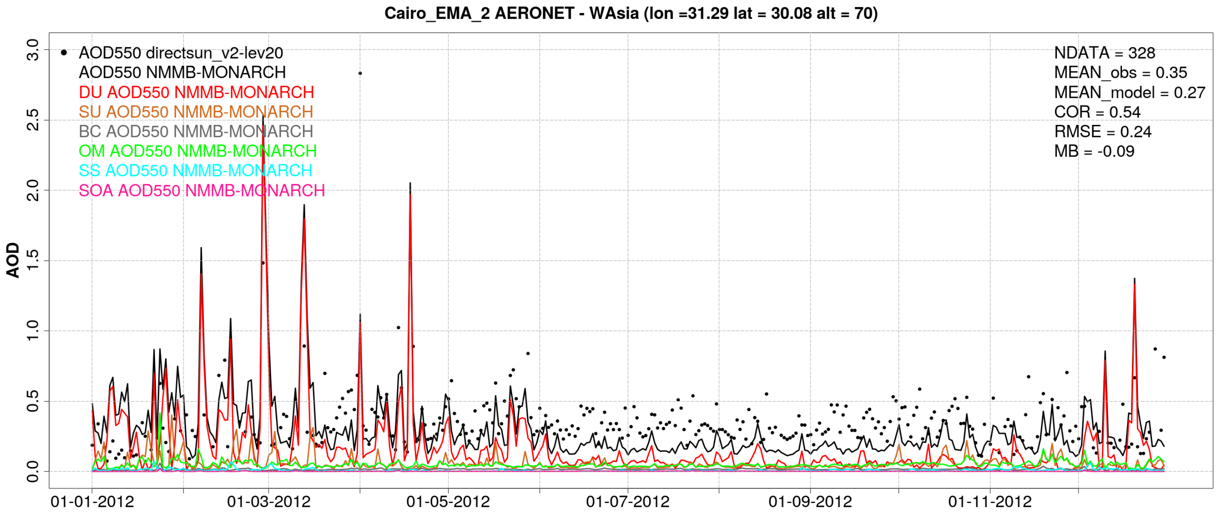

Figure B.5: **Model (per species) vs observed AOD timeseries for 2012 in Cairo_EMA_2.**

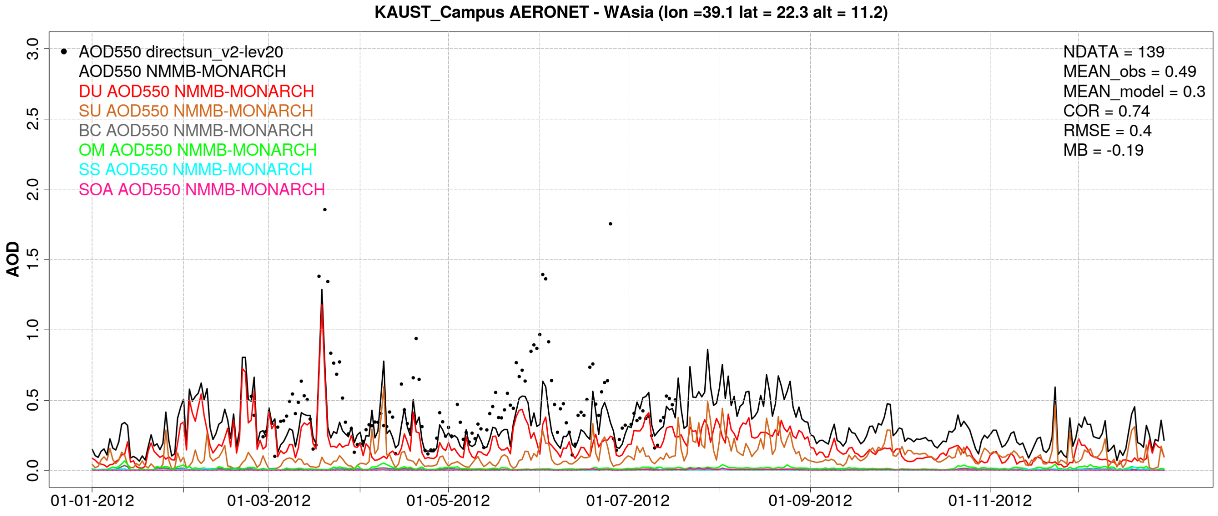

Figure B.6: **Model (per species) vs observed AOD timeseries for 2012 in KAUST_Campus.**

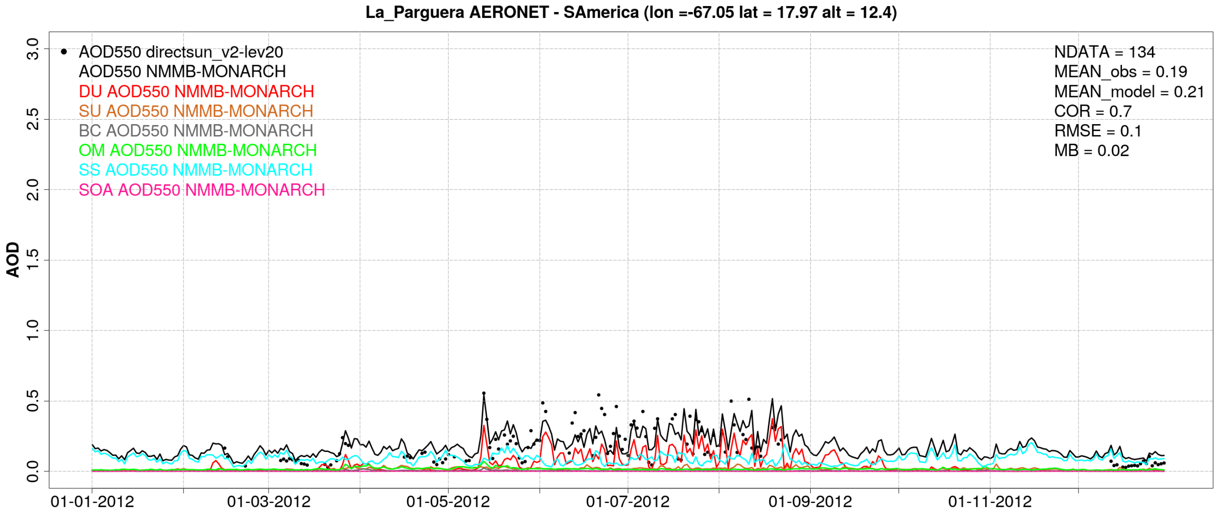

Figure B.7: **Model (per species) vs observed AOD timeseries for 2012 in La_Parguera.**

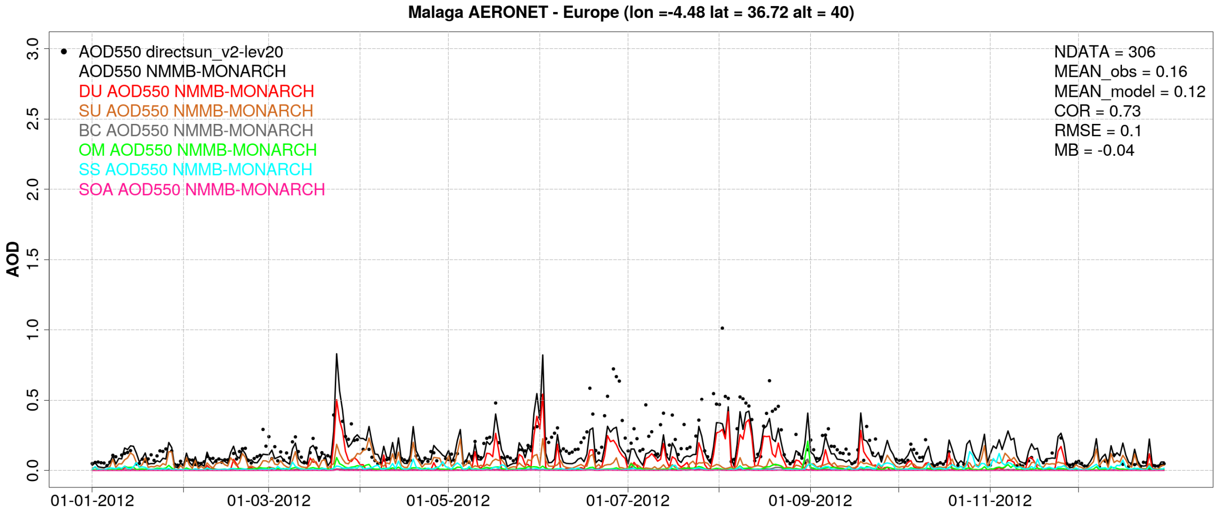

Figure B.8: **Model (per species) vs observed AOD timeseries for 2012 in Malaga.**

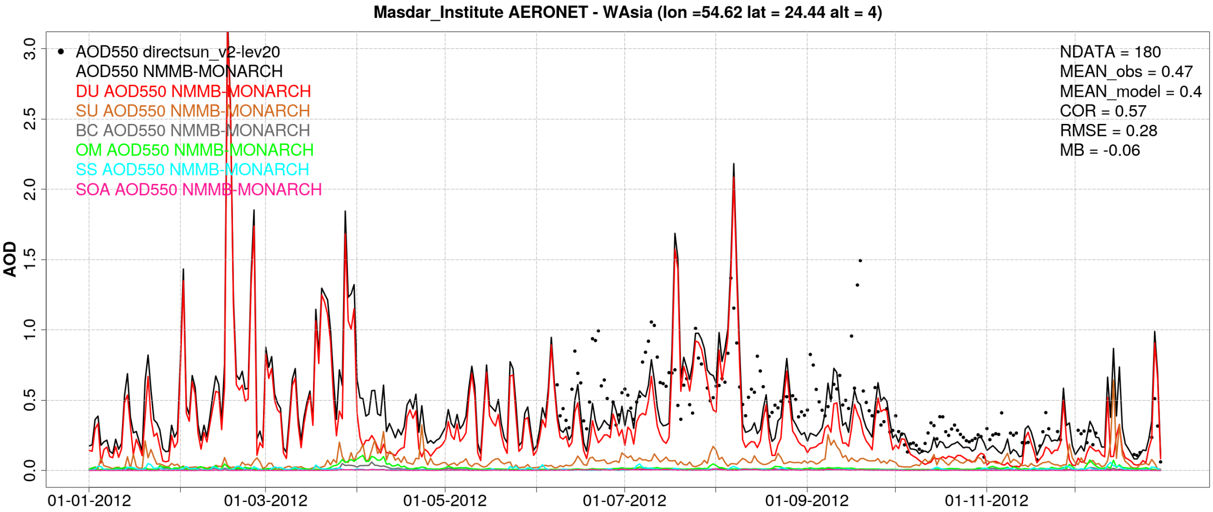

Figure B.9: **Model (per species) vs observed AOD timeseries for 2012 in Masdar_Institute.**

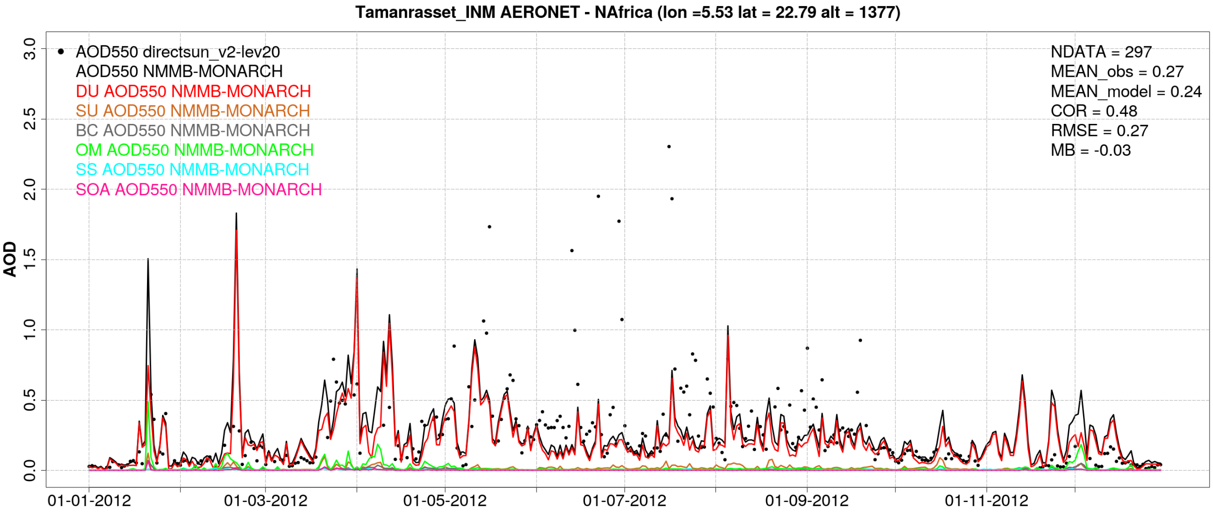

Figure B.10: **Model (per species) vs observed AOD timeseries for 2012 in Tamanrasset_INM.**

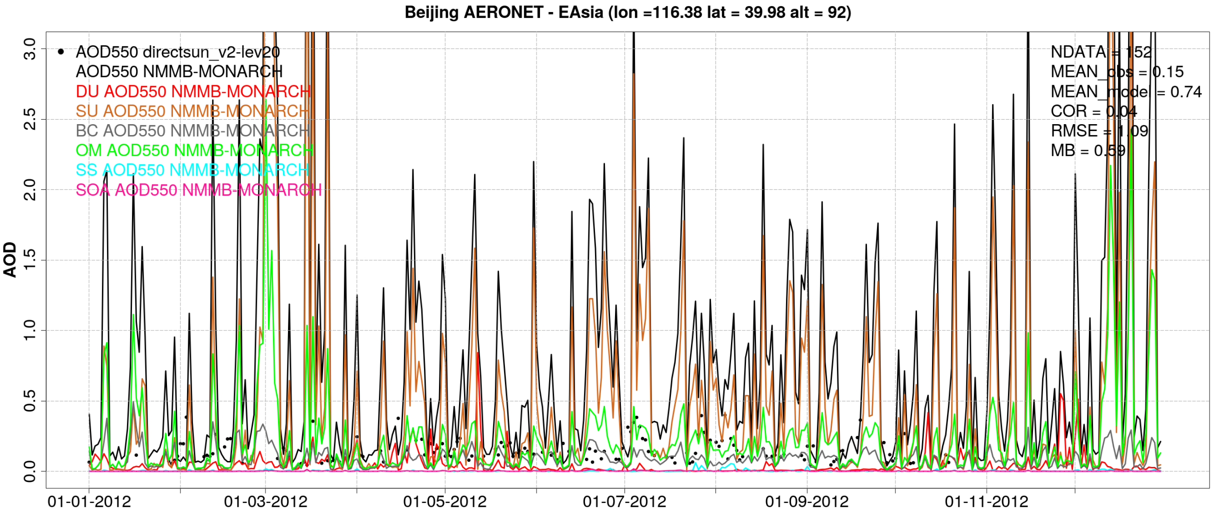

Figure B.11: **Model (per species) vs observed AOD timeseries for 2012 in Beijing.**

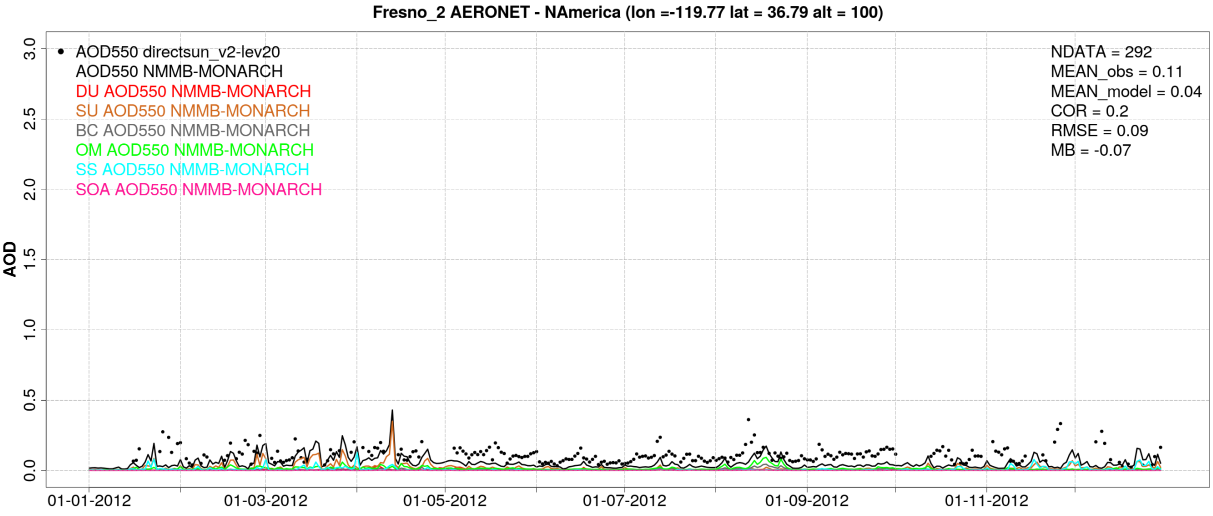

Figure B.12: **Model (per species) vs observed AOD timeseries for 2012 in Fresno_2.**

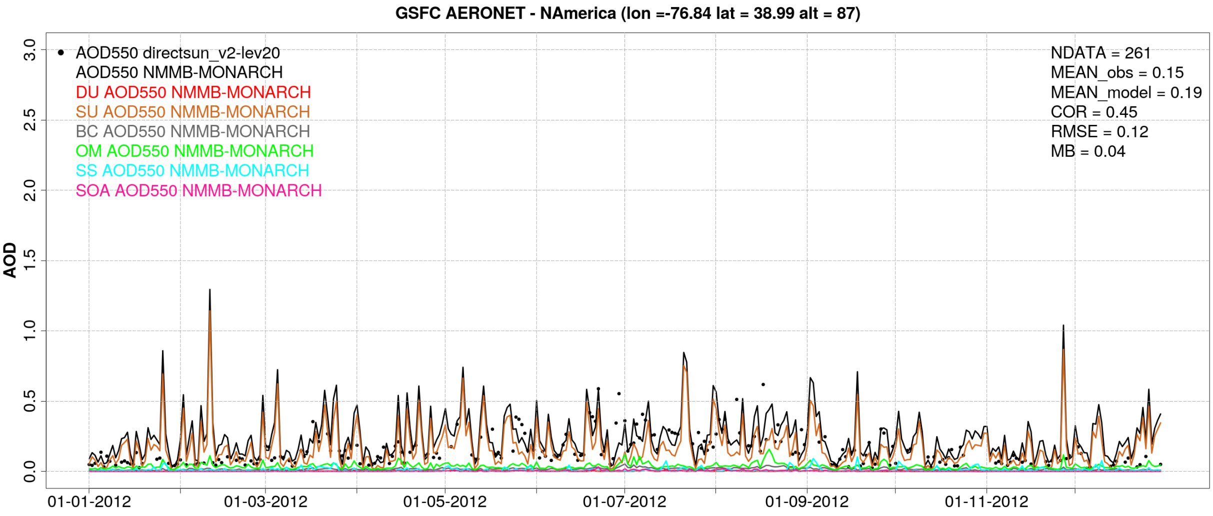

Figure B.13: **Model (per species) vs observed AOD timeseries for 2012 in GSFC.**

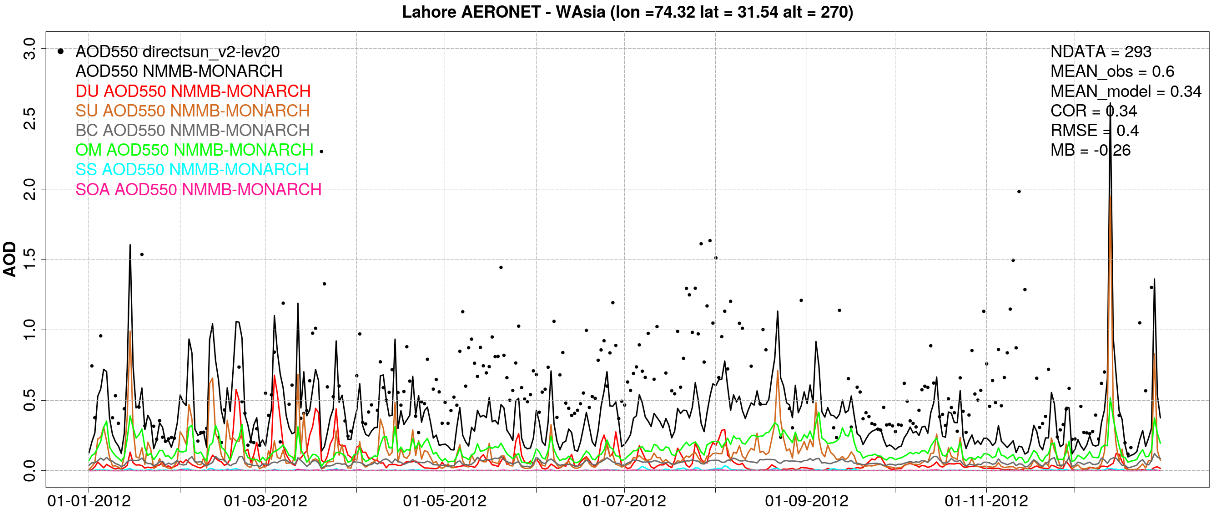

Figure B.14: **Model (per species) vs observed AOD timeseries for 2012 in Lahore.**

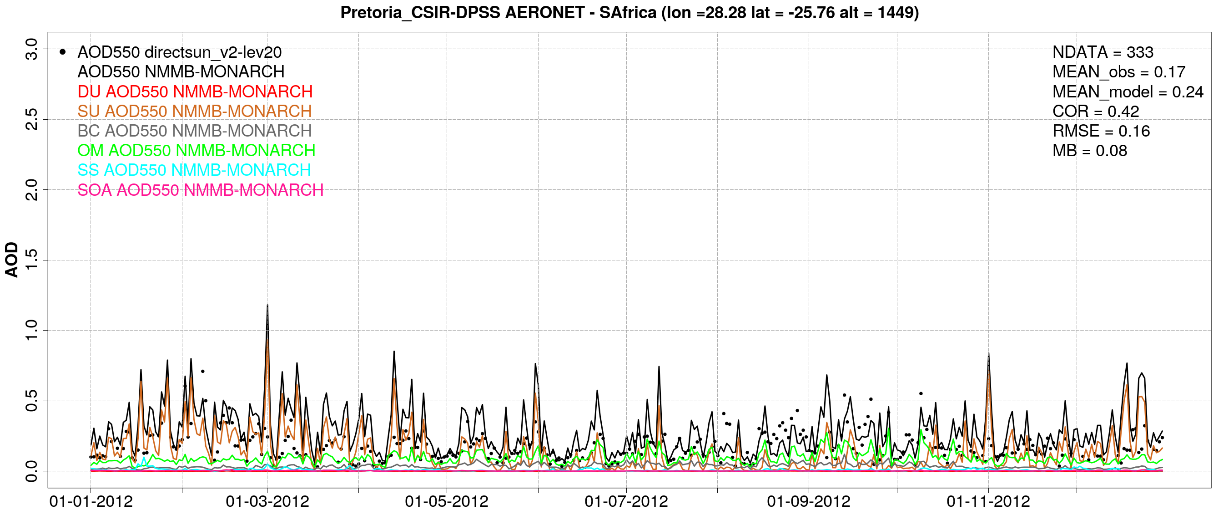

Figure B.15: **Model (per species) vs observed AOD timeseries for 2012 in Pretoria_CSIR-DPSS.**

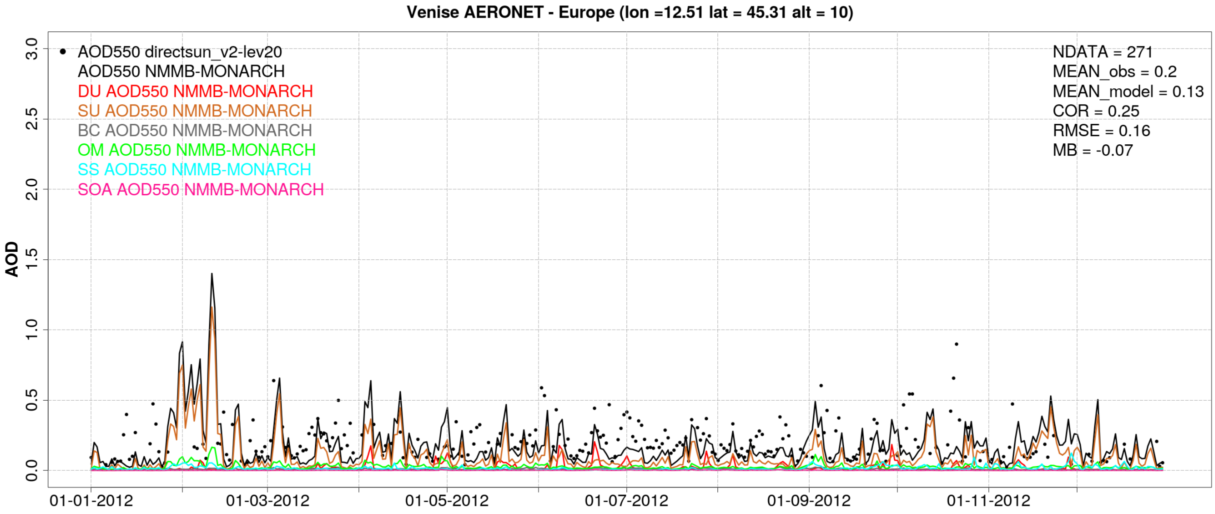

Figure B.16: **Model (per species) vs observed AOD timeseries for 2012 in Venise.**